TEM Investigations on Bismuth-based Perovskite Oxides

Lina Gunawan

TEM INVESTIGATIONS ON BISMUTH-BASED PEROVSKITE OXIDES

By
LINA GUNAWAN, M. A. SC.

A Thesis
Submitted to the School of Graduate Studies
in Partial Fulfilment of the Requirements
for the Degree
Doctor of Philosophy

McMaster University

DOCTOR OF PHILOSOPHY (2010) McMaster University
(Department of Materials Science and Engineering) Hamilton, Ontario

TITLE: TEM Investigations on Bismuth-based Perovskite Oxides

AUTHOR: Lina Gunawan, M. A. Sc. (McMaster University)

SUPERVISOR: Prof. Gianluigi. A. Botton

NUMBER OF PAGES: xxxiv, 161

Abstract

The research presented in this thesis aims to provide fundamental understanding about the structure-property relationships in Bi-based perovskite oxides from the nanoscale to the atomic level so that the properties of these materials can eventually be tuned. This study focused on the investigations of structure and ordering phenomena in several Bi-based compounds, namely a combination of $BiFeO_3$ (BFO) and $BiCrO_3$ (BCO) as well as a layered perovskite $Bi_{4-x}La_xTi_3O_{12}$ ($x = 0.75$) (BLT), using a variety of transmission electron microscopy (TEM) techniques. The performance of the new generation of spherical aberration (C_S)-corrected TEMs with sub-Å spatial resolution was also demonstrated.

The investigations were performed using both conventional TEMs as well as the entirely new generation TEMs (based on aberration correction) as the major characterization instruments. Aberration-corrected TEMs were specifically utilized for analysis at the atomic level, the observation of the structure of defects and probing of valence changes. The importance and advantages of using a C_S-corrector in improving spatial resolution for observations of atomic structure were reviewed in detail.

First, the Bi-based perovskite oxide films of Bi_2FeCrO_6 (BFCO 1/1), consisting of BFO and BCO with a 1:1 ratio and epitaxially grown by the pulsed laser deposition (PLD) technique, were investigated in order to understand the remarkable increase in saturation magnetization. The selected area electron diffraction (SAED) and convergent beam electron diffraction (CBED) experiments revealed various weak reflections, which were explained through systematic elimination of several possible factors. The extra weak reflections in the CBED pattern of the sample oriented with the zone axis <110> arose due to B-site cationic ordering and anti-phase tilting of BO_6 octahedra.

Other weak reflections in the CBED pattern acquired at an orientation parallel to the <100> zone axis correspond to the reflections of a secondary phase, Bi_2O_3, which was formed during the deposition of the film. Electron energy loss spectroscopy (EELS) experiments revealed that both B-site cations, i.e., Fe and Cr, possess the same valence of 3+.

Second, the oxide films produced by the co-deposition of BFO and BCO in a 1:3 ratio, $Bi_2Fe_{0.5}Cr_{1.5}O_6$ (BFCO 1/3), were investigated to study the predicted B-site cationic ordering. Through high angle annular dark field (HAADF) imaging, our results revealed a structure that is different from the double perovskite structure previously expected. The two-dimensional XRD experimental results gave a 3D reciprocal space map, which showed patterns consistent with the SAED patterns and revealed the presence of twinning and variation of in-plane orientations in the film. A modified Ruddlesden-Popper (RP) structure, which closely resembles the atomic structure in the HAADF images, was proposed as an alternate structure for the new model of the BFCO 1/3 unit cell. The refinement of the XRD I-2θ result on the BFCO 1/3 film gives a monoclinic unit cell (space group #14, P 2_1/n) with lattice parameters of a = 10.9764 Å, b = 10.8479 Å, and c = 15.9073 Å, with $\alpha = \gamma = 90^o$ and $\beta = 90.3^o$. The agreement between the simulated and the experimental SAED patterns, however, was limited to the major reflections only.

The last investigated oxide is a well known layered perovskite oxide $Bi_{4-x}La_xTi_3O_{12}$ (x = 0.75), BLT, a candidate material likely to replace lead-based ferroelectric materials in various non-volatile memory devices. The TEM investigations focused on the study of the location of the La dopants in the $Bi_4Ti_3O_{12}$ (BiT) parent unit cell so as to provide new information on the good fatigue resistance of BLT. Through HAADF imaging, we showed the presence of translational defects, out-of-phase boundaries (OPBs), which originate from the film-substrate interface. The EELS maps revealed that La ions are most likely to occupy the top part of the Bi_2O_2 layer in the BiT parent unit cell structure, instead of the perovskite-like layer. The preferential location of La dopants in the BiT unit cell and the presence of OPBs within the films are discussed in terms of the mechanism of the good fatigue resistance of BLT.

In summary, the TEM investigations on several Bi-based perovskite oxides give insights on various structures and defects at atomic scale, which contribute to further un-

derstanding of their physical properties. Throughout the study, the use of aberration-correctors has demonstrated significant improvement in the quality of TEM imaging and analyses, revealing atomic scale information which was previously unattainable with conventional TEMs.

Acknowledgements

I would like to express my deepest and sincere gratitude to my supervisor Dr. Gianluigi A. Botton for his invaluable guidance, extreme patience and countless fruitful discussions throughout my period of study until completion of this thesis. Thanks for giving me a huge opportunity to get involved in operating one of the best TEMs in the world. Additionally, I would like to address considerable appreciation to my PhD committee members, Dr. John Preston and Dr. Adam Hitchcock, of their critical advices, consultations and encouragements in every year of my study period here in McMaster University.

I would like to express my thanks to Dr. Christian Maunders, Dr. Carmen Andrei, Dr. Shery Chang, and Dr. Sorin Lazar, my coaches and mentors in comprehending various microscopes as well as grasping various practical operational tips. Thanks to my sample providers and collaborators from INRS Énergie, Materiaux et Télécommunications, Riad Nechache, Olivier Gautreau, and Dr. Alain Pignolet. Our collaboration was exceptionally fruitful and rewarding. Thanks to Yang Shao and Yuepeng Zhang, for always being there, providing constructive discussions and insights regarding perovskite materials and other characterization methods other than TEM.

Thanks to Lena Fitting Kourkoutis (Cornell University) for hints and tips in MultiPrep sample preparation. Thanks to Dr. Michael Robertson (Acadia University) for useful tips and tricks on using MultiPrep instrument and electron microscopy multislice simulation. Thanks to Dr. Jim Britten (Dept. of Chemistry, McMaster University) for help in XRD experiments, and to Fred Pearson and Andy Duft for countless help in any kind of instrumental problems I faced repeatedly in the microscopy lab.

Thanks for constant and cordial friendship to all my friends, Mariana Budiman, Daisman Purnomo, Somaradi Khiev, Julia Huang, Edgar Huante-Ceron, Ana Villafranca, Manuel Campidelli, and Nicholas Mailman. I cherished your presence in my graduate student life. Thanks to all occupants of JHE A-406, especially Beth McNally and Nadi Braidy. Thanks also to all other members of Botton's group.

Special thanks to my beloved husband, Herdawandi Halim, for providing patient and attentive ears to my erratic complaints, being an excellent partner in prayer, and rescuing me from malnutrition. It would be impossible for me to accomplish this without your presence by my side.

Thanks to all members of *True Jesus Church Toronto*, especially Michael and Janet Yaw, for spiritual support and constant reminder that God makes everything beautiful in His time.

Finally, I deeply appreciate financial support for this study that was provided by the *Natural Sciences and Engineering Research Council of Canada* and *Ontario Center of Excellence.*

Contents

1 Introduction **1**

1.1 Perovskite Oxides 1

1.2 C_S-corrected Transmission Electron Microscopy 3

1.3 Overview 4

2 Literature Review **7**

2.1 Background of C_S-corrector in TEM 9

2.2 The Resolution Limits of TEM 11

2.3 Principles of imaging techniques 17

2.3.1 Diffraction Contrast and Phase Contrast (High Resolution TEM) Imaging 17

2.3.2 Image formation in Phase Contrast Imaging 18

2.3.3 The C_S-corrector role 24

2.3.4 Fundamental mechanism of C_S-corrector 26

2.4 Perovskite Oxides 31

2.5 Bismuth-based perovskite oxides 34

2.5.1 $BiFeO_3$ (BFO) 34

2.5.2 $BiCrO_3$ (BCO) 35

2.5.3 Bi_2FeCrO_6 (BFCO) 36

2.5.4 $Bi_{4-x}La_xTi_3O_{12}$ (BLT) 37

3 Experimental Procedures **43**

3.1 Pulsed Laser Deposition 43

3.2 TEM Sample Preparation 45

3.2.1 Conventional Sample Preparation 45

3.2.2 Tripod Polishing by MultiPrep™ 47

3.2.3 Gentle Mill™ 48

3.3 TEM Instruments 50

4 Results and Discussion **55**

4.1 Bi_2FeCrO_6(BFCO 1/1) 58

4.1.1 Observation of Ordering Using Electron Diffraction Techniques 58

4.1.2 Compositional Modulation of Fe and Cr by EDX Analysis 59

4.1.3 Structural Investigations by CBED Technique 62

4.1.4 Determination of Fe and Cr Valence by Electron Energy Loss Spectroscopy 76

4.2 $Bi_2(Fe_{0.5}Cr_{1.5})O_6$ (BFCO 1/3) 84

4.2.1 Layered patterns of BFO/BCO (1/3) 85

4.2.2 EDX Analysis of BFCO 1/3 film 87

4.2.3 Analysis of SAED Patterns and XRD2 3D Reciprocal Space . . 92

4.2.4 Lattice Parameters Determination 101

4.2.5 Simulated SAED Patterns and Atomic Projection 103

4.2.6 Elemental Distribution of BFCO 1/3 at Atomic Scale by EELS 107

4.3 $Bi_{4-x}La_xTi_3O_{12}$ (BLT) 111

4.3.1 Compositional Analysis and Elemental Distribution by EDX . . 112

4.3.2 Structural Investigation in Atomic Scale 115

5 Summary and Future Work **143**

A Titan Ray Diagrams in TEM/STEM Modes **149**

B List of Software **153**

Bibliography **155**

List of Figures

2.1 Some of the TEM features consist of imaging, diffraction and analytical techniques. (Legend: SAD = Selected Area Diffraction; CBED = Convergent Beam Electron Diffraction; EELS = Electron Energy Loss Spectroscopy; EDX = Energy Dispersive X-ray spectroscopy; and EFTEM = Energy Filtered TEM) 8

2.2 Ray diagrams illustrating the reciprocity theorem between TEM and STEM modes. The reciprocity applies when the STEM illumination angle is equal to TEM objective angle and TEM illumination angle is equal to STEM detector angle. (adapted from Sande and Hall, 1979) . 8

2.3 The Contrast Transfer Function of an electron microscope simulated with the JEMS software shows the point resolution limit and the information limit between (a) non-C_S-corrected and (b) C_S-corrected microscope. (Red line represents the product of the envelope functions, green line spatial envelope, blue line temporal envelope, and black line the contrast transfer function) 12

2.4 Illustration of several lens aberrations: (a) a perfect lens; (b) spherical aberration; (c) chromatic aberration (different colour indicates different energy). (from Pennycook et al., 2006) 15

2.5 Schematic illustration of diffraction from a point which results in the formation of an Airy disk. Two well-separated objects give rise to easily resolved Airy disks. With decreasing distance between two objects, Airy disks start to overlap and reach a diffraction limit (Rayleigh criterion). Further overlap of two Airy disks beyond the Rayleigh criterion results in unresolved two objects. (adapted from http://hyperphysics.phy-astr.gsu.edu/Hbase/phyopt/Raylei.html, Nave, 2006) 16

2.6 Schematic illustrations of (a) bright field (BF) imaging and (b) dark field (DF) imaging modes. Distinct objective aperture selection of the transmitted beam in (a) and the diffracted beam in (b) is indicated. (adapted from http://microscopy.ethz.ch, Krumeich, 2007) 17

2.7 Schematic illustration of (a) the ray diagram for phase-contrast or High Resolution TEM (HRTEM) imaging (adapted from http://www. microscopy.ethz.ch, Krumeich, 2007), (b) the incident beam-sample interaction, (c) the interference between a transmitted beam and one diffracted beam, and (d) the interference between transmitted beam and six diffracted beams resulting in lattice fringes image (adapted from Williams and Carter, 1996) 19

2.8 Schematic illustration of the electron beam interaction during the HRTEM image formation. (adapted from Kirkland, 1998) 20

2.9 (a) Division of a thick sample into thin slices, where each slice is considered as a phase grating at which transmission of the wavefunction occurs. (b) Propagation of the wavefunction between two slices. The wavefunction in an x,y plane at z propagates to the x,y plane at $z+\Delta z$. Each point in the wavefront at z emits a spherical wave and all these waves combine at each point in the x,y plane at $z+\Delta z$. (from Kirkland, 1998) 22

2.10 (a) Hexapole correctors as proposed by Rose (1990), located after the objective lens (OL), consists of two hexapoles (HP1, HP2) and two doublet transfer lenses (TL11, TL12, and TL21, TL22) (from Hetherington, 2004). (b) Quadrupole-octupole correctors as proposed by Krivanek (2003). C2 corresponds to the second condenser lens and OL the objective lens. (from Bleloch and Lupini, 2004) 27

2.11 Diffractogram tableau from the uncorrected and C_S-corrected TEM. The beam tilt angle, $|\tau|$, is 10.8 mrad and the azimuthal angles are between 0 – 2π with increment of $\pi/6$. (from Uhlemann and Haider, 1998) 28

2.12 The diffractograms pertaining to various wave aberrations: (a) A_1 twofold astigmatism, (b) C_1 defocus, (c) A_2 threefold astigmatism, (d) B_2 second order axial coma, (e) A_3 fourfold astigmatism, (f) S_3 star aberration, (g) C_3 third order spherical sberration, (h) A_4 fivefold astigmatism, (i) B_4 fourth order axial coma, (j) D_4 three lobe aberration, (k) A_5 sixfold astigmatism, and (l) C_5 fifth order spherical aberration (*Courtesy of: Shery Chang, Monash University, Melbourne, Australia*). 30

2.13 Diffractograms from (a) uncorrected with C_S of 0.5 mm and (b) C_S-corrected TEM with C_S of 0.01 mm (from Sawada et al., 2005). The slanted lines in (b) resulted from the image shift that is intentionally introduced during the image acquisition. 31

2.14 (a) The unit cell and the stacking sequence of perovskite ABO_3. (b) The 180° polarization reversal for two of the six possible polarization states is produced by displacement of the central cation in the tetragonal plane. (from Haertling, 1999) 32

2.15 Classification of piezoelectrics and their subgroups on the basis of symmetry (from Haertling, 1999). The abbreviations in the ceramic perovskites correspond to lead zirconate titanate (PZT), lead lanthanum zirconate titanate (PLZT), lead titanate (PT), and lead magnesium niobate (PMN). 33

2.16 Magnetization hysteresis of a 300 nm thick BFCO film (squares) compared to that of a 300 nm thick BFO film (circles) at room temperature. The inset shows a zoom around the origin. The direction of applied magnetic field H was in the plane of the films, along the <100> direction of STO. (from Nechache et al., 2006) 38

2.17 Fatigue, one of the major problems with ferroelectric materials for non-volatile memory applications, occurs due to the decreasing number of switchable domains with increasing number of polarization reversal (write/read cycles) (from Ishiwara et al., 2004) 39

2.18 (a) The widely-accepted crystal structure of BiT. Perovskite $Bi_2Ti_3O_{10}$ and fluoritelike Bi_2O_2 layers stacked alternatively along the c-axis. (Kim et al., 2007) (b) Lattice structure of the La-doped bismuth titanate. The compound studied is $Bi_{3.25}La_{0.75}Ti_3O_{12}$ (BLT) where La ions can also be substituted by other rare-earth ions such as Pr, Nd, or Sm. (Park et al., 1999) 40

3.1 An illustration of the basic PLD system (from Lowndes et al., 1996). . 44

3.2 (a) An illustration of the configuration of the Si-clamped sample in conventional TEM sample preparation. The thin film on the two pieces of sample was glued face-to-face. (b) The position of the ultrasonic circular cut on a $\sim$ 200 μm thick Si-clamped sample. 46

3.3 An illustration of the sample position on the MultiPrep sample holder. 48

3.4 (a) A picture of Allied High-Tech MultiPrep^{TM} instrument. (b) A closer look of the position of the (static) sample holder relative to the diamond lapping film on the (rotating) platen. The rotation of the platen used in this study is in clock-wise direction. (from http:// www.alliedhightech.com, Allied, 2008) 49

3.5 High resolution HRTEM images of an interface acquired by (a) non-corrected Titan (Cs-corrector OFF) and (b) corrected Titan (Cs-corrector ON) 52

4.1 (a) A cross sectional bright field TEM image, (b) corresponding SAED pattern of a BFCO film on (100)SRO/STO, and (c) SAED pattern of (100)STO substrate. The major reflections in the SAED pattern of BFCO 1/1 film were indexed based on the STO substrate. The yellow arrows in (b) highlight the weak reflections along $<110>_{STO}$ 60

4.2 (a) The ADF image of BFCO sample; (b) - (f) elemental EDX maps of titanium (Ti), strontium (Sr), bismuth (Bi), iron (Fe) and chromium (Cr), respectively. 61

4.3 The EDX linescans of Cr and Fe from the region defined by vertical lines in the image (a) are displayed as red and black curves, respectively, in (b). The compositional modulation is clearly demonstrated as Cr signals decrease where Fe signals increase, and vice versa. 62

4.4 (a) Bright field image and (b) HREM image of the sample; SAED patterns of (c) BFCO + substrate (STO) and (d) substrate alone in the direction parallel to the zone axis (ZA) $<100>_{STO}$ 64

4.5 CBED patterns of a BFCO film acquired with the sample oriented at the ZA $<100>_{STO}$ from the thin area to gradually thicker areas, (a) - (e), were acquired along the direction indicated by the white arrow. The electron beam diameter is $\sim$ 150 nm. 66

4.6 (a)-(c) CBED patterns of BFCO films at different locations of the BFCO film as indicated in the corresponding images, where (a) is the thinnest area and (b) and (c) are thicker areas with overlapping grains. 67

4.7 An illustration of octahedra in (a) an ideal perovskite system, ABX_3, (b) a B-site ordering double-perovskite system, AB'B"X_3, (c) an in-phase tilt system, (d) an anti-phase tilt system (from Thesis of Knapp, 2006), (e) a cooperative Jahn-Teller distortion (CJTD) of the first layer of $KCuF_3$, and (f) a CJTD of succesive layer of $KCuF_3$ (from Lufaso and Woodward, 2004). In both in-phase and anti-phase tilt systems, the tilt axis is along the *c*-axis and perpendicular to the page. The thick black lines in the CJTD systems represent the long B-X bonds, while the thinner lines represent the short or medium length B-X bonds. 68

4.8 Schematics of diffracton patterns at different zone axes for pseudo-cubic settings where α, β and γ are in the $\{h+1/2,\ k+1/2,\ l+1/2\}$, and $\{h+1/2,\ k,\ l\}$, and $\{h+1/2,\ k+1/2,\ l\}$ (where $h \neq k$) positions. (from Reaney et al., 1994) 71

4.9 CBED patterns recorded in the direction parallel to the ZA$<110>_{STO}$ of (a) STO substrate and (b) BFCO film; CBED pattern recorded in the direction parallel to the ZA$<100>_{STO}$ of (c) BFCO film. White arrows in (b) indicate the extra reflections due to antiphase tilting of BO_6 octahedra or B-site cationic ordering along <111> direction. White arrows in (c) indicate the extra reflections along (*0kl*) directions, which correspond to neither in-phase tilting nor anti-parallel shifts of A-site cations. 72

4.10 (a) The CBED pattern and (b) the schematic of the corresponding reflections and indices in the direction parallel to the ZA <100> of BFCO 1/1, where the Bi_2O_3 reflections are indicated by yellow arrows. (c) The CBED pattern and (d) the schematic of the corresponding reflections and indices in the direction parallel to the ZA <110> of BFCO 1/1, where the Bi_2O_3 reflections are indicated by yellow arrows and the extra weak reflections by blue arrows. 73

4.11 (a) The ADF image of BFCO 1/1 from which the elemental maps were acquired. (b)-(f) The elemental maps of Bi, Sr, Fe, Cr and Ti, respectively. 75

4.12 (a) and (c) Reference spectra of Cr L-edge and Fe L-edge taken by non-monochromated (top, energy resolution $\sim$ 0.65 eV) LaB_6 CM20 and monochromated (bottom, energy resolution $\sim$ 0.15 eV) Tecnai F20 microscopes. (Mitterbauer et al., 2003), (b) and (d) Experimental spectra of Cr $L_{2,3}$ edge and Fe $L_{2,3}$ edge taken by VG HB 601 STEM (100 kV, energy resolution at the Zero Loss Peak of $\sim$ 0.4 eV). 78

4.13 Background subtracted Mn-$L_{2,3}$ ionization edge in MnO_2. The cross section removal by Hartree–Slater and modified double-step hydrogenic continuum models are performed at peak maxima with height ratio of 2:1. The shaded regions indicates the positions of normalization and integration windows. (from Schmid and Mader, 2006) 79

4.14 (a) and (b) Reference spectra of O K-edge from Cr_2O_3 and α-Fe_2O_3 as taken by non-monochromated (top, energy resolution $\sim$ 0.65 eV) LaB_6 CM20 and monochromated (bottom, energy resolution $\sim$ 0.15 eV) Tecnai F20 microscopes; (c) Experimental O K-edge from the BFCO film acquired with VG HB 601 STEM(100 kV, energy resolution at the Zero Loss Peak of $\sim$ 0.4 eV). (Mitterbauer et al., 2003) 80

4.15 Splitting of the energy level of orbitals due to the crystal field effect (octahedral symmetry) and further due to the Jahn-Teller distortion (tetragonal symmetry). 82

4.16 The in-field hysteresis loop of piezo force microscopy (PFM) are displayed for (a) BFCO 1/3 (111)-oriented film and (b) BFCO (BFCO 1/1) (111)-oriented film, respectively. The PFM signals were recorded in z- (growth) and x- (lateral) directions. (from Nechache et al., 2007) 86

4.17 The hysteresis-magnetization (M-H) curves of BFCO 1/1 and BFCO 1/3 film grown by dual-beam PLD and BFCO 1/1 film grown by conventional PLD (legend: BFCO). All films were grown on a (111)-oriented substrate. (from Nechache et al., 2007) 87

4.18 (a) Non C_S-corrected ADF image of BFCO 1/3 thin film recorded with the sample oriented at the ZA $<101>_{STO}$ indicates a smooth film with a slight variation of grain orientation along in-plane (horizontal) direction. C_S-corrected HRTEM (phase-contrast) images of BFCO 1/3 recorded from (b) top surface of the film and (c) interface region. (d) The probe-corrected ADF image of the film-substrate interface in the direction parallel to the ZA $<121>_{STO}$ showing clearly the presence of an amorphous phase and the transition from a double-layer configuration into a four-layer configuration. 88

4.19 The ADF images taken by the INCA software showing the location, namely (a) site A and (b) site B, from which the EDX signals were extracted. 89

4.20 (a) The ADF image of BFCO 1/3 (sample ID BFC 48) shows the area from which the elemental maps of Bi, O, Fe and Cr (b-e), respectively, were generated. 91

4.21 The experimental SAED patterns of BFCO 1/3 film with the sample oriented at (a) the ZA $<101>_{STO}$ and (b) the ZA $<121>_{STO}$. The JEMS simulated SAED patterns of a double perovskite BFCO 1/3 structure in the direction parallel to (c) ZA $<102>_{BFCO\ 1/3}$ and (d) ZA $<121>_{BFCO\ 1/3}$. 93

4.22 (a) C_S-corrected HAADF image of BFCO 1/3 film with the sample oriented at the ZA $<101>_{STO}$ and JEMS atomic projection of double perovskite in the direction parallel to ZA $<102>_{BFCO\ 1/3}$; (b) C_S-corrected HAADF image of BFCO 1/3 film with the sample oriented at ZA $<121>_{STO}$ and JEMS atomic projection of double perovskite in the direction parallel to ZA $<121>_{BFCO\ 1/3}$ (Bi = green, Fe = blue, Cr = red, and O = black); (c-d) The Fast Fourier Transform of HAADF images in (a) and (b) only reproduce the major reflections in the experimental SAED patterns. 94

4.23 Cross-sections of 3D XRD2 reciprocal space maps generated by the *Max3D* software. The cross-over between two vertical planes formed $\sim 120^{o}$ angle to each other. (a) Similar splitting of major reflections along the vertical direction was also observed in the SAED pattern as the horizontal major reflections. (b) The pair of faint reflections alongside the major reflections may contribute to the appearance of the weak reflections in SAED pattern along vertical direction due to overlapping reflections in projection. 96

4.24 The twinning present along the growth direction of BFCO 1/3 (from Lebeugle et al., 2008) 96

4.25 Two different masks for filtering the reflections pertaining to the film were applied on the FFT of the ADF image of BFCO 1/3 with the sample oriented at the ZA $<101>_{STO}$. The mask was applied on the longest and second longest vertical distance in reciprocal space as shown in (a) and (c) and the associated inverse FFTs are shown in (b) and (d). 98

4.26 Two different masks for filtering the reflections pertaining to the film were applied on the FFT of the ADF image of BFCO 1/3 witht the sample oriented at ZA $<101>_{STO}$. The mask was applied on the second shortest and the shortest vertical distance in reciprocal space as shown in (a) and (c) and the associated inverse FFTs are shown in (b) and (d). 99

4.27 The schematic illustration of XRD2 collections, where χ_g (chi) is fixed at 54.7°, Ω (omega) defines the swing angle between sample and detector, and ϕ (phi) is the rotation angle of the sample with respect to the incident X-ray. (from Bruker AXS GADDS manual) 100

4.28 The I-2θ data of the BFCO 1/3 film on (111)-STO substrate acquired by XRD2 for lattice parameter determination. The black curve is the raw experimental data, the red and blue curves are the fits to the data, and the bottom black curve is the difference between experimental and fitted data. 102

4.29 Schematic illustrations of (a) the ideal perovskite and (b) the Ruddlesden-Popper layered perovskite structures. 104

4.30 C_S-corrected HAADF images with insets of the atomic projection in the direction parallel to the ZA $<101>_{STO}$ or $<122>_{BFCO}$ and the ZA $<121>_{STO}$ or $<121>_{BFCO}$ are displayed in (a) and (b). Side-by-side comparisons between experimental and simulated SAED patterns are shown in (c-d) and (e-f) at the ZA $<101>_{STO}$ and the ZA $<121>_{STO}$, respectively. Note that the experimental and simulated SAED patterns are not at the same scale. 105

4.31 Cr L_3 and L_2 signals (575 eV, 584 eV) along EELS linescan were detected along the dark (low intensity signals) band in the ADF image, as pointed out by the arrows. 108

4.32 (a) HAADF image from which EELS spectrum image was acquired from BFC 48 sample is indicated by green rectangle. The overlap of HAADF image and extracted (b) Cr $L_{2,3}$ (575, 584 eV), (c) Fe $L_{2,3}$ (708, 721 eV) and (d) O K (532 eV) maps, respectively. The EELS spectrum image is 128 $\times$ 64 pixel with dwell time of 30 ms/pixel and frame time of $\sim$5 minutes. (*Courtesy of: Sorin Lazar, FEI Electron Optics, The Netherlands* and *McMaster University*) 109

4.33 (a) The region from which EDX spectra were acquired and (b) the same region after the EDX spectra acquisition. Spectra 1-6 were taken from the BLT thin film (sample ID BL 10), spectrum 7 from the SRO buffer layer, and spectrum 8 from the STO substrate. The bright spots in the enhanced contrast area pointed out by the arrows in (b) indicate the beam damage that occurred during the acquisition. 113

4.34 (a) The ADF image of BLT (sample ID BL 10) shows the region from which EDX maps are generated. The EDX maps of O, Ti, Sr, Bi and La are shown in (b) to (f), respectively. 116

4.35 Low angle ADF images (acquired without probe corrector) of ~250 nm thick BLT film epitaxially grown on (a) SRO/(111) STO in a direction parallel to the zone axis (ZA) $<110>_{STO}$ and (b) SRO/(100) STO in a direction parallel to the zone axis $<100>_{STO}$. The BLT film on (111) STO was grown with the *a*-axis forming a 57° angle to the interface, while the BLT film on (100) STO was grown with the *c*-axis normal to the interface. 118

4.36 SAED patterns of (a) the BLT film and (b) the STO substrate. 119

4.37 XRD θ-2θ scan of BLT films on (a) (111) $SrRuO_3/SrTiO_3$ substrate and (b) (001) $SrRuO_3/SrTiO_3$. The spectra show non-ideal peaks generated from the Cu-Kβ and W-Lα sources. (*Courtesy of: Olivier Gautreau*) . 120

4.38 An atomic resolution HAADF image of BLT on (001)STO acquired using the probe corrector is displayed. The inset marked with a red rectangle is the simulated HAADF image of the BLT film parallel to the zone axis $<110>_{BLT}$ with the space group of *B1a1*, following the unit cell structure and atomic coordinates from the neutron diffraction refinement (Kim et al., 2005). The parameters used for the simulation were acceleration voltage of 300 kV, C_S value of 0.002 mm, condenser aperture of 5 mrad, sample thickness of 40 nm, defocus of 0 nm (at the top of the sample), and inner-outer detector angle of 45-113 mrad. (*The simulated HAADF image is courtesy of Yang Shao*) 121

4.39 (a) A non-probe corrected atomic resolution ADF image of the BLT film, recorded with the sample oriented at the ZA $<010>_{BLT}$, shows translational defects highlighted inside the dashed red square. (b) Another type of defect, showing vanishing and appearing rows pointed out by yellow arrows, are located between the Bi_2O_2 layer and the perovskite-like layer, at the region of the film closer to the substrate. . 122

4.40 Schematic illustrations of polarization reversals (switching) in PZT (a-d) and SBT (e-h). The APBs, which only exist in SBT and are depicted as irregular curves in (e-h), help in the nucelation of new domains during switching. The arrows indicate the direction of polarization in each ferroelectric domain. The bold arrows and letter Es indicate the direction of the electric field. (adapted from Ding et al., 2001) 125

4.41 (a) A probe-corrected atomic resolution HAADF image of BLT film grown on (100)-STO substrate recorded in a direction parallel to the ZA $<110>_{BLT}$ shows a modulation of ideal and defected regions along the lateral direction. The white lines indicate the approximate width of the defect-free atomic layers located at the SRO/BLT interface. (b) A numerically filtered image of (a) enhances the specific periodicity of $c/3$ in the BLT unit cell and clearly shows the structural modulation, represented as bright and dark patches, along the lateral direction. . . . 126

4.42 A probe-corrected HAADF image of BLT on (100) SRO/STO recorded with the sample oriented at the ZA $<110>_{BLT}$ shows (a) a defect-free region at the top part of the sample and (b) alternating defect-free and defected regions along the BLT/SRO interface separated by a yellow vertical line. The shadowed areas in (a) indicate herringbone pattern intensity trails, which appear due to the position of Ti ions in the BLT unit cells. These patterns confirm the presence of octahedral tilting in the BLT unit cell. (c) The distribution of the intensity signal in the HAADF image along the first layer of atoms in the region identified by a blue rectangle in (b). Since HAADF intensity represents the contrast related to the atomic number (Z) of element, the higher signal intensity indicate the presence of higher Z elements, and vice versa. 129

4.43 An illustration describing a misregistry of BLT unit cells along the beam direction, i.e., (100) BLT, which creates an appearance of extra rows between the Bi_2O_2 layer and the perovskite-like layer due to the overlap of the two unit cell configurations. Bi_1 corresponds to Bi ions in the perovskite-like layer, and Bi_2 to Bi ions in the Bi_2O_2 layer. EELS investigations show that La ions are more dominant in substituting Bi ions in the Bi_2O_2 layer. 132

4.44 The BLT/SRO interface shows the presence of an atomic step inclined to the viewing axis (highlighted in the blue shaded rectangle) and dislocation (highlighted in the green shaded square). The border of the interface atomic step is indicated by the yellow lines, while the red arrows point out the vanishing atomic rows. The inset is a masked, numerically-filtered image corresponding to the green shaded square, which shows a dislocation at the interface. 133

4.45 Nucleation mechanisms of layered perovskite on $SrTiO_3$ may be induced by (a) steric nucleation, in which the same layering unit cells nucleate at an interface step and form out-of-phase boundary, and (b) at a misfit dislocation which perturbs the structural correlation of the nucleating layers, causing two regions beside the dislocation to grow with different stacking configurations. (from Zurbuchen et al., 2007) 136

4.46 Background subtracted EELS linescans in the BLT unit cell viewed along ZA$<110>_{BLT}$were performed along (a) the Bi_2O_2 layer and (b) the perovskite-like layer. The location where the EELS linescan was performed in the BLT unit cell is indicated by the white line. The red dots along the white line (from left to right) are associated with the numbered EELS spectra. 137

4.47 (a) HAADF image indicating the location of the ideal region in BL 06 sample, highlighted by a green rectangle, used for EELS mapping; (b) HAADF intensity recorded simultaneously while the EELS spectra in the region of interest (the green rectangle in (a)) were acquired; (c) the EELS composite Ti (red) and La (green) map, (d) La N edge (99 eV) signal, (e) Ti L edge (456 eV) signal, and (f) La M edge (832 eV) signal. The EELS sprectrum image is 32 × 32 pixel with dwell time of 30 ms/pixel. (*Courtesy of: Sorin Lazar, FEI Electron Optics, The Netherlands* and *McMaster University*) 138

4.48 (a) HAADF image indicating the location of the defected region in BL 06 sample, highlighted by a green rectangle, used for EELS mapping; (b) HAADF intensity recorded simultaneously while the EELS spectra in the region of interest (the green rectangle in (a)) were acquired; (c) the EELS composite Ti (red) and La (green) map, (d) La N edge (99 eV) signal, (e) Ti L edge (456 eV) signal, and (f) La M edge (832 eV) signal. The EELS spectrum image is 96 × 36 pixel with dwell time of 40 ms/pixel and frame time of 4 minutes. (*Courtesy of: Sorin Lazar, FEI Electron Optics, The Netherlands* and *McMaster University*) . . . 139

4.49 (a) The "off-center" coordination environment of Bi ion in the Bi_2O_2 layer and (b) the more symmetrical local environment of Sr ion in the Bi_2O_2 layer. The Sr2 ion is offset of $\sim$ 0.8 Å from the Bi2 ion along the *c*-axis in order to achieve more regular local geometry with eight approximately equal bond lengths (Hervoches and Lightfoot, 2000). . . 141

A.1 The two basic settings of (a) TEM (parallel illumination) and (b) STEM (probe illumination). The locations of lenses, aperture and specimen are indicated by the arrows on the side, where C1, C2, C3 and MC are first condenser, second condenser, third condenser and mini condenser lens, respectively. (from FEI-Titan manual) 150

A.2 The C2-C3 system zooming system in a Titan 30-800 TEM (from FEI-Titan manual). 151

A.3 Ray diagrams of Titan operation in TEM mode with the C3 lens 'OFF', where the electron beam changes from converging (a) to parallel (b) and to diverging (c) with increasing area of illumination. The locations of lenses, aperture and specimen are indicated by the arrows on the side. (from FEI-Titan manual) 152

B.1 The step-by-step schematic for running Michael Robertson's codes (from: CCEM Summer School 2008). 154

List of Tables

2.1 The wave aberration coefficients and their magnitude calculated from the $\pi/4$ limit at 200 kV (from Uhlemann and Haider, 1998) 29

2.2 List of experimental unit cell and lattice parameters of $BiFeO_3$, $BiCrO_3$, $SrTiO_3$, $SrRuO_3$, and calculated atomic position and lattice parameters of Bi_2FeCrO_6. (Baettig et al., 2005) 37

2.3 Properties of PZT, SBT, and BLT thin films prepared on conventional Pt electrodes (Park et al., 1999). 39

4.1 The distortion of perovskites in terms of in-phase and anti-phase tilting categorized by the value of tolerance factor. 70

4.2 The ionic radii of bismuth, chromium, iron and oxygen (Shannon, 1976) 70

4.3 The experimental and the theoretical d-spacings of the extra reflections, as indicated in Figure 4.10 by the yellow arrows. The 2R column corresponds to the distance between two collinear reflections. The CF value for a camera length of 770 mm is ~ 0.93. 74

4.4 List of possible combination of valences of Fe and Cr in BFCO film while maintaining charge neutrality 77

4.5 The L_3/L_2 ratio of experimental and reference Fe and Cr and its corresponding valence. 81

4.6 The list of origins of the weak and the extra weak reflections in the CBED patterns of the BFCO 1/1 film. 83

4.7 The results of quantification of EDX spectra of the BFCO 1/3 film . . 90

4.8 The elemental composition of the BFCO 1/3 film 90

4.9 The experimental parameters applied during the acquisition of XRD spectra for lattice parameters determination. The axis '3' corresponds to the phi(ϕ)-axis, parallel to the normal direction of the sample. The width indicates the phi (ϕ) increment. 102

4.10 List of reflections in the SAED pattern recorded with the sample oriented at the ZA<101>$_{STO}$ || ZA<122>$_{BFCO\ 1/3}$ monoclinic 106

4.11 List of reflections in the SAED pattern recorded with the sample oriented at the ZA<121>$_{STO}$ || ZA<121>$_{BFCO\ 1/3}$ monoclinic 106

4.12 EDX data acquired from various different regions of the BLT thin film (in atomic percentage). 114

4.13 The normalized values based on the assumed stoichiometric Bi value of 3.25 114

List of Symbols

$A(u)$ aperture function

α convergence semi-angle of electron source

$\chi(u)$ aberration function

C_C chromatic aberration coefficient

C_S spatial aberration coefficient

Δf spread of focus of electron probe, defocus of objective lens

ΔE energy spread of electron source

ΔE energy spread of electron source

Δf_{sch} Scherzer defocus

ΔI current instabilities of objective lens

ΔV voltage instabilities of electron source

$E(u)$ envelope function

$E_C(u)$ temporal incoherence

$E_S(u)$ spatial incoherence

h Planck's constant, $6.31 \cdot 10^{34}$ J.s

$I_{\text{L}}(u)$ Image intensity in the reciprocal space assuming the condition of linear interference of only one pair of diffracted beams

$I(x,y)$ image intensity, square of the image wavefunction in real space

λ electron wavelength

λ_r relativistic electron wavelength

me mass of electrons

π pi, 3.14

$\psi_e(x,y)$ spherical exit wave function

$\psi_i(x,y)$ image wave function

$\phi_o(x,y)$ planar waves of incident electrons

ϕ_p projected potentials of the sample along the z-direction

r point resolution limit, the minimum resolvable distance

σ interaction constant

u reciprocal space notation, spatial frequency

$V(u)$ Fourier component of the real projected potential

(x,y) real space notation

Chapter 1

Introduction

1.1 Perovskite Oxides

Perovskite oxides, which have a chemical formula ABO_3, are materials that have been extensively researched and investigated due to their wide-ranging structures and physical properties as a function of composition and synthesis parameters. Electrical conductivity of the perovskite oxides, for instance, ranges from insulator, semiconductor, conductor to even superconductor depending on their chemical composition and temperature. The abundant varieties of such interesting properties of perovskite oxides make them potential materials for various magnetic, electrical, optical and electronic applications (Haertling, 1999).

The discovery of piezoelectricity, which is a material's ability to generate electricity as a result of mechanical pressure, in one of perovskite oxides, i.e., Rochelle salt, was recorded in 1880 (Valasek, 1921). Further, discovery of ferroelectricity, which is a material's ability to undergo a spontaneous electric polarization that is reversible under the application of an external electric field, in Rochelle salt in 1921 and later on in $BaTiO_3$ in 1940 (Kanzig, 1987), has sparked significant interest of perovskite oxides in both academic and industrial fields. Besides piezoelectricity and ferroelectricity, perovskite oxides also possess high dielectric constants and low dielectric loss, which are remarkable driving forces for creating new niches in electronic industries along-

side conventional electronic materials. Until recently, perovskite oxides in electronic devices were mostly used in non-volatile ferroelectric random access memories (NV-FRAM), tunable microwave devices, and sample stages in various characterization instruments that require precise and delicate movement, etc. (Haertling, 1999).

Not only the abovementioned ferroelectricity, but also a simultaneous combination of ferromagnetism and ferroelasticity, so called multiferroism, is provided by perovskite oxides. Multiferroics, one of the most recently found class of materials, exhibit unique properties, mechanisms and atomic scale interactions, some of which have not been fully established (Ramesh and Spaldin, 2007). The reason is that the well-established mechanism of generation of ferroelectricity, requiring an off-centered cation with empty d orbitals, and of generation of magnetism, requiring the formation of magnetic moments resulting from partially filled d orbitals, are rather contradictive. Such contradictive mechanisms result in the scarcity of ferromagnetic ferroelectrics. In principle, the coexistence of both ferroelectricity and magnetism in a single phase could be achieved through an alternative mechanism (non-d-electron) for magnetism or an alternative mechanism for ferroelectricity. Overall, the exact mechanism has yet to be established. Consequently, the interest in identifying the mechanism on how multiferroics work in comparison to the observed phenomena in either ferroelectrics or ferromagnets alone has motivated a lot of research in this field. Furthermore, a range of attempts have been performed in integrating their potentially superior properties into more advanced electronic applications, for example, memory devices that can be electrically written and magnetically read (Scott, 2007).

With regards to applications in nanotechnology, integration of perovskite oxides is expected to provide remarkable impacts in scaling down the sizes of electronic devices, thus enhancing capability and performance. The scaling down of perovskite oxides, however, has demonstrated numerous challenges, due to the presence of strain, defects and compatibility issues with adjacent layers of different materials, particularly at interface regions (Falke et al., 2004, 2005). The reason is that interface regions have distinct physical properties from those of the parent layers (Hwang, 2006; Maurice et al., 2006) and can behave as a third material. Distinguishing features of thin film-substrate interfaces, attributed to different interfacial atomic and electronic structures, will be reviewed in this study.

The relationship between structural configuration and physical properties, as well as the associated mechanisms of fatigue resistance of perovskite oxides in general, and ferroelectrics and multiferroics, in particular, especially with reduction of dimensionality and scaling down to nanometer size, have not been well-established and remains a debatable subject. Therefore, the objective of this study is to further understand such stucture-property relationships of nano-scale Bi-based perovskite oxides in multilayered structures in order to provide insight into establishing the phenomena and mechanisms involved in new generation perovskite oxides.

1.2 C_S-corrected Transmission Electron Microscopy

A transmission electron microscope (TEM) utilizes electrons as its source, and thus it theoretically provides spatial resolution in the range of the electron wavelength, i.e., at the picometer scale, depending on the applied acceleration voltage. However, the limitation in achieving the theoretical spatial resolution lies in the imperfections or aberrations, primarily the spatial-aberration, of the electromagnetic lenses used in the TEM column. Scherzer (1947) proved that electron optics with symmetrically round lenses always suffers from simultaneous spatial and chromatic aberrations. These aberrations limit TEM resolution, and hence, in probing the structures of materials at the atomic scale.

The challenging task of probing the structural configuration of nm-scale oxides down to atomic resolution can be performed by utilizing an aberration corrected transmission electron microscope (C_S-corrected TEM). Recently, the development of a spherical aberration (C_S) corrector for the objective lens has resulted in the compensation of C_S of microscope lenses (Haider et al., 1998; Krivanek et al., 1997; Rose, 2009), enabling picometer scale spatial resolution (Lupini et al., 2004). The addition of a C_S-corrector, containing a series of multipolar lenses which break the rotational symmetry of the electromagnetic lens, provides a negative C_S-value. The combination of a negative C_S-value with a positive C_S-value of the image-forming (objective) lens gives nearly-spatial aberration free optics, enabling the spatial resolution of the C_S-corrected TEM to reach picometer scale. The sub-Å imaging capability of C_S-corrected TEMs provide means for obtaining information of atomic structure in the

presence of non-periodic features, such as defects and interfaces. The combination of dual C_S-correctors for probe forming (condenser) and image forming (objective) lenses is promising even more powerful capability, in that spectrum collection can be done in precise atom-by-atom increments.

The integration of a monochromator for limiting energy spread of incident electrons has been demonstrated in improving the energy resolution of Electron Energy Loss Spectroscopy (EELS) down to $\sim$ 0.15 eV (Egerton, 1996, 2007). Such energy resolution offers a pathway to extract information on the electronic interactions, from which explanations of various physical properties of a material can be formulated.

All the abovementioned advanced features in C_S-corrected TEM, along with conventional TEM, will be utilized to yield detailed and comprehensive information on atomic and electronic configurations of different perovskite oxides, which eventually will enable further tailoring of these materials according to desired properties.

Despite the superiority of having nearly aberration free images in both phase contrast image (TEM mode) and high-angle annular dark field (HAADF) image (STEM mode), image simulation still holds an extremely important role in both the image interpretation and the removal of higher order aberrations of objective lens that cannot be fully removed by hardware correction. Several available image simulations are *MacTempas*, *Crystal Kit*, and *Multislice*, which may be used in order to attain easier interpretation of HRTEM/ phase contrast images, which vary according to sample thickness and objective lens focus, and Z-contrast or HAADF images, which are a function of convergence and collection angles. The softwares used for data processing and interpretation are listed in Appendix B.

1.3 Overview

The emerging new class of materials with distinct and exciting physical properties, namely ferroelectrics and ferromagnets, and the development of sub-Å resolution TEM are the major driving forces of this study. The perovskite oxides that were analyzed were in form of multilayered thin films, which were epitaxially grown on a substrate

by a pulsed laser deposition method.

Several objectives of this study are as follows:

1. Characterizing the structural arrangement and electronic environment (bonding, oxidation state/valence) of perovskite oxide thin films.
2. Establishing the relationship between different atomic structures and physical properties.
3. Utilizing a C_S-corrected TEM to provide new information in terms of imaging and analytical spectroscopy that is impossible to attain by using a conventional TEM.

Chapter 1 gave a general description of motivation and main objectives behind this study and introduced the capability of the research instruments utilized to achieve the objectives. Details of the materials and the characterization instrument are reviewed in Chapter 2, where advantages of the C_S-corrector in TEM and several new techniques related to imaging and spectrum acquisition at interfaces using C_S-corrected TEM is reported. In addition, the field of ferroelectric and multiferroic perovskite oxides, in general, and bismuth-based perovskite oxides, in particular, is assessed in this chapter. Chapter 3 presents the growth method of the thin films and the details of TEM sample preparation. Chapter 4 provides experimental results and discussion on the structure and physical property relationships of Bi-based perovskite oxides. Finally, Chapter 5 gives a summary and highlights of this study. Some suggestions for future work pertaining to the investigated materials are also provided.

Chapter 2

Literature Review

A transmission electron microscope (TEM) is one of the most powerful characterization tools for investigating material structures and properties at a very small length scale, which previously were unattainable with light microscopes due to their limited image resolution imposed by the wavelength of visible light. In general, a TEM provides not only visual information or images, but also structural information from diffraction techniques and analytical information regarding elemental composition and bonding nature from spectroscopy techniques. Features of the TEM and their related types of information that can be attained are schematically presented in Figure 2.1.

A TEM instrument can usually be operated in two modes, i.e., TEM mode with parallel illumination and STEM (Scanning TEM) mode with converged illumination. The two modes are related by a reciprocity theorem (Zeitler and Thomson, 1970), whereby an image and an electron source are interchangeable since electron intensities and ray paths remain the same with reversals of the ray directions or interchange of the source and the detector. The schematic of TEM-STEM ray diagrams based on the reciprocity theorem, which is only applicable to the elastically scattered electrons, is depicted in Figure 2.2, where the source plane in TEM mode is equivalent to the detector plane in STEM mode.

Since electrons are used as the illumination source, theoretically, TEM resolution should be comparable to the electron wavelength, in the range of picometers depend-

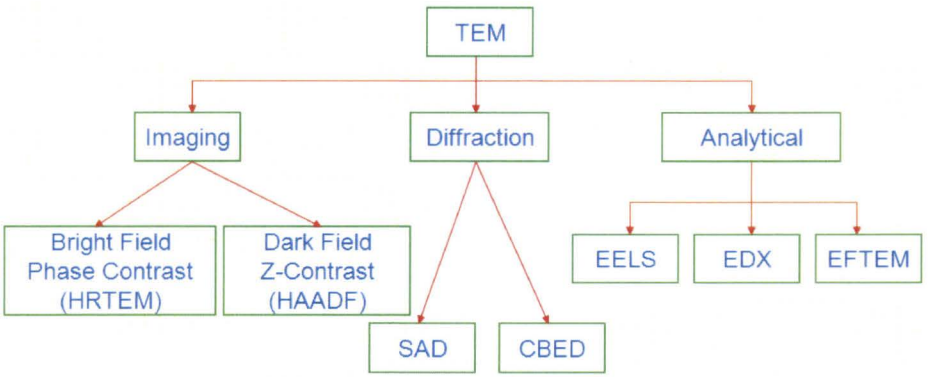

Figure 2.1: Some of the TEM features consist of imaging, diffraction and analytical techniques. (Legend: SAD = Selected Area Diffraction; CBED = Convergent Beam Electron Diffraction; EELS = Electron Energy Loss Spectroscopy; EDX = Energy Dispersive X-ray spectroscopy; and EFTEM = Energy Filtered TEM)

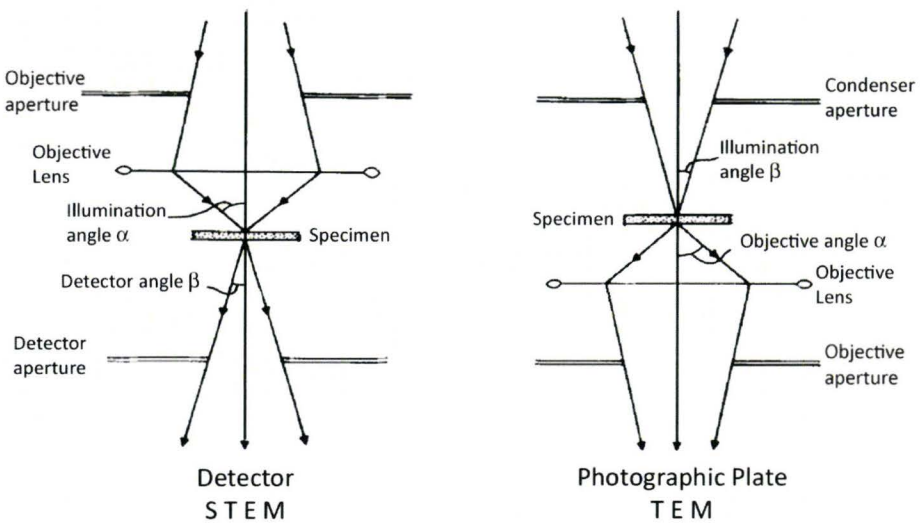

Figure 2.2: Ray diagrams illustrating the reciprocity theorem between TEM and STEM modes. The reciprocity applies when the STEM illumination angle is equal to TEM objective angle and TEM illumination angle is equal to STEM detector angle. (adapted from Sande and Hall, 1979)

ing on the acceleration voltage. Therefore, a TEM is expected to be able to reveal detail of a sample well below the atomic level. However, in reality, TEM resolution is mainly limited by the objective lens (the image forming lens) which always possesses aberrations due to the nature of fields of an electromagnetic lens. In the early development of telescopes, the refractive telescope utilized a lens to form an image. Such a lens behaves as a prism and suffers from severe chromatic aberration, i.e., white light is dispersed into various colours, as well as spherical aberration. Later on, Newtonian optics, which utilized a series of curved or parabolic mirrors, had been able to eliminate chromatic aberration in refractive telescopes and had made a breakthrough in the development of reflecting telescopes. However, Newtonian optics still suffer from spherical aberrations, such as off-axis coma, when the incoming beams are not parallel to the optic axis, which degrades the quality of captured images.

In TEM instruments, electron mirrors are rather difficult to integrate into the optics due to the limited space in a TEM column. Instead, a TEM utilizes an electromagnetic lens as its objective, which causes the attainable resolution of TEM to be mainly limited by the spherical and chromatic aberrations. The origin of spherical aberration of the objective lens and its effects on the TEM resolution is described in the next section.

2.1 Background of C_S-corrector in TEM

During the development of optical microscopy, light sources have been able to be nearly perfectly focused by using a combination of glass lenses. Imperfections, which may be present in a convergent lens, such as spherical aberration (C_S), can be compensated by subsequently placing a divergent lens where the negative C_S value of the diverging lens cancels out the positive C_S value of the convergent lens, giving an aberration free image. Additionally, the control of fabrication of glass lenses is relatively easy in comparison to that of electromagnetic lenses, yielding an essentially defect-free lens and leads to significantly suppressed C_S values in the glass lens itself. In brief, both ease of fabrication and simple configuration of glass lenses contribute to the C_S-free optical microscope.

In contrast to the optical microscope, spherical and chromatic aberrations in the static, rotationally symmetric electromagnetic lens used as the objective lens in electron microscope are inevitable. Such a lens will always give a positive value of C_S (Scherzer, 1947, 1949). Consequently, the ideal spherical wave of the propagating electrons deviates as a function of the distance from the optic axis as the electrons travel through the objective lens, resulting in a loss of spatial and energy resolution.

Despite the abovementioned weaknesses of rotationally symmetric electromagnetic lenses, Scherzer (1949) pointed out a solution for overcoming aberration problems by abandoning rotational symmetry, i.e., by introducing asymmetrical or multipolar lenses, such as quadrupoles, hexapoles, octupoles, etc. However, the early development of aberration correctors, so called Scherzer correctors, experienced a major obstacle due to insufficient stability in the mechanical alignment. The improvement of the resolution of the microscope by Scherzer correctors was then mainly limited by mechanical and electromagnetic instability, rather than by static defects of the objective lens. (Rose, 2009)

Following many unsuccessful attempts in managing multipolar lenses for compensating C_S of an electromagnetic lens, scientists strived to look for another approach for improving spatial resolution of the TEM, i.e., the reduction of electron wavelength by increasing the accelerating voltage of the electrons, up to $\sim$ 3 MV. The cost of building and installation to achieve extremely high acceleration voltage, nonetheless, was very expensive. In addition, the impact of high energy electrons was sufficient to cause extensive structural damage to the specimens. Therefore, the method of increasing acceleration voltage at the expense of specimen damage, in order to obtain better resolution, was deemed unsatisfactory.

A decade ago there was a remarkable breakthrough in TEM technology, marked by the arrival of C_S-correctors consisting of a combination of either hexapole and doublet transfer lenses (Haider et al., 1998) or quadrupoles and octupoles (Zach and Haider, 1995; Krivanek et al., 2003). The ability to provide mechanical and electromagnetic stability as well as fully automated iteration of aberration correction has made possible the compensation of the positive C_S value of the objective lens. This breakthrough has led us to an exceptional spatial resolution attainable in TEM without imposing extensive damage on the investigated specimen.

2.2 The Resolution Limits of TEM

In order to appreciate the significance and advantages of C_S-correctors in TEM, it is essential to understand what instrumental parameters influence the resolution of TEM. Ideally, the ultimate resolution of a TEM would be comparable to the electron wavelength itself, i.e., in the picometer range and much less than the interatomic spacing. This ideal condition, nevertheless, will only be attainable by having a nearly aberration-free objective lens without residual aberrations, which is not the case in realistic systems that employ rotationally symmetric electromagnetic lenses.

In principle, the performance of a TEM in terms of resolution is governed by the Contrast Transfer Function (CTF) of the objective lens (Williams and Carter, 1996; Buseck et al., 1989; Spence, 2003). The CTF, controlling the information transfer from the sample to the image plane, mainly consists of three contributors, namely:

- the Aperture function, $A(u)$, determining the cutoff spatial frequency of the CTF,
- the Envelope function, $E(u)$, describing the attenuation of the CTF at higher spatial frequencies due to temporal and spatial incoherence of the microscope,
- the Aberration function, $\chi(u)$, which is a phase shift due to the imperfection of the objective lens.

Note that the CTF components are assigned with reciprocal space notation, u, rather than the real space notation, (x,y), indicating that the calculation pertaining to the CTF is carried out in reciprocal space as it is computationally more efficient. Reciprocal and real spaces are related by a Fourier Transform, i.e., $F(u) = \int f(x,y) \exp(iu \cdot (x,y))$.

The resolution limit in TEM can be defined in two different terms, one is the Information Limit, and the other is the (Scherzer) Point Resolution Limit, or so called the Interpretable Limit (see Figure 2.3). The former is mainly governed by the 'damping envelope' functions associated with partial temporal coherence manifested as a

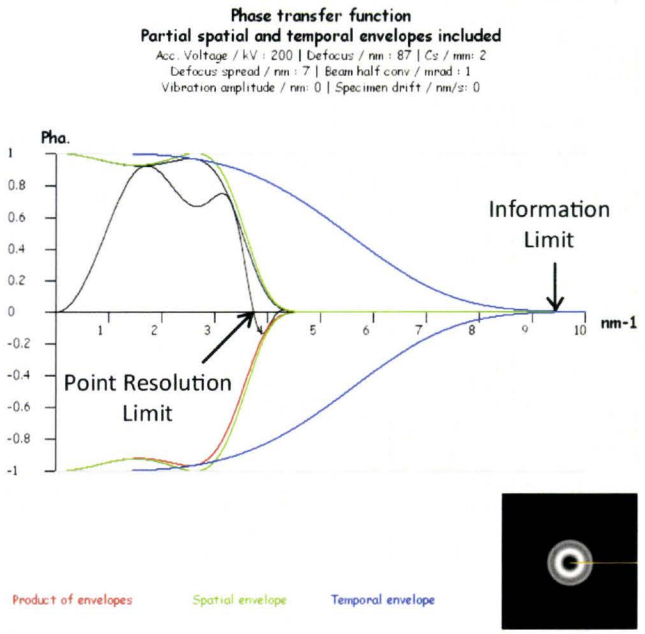

(a)

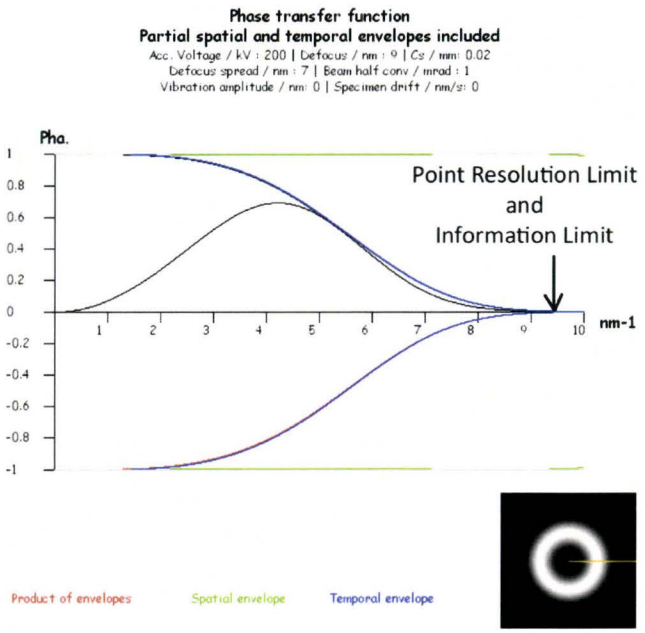

(b)

Figure 2.3: The Contrast Transfer Function of an electron microscope simulated with the JEMS software shows the point resolution limit and the information limit between (a) non-C_S-corrected and (b) C_S-corrected microscope. (Red line represents the product of the envelope functions, green line spatial envelope, blue line temporal envelope, and black line the contrast transfer function)

spread of focus and partial spatial coherence due to incident beam convergence. The damping envelope function for temporal incoherence, $E_C(u)$, is defined as,

$$E_C(u) = exp\left\{-\frac{1}{2}\pi^2\lambda^2\Delta f^2 u^4\right\} \tag{2.1}$$

where λ is the electron wavelength, u the spatial frequency, and Δf the spread of focus of the electron probe as a function of the chromatic aberration coefficient (C_c), energy spread and voltage instabilities of the electron source, as well as current instabilities of objective lens, as formulated in Equation 2.2.

$$\Delta f = C_c\sqrt{\left(\frac{\Delta E}{eV}\right)^2 + \left(\frac{\Delta V}{V}\right)^2 + \left(\frac{2\Delta I}{I}\right)^2} \tag{2.2}$$

Meanwhile, the damping envelope function for spatial incoherence, $E_S(u)$, assuming the source has a Gaussian distribution, is given by,

$$E_S(u) = exp\left\{-\left(\frac{\pi\alpha}{\lambda}\right)^2\left(C_S\lambda^3u^3 + \Delta f\lambda u\right)^2\right\} \tag{2.3}$$

where α is the semi-angle characterizing the Gaussian distribution and $\Delta f = -\frac{3}{4}C_S\lambda^2u^2$.

No information is accesible beyond the Information Limit, or in other words, it represents the maximum obtainable resolution in a TEM instrument.

The second resolution limit, i.e., the Point Resolution Limit, is governed largely by the aberration function of the objective lens, described by Equation 2.4,

$$\chi(u) = 2\pi\left(\frac{1}{2}\Delta f\lambda u^2 + \frac{1}{4}C_S\lambda^3u^4\right) \tag{2.4}$$

where Δf and C_S are defocus and spherical aberration coefficient of objective lens, respectively. Physically, the aberration function, $\chi(u)$, causes a point in the sample plane to be imaged as a disk.

The point resolution limit, r, defined as the first zero cross-over of the CTF curve with the u-axis (spatial frequency), can be formulated by differentiating Equation 2.4 with respect to u. The differentiation at Scherzer defocus, $\Delta f_{sch} = -1.22\,(C_S\lambda)^{1/2}$, results in,

$$r = A\,C_S^{1/4}\lambda^{3/4} \tag{2.5}$$

where A is a constant with a typical value of ~0.66. Information beyond this limit is not easily interpretable due to the oscillatory nature of the transfer function, which causes the fine details present in the image at such resolution will not be easily related to specimen features. As such, the point resolution limit demonstrates the true performance of a TEM.

Moreover, Equation 2.5 indicates two ways for enhancing the TEM resolution, either by reducing λ or decreasing the C_S value. The former way is straightforwardly achievable by increasing the acceleration voltage of electrons. Despite its relative ease in control and assembly compared to the reduction of C_S by employing multipolar lenses, the reduction in λ by increasing acceleration voltage has a few drawbacks, i.e., sample damage and exorbitant cost. Thus, the latter method through C_S reduction becomes a more appealing method, in the sense that considerable damage to the specimen can be avoided.

Most notably, the main component limiting TEM resolution is the image forming lens, namely the objective lens. Therefore, it is essential to comprehend the limitations of this lens before understanding the role of aberration correctors. The three major limitations are classified as follows:

1. Spherical Aberration (C_S), which causes incident electrons traveling at higher angle or further away from optic axis to be focused at a shorter focal distance than those traveling closer to the optic axis. Consequently, a point source in the sample appears as a disk in the image plane, as illustrated in Figure 2.4 (b).

2. Chromatic Aberration (C_C), which causes electrons with different energy (as indicated by different colors in Figure 2.4 (c)) to be focused at different points.

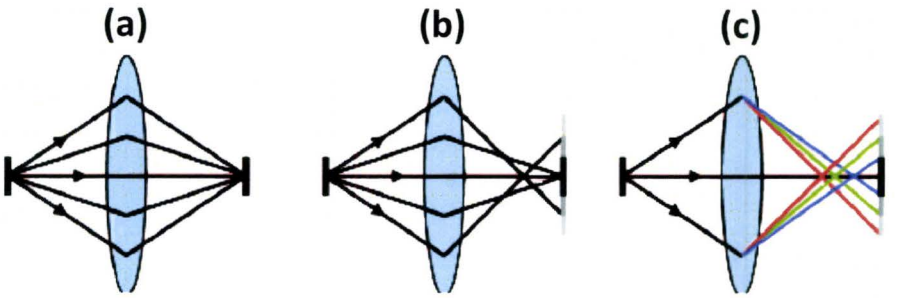

Figure 2.4: Illustration of several lens aberrations: (a) a perfect lens; (b) spherical aberration; (c) chromatic aberration (different colour indicates different energy). (from Pennycook et al., 2006)

The energy spread of incident electrons results in smearing out of image details on the image plane.

3. Diffraction (Rayleigh) limits. The Rayleigh criterion states that the minimum distance between two distinguishable objects requires the center of the first Airy disk, which originated from diffraction of one point, to be located at the first minimum of the second Airy disk (Figure 2.5). The Rayleigh criterion is expressed as:

$$r = 0.61\lambda/\beta \tag{2.6}$$

where r is the minimum resolvable distance, λ the electron wavelength and β the collection angle, which is a function of the objective aperture diameter.

For imaging purposes, high angle scattered electrons are undesirable since they result in image blurring due to spherical aberration. A smaller objective aperture diameter is therefore preferable to exclude electrons scattered by the sample far from optic axis; hence the extent of spherical aberration in the image may be suppressed. On the contrary, the Rayleigh criterion suggests that high spatial frequency information can only be attained by choosing a larger diameter objective aperture. Evidently, there is a trade-off between limiting the effects of spherical aberration by inserting an objective aperture and increasing diffraction limits for enhancement of resolution; a compromise of the two gives a range of optimum objective aperture size, below and above which TEM resolution decreases.

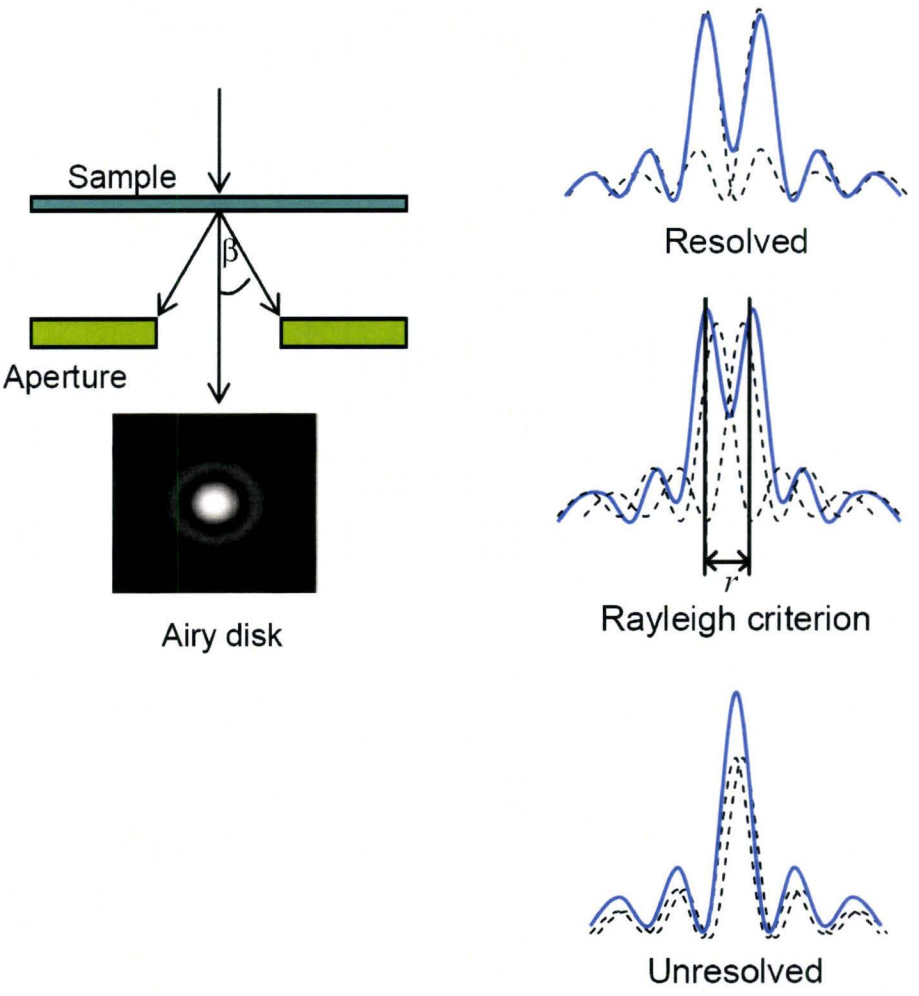

Figure 2.5: Schematic illustration of diffraction from a point which results in the formation of an Airy disk. Two well-separated objects give rise to easily resolved Airy disks. With decreasing distance between two objects, Airy disks start to overlap and reach a diffraction limit (Rayleigh criterion). Further overlap of two Airy disks beyond the Rayleigh criterion results in unresolved two objects. (adapted from http://hyperphysics.phy-astr.gsu.edu/Hbase/phyopt/Raylei.html, Nave, 2006)

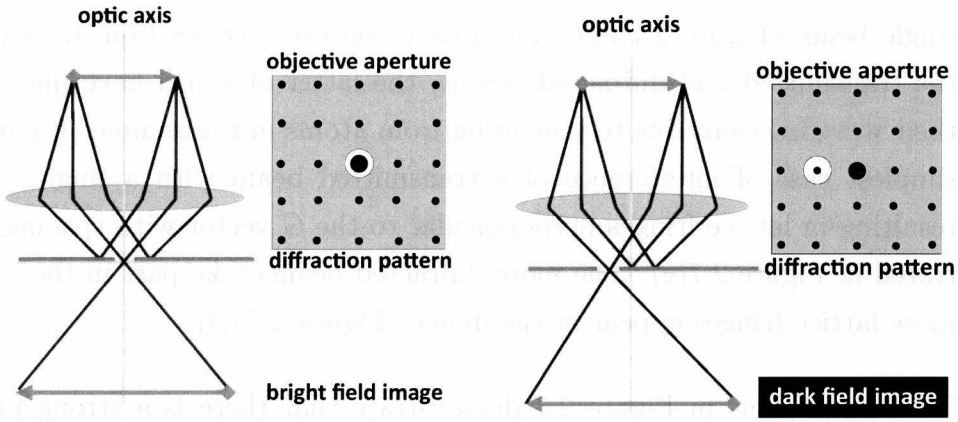

(a) (b)

Figure 2.6: Schematic illustrations of (a) bright field (BF) imaging and (b) dark field (DF) imaging modes. Distinct objective aperture selection of the transmitted beam in (a) and the diffracted beam in (b) is indicated. (adapted from http://microscopy.ethz.ch, Krumeich, 2007)

2.3 Principles of imaging techniques

As there are several modes of imaging available in TEM, it is crucial to understand the commonly used mode in high-resolution imaging, and to understand how spherical aberration influences the quality of the image. In this section, the formation of phase contrast images and the influence of spherical aberration is described.

2.3.1 Diffraction Contrast and Phase Contrast (High Resolution TEM) Imaging

The most common TEM modes of imaging are bright field (BF) and dark field (DF) diffraction contrast imaging. Both techniques are similar in the sense that both are utilizing a single beam, namely a transmitted beam in BF imaging and a diffracted beam in DF imaging, as illustrated in Figure 2.6. Beam selection is performed by positioning the objective aperture around the desired beam.

The main difference of phase contrast imaging from both BF and DF diffraction

contrast imaging lies in the utilization of more than one beam, instead of use of a single beam (Figure 2.7(a)). The image contrast derives from interference between the transmitted and diffracted beams, the latter of which have phase differences in their wavefunctions due to scattering from atoms in the sample (Figure 2.7(b)). The simplest case of interference of a transmitted beam with a single diffracted beam resulting in lattice fringes perpendicular to the G vector with spacing of $1/g$ is illustrated in Figure 2.7(c). The more diffracted beams take part in the interference, the more lattice fringes appear in the image (Figure 2.7(d)).

The illustrations in Figure 2.7 demonstrate that there is a strong interdependency between the resolution of a phase contrast image and the number of beams selected by the objective aperture. However, the diameter of objective aperture cannot be expanded indefinitely as the higher angle diffracted beams introduce more spherical aberration, degrading the image resolution. The utilization of C_S-corrector, which in principle compensates the C_S value of objective lens, permits an increase of the objective aperture size resulting in achievement of a spatial resolution approaching the information limit.

The contrast variation in phase contrast images revealing projected atomic columns of the sample is very sensitive to changes in thickness and orientation of the sample. Moreover, the image contrast is also highly dependent on instrumental parameters, such as defocus and objective astigmatism of the image forming lens. Such complex interactions between incident electrons and sample, and further convolution of the object exit wavefunction with the contrast transfer function (CTF) of the objective lens, make the interpretation of phase contrast images complicated. In order to fully look into the complexity of phase contrast images, step-by-step image formation in the high resolution imaging mode is described in the following sub-section.

2.3.2 Image formation in Phase Contrast Imaging

The illustration of image formation in Phase Contrast Imaging (Figure 2.8) points out that the incident electrons can be depicted as planar waves, $\psi_0(x, y)$. Interaction of planar waves with the projected periodic potential of atoms within the sample,

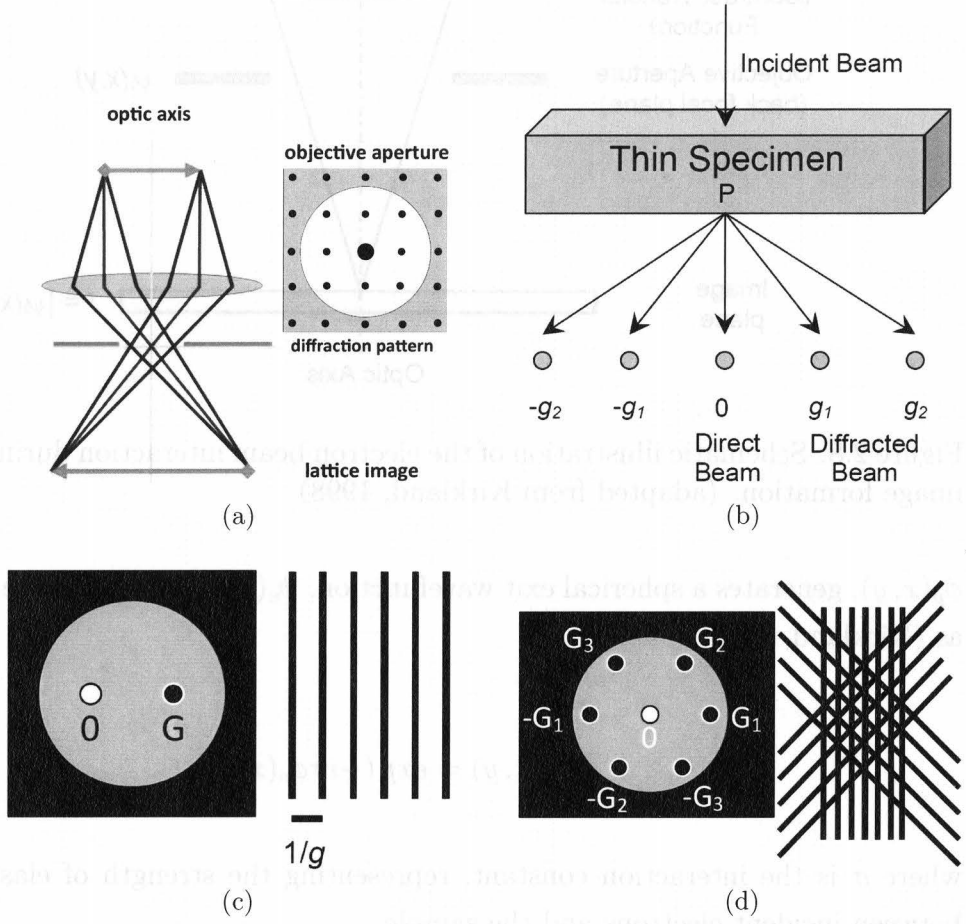

Figure 2.7: Schematic illustration of (a) the ray diagram for phase-contrast or High Resolution TEM (HRTEM) imaging (adapted from http://www. microscopy.ethz.ch, Krumeich, 2007), (b) the incident beam-sample interaction, (c) the interference between a transmitted beam and one diffracted beam, and (d) the interference between transmitted beam and six diffracted beams resulting in lattice fringes image (adapted from Williams and Carter, 1996)

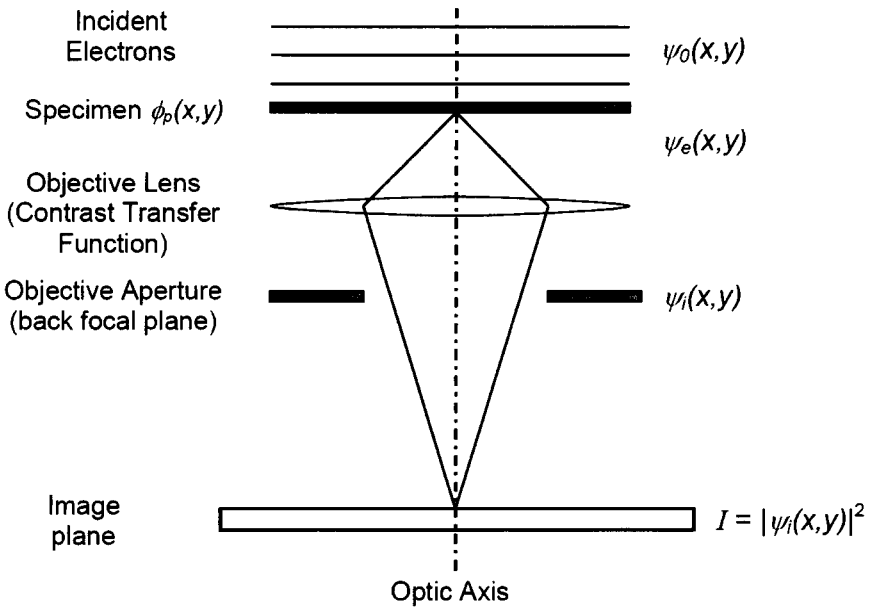

Figure 2.8: Schematic illustration of the electron beam interaction during the HRTEM image formation. (adapted from Kirkland, 1998)

$\phi_p(x,y)$, generates a spherical exit wavefunction, $\psi_e(x,y)$, which can be approximated as (Kirkland, 1998):

$$\psi_e(x,y) = exp\left(-i\sigma\phi_p(x,y)\right) \tag{2.7}$$

where σ is the interaction constant, representing the strength of elastic interaction between incident electrons and the sample,

$$\sigma = \frac{2\pi m_e \lambda_r}{h^2} \tag{2.8}$$

and ϕ_p is the projected potential of the sample along the z-direction, parallel to the direction of incident electrons,

$$\phi_p = \int_{-t/2}^{t/2} \phi(x,y,z)\, dz \tag{2.9}$$

A weak phase object approximation, in which electrons are considered to scatter only once while travelling through the sample thickness, is applicable for light elements ($\sigma\phi_p \ll 1$) only, such as C, N, and O, but not for heavier elements. According to the weak phase object approximation, the object exit wavefunction, $\psi_e(x, y)$, is formulated in Equation 2.10.

$$\psi_e(x, y) = 1 - i\sigma\phi(x, y) \tag{2.10}$$

Despite its simplicity, the accuracy of this approximation is insufficient in calculating the complex interaction between the incident electron with heavier elements and a thicker sample. For material containing defects or non-periodic structures, such as grain boundaries or interfaces, another popular computational method, the multislice method, has also been employed (Kirkland, 1998). In principle, the multislice method divides a sample into several thin slices perpendicular to the direction of the incident electrons (z-direction), usually in a fraction or multiple integral of the repeat unit cell. The exit wavefunction is calculated sequentially slice by slice, while adding a propagation term between each slice, as illustrated in Figure 2.9.

Afterwards, the exit wavefunction is convoluted with the CTF of the objective lens (illustrated in Figure 2.3). The calculation of all CTF components and the convolution of the CTF and the exit wavefunction are most commonly carried out in reciprocal space. The mathematical operations of Fourier Transform (FT) and Inverse Fourier Transform (IFT) have been extensively used for fast, time efficient, and convenient computations in reciprocal space and the conversion back to the real space.

Once the convolution between the exit wavefunction and the CTF of the objective lens is accomplished, and the convoluted wavefunction is converted back to real-space coordinates by an IFT, an image wavefunction, $\psi_i(x, y)$, is formed at the backfocal plane of an objective lens. Note that at the backfocal plane, the image wavefunction is represented as a diffraction pattern pertaining to the sample, instead of the image of the sample. Further, the interference of the transmitted wave and diffracted wave forms the image intensity. The image intensity (square of the image wavefunction in real-space) can be formulated as:

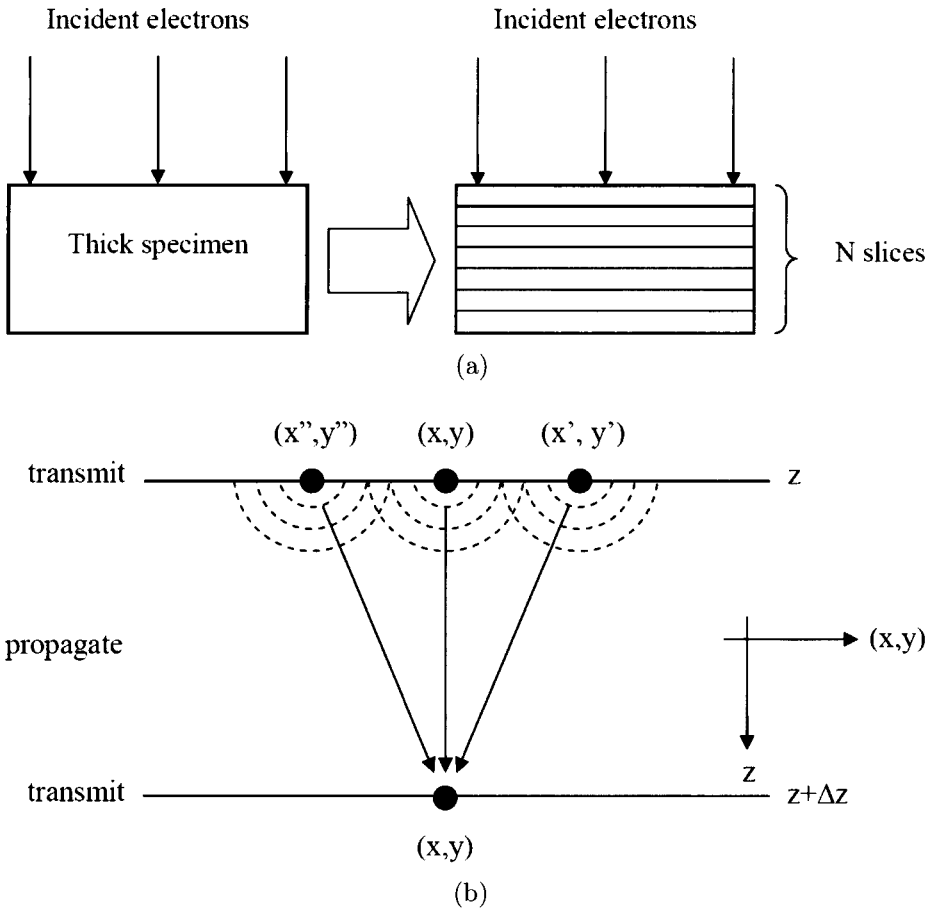

Figure 2.9: (a) Division of a thick sample into thin slices, where each slice is considered as a phase grating at which transmission of the wavefunction occurs. (b) Propagation of the wavefunction between two slices. The wavefunction in an x,y plane at z propagates to the x,y plane at $z+\Delta z$. Each point in the wavefront at z emits a spherical wave and all these waves combine at each point in the x,y plane at $z+\Delta z$. (from Kirkland, 1998)

$$I(x,y) = |\psi_i(x,y)|^2 = \psi_i(x,y) \cdot \psi_i^*(x,y) \tag{2.11}$$

where $\psi_i^*(x,y)$ is the complex conjugate of the image wavefunction.

Assuming the condition of linear interference, only one pair of diffracted beams contributes to each spatial frequency in the image intensity spectrum:

$$I_L(u) = \Psi_e(u) \cdot exp[-i\chi(u)] + \Psi_e^*(u) \cdot exp[i\chi(u)] \tag{2.12}$$

As $\{exp[i\chi(u)] - exp[-i\chi(u)]\} = 2i\ sin\chi(u)$, and at Scherzer defocus the value of $sin\chi(u)$ is equal to -1, the linear interference image intensity can be written as:

$$I_L(u) = \delta(u) + 2\sigma V(u)\ sin\chi(u) \tag{2.13}$$

where *V(u)* is the Fourier component of the real projected potential, $\phi_p(x,y)$. Applying an Inverse Fourier Transform to Equation 2.13, converting the total image intensity back to real space notation, gives the image intensity:

$$I_L(x,y) = 1 - 2\sigma\phi_p(x,y) \tag{2.14}$$

This image intensity is represented as a phase contrast image visible at the image plane, or on the microscope screen.

Quite recently, Jia, et al. (2004) reported a breakthrough in High Resolution Electron Microscopy (HREM) imaging by setting the total C_S of the microscope to a negative value. This imaging technique, Negative-C_S Imaging (NCSI), demonstrates non-linear imaging by taking into account not only the linear terms, i.e., the interaction between the transmitted beam and diffracted beams, but also the quadratic terms, i.e., both interactions between transmitted beam and diffracted beams and between the diffracted beams themselves. However, such a non-linear phenomenon has not been analytically

studied due to the intricate multi-beam effect, which means that not only N linear interference terms exist between transmitted beam and diffracted beams but also N^2 interference terms between diffracted beams must be analyzed in order to explain the non-linear effect quantitatively.

The interpretation of Jia, et al. (2004) was based on the weak phase object approximation. They claimed that by adjusting the C_S coefficient to a negative value, and compensating it with positive defocus, a positive aberration function, $\chi(u)$, can be achieved. Such alteration of imaging condition gives an additional phase of $-\pi/2$ to the diffracted wave, which results in the same sign for both the linear and the quadratic contribution (see Jia, et al. (2004) eq. (12)-(15)). Consequently, the contrast modulation is significantly enhanced, which allows one to observe image intensity of a low-Z element in the vicinity of high-Z elements. Despite the lack of analytical study in terms of non-linear image formation, the negative C_S-imaging technique has been experimentally proven to enhance the contrast of a low-Z element surrounded by high-Z elements, namely oxygen in a $SrTiO_3$ perovskite.

2.3.3 The C_S-corrector role

As previously described in Section 2.2, the aberration function of the objective lens (Equation 2.5) suggests two ways of improving the point resolution limit of a TEM, either by decreasing λ or C_S. Presently, the method of improving resolution by C_S reduction is becoming more popular, due to the ease of computerized controls and iterations of the series of multipolar lenses in the C_S-corrector.

The C_S-corrector consisting of a series of asymmetrical lenses of either hexapole lenses and doublet transfer lenses (Haider et al. (1998);(1998, b)) or quadrupole-octupole lenses (Krivanek et al., 2003), generates a negative C_S value, compensating the positive C_S value of the objective lens, giving a total C_S value of nearly zero or even slightly negative. Moreover, not only the generation of negative C_S values, but also removal of residual parasitic aberrations has been attained resulting in nearly aberration-free images. Such compensation eventually makes the achievement of the ultimate resolution possible for an electron microscope.

Besides the formation of a nearly aberration-free image, there are other advantages of utilizing a C_S-corrector in TEM, such as:

- Negligible sample knock-on damage by working at lower acceleration voltage.
- Larger space for sample movement between pole pieces enabling in-situ experiments inside a TEM.
- Remarkably diminished point spread (delocalization) of object information. As a result, images of irregularities in a crystalline object, such as defects and interfaces, are now observed in much more detail, leading to a more intuitive interpretation. In addition, the nearly absent contrast delocalization also simplifies interpretation of atomic structure of a phase contrast image. (Haider et al., 1998; Pennycook et al., 2006)
- Utilization of larger aperture sizes, i.e., objective aperture in HRTEM mode and condenser aperture in STEM mode. In TEM mode, the C_S-corrector compensates the axial aberration and removes higher order aberrations that cannot be corrected directly. In a similar manner, the utilization of a C_S-corrector in STEM mode allows small changes in illumination source, namely tilt, shift and convergence, without inducing significant residual or off-axis wave aberrations. By using the right defocus, the damping effect due to spatial incoherence of the source towards the CTF also becomes negligible. These factors permit the widening of the condenser aperture up to 40 mrad of convergence angle, resulting in a much higher intensity STEM probe, up to 10 times higher than that of a conventional uncorrected STEM. (Pennycook et al., 2006)
- Tuning of C_S value. Compensation of the positive C_S value of the objective lens by a negative C_S value of the C_S-corrector facilitates the control of total C_S value, ranging from nearly zero to slightly negative. The significance of reaching a slightly negative C_S value has been demonstrated for enhancing contrast of low-Z elements surrounded by high-Z elements. (Jia et al., 2003, 2004, 2005, 2006)

2.3.4 Fundamental mechanism of C_S-corrector

Referring to Section 2.2, the two major aberrations impacting the operation of the objective lens in an electron microscope are spherical aberration and chromatic aberration. Between the two, spherical aberration, of the order of mm in magnitude, is dominant since the energy deviation at the electron source is almost negligible, of the order of 10^{-6}, which is 0.1 eV for a 100 keV beam. Therefore, more development had been focused on reducing the spherical aberration in TEM.

As stated in the previous section, the asymmetrical or multipolar electromagnetic lenses, namely quadrupole/octupole or hexapole assembly, generates a negative C_S value, which cancels out the positive C_S value of the round-symmetrical lens. This spherical aberration compensation enables the electrons scattered at various angles to be brought into focus at the same point, demonstrating the perfect lens characteristic as illustrated in Figure 2.4(a). The electrons scattered at high angles relative to the optic axis are now brought to the correct focal point resulting in an extended point resolution limit and an information limit down to the sub-Å regime. A much larger objective aperture in HRTEM and condenser aperture in STEM, consequently, can be employed.

A detailed description and mechanism of operation of hexapole correctors by Rose and Haider, et al. (1990) and those of quadrupole-octupole correctors by Krivanek, et al. (1999; 2003) have been presented by Hetherington (2004) and Bleloch and Lupini (2004). Schematic illustrations of the series of lenses are depicted in Figure 2.10 (a) for a hexapole configuration and in Figure 2.10 (b) for a quadrupole-octupole combination.

In conventional microscopes, the Scherzer defocus (Δf or C_1) and the spherical aberration (C_S or C_3) are adjusted to cancel one anothers phase shifts. In addition, a stigmator is positioned for compensating the two-fold astigmatism (A_1) of the objective lens. Despite the existence of a stigmator, higher symmetry astigmatisms, which possess remarkably detrimental effects at the sub-Å scale, remain uncompensated. As such, compensation of higher order aberrations, such as three-fold astigmatism (A_2), star aberration (S_3), and axial coma (B_2) is crucial in order to achieve the ultimate

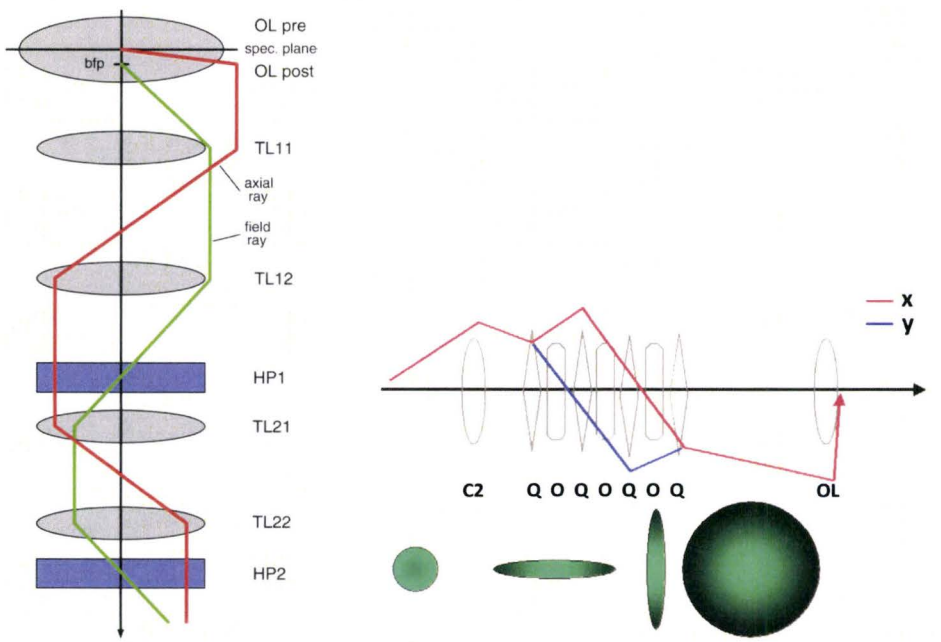

(a) (b)

Figure 2.10: (a) Hexapole correctors as proposed by Rose (1990), located after the objective lens (OL), consists of two hexapoles (HP1, HP2) and two doublet transfer lenses (TL11, TL12, and TL21, TL22) (from Hetherington, 2004). (b) Quadrupole-octupole correctors as proposed by Krivanek (2003). C2 corresponds to the second condenser lens and OL the objective lens. (from Bleloch and Lupini, 2004)

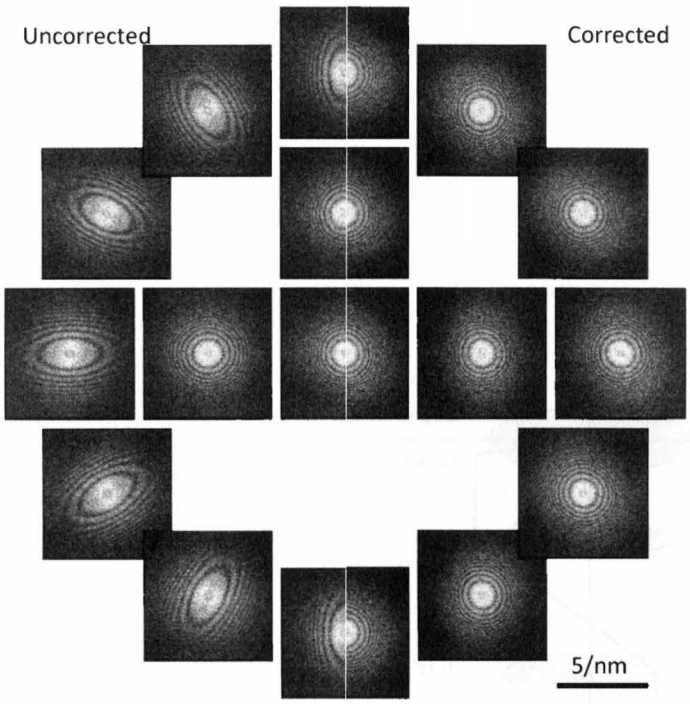

Figure 2.11: Diffractogram tableau from the uncorrected and C_S-corrected TEM. The beam tilt angle, $|\tau|$, is 10.8 mrad and the azimuthal angles are between $0 - 2\pi$ with increment of $\pi/6$. (from Uhlemann and Haider, 1998)

resolution of electron microscope.

Accurate measurement of the first-order aberrations, namely defocus and twofold astigmatism, is carried out by acquiring a diffractogram taken from a thin amorphous object with untilted illumination using the Zemlin tableau (Zemlin et al., 1978). Subsequently, higher order aberrations can be calculated from the systematically tilted illumination with different azimuthal angles, which induce intentional aberration to the diffractogram. The comparison of a tableau of diffractograms before and after C_S correction is shown in Figure 2.11.

The mathematical formula and derivation of wave aberration coefficients are rather complex and the details can be consulted in the articles by Zemlin (1978) and Uhlemann and Haider (1998). In this study, the calculation and compensation of both axial and residual aberrations were performed using the fully automated interface of the *CEOS GmbH* C_S-corrector software. In principle, higher tilt angle and smaller increment of azimuthal angle result in a more refined calculation of higher order aber-

Table 2.1: The wave aberration coefficients and their magnitude calculated from the $\pi/4$ limit at 200 kV (from Uhlemann and Haider, 1998)

Coefficient	Symbol	$\pi/4$ limit	$\pi/4$ limit at 200 kV for g_{max} =		
			4/nm	7/nm	10/nm
Defocus	$C_1, -\Delta f$	$\frac{1}{4}(\lambda g_{max}^2)^{-1}$	6.2 nm	-2.0 nm	1.0 nm
Scherzer focus:			-69 nm	-22 nm	-11 nm
Twofold Astigmatism	A_1	$\frac{1}{4}(\lambda g_{max}^2)^{-1}$	6.2 nm	2.0 nm	1.0 nm
Threefold Astigmatism	A_2	$\frac{3}{8}(\lambda^2 g_{max}^3)^{-1}$	0.93 µm	0.17 µm	60 nm
Axial coma	B_2	$\frac{1}{8}(\lambda^2 g_{max}^3)^{-1}$	0.31 µm	58 nm	20 nm
Spherical Aberration	C_3, C_S	$\frac{1}{2}(\lambda^3 g_{max}^4)^{-1}$	0.12 mm	13 µm	3.2 µm
Scherzer focus:			1.3 mm	130 µm	32 µm
Fourfold Astigmatism	A_3	$\frac{1}{2}(\lambda^3 g_{max}^4)^{-1}$	0.12 mm	13 µm	3.2 µm
Star Aberration	S_3	$\frac{1}{8}(\lambda^3 g_{max}^4)^{-1}$	31 µm	3.3 µm	0.79 µm
Fivefold Astigmatism	A_4	$\frac{5}{8}(\lambda^4 g_{max}^5)^{-1}$	15 mm	0.94 mm	0.16 mm
Axial coma	B_4	$\frac{1}{8}(\lambda^4 g_{max}^5)^{-1}$	3.1 mm	0.19 mm	32 µm
Three lobe Aberration	D_4	$\frac{1}{8}(\lambda^4 g_{max}^5)^{-1}$	3.1 mm	0.19 mm	32 µm
Spherical Aberration	C_5	$\frac{3}{4}(\lambda^5 g_{max}^6)^{-1}$	1.8 m	64 mm	7.6 mm
Sixfold Astigmatism	A_5	$\frac{3}{4}(\lambda^5 g_{max}^6)^{-1}$	1.8 m	64 mm	7.6 mm

rations, leading to a better compensation by the C_S-corrector and a higher achievable resolution. Nowadays, the C_S value can be iterated and compensated to the order of hundreds of nm, depending on the resolution to be achieved in the microscope.

The list of wave aberration coefficients and their allowed magnitude for achieving $\pi/4$ phase difference limit at 200 kV as calculated by Uhlemann and Haider (1998) are listed in Table 2.1. The various distortions of phase shift by various wave aberrations listed in Table 2.1 are represented by the diffractograms displayed in Figure 2.12.

The remarkable impact of using a C_S-corrector towards improving the point resolution of a TEM has been concisely reported by Hetherington (2004) and Sawada, et al. (2005) by comparing two diffractograms obtained before and after C_S correction (Figures 2.13(a) and (b)). The dark ring, visible in the diffractogram from the uncorrected microscope as marked with the white arrow, corresponds to the undesirable contrast reversal effect in the image beyond the point resolution limit, which is 0.19 nm in this case. In the diffractogram obtained from the C_S-corrected microscope,

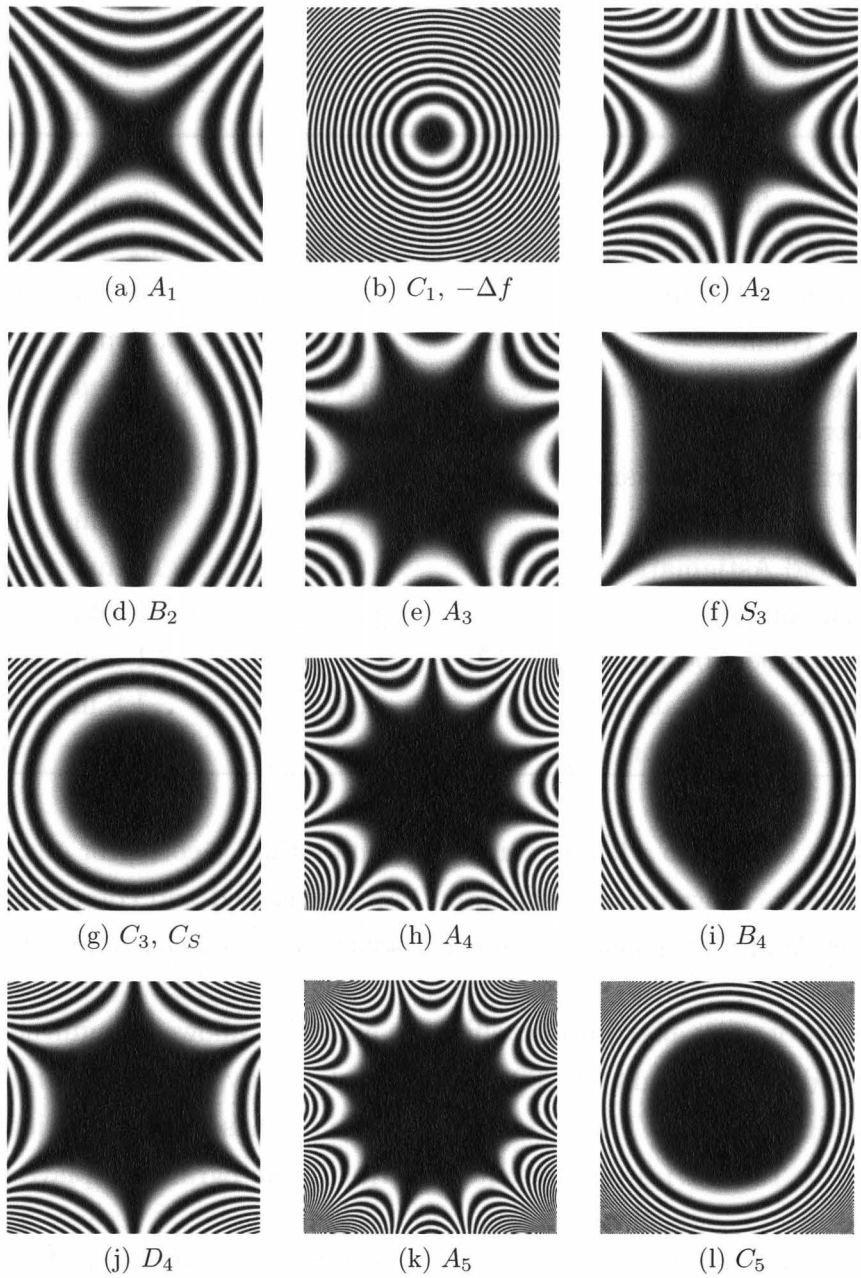

(a) A_1 (b) C_1, $-\Delta f$ (c) A_2

(d) B_2 (e) A_3 (f) S_3

(g) C_3, C_S (h) A_4 (i) B_4

(j) D_4 (k) A_5 (l) C_5

Figure 2.12: The diffractograms pertaining to various wave aberrations: (a) A_1 twofold astigmatism, (b) C_1 defocus, (c) A_2 threefold astigmatism, (d) B_2 second order axial coma, (e) A_3 fourfold astigmatism, (f) S_3 star aberration, (g) C_3 third order spherical sberration, (h) A_4 fivefold astigmatism, (i) B_4 fourth order axial coma, (j) D_4 three lobe aberration, (k) A_5 sixfold astigmatism, and (l) C_5 fifth order spherical aberration (*Courtesy of: Shery Chang, Monash University, Melbourne, Australia*).

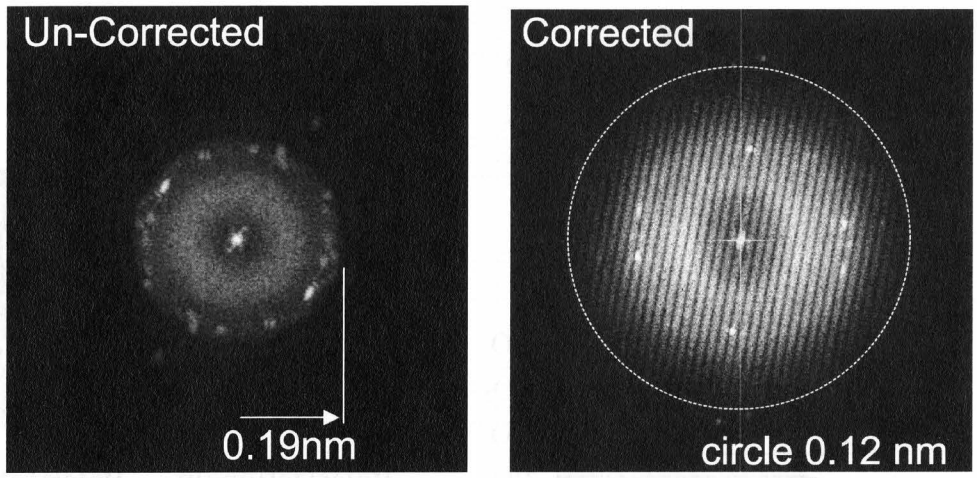

(a) (b)

Figure 2.13: Diffractograms from (a) uncorrected with C_S of 0.5 mm and (b) C_S-corrected TEM with C_S of 0.01 mm (from Sawada et al., 2005). The slanted lines in (b) resulted from the image shift that is intentionally introduced during the image acquisition.

contrast reversals are avoided; there are no rings in the diffractogram, and thus image interpretation is simplified. The continuous contrast extends to 0.12 nm with 10 % signal transfer, indicated by a dotted white circle in Figure 2.13(b).

In summary, the utilization of a C_S-corrector has been demonstrated and proven extremely beneficial in achieving ultimate resolution in electron microscope, both in TEM and STEM mode. In the next section, various interesting phenomena occurring in perovskite materials will be reviewed and some remaining problems pertaining to their magnetic and ferroelectric properties will be addressed.

2.4 Perovskite Oxides

Various composition-dependent physical properties of perovskite oxides offer enormous potential for electronic industries. Considered as relatively new emerging materials, their properties have not yet been fully established and understood. The intensity of scientific publication regarding these materials has remarkably increased

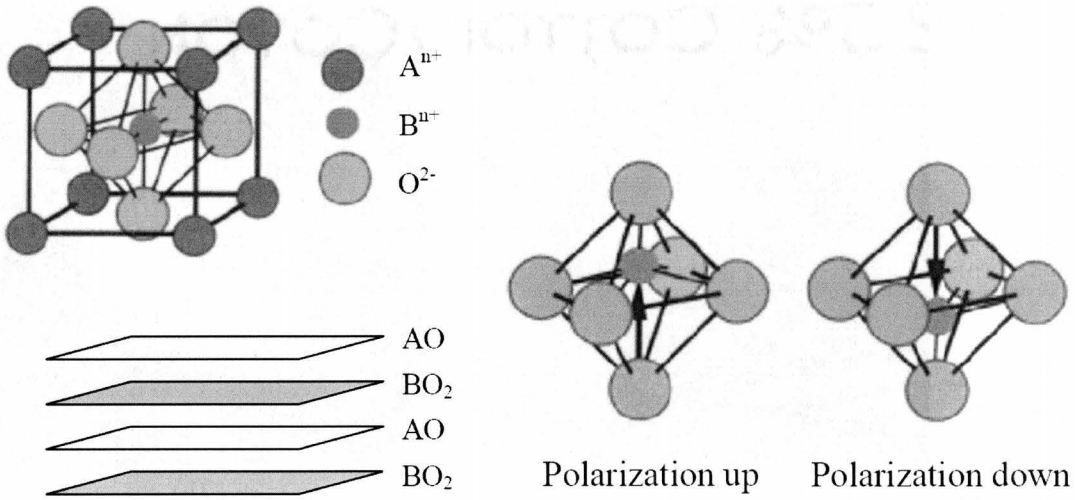

Figure 2.14: (a) The unit cell and the stacking sequence of perovskite ABO_3. (b) The 180° polarization reversal for two of the six possible polarization states is produced by displacement of the central cation in the tetragonal plane. (from Haertling, 1999)

as the perovskite oxides continue to exhibit significant challenges and complications in their integration into the world of nanotechnology.

The unit cell structure of an ideal perovskite oxide, ABO_3, (Figure 2.14(a)) is composed of alternating AO and BO_2 layers, where A is a large sized cation (e.g., Bi, Pb, Ba, etc.), B is a smaller sized cation (usually transition metals, e.g., Ti, Fe, Cr, etc.) and O is an oxygen anion. The extraordinary part of some, but not all, perovskite unit cells is that the position of the central B-site cation is not centro-symmetric, but instead has a slight distortion from the centre of the octahedra (Figure 2.14(b)). Such non-centrosymmetry of a unit cell is responsible for the generation of piezoelectricity, which is a change in electric polarization under a strained condition. Under the category of piezoelectrics, there is a sub-category of pyroelectric materials, which possess the characteristic of being permanently polarized within a given temperature range. The spontaneous polarization of pyroelectric materials also changes with temperature. A subgroup of the pyroelectrics is ferroelectrics, whose electric polarization is spontaneous and reversible by an external electric field. The classification of piezoelectrics and their subgroups based on the symmetry is displayed in Figure 2.15.

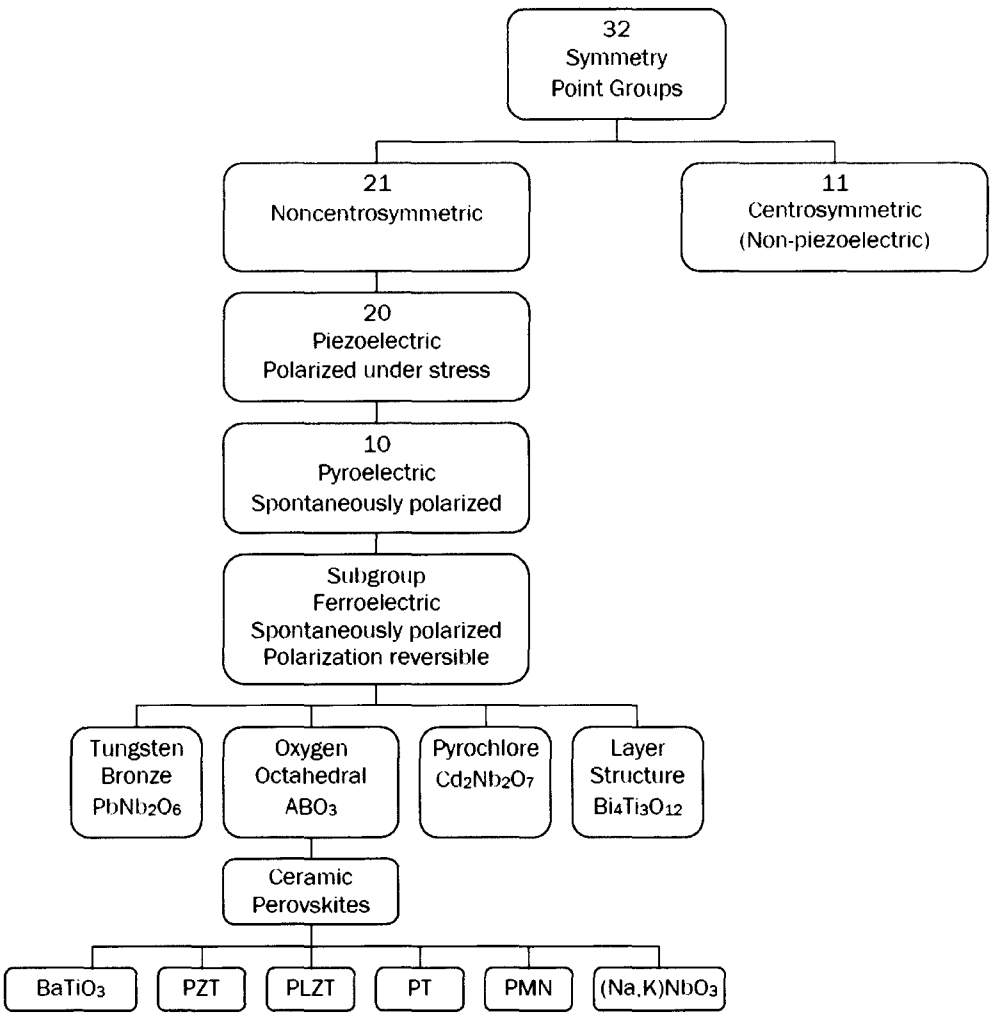

Figure 2.15: Classification of piezoelectrics and their subgroups on the basis of symmetry (from Haertling, 1999). The abbreviations in the ceramic perovskites correspond to lead zirconate titanate (PZT), lead lanthanum zirconate titanate (PLZT), lead titanate (PT), and lead magnesium niobate (PMN).

The investigation of atomic and electronic structure of perovskite materials is expected to reveal basic phenomena and mechanisms responsible for a specific physical property, for example ferroelectricity or multiferroicity, i.e., simultaneous coupling of magnetic, electric or elastic orderings. Such knowledge and understanding of the corresponding phenomena or mechanism may eventually enable the tailoring and utilization of novel properties for various device or industrial applications. Further investigation will involve the observations of defects and irregularities, which may be responsible for abnormal characteristics or deviation from bulk properties.

2.5 Bismuth-based perovskite oxides

Nowadays electronic technology relies heavily upon the use of various magnetic and ferroelectric materials for better and faster data processing as well as far much larger capacity and more stable and reliable data storage. The improvement in those qualities requires the presence of combined properties of stable and relatively large ferromagnetism and ferroelectricity in a single material, so called multiferroic material. The idea of implementing properties of multiferroic materials, whose electric and magnetic ordering interaction may display the giant magnetoelectric effect, becomes the driving force for further miniaturization of multifunctional devices. One major class of perovskite oxides that show ferroelectric and/or multiferroic behaviour is bismuth based oxides. This investigation was focused on characterizing the structure-properties relationship of the Bi-based perovskite oxides. The background, motivation and development of several Bi-based perovskite oxides that are the focus of this study, are reviewed in the following sections.

2.5.1 $BiFeO_3$ (BFO)

One of the most popular Bi-based perovskite oxides available and offering remarkable potential for industrial applications is bismuth ferrite (BFO). BFO is a natural ferroelectromagnet, which exhibits ferroelectricity (T_C ~1,100 K) and antiferromagnetism (T_N ~640 K). It was first synthesized in 1956, however, the characterization of its

intrinsic properties has been a challenge due to poor sample quality, as it was difficult to synthesize high quality single crystals in bulk form(Bea et al., 2005; Lebeugle et al., 2008). Recently, Bea et al. (2006) has successfully reported the physical properties of single-phase BFO films, which were obtained in a narrow range of deposition pressure P_{O2} and temperature. The pure BFO film without a parasitic Fe-rich phase exhibits a low bulk-like magnetic moment (~0.02 μ_B/Fe) and the BFO film with parasitic Fe-oxides (mostly γ-Fe_2O_3) displays a weak ferromagnetic behaviour.

The simultaneous presence of magnetization and electrical polarization, multiferroicity, in BFO offers independent encoding of information in a single multiferroic bit. A four-state memory has been demonstrated, (Gajek et al., 2007) which may permit data to be electrically written and magnetically read, and therefore enable a combination of the best aspects of ferroelectric random-access memory (FeRAM) and magnetic data storage (MRAM). Despite such demonstrated performance, one challenge remains in that the multiferroicity only appears at a relatively low temperature rather than at room temperature.

A relatively recent investigation by Nechache, et al. (2006) reported that combining BFO with another closely lattice-matched Bi-based perovskite oxide, $BiCrO_3$ (BCO), induces a significant boost in magnetization in comparison to BFO alone. More interestingly, the large magnetization existed at room temperature, which further increases the interest in this material. A more detailed review of the properties and predicted structure of combined BFO and BCO, which was one of Bi-based perovskite oxides studied here, is elaborated in Section 2.5.3.

2.5.2 $BiCrO_3$ (BCO)

BCO is an antiferromagnet (T_N ~123 K), which was first synthesized by a high-pressure firing method in 1968 (Sugawara et al., 1968). This material exhibited a magnetic anomaly around 95 K, and its magnetic moment increases with decreasing temperature, due to a change in the easy direction of magnetization. BCO undergoes a first order structural phase transition at ~410 K. Below the transition temperature, the unit cell structure of BCO is triclinic with lattice parameters $a = c = 3.906$ Å, b

= 3.870 Å $\alpha = \gamma = 90.5°$ and $\beta = 89.1°$ (at 300 K). Above the transition temperature, it is pseudomonoclinic with $a = c = 3.878$ Å, $b = 7.765$ Å, and $\beta = 88.8°$ (at 460 K). Even though the dielectric properties of BCO have not been extensively investigated, Hill, et al. (2002) have predicted from first principle density functional calculations that BCO may exhibit ferroelectricity due to an antiferroelectric distortion.

Kim, et al. (2006) have reported that BCO capacitors exhibited well-defined double hysteresis loops, which correspond to antiferromagnetic behaviour. This behaviour is in agreement with theoretical predictions that Bi lone pair induces polarization in bismuth-based perovskites, as observed in ferroelectric $BiMnO_3$ and $BiFeO_3$. A weak parasitic ferromagnetism resulting from the antiferromagnetic ordering was observed below 140 K. Despite a report by Murakami and Wuttig (2006) suggesting that the presence of a small hysteresis of non-linear dielectric signal was a function of DC voltage at room temperature, so far there has been no conclusive evidence of the presence of ferroelectricity in BCO (Kim et al., 2006).

2.5.3 Bi_2FeCrO_6 (BFCO)

In the early stage of finding various multiferroic materials, Baettig and Spaldin (2005) have reported their theoretical prediction on design and properties of a new multiferroic material, Bi_2FeCrO_6. They used first-principles density-functional theory in predicting that BFCO would have a rhombohedral structure, similar to that of BFO, but with an ordering of Fe^{3+} and Cr^{3+} cations along the <111> direction. BFCO has also been predicted to be ferrimagnetic at 0 K with a magnetic moment of 2 μ_B/u.c. and ferroelectric with a polarization of 80 $\mu C/cm^2$.

Pignolet and co-workers (Nechache et al., 2006) have reported the first successful synthesis of BFCO by a pulsed laser deposition technique on a $SrTiO_3$ substrate with a $SrRuO_3$ buffer layer. The unit cell parameters of the oxide compounds employed for epitaxial growth of BFCO are listed in Table 2.2 (from Baettig and Spaldin (2005)). The experimental BFCO thin film surprisingly demonstrated superior properties than expected (Figure 2.16). The saturation magnetization and remanent magnetization increased to nearly ten times and four times, respectively, as compared to those of a

Table 2.2: List of experimental unit cell and lattice parameters of $BiFeO_3$, $BiCrO_3$, $SrTiO_3$, $SrRuO_3$, and calculated atomic position and lattice parameters of Bi_2FeCrO_6. (Baettig et al., 2005)

	$BiCrO_3$	**Bi_2FeCrO_6**	**$BiFeO_3$**	**$SrTiO_3$**	**$SrRuO_3$**
Structure	**Triclinic**	**Rhomb. (calc)**	**Rhomb.**	**Cubic**	**Cubic**
a (Å)	3.906 (a=c)	5.47	5.6343	3.905	3.928
α(°)	90.5 (α=γ)	60.09	59.348	–	–
	β= 89.15				
b (Å)	3.870	–	–	–	–
		Atomic Coordinates			
Bi	–	0.00/0.503	–	–	–
Cr/Fe	–	0.226 / 0.732	–	–	–
O_x	–	0.545 / 0.047	–	–	–
O_y	–	0.950 / 0.905	–	–	–
O_z	–	0.398 / 0.448	–	–	–

BFO film alone for the same film thickness (~300 nm). Furthermore, such magnetization behaviour, predicted to exist below 110 K was observed at room temperature.

Such astonishing findings offer a challenging opportunity to provide insights into the structure and behavior of BFCO. The TEM study is aimed to provide structural information which can be used to further understand the behaviour of the material with respect to the previous predictions.

2.5.4 $Bi_{4-x}La_xTi_3O_{12}$ (BLT)

$Bi_{4-x}La_xTi_3O_{12}$(BLT) is a popular bismuth-based ferroelectric material, which has been used in the field of non-volatile random access memory (NV-RAM) due to its relatively large remanent polarization and good fatigue resistance. BLT, along with $SrBi_2Ta_2O_9$ (SBT), has been a strong candidate for replacing PZT ($Pb_{1-x}Zr_xTiO_3$) for lead-free NV-RAM applications in various electronic devices in response to increased worldwide environmental concerns.

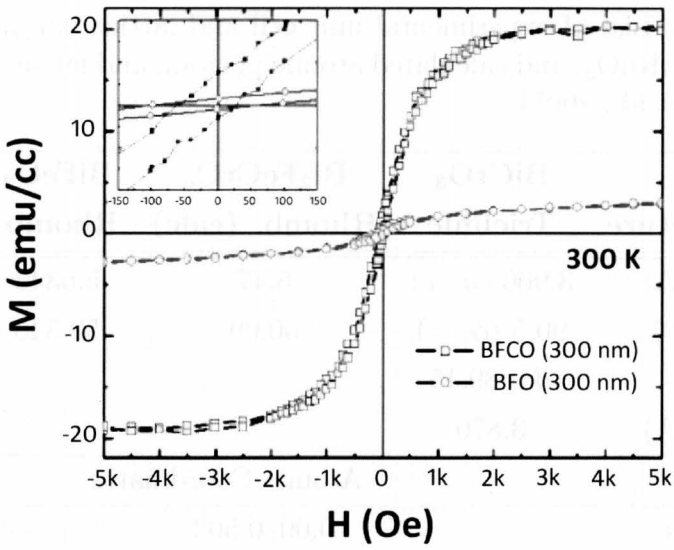

Figure 2.16: Magnetization hysteresis of a 300 nm thick BFCO film (squares) compared to that of a 300 nm thick BFO film (circles) at room temperature. The inset shows a zoom around the origin. The direction of applied magnetic field H was in the plane of the films, along the <100> direction of STO. (from Nechache et al., 2006)

BLT is also known as a lanthanum doped Bismuth Titanate, $Bi_4Ti_3O_{12}$ (BiT), which is a layered perovskite classified in the Aurivillius family, with three layers of Ti-O octahedra between $(Bi_2O_2)^{2+}$ layers (Figure 2.18). The parent stucture of BiT consists of a pseudo-orthorhombic unit cell with lattice parameters of $a = 0.544$ nm, $b = 0.541$ nm, and $c = 3.284$ nm. BiT was initially explored as a potential material for memory applications due to its ferroelectric properties.

Despite its high remanent polarization of $\sim$30 μC/cm^2 and its fatigue-free characteristic up to 10^{10} read/write cycles in bulk form, BiT is no longer satisfactory in fulfilling the criteria for non-volatile memory (NVM) purposes when its dimensionality decreases down to a thin film. BiT thin films show low fatigue resistance and surprisingly low values of remanent polarization ($2P_r$ of 4 - 8 μC/cm^2) (Joshi and Krupanidhi, 1993; Kijima et al., 1999). The schematic illustration of fatigue behaviour in ferroelectric materials is shown in Figure 2.17, where the remanent polarization value decreases with increasing number of polarization reversals. (Ishiwara et al., 2004) Later findings demonstrated that addition of lanthanides, La in particular, facilitates fatigue resistance of BiT, so that it becomes sufficiently fit for non-volatile memory applications. The comparison of BLT with other ferroelectric compounds for potential

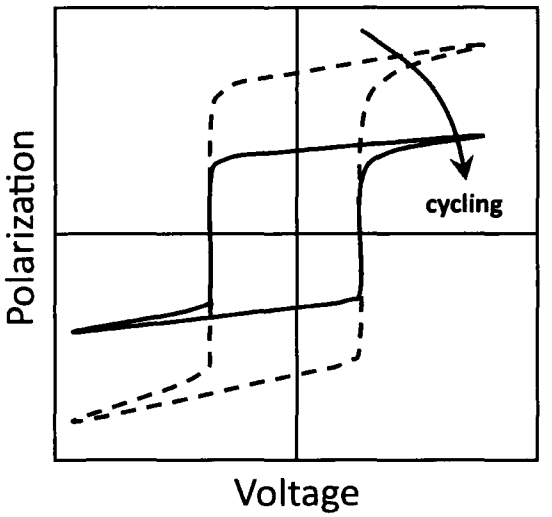

Figure 2.17: Fatigue, one of the major problems with ferroelectric materials for non-volatile memory applications, occurs due to the decreasing number of switchable domains with increasing number of polarization reversal (write/read cycles) (from Ishiwara et al., 2004)

Table 2.3: Properties of PZT, SBT, and BLT thin films prepared on conventional Pt electrodes (Park et al., 1999).

Characteristics	**PZT**	**SBT**	**BLT**
$2P_r$ (μC·cm^{-2})	20-70	4-16	16-20
Fatigue resistance	Poor	Good	Good
Leakage current at 5 V (A·cm^{-2})	10^{-7}	10^{-9}	10^{-7}
Processing temperature (°C)	500-600	750-850	650-700

NVM applications is displayed in Table 2.3.

The optimum amount of lanthanum (La) added into BiT layered perovskite, $Bi_{4-x}La_x Ti_3O_{12}$, has been experimentally determined to be around $x = 0.75$. Despite the relatively small fraction of La in BLT, the addition significantly improved the fatigue-resistance of BiT (de Araujo et al., 1995; Park et al., 1999). Park, et al. (1999) has also proposed that the fatigue-free property in bulk BiT is generated due to the simple charge compensating role of the $(Bi_2O_2)^{2+}$ layers. Moreover, they also explained that the chemical stability of the perovskite layers against oxygen vacancies, the source of fatigue in most ferroelectric materials, may also be responsible for the fatigue-free

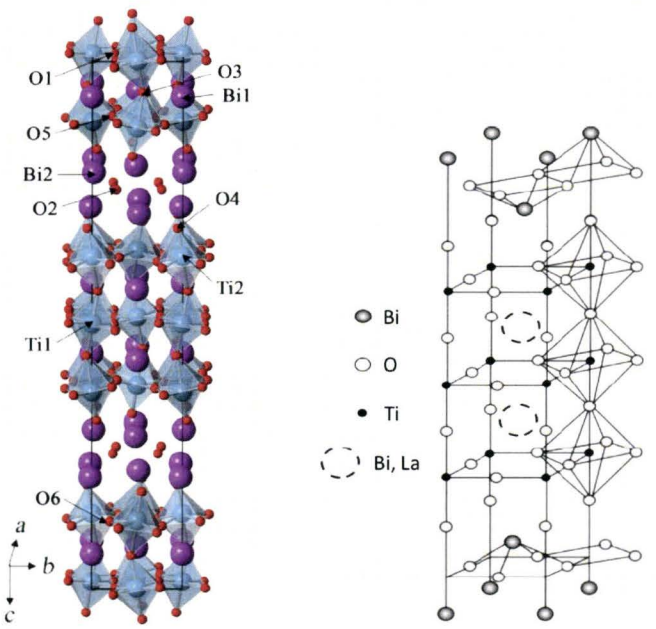

(a) (b)

Figure 2.18: (a) The widely-accepted crystal structure of BiT. Perovskite $Bi_2Ti_3O_{10}$ and fluoritelike Bi_2O_2 layers stacked alternatively along the c-axis. (Kim et al., 2007) (b) Lattice structure of the La-doped bismuth titanate. The compound studied is $Bi_{3.25}La_{0.75}Ti_3O_{12}$ (BLT) where La ions can also be substituted by other rare-earth ions such as Pr, Nd, or Sm. (Park et al., 1999)

behaviour (Park et al., 1999, b).

In order to understand the factors responsible for the deterioration in the physical properties of BiT, especially in fatigue resistance, with thickness reduction, it is essential to first identify the mechanism and role of La ions in improving the remanent polarization and fatigue properties of the parent BiT structure. Several mechanisms have been proposed to explain this phenomenon:

- The domain clamping, resulting in a decrease in number of switchable domains under application of an electric field, has been widely recognized as a factor responsible for polarization fatigue and small P_r value and attributed to a strong interaction between domain walls and defects, such as oxygen vacancies. Kim et al. (2007) pointed out that La ions are likely to substitute Bi ions in perovskite layers, due to the almost completely ionized nature of La and higher ionic valence of Bi in the perovskite layers than Bi in the Bi_2O_2 layer. The fraction of La ions substituting Bi ions in the Bi_2O_2 layers, if present, would be relatively small. The location of La ions, whether in the perovskite layer or in the Bi_2O_2 layer, will significantly influence the chemical bonding of Bi-O. In BiT, the chemical bonding resulting from orbital hybridization of Bi-O in the perovskite layer is stronger in the direction of the *a*-axis relative to that of the *b*-axis. In contrast, the chemical bonding in BLT becomes more isotropic along both *a*- and *b*- axes, due to the substitution of Bi by La ions. The isotropic chemical bonding in BLT stabilizes oxygen in the perovskite layers and prevents formation of oxygen vacancies, which consequently improves the fatigue resistance of BLT.

- Kim, et al. (2008) addressed the effect of bond covalency in explaining the fatigue-free behaviour of BLT, similar to that previously described by Kim et al. (2007). The incorporation of more ionic La ions in the perovskite layers essentially depressed the covalent anisotropic bonding from the orbital hybridization of Bi-O. The depressed covalent bonding also minimized orbital interaction between perpendicularly aligned Bi-O and Ti-O bonds. Consequently, the interaction between collinear Ti-O bonds becomes stronger than the perpendicular interaction of Bi-O-Ti, resulting in higher lattice stability. Further, the better lattice stability helps in stabilization of O ions and reduction of Bi volatility, which in turn improve the memory performance of BLT relative to BiT.

- Hervoches and Lightfoot (2000), however, explained in a different way that La ions may also substitute for Bi ions either in the Bi_2O_2 layer or in the perovskite $Bi_2Ti_3O_{10}$ layer with a different level of occupancy. For $Bi_3LaTi_3O_{12}$, the occupancy proportion was predicted to be 94% of Bi and 6% of La in the Bi_2O_2 layer, and 79% of Bi and 21% of La in the perovskite layers. Despite the similar ionic radii between Bi^{3+} and La^{3+}, such cationic disorder of La in both perovskite and Bi_2O_2 layers, with a greater tendency of La present in the Bi_2O_2 layers, arises as the mechanism of strain relief, while simultaneously allowing off-centering of Bi ions in the perovskite layer.

- Hur, et al. (2004) stated that cationic substitution of Bi by La causes volumetric contraction of the unit cell, due to the smaller size of the substituent cation and reduction of structural distortion induced by octahedral tilting of TiO_6, as observed in BiT. Their X-ray Absorption Near Edge Structure (XANES) results showed the strengthening of Ti-O bonds, which stabilizes the TiO_6 octahedra and weakens the existing Bi bond with adjacent oxygen ions. Consequently, all the impacts lead to prevention of oxygen vacancy formation, giving rise to a fatigue-free behaviour of ferroelectric BiT.

- Ding, et al. (2001) has proposed that antiphase boundaries (APBs), which are present in BLT but not in BiT, has some contribution in enhancing fatigue resistance. Without APBs, new ferroelectric domains are able to nucleate only at the electrode/ferroelectric capacitor interface. The presence of APBs facilitates nucleation of the new domain during polarization reversals, removing the sole dependency of domain nucleation on the electrode interface.

So far, the abovementioned investigations suggest the importance of locating the cation substituent in the unit cell of BiT parent material in order to be able to fully understand the mechanism of fatigue-free generation in BLT. Here TEM investigation will be performed to clarify the location of La as well as the role of previously unidentified defects responsible for improved physical properties of BLT.

Chapter 3

Experimental Procedures

3.1 Pulsed Laser Deposition

Thin film growth of the samples investigated in this study was carried out at INRS Énergie, Materiaux et Télécommunications by Riad Nechache and Olivier Gautreau by utilizing a pulsed laser deposition (PLD) instrument. The laser source was a KrF excimer pulsed laser with a wavelength of 248 nm. For $BiFeO_3/BiCrO_3$ (1/1) and $Bi_{3.25}La_{0.75}Ti_3O_{12}$ film deposition on $SrTiO_3$ substrates, the source material used was a single target. Two separate targets of $BiFeO_3$ and $BiCrO_3$ were used for deposition of $BiFeO_3/BiCrO_3$ (1/3) thin films.

A schematic diagram of the PLD instrument is given in Figure 3.1 (Lowndes et al., 1996). Conceptually, the PLD process can be simply described as follows:

1. A focused pulsed (excimer) laser beam is directed onto a rotating polycrystalline target.

2. The rapid heating and vaporization of the target from the laser pulse forms a plasma plume containing neutral atoms, molecules, and ions, in both ground and excited states, as well as energetic electrons.

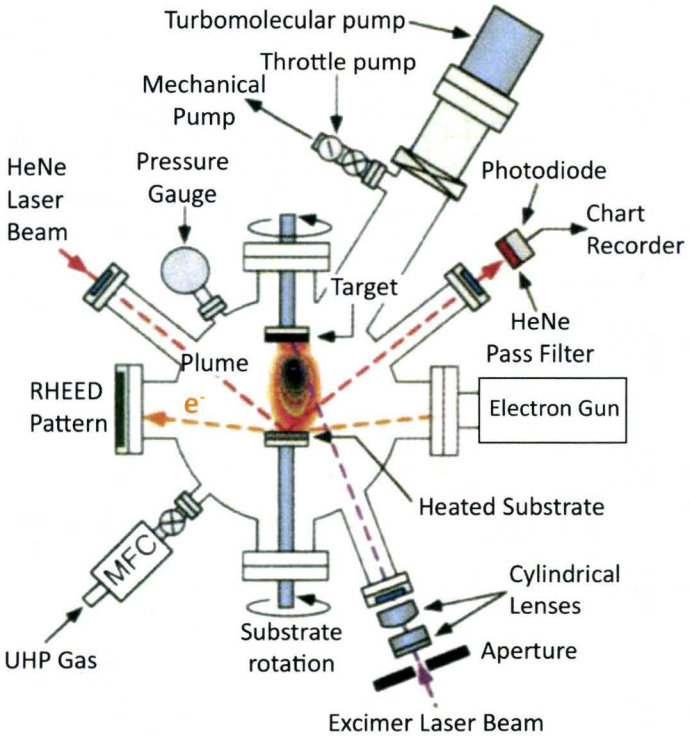

Figure 3.1: An illustration of the basic PLD system (from Lowndes et al., 1996).

3. The atoms and ions then propagate toward a heated substrate where deposition of the growth species takes place.

Lowndes, et al. (1996) have stated that the PLD method is an effective method for growing oxides and other chemically complex materials. Several main advantages of PLD are: (i) congruent/stoichiometric material transfer from target to substrate, (ii) deposition by utilizing an energetic plasma beam, and (iii) capability for reactive deposition in ambient gases. All these advantages contribute to the flexibility of growing multilayers of heterostructures and controlling different types of crystallinity of the film, i.e., amorphous, polycrystalline or epitaxial single crystal film. The types of deposited thin film are strongly dependent on the nature of the substrate and the growth conditions, which are governed by several parameters, namely the energy of the laser pulse, the pulse frequency, the target to substrate distance, the substrate temperature and the gas pressure.

Despite the abovementioned advantages, there is one drawback of PLD for thin film

growth; it can only be utilized for depositing rather small areas. Large areas of thin film with uniform thickness are difficult to achieve due to the strongly directed plasma plume. The thickness uniformity of the deposited film, however, can be manipulated and optimized by either altering the motion of the ablation plume to make a 'painting' or using a 'rastering' mode onto the substrate or rotating the substrate under the ablation plume.

3.2 TEM Sample Preparation

TEM sample preparation requires a series of complex steps, most of which are quite delicate, in order to reduce the thickness of the bulk sample down to electron transparency (usually $\leq$ 100 nm). There were two approaches implemented in this study, namely conventional sample preparation and tripod polishing. Conventional sample preparation involves various instruments, yet sample handling is easier relative to tripod polishing. Tripod polishing, in contrast, involves only a single instrument yet requires very delicate sample handling as the sample was basically mechanically ground down to $\sim$ 1 μm thick. The major advantage of tripod polishing lies in a much shorter period of ion milling for the final thickness reduction to electron transparency, which results in a reduced amorphous layer on the sample. The prevention of formation of a thick amorphous layer results in higher quality TEM samples, so that higher quality TEM images, demonstrating atomic resolution, can be attained.

3.2.1 Conventional Sample Preparation

The arrangement of samples in the initial stage of conventional sample preparation is displayed in Figure 3.2(a). Two pieces of sample with dimension of at least 1 mm wide were glued with the thin film side of interest face-to-face and clamped between Si supporting bars, four bars of similar width on both sides (Figure 3.2(a)). The glue between the sample and Si bars was a hard, fast-curing epoxy adhesive (*Allied EpoxyBond110*^{TM}), which is a mixture of part A and part B (hardener) with a weight ratio of 10:1, respectively. The ensemble was then cured at 150°C for about seven

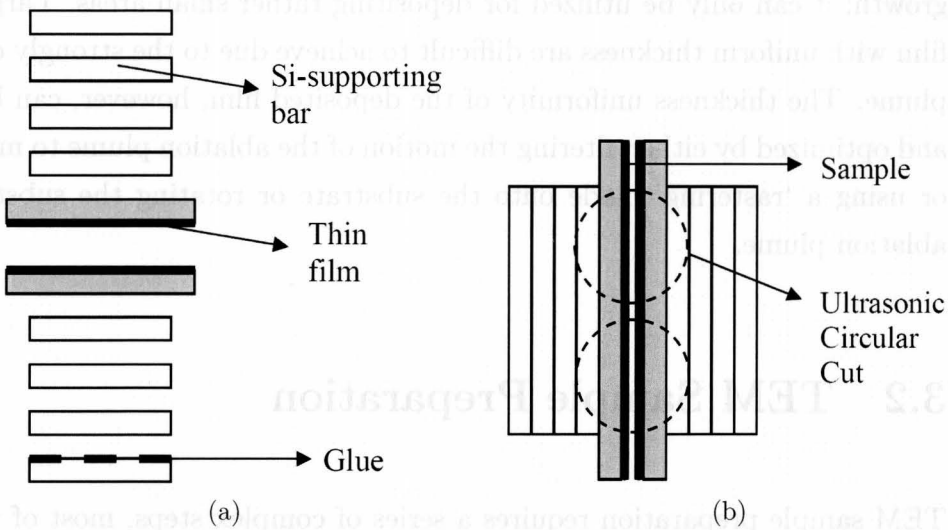

Figure 3.2: (a) An illustration of the configuration of the Si-clamped sample in conventional TEM sample preparation. The thin film on the two pieces of sample was glued face-to-face. (b) The position of the ultrasonic circular cut on a $\sim$ 200 μm thick Si-clamped sample.

minutes, until the glue set. Next, the ensemble was mounted using wax glue onto a sample holder of the manual grinding device from *South Bay Technology Inc.* with minimum grinding increment of $\sim$ 25 μm. The mounted sample was then thinned by manual polishing with a series of abrasive SiC papers until reaching a thickness of $\sim$ 150-200 μm.

The manually thinned sample was then cut with an ultrasonic cutter with 600 grit SiC powder. The resulting samples after this process were two 3-mm circular disks (Figure 3.2(b)). A molybdenum ring of the same diameter with a thickness of $\sim$ 15 μm was attached around the perimeter of the disk giving extra support for the bars during further steps of thickness reduction by dimpling and ion milling.

The ring-supported disk was then mounted to a holder of the dimple grinder (*Gatan Inc.*) and dimpled using a copper wheel coated with diamond paste with particle sizes of 5 μm, 2 μm and 1 μm, sequentially, until reaching a thickness of $\sim$ 20-30 μm. The last step of polishing was carried out with the same instrument using a buffer wheel saturated with 0.75 μm diamond paste. The polishing period for this final removal of scratches generated from previous steps usually takes about five minutes. Throughout

dimpling and polishing, the thickness removal rate of the sample was controlled by applying a certain amount of adjustable load. In this study, the load used was 15 grams and 30 grams for dimpling and polishing, respectively, regardless of the type of material.

The final stage of conventional TEM sample preparation was performed by ion milling making use of a *Gatan Inc.* PIPS^{TM} (Precision Ion Polishing System) under an argon environment. In principle, Ar ions sputter the dimpled sample and further reduce the sample thickness until reaching electron transparency of $\sim$ 50-200 nm. Double modulation of the ion guns was commonly applied during the milling process in order to prevent bombardment of the aluminum milling holder. The energy, current and incident angle of the Ar ion beams were adjusted accordingly depending on milled materials. For transparent oxides, the ion milling recipe used was 3.5 kV with $\pm$ 4° inclination angle at 3 rpm rotation speed. The electron transparency of the sample reached after this final stage was inspected using the Philips CM12 TEM operated at 120 kV. In the case that electron transparency was not achieved, the sample could always be re-inserted into the ion milling instrument for further thickness reduction.

3.2.2 Tripod Polishing by MultiPrep^{TM}

Two pieces of sample, 3 mm long and 1 mm wide, as illustrated in Figure 3.3, were glued face to face using the same epoxy glue used in the conventional TEM sample preparation, and then mounted on the sample holder. The mechanical grinding was performed on a static mounted sample by a rotational motion of various diamond lapping films, starting from 30, 15, 9, 6, 3, 1, 0.5, and 0.1 μm, respectively. The first side thinning was accomplished with a flat-type configuration, while the second side thinning was performed with a wedge-type configuration of $\sim$ 2.5° angle. An alcohol based lubricant (Blue Lube^{TM} from *Allied Inc.* - containing a mixture of alcohol and isopropyl alcohol) was used allowing the diamond to cut the sample more aggressively.

Final polishing was performed using 0.1 μm diamond lapping film once the sample reached a thickness below 1 μm and started to show interference fringes under 600$\times$ magnification in an optical microscope. Further details of a similar process on Si

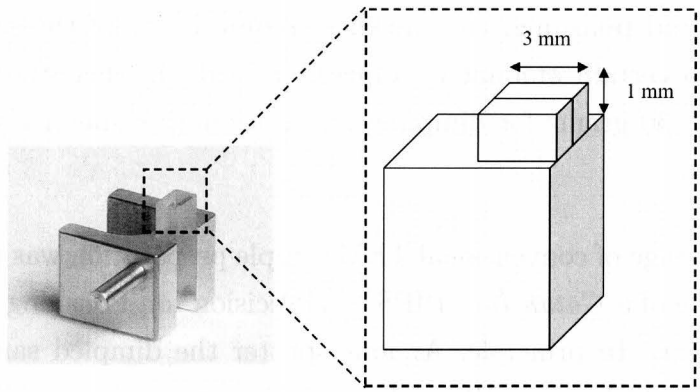

Figure 3.3: An illustration of the sample position on the MultiPrep sample holder.

have been elaborated in an article by Robertson et al. (2006). Since the samples investigated in this study were brittle and very fragile, the applied load was maintained between 0 - 100 grams throughout the mechanical grinding process.

Despite its delicate sample handling, the tripod polishing method offers significant advantages in comparison to the conventional preparation method, especially reduction of milling time, which contributes to less damage and thinner amorphous layers on the sample. This allowed the achievement of higher quality of high resolution images both in phase contrast and HAADF imaging with the aberration-corrected TEM.

3.2.3 Gentle Mill™

Besides the *Gatan* PIPS ion milling instrument working at an acceleration voltage of $\geq$ 3 keV, a *Technoorg Linda* low energy ion mill instrument was also employed for amorphous layer removal or cleaning of the ready-to-use TEM sample and for final thickness reduction for achieving electron transparency. The low energy milling of 0.2 - 0.8 keV is rather crucial for sample observation in the aberration-corrected TEM, as the ultimate quality of images is not determined solely by the microscope performance, but also by the TEM sample quality in terms of less radiation damage due to the reduction of defects and prevention of amorphous layer formation.

The basic operating principle of the Gentle Mill™ is to clean the sample surface by removing the amorphous layer covering the electron transparent region as well

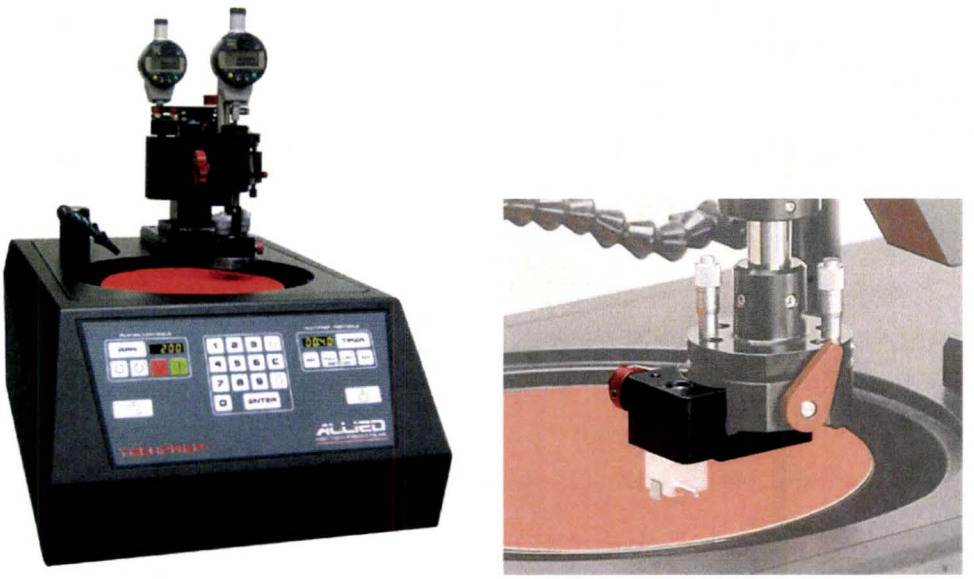

(a) (b)

Figure 3.4: (a) A picture of Allied High-Tech MultiPrep^{TM} instrument. (b) A closer look of the position of the (static) sample holder relative to the diamond lapping film on the (rotating) platen. The rotation of the platen used in this study is in clock-wise direction. (from http://www.alliedhightech.com, Allied, 2008)

as to expand the observable region within the sample. In addition, the instrument also offers the capability of trimming or further thinning from the not-so-electron-transparent sample from previous PIPS milling. The mode of cleaning or trimming can be simply adjusted by tuning the acceleration of Ar ions extracted from the ion gun. The cleaning procedure was carried out by utilizing very low energy Ar ions of 0.2 - 0.35 keV for about 10 mins, while the trimming procedure was performed at 0.5 - 0.8 keV for a shorter period of 3-5 mins. The cleaning and trimming procedures were carried out on both top and bottom sides of the samples.

When used as a conventional ion mill, the *Technoorg Linda* Gentle Mill instrument is also capable of milling with a maximum ion energy of 2 keV. However, for the milling step right after dimpling, it is not recommended to use the gentle mill, especially for perovskite oxides. The hard nature of perovskite oxides requires a long period of milling, even at relatively high ion energy. Using an acceleration voltage of 3.5 kV in the PIPS ion mill, the sample removal rate was $\sim$ 1 μm per hour. At a maximum accelerating voltage of 2 keV in the gentle mill, the removal rate of perovskite oxide samples is even slower. Consequently, the milling of perovskite oxides using the gentle mill requires an even longer milling period relative to PIPS, or in other words, it is simply not time efficient. In addition, prolonged exposure to an aggressive ion bombardment environment can eventually induce radiation damage on the sample.

3.3 TEM Instruments

Five TEM instruments were employed during this course of study for various purposes, for example (i) checking electron transparency of TEM sample after ion milling, (ii) acquiring low-resolution and high-resolution HRTEM and HAADF images, (iii) determining phase uniformity and orientation relationship between film and substrate by diffraction techniques, (iv) checking elemental distribution and composition of epitaxially grown samples by elemental maping and (v) investigating atomic and electronic structure of various ferroelectric and multiferroic perovskite oxides by acquiring EELS spectra.

A Philips CM12 120 kV TEM with a LaB_6 filament was used to check the elec-

tron transparency of TEM samples. In addition, the instrument was also frequently employed for acquiring bright-field and dark-field images, as well as Selected Area Electron Diffraction (SAED) and Convergent Beam Electron Diffraction (CBED) patterns. The microscope is also equipped with an Energy Dispersive X-ray Spectrometry (EDX) detector for elemental composition analysis. In general, the Philips CM12 TEM was used for low magnification imaging and preliminary investigation steps before further investigation with higher resolution microscopes.

A VG HB-601 100 kV dedicated STEM was used for acquiring EELS spectra in the early stages of the research, prior to the arrival of the Titan 300kV TEMs. The EELS experiments, with an energy resolution of ~0.4 eV at the zero loss peak, were mostly aimed for determining the valence of elements in the thin films.

A JEOL 2010F 200 kV TEM, equipped with a field-emission gun, has a 0.14 nm resolution for lattice (TEM) images and 0.23 nm resolution for STEM images. For analytical purposes, the microscope was equipped with both EELS and EDX detectors, enabling collection of information on elemental composition of the sample. Overall, the instrument is suitable for acquiring high-magnification TEM and STEM images and compositional and near edge fine structure information with a low energy resolution.

Two FEI-Titan^{TM} 80-300 microscopes were extensively employed for the investigations of perovskite oxides. The low-base Titan is equipped with a monochromator and an image corrector, while the other instrument, a high-base Titan (cubed), is similarly equipped with an additional probe corrector. Both instruments are capable of yielding atomic resolution images in both HRTEM and HAADF images. The monochromator improves the energy resolution of EELS by dispersing and filtering electrons extracted from the gun.

The ultimate resolution of the Titan^{TM} 80-300 cubed has been confirmed on many occasions on various materials. The ability to compensate the spherical aberration coefficient of the objective lens pushed the point resolution limit to its information limit, which indicates the stability, quality and performance of the microscope. In this study, the information limit of the Titan^{TM} 80-300 achieved was 0.65 Å.

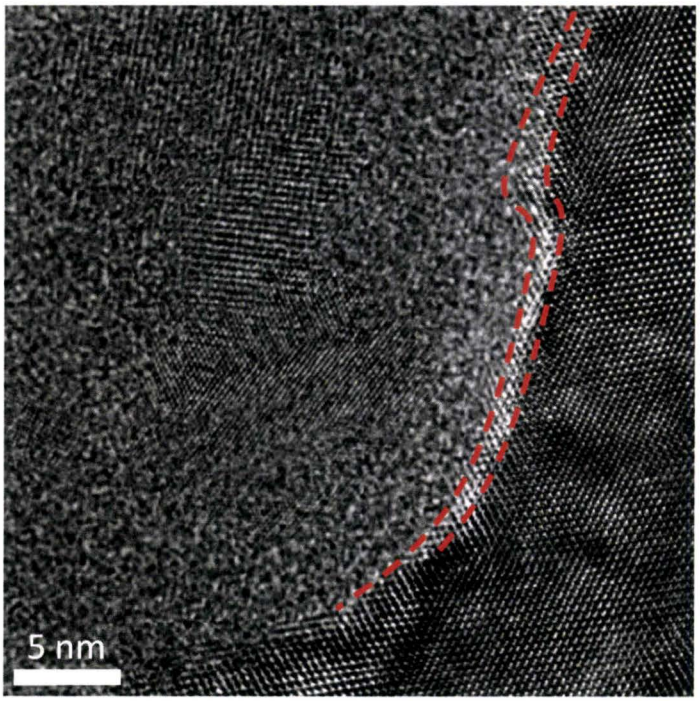

(a)

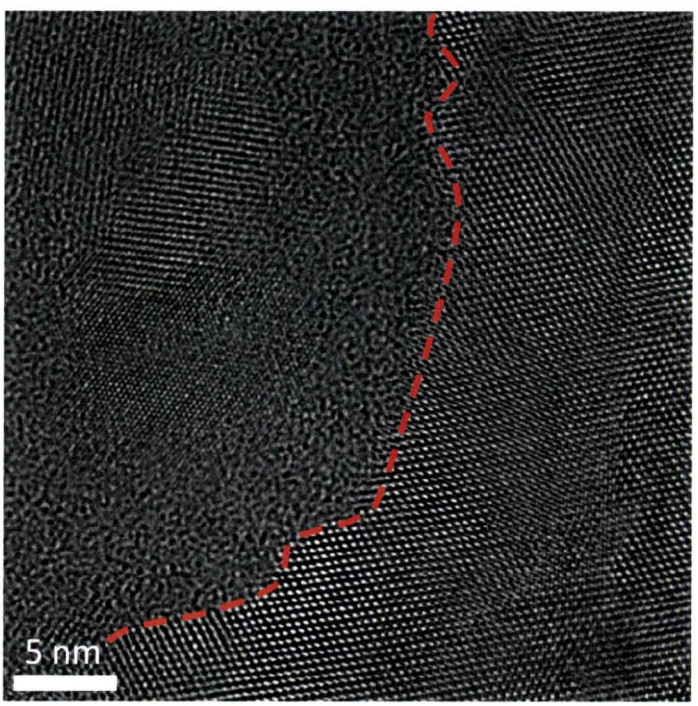

(b)

Figure 3.5: High resolution HRTEM images of an interface acquired by (a) non-corrected Titan (Cs-corrector OFF) and (b) corrected Titan (Cs-corrector ON)

The advantages of using aberration (C_S) correction are obvious when comparing HRTEM images acquired with the aberration corrector OFF (Figure 3.5(a)) and ON (Figure 3.5(b)), in that a sharp interface can be clearly seen due to suppressed electron delocalization. Further, a simpler visualization of lattice fringes and edges of particles can be deduced due to the more uniform contrast. In other words, the contrast variation as a function of reciprocal dimension of features in the sample was significantly minimized.

Spherical aberration correction is not solely for image correction but also for probe formation in STEM mode, which gives a remarkable reduction of the point spread function. Since the resolution of an HAADF image is limited by the probe size, defined by the size of the electron beam cross-over, the reduction of the point spread function is extremely important for achieving high-resolution HAADF images. The utilization of the probe corrector has pushed the point spread function down to $\sim$ 0.7 Å. The probe corrector allows the usage of larger diameter condenser aperture without introducing significant spherical aberration. A combination of the smaller point spread function and the larger condenser aperture results in higher current density relative to that of the non-Cs-corrected probe. The higher current density is crucial for higher quality HAADF imaging and EELS signals.

Moreover, the isolating enclosure surrounding the microscope column provides a higher quality environment that ensures optimal stability in terms of mechanical vibration, thermal fluctuation and electromagnetic field interference. The use of the monochromator enables the achievement of an energy resolution of $\sim$ 0.13 eV in EELS. All these superior qualities of the microscopes utilized in this study enabled simultaneous acquisition with optimum resolution for both images and spectroscopic information, revealing previously undiscovered atomic and electronic structures in various perovskite-oxides.

Further details about the difference between TEM and STEM modes in the Titan 80-300 microscope can be consulted in Appendix A.

Chapter 4

Results and Discussion

Since the interest and understanding of the fundamental physics of ferroelectric materials have been significantly growing in the past decade due to their interesting physical properties for various electronic industry applications, the pursuit of the comprehensive understanding of multiferroics becomes more important in order to explore new potential applications and device designs. (Hill, 2000) As such, Bi-based perovskite oxides have been extensively studied due to their wide-ranging physical properties, such as ferromagnetism, piezoelectricity, ferroelectricity, and multiferroicity.(Hill and Rabe, 1999; Niitaka et al., 2004; Baettig et al., 2005; Bai et al., 2005; Ederer and Spaldin, 2005; Bea et al., 2006, 2008)

Amongst various Bi-based perovskite oxides, the recently synthesized BFCO, which is a combination of BFO and BCO, in the form of a thin film has shown remarkable magnetic properties described in Subsection 2.5.3. Although the magnetic properties of BFCO have been predicted by Baettig, et. al. (2005), the experimental saturation magnetization exceeded the expectation. The difference between theoretical calculation and experimental results provided a driving force to further investigate the atomic structure and related phenomena responsible for these remarkable magnetic properties. In this study, two different combinations of BFO and BCO, with ratios of 1:1 and 1:3 were investigated. The 1:1 combination with a stoichiometric formula of Bi_2FeCrO_6 is referred to as BFCO 1/1, and the 1:3 combination with a stoichiometry of $Bi_2(Fe_{0.5}Cr_{1.5})O_6$ is referred to as BFCO 1/3.

The purposes of TEM investigations on BFCO 1/1, as described in Subsection 2.5.3, are firstly to obtain structural information at the atomic scale responsible for the increase of saturation magnetization of ten times of that of the BFO film alone, and secondly, to identify the mechanism of the generation of the large magnetization in BFCO 1/1 with respect to the proposed mechanism based on the theoretical calculations by Baettig et al. (2005). Accordingly, in BFCO 1/3 the TEM investigations were performed to verify the consistency of phenomena observed in BFCO 1/1 and to discover the role of defects or imperfections towards its magnetic properties.

Investigations on BFCO 1/1 were carried out using EDX to reveal the distribution of elements throughout the films. Afterwards, electron diffraction experiments, namely SAED and CBED, were performed for extensive exploration of the possibility of ordering within the film. The appearance of some interesting weak reflections in CBED patterns was analyzed by proposing and eliminating several possible factors. The systematic elimination finally lead to a conclusion that the extra weak reflections at ZA<110> were due to the anti-phase tilting of BO_6 octahedra and the B-site cationic ordering along <111> direction. The weak reflections at ZA<100> were associated with the presence of a secondary phase, Bi_2O_3, in the BFCO 1/1 film.

Next, further investigation of B-site cationic ordering was carried out on similar films with a modified BFO/BCO ratio, i.e., BFCO 1/3, as determined by EDX and SAED experiments. The understanding of more complex SAED patterns of the BFCO 1/3 film than those of the BFCO 1/1 film was further supported by employing atomic resolution HAADF imaging and by two-dimensional X-ray diffraction (XRD2). Both observations suggested that the formation of a new unit cell structure, different from what has been predicted for BFCO 1/1, is responsible for the decrease of saturation magnetization of BFCO 1/3 relative to BFCO 1/1. The type and lattice parameters of the new unit cell were acquired from the refinement of XRD I-2θ results. However, the determination of the exact atomic positions in the BFCO 1/3 unit cell was not accomplished during the duration of this study due to the limited availability and complex nature of the sample. The best XRD refinement gave information on the type and lattice parameters of the new BFCO 1/3 unit cell.

Another high-impact Bi-based oxide is the Bi-layered perovskite $Bi_{4-x}La_xTi_3O_{12}$ (x = 0.75), so called BLT, which is one of the candidate materials to replace lead-based

ferroelectric materials in various non-volatile random access memory devices (Chon et al., 2003; Bae et al., 2005). The intensive research regarding BLT has been mainly aimed in establishing the mechanism behind its high fatigue resistance and relatively large remanent polarization (Park et al., 1999). Some of the postulated mechanisms in the literature to date have been summarized in Subsection 2.5.4.

Despite the various proposed mechanisms, the exact mechanism is controversial, and therefore needs to be established. The purpose of the BLT investigation in this study, as stated in Subsection 2.5.4, is to pinpoint the location of substituent La ions in the parent bismuth titanate (BiT) structure and to relate this information with the generation of high fatigue resistance and relatively large remanent polarization in BLT. The identification of other defects and their roles in improving the fatigue resistance of BLT thin films was also carried out in this study.

Several EDX experiments were performed to check the stoichiometric composition and elemental distribution of BLT films. More detailed investigations were completed by utilizing atomic-resolution HAADF imaging and atom-by-atom EELS making use of the probe-corrector to yield sufficient detectable currents. The atomic-resolution HAADF images revealed the presence of interesting out-of-phase boundaries (OPBs) originating from various imperfections at the film-substrate interface. The mechanism of formation of OPBs in BLT were revealed from atomic-resolution HAADF imaging. The observation of OPBs may experimentally resolve the controversial issue regarding the mechanism of high fatigue resistance of BLT. The EELS linescans and mapping indicated that La ions substitute Bi ions in both the Bi_2O_2 layers and the perovskite-like layers of the bismuth titanate unit cell, with a higher tendency at the top of the Bi_2O_2 layer. Moreover, EELS maps also demonstrated the higher tendency of La ions to occupy the translational defects. Such results are different from what have been predicted in the literature, i.e., La ions are likely to substitute for Bi ions in the perovskite-like layers. Overall, the results of this study help to establish a more comprehensive fundamental understanding in terms of structure-properties relationship in BLT ferroelectric thin films.

4.1 Bi_2FeCrO_6(BFCO 1/1)

Firstly, the investigation of the BFCO 1/1 thin film was aimed at probing for the presence of B-site cationic ordering and other phenomena responsible for the much larger magnitude of magnetization in comparison to what had been observed in BFO thin film alone. Electron diffraction techniques, both SAED and CBED, were employed for this purpose.

Secondly, further investigation was aimed at determining the charge of each of the B-site cations, i.e., Fe and Cr. Baettig, et al. (2005) have predicted that Fe and Cr in BFCO 1/1 would adopt a 3+ valence and be ordered along the <111> direction of its pseudocubic unit cell. Since Fe and Cr are multivalent elements, several possible combinations of valence of both elements, while maintaining charge neutrality of the film, are possible. This issue was investigated by utilizing EELS.

The purpose of both abovementioned investigations is to experimentally check the prediction obtained from calculation using first principles density functional theory (Baettig et al., 2005) as to whether Fe^{3+} and Cr^{3+} cationic ordering truly exists along the <111> direction of pseudocubic BFCO unit cell.

4.1.1 Observation of Ordering Using Electron Diffraction Techniques

Thin films of Bi_2FeCrO_6 (BFCO) with a 1:1 stoichiometric combination of $BiFeO_3$ (BFO) and $BiCrO_3$ (BCO), were deposited on a $SrRuO_3$ (SRO) buffer layer and a (100)-oriented $SrTiO_3$ (STO) substrate by pulsed laser deposition (PLD) (sample ID BFC 17). TEM bright field imaging of a cross sectional sample taken with the Philips CM12 120 kV electron microscope, as shown in Figure 4.1 (a), displayed a $\sim$ 150 nm thick film, consisting of 100-150 nm wide columnar grains, and 30 nm SRO buffer layer. Despite its columnar features, the surface of the film is quite smooth with height variation less than 2 nm.

The major reflections of the SAED pattern of the BFCO film in Figure 4.1(b) show

excellent alignment with those of the substrate shown in Figure 4.1(c), indicating heteroepitaxy between them. Furthermore, overlap of reflections between the BFCO thin film and the STO substrate indicates that the unit cell of BFCO can be regarded as a pseudo-cubic unit cell. The indices used in the SAED patterns pertain to those of the pseudo-cubic single perovskite BFCO unit cell extending the STO substrate.

Other than the overlapping major reflections, several weak reflections, as pointed out by yellow arrows in Figure 4.1(b), consistently appear in a periodic array along $<110>_{STO}$ direction. The periodic nature of these weak reflections strongly suggests the presence of ordering, resulting in the formation of larger periodic unit cell. The weak reflections appearing at 1/4, 1/2, and 3/4 of reciprocal space dimension (g_{110}) may be attributed to the formation of superlattices with double, triple and quadruple the lattice dimension of the parent BFCO unit cell. One of the possible origins of the formation of the superlattices could be the assumed cationic ordering. It is too early, however, to conclude that those weak reflections are generated by Fe^{3+}/Cr^{3+} B-site cationic ordering and thus, further structural investigations on different sample were carried out and described in Section 4.1.3.

4.1.2 Compositional Modulation of Fe and Cr by EDX Analysis

Detailed investigation of the elemental distribution in the BFCO 1/1 film was carried out using the EDX technique, with INCA (*Oxford Instrument*) software for data analysis. EDX maps for Ti, Sr, Bi, Fe, and Cr (Figure 4.2(b-f)) were associated to the rectangular region marked in Figure 4.2(a). The Bi signals decreased slightly at the right-hand side of the image due to a decrease in the thickness of the film. The decrease in signal is consistently observed for other elemental maps. The Sr map indicates a thicker layer of Sr than Ti, which actually represents the presence of a SRO layer.

The maps of Fe and Cr interestingly show alternating layers tens of nanometres thick. The stripe pattern in Fe and Cr elemental maps suggests the presence of minor excess and depletion of Fe and Cr, as shown in Figure 4.3(b). At the stripe area where the

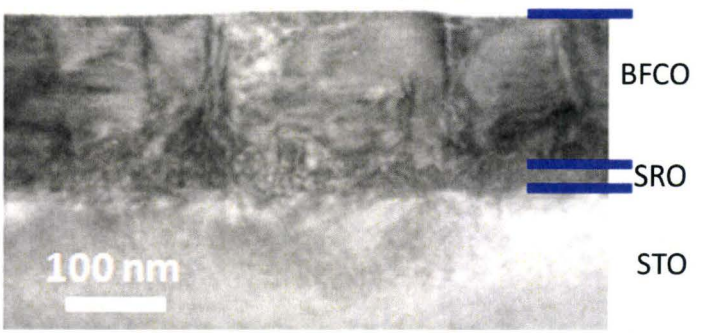

(a)

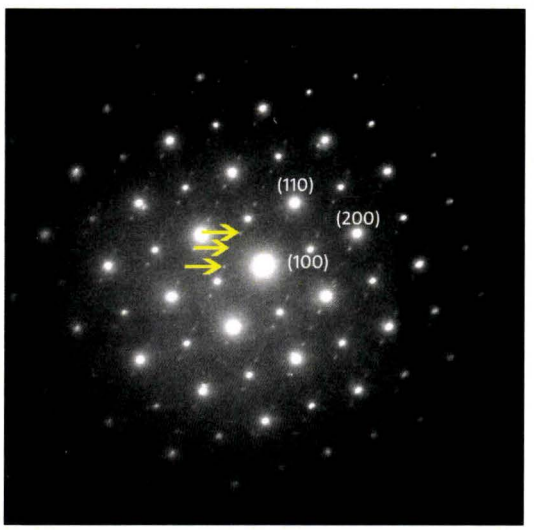

(b)

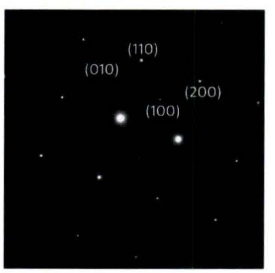

(c)

Figure 4.1: (a) A cross sectional bright field TEM image, (b) corresponding SAED pattern of a BFCO film on (100)SRO/STO, and (c) SAED pattern of (100)STO substrate. The major reflections in the SAED pattern of BFCO 1/1 film were indexed based on the STO substrate. The yellow arrows in (b) highlight the weak reflections along $<110>_{STO}$

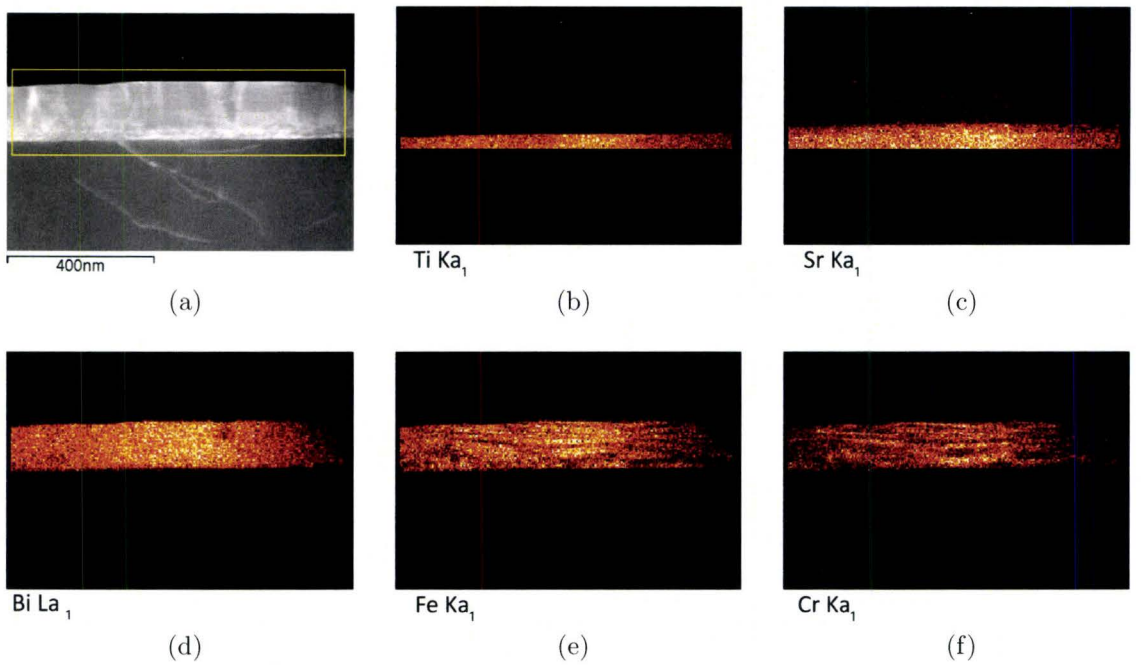

Figure 4.2: (a) The ADF image of BFCO sample; (b) - (f) elemental EDX maps of titanium (Ti), strontium (Sr), bismuth (Bi), iron (Fe) and chromium (Cr), respectively.

Fe signal increases, the Cr signal decreases, and vice versa. Despite the alternating signals of Fe and Cr across the stripes, the compositional modulation does not indicate a complete separation of Fe and Cr, since neither Fe nor Cr signal intensities drop to zero over the linescan. The tens-of-nm compositional modulation across the thickness of the BFCO 1/1 film is attributed to the presence of compositional fluctuations over a long range, whose extent is on a much longer scale than the assumed Fe^{3+}/Cr^{3+} cationic ordering. In spite of the evidence of the compositional modulation, such long-range fluctuations must not be confused with the ordering observed in SAED pattern described in Section 4.1.1.

Previously, Nechache, et al. (2006) reported that a combination of BFO and BCO yields a much higher saturation magnetization (M_S), nearly ten times of that of BFO alone for the same film thickness. In addition, such remarkable magnetization exists at room temperature, i.e., at higher temperature than what has been predicted by Baettig, et al. (2005). Nechache, et al. claimed that the increase in magnetization is due to the superexchange interaction, a magnetic coupling between Fe^{3+} and Cr^{3+},

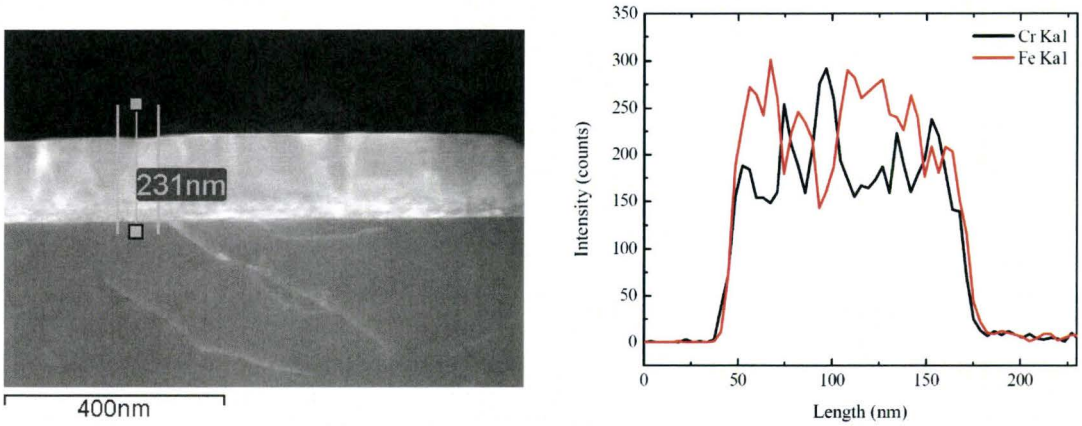

(a) (b)

Figure 4.3: The EDX linescans of Cr and Fe from the region defined by vertical lines in the image (a) are displayed as red and black curves, respectively, in (b). The compositional modulation is clearly demonstrated as Cr signals decrease where Fe signals increase, and vice versa.

which occurs at the interface between BFO and BCO. As such, the compositional modulation of Fe and Cr increases the overall BFO-BCO interface within BFCO film, which is consequently responsible for its high saturation magnetization.

In addition to the increased BFO-BCO interfacial area, the increase in saturation magnetization most likely originates from the increasing Fe^{3+}/Cr^{3+} superexchange interactions, which is possible only if B-site cationic ordering exists in the sample. The presence of B-site cationic ordering in the pseudo-cubic structure of BFCO, as observed earlier in SAED patterns in Section 4.1.1, was further investigated and verified employing the CBED technique through a systematic elimination of several possible origins for the observed weak reflections.

4.1.3 Structural Investigations by CBED Technique

Another sample (sample ID BFC 151) of Bi_2FeCrO_6 (BFCO) with the same composition as the previous sample in Section 4.1.1 was grown by PLD. Similar to the previous sample, the TEM bright-field image acquired with the Philips CM12 120 kV TEM, shown in Figure 4.4(a), revealed a $\sim$ 150 nm thick film with 100-150 nm wide

columnar grains. The surface of the film is quite smooth with a $\sim$ 30 nm thick SRO buffer layer. A higher magnification image (Figure 4.4(b)) shows that even though the interface between the SRO buffer layer and the STO substrate is quite smooth, the interface between the SRO and the BFCO film, where columnar grains start to form, is rough. Such interface roughness may be due to strain built-up during epitaxial growth of BFCO film ($a_{pseudocubic}$ =0.391 nm, $c_{pseudocubic}$ =0.395 nm) on the strained SRO buffer layer (a = 0.3928 nm) grown on the STO substrate (a = 0.3905 nm). The grain boundaries in the BFCO film along the lateral direction are likely to form as a means of stress relief of such interfacial strain. Another possibility for columnar growth arises from the relatively low growth temperature of $\sim$ 700 °C in order to avoid any parasitic phase, such as Bi_2O_3 and Fe_2O_3, during the deposition of the thin film. It is well known that the low T/T_M value prevents the formation of a single crystal film, and rather forms the columnar grains within the film. (Ohring, 2002)

The SAED pattern of the film (Figure 4.4(c)) indicates good epitaxy between the film and the substrate, as demonstrated by a good degree of overlap between the major reflections of both BFCO film and STO substrate. The SAED pattern of STO alone is presented in Figure 4.4(d). However, extra minor reflections, highlighted by yellow arrows, are present along $<100>_{STO}$ direction. As the SAED pattern of the substrate shows only the major reflections, it is clear that the extra reflections along the $<100>_{STO}$ direction originate in the film, and their exact source may be explained due to these potential factors:

1. Double diffraction due to thickness of the sample.
2. Overlap of grains having different in-plane orientation.
3. In-phase or anti-phase tilting of BO_6 octahedra.
4. Charge ordering of B-site cations.
5. Second phase materials, e.g., Bi_2O_3.
6. Ordering of A-site cations or oxygen vacancies.
7. B-site cationic ordering.

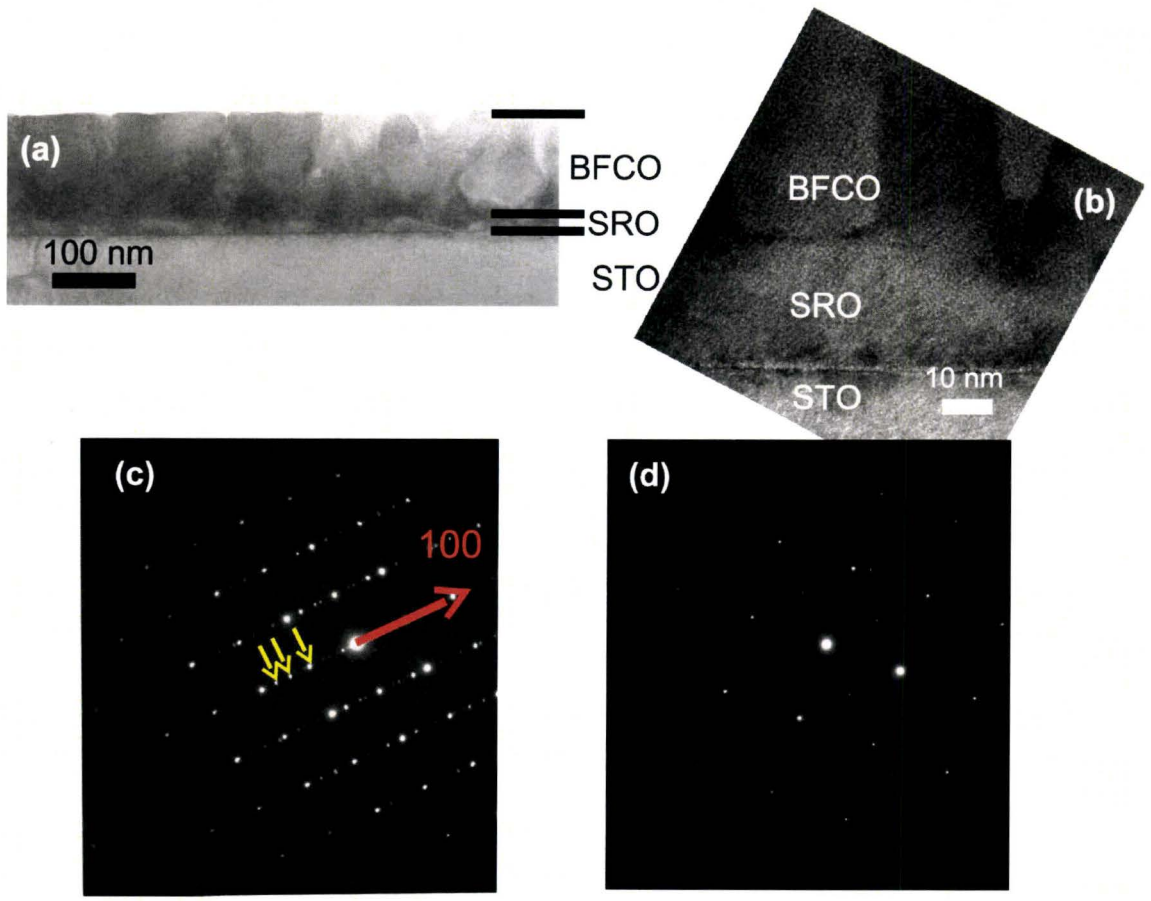

Figure 4.4: (a) Bright field image and (b) HREM image of the sample; SAED patterns of (c) BFCO + substrate (STO) and (d) substrate alone in the direction parallel to the zone axis (ZA) $<100>_{STO}$

Due to the grain size of $\sim$ 100-150 nm in the lateral dimension, the SAED technique would not be suitable for further investigation as it covers a much larger area, as determined by the virtual size of SAED apertures at the image plane (the smallest size of physical SAED aperture was $\sim$ 10 µm). Therefore, CBED technique was utilized for investigating the origin of the extra weak reflections in the SAED pattern of Figure 4.4(c).

The electron beam used was $\sim$ 150 nm in diameter and focused on each columnar grain along the direction indicated by the white arrow in Figure 4.5, i.e., from thin areas to thicker areas. The recorded CBED patterns are displayed consecutively as a function of thickness in Figure 4.5(a-e). The CBED patterns from (a) to (e) were consistent in that the extra weak reflections are always present despite variation in sample thickness. Such observations lead to a conclusion that the extra weak reflections are not caused by double or multiple diffraction due to the thickness of the sample.

Another CBED pattern was also acquired from the thinnest area of the sample, next to the hole created during ion milling. The result, shown in Figure 4.6(a), also demonstrates the presence of extra reflections. As a comparison, the CBED patterns acquired from overlapping grains in thicker areas of the film are displayed in Figures 4.6(b) and (c). It is obvious that the pattern from the thinnest area (indicated by **a**), where there is no grain overlap, is similar to the pattern acquired from the thicker area with overlapping grains (indicated by **b** and **c**). As such, the appearance of extra weak reflections cannot be associated with grain overlap.

Another possible explanation of a source of the weak reflections in the SAED patterns may be in-phase or anti-phase tilting of corner sharing oxygen octahedra (Woodward and Reaney, 2005). The tilting of perovskites, which is one of the mechanisms of perovskite distortion from cubic prototype symmetry, gives extra reflections in SAED pattern that appear only at certain zone axes. The tilting referred to the in-phase and anti-phase tilting pertains not to the adjacent octahedra, but to the upper and bottom octahedra. When the upper and bottom octahedra tilt themselves in the same direction as the central octahedra, this is classified as in-phase tilting (Figure 4.7(c)). In contrast, if they tilt in the opposite sense, the octahedral tilting is classified as anti-phase tilting, as shown in Figure 4.7(d).

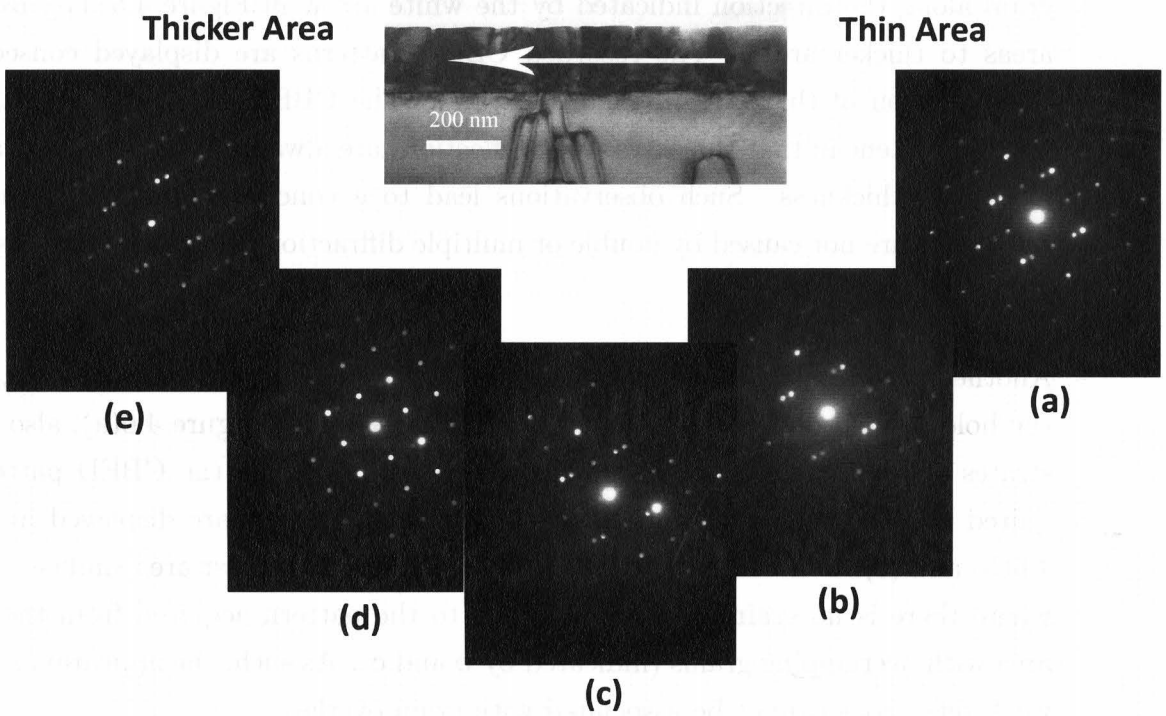

Figure 4.5: CBED patterns of a BFCO film acquired with the sample oriented at the ZA $<100>_{STO}$ from the thin area to gradually thicker areas, (a) - (e), were acquired along the direction indicated by the white arrow. The electron beam diameter is $\sim$ 150 nm.

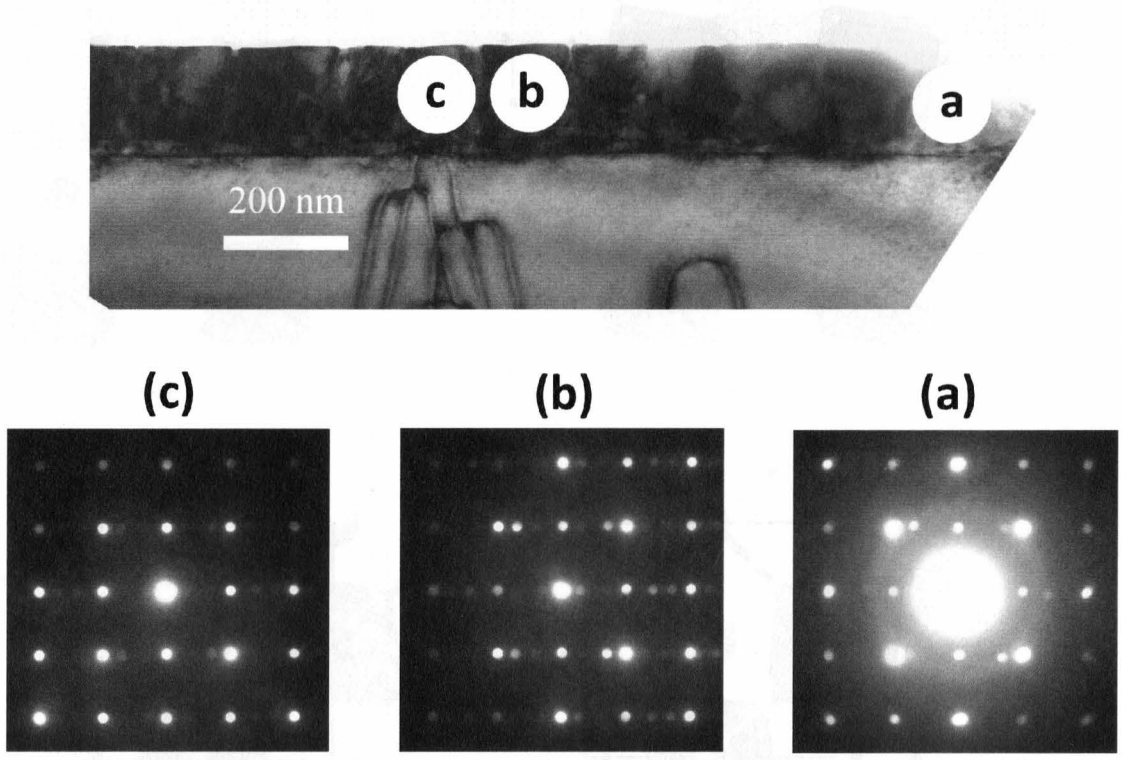

Figure 4.6: (a)-(c) CBED patterns of BFCO films at different locations of the BFCO film as indicated in the corresponding images, where (a) is the thinnest area and (b) and (c) are thicker areas with overlapping grains.

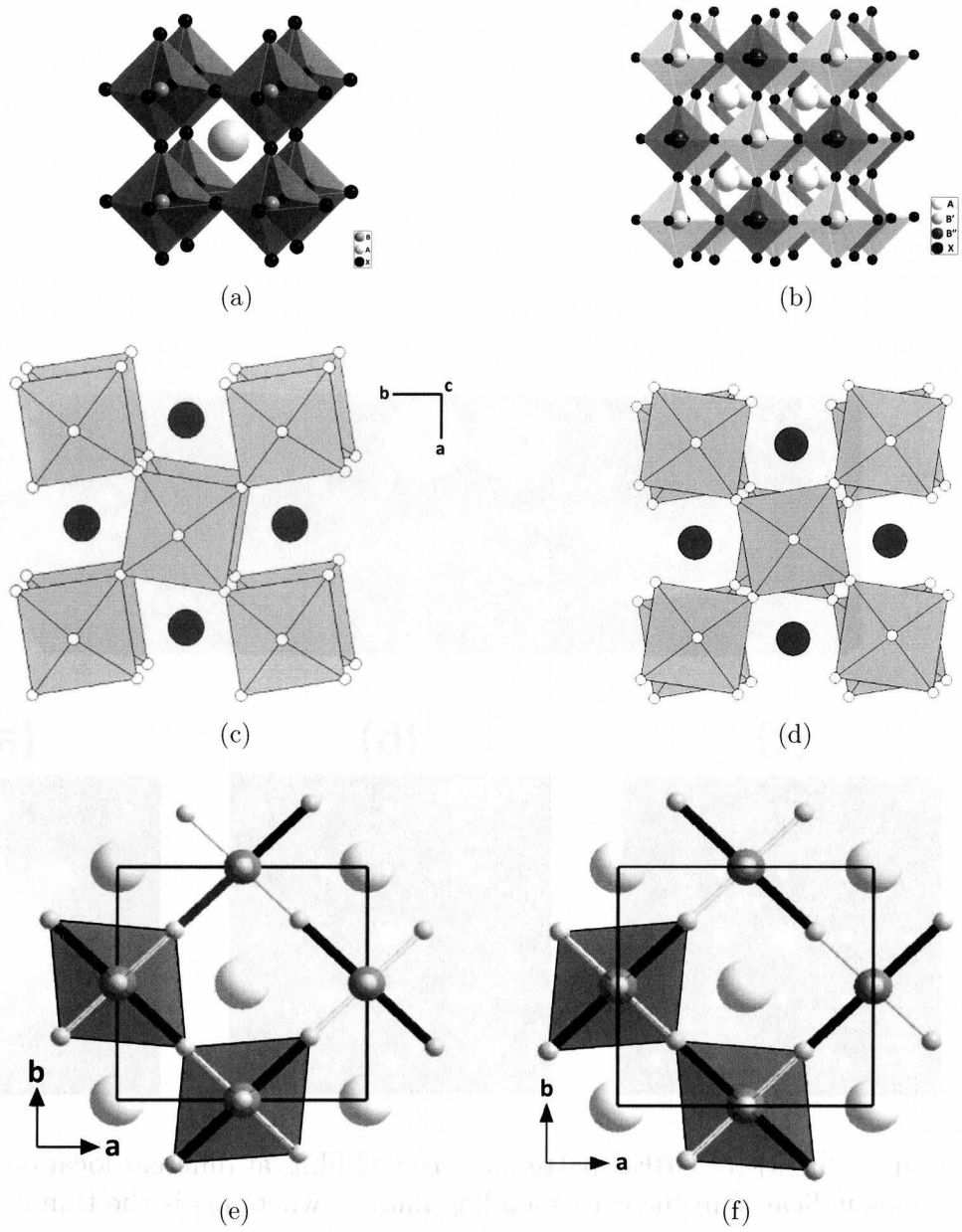

Figure 4.7: An illustration of octahedra in (a) an ideal perovskite system, ABX_3, (b) a B-site ordering double-perovskite system, AB'B"X_3, (c) an in-phase tilt system, (d) an anti-phase tilt system (from Thesis of Knapp, 2006), (e) a cooperative Jahn-Teller distortion (CJTD) of the first layer of $KCuF_3$, and (f) a CJTD of succesive layer of $KCuF_3$ (from Lufaso and Woodward, 2004). In both in-phase and anti-phase tilt systems, the tilt axis is along the *c*-axis and perpendicular to the page. The thick black lines in the CJTD systems represent the long B-X bonds, while the thinner lines represent the short or medium length B-X bonds.

The distortion of perovskites, however, is not solely a result of the tilting of corner-sharing octahedra, but also on other mechanisms, such as antiparallel shifts of A-site cations and charge ordering of multivalent B-site cations. The degree of distortion depends considerably on several factors, namely (i) different sizes of A, B, and O ions, (ii) degree of covalency of each ion, (iii) metal-metal interactions, and (iv) Jahn-Teller and lone pair effects (Woodward and Reaney, 2005; Davies et al., 2008). Further, perovskite oxides containing multivalent B-site cations, such as Cu^{2+} and Mn^{3+} also have a tendency to undergo orbital ordering, which results in a cooperative Jahn-Teller distortion (CJTD) (Lufaso and Woodward, 2004). One example of CJTD in a perovskite structure can be found in $KCuF_3$. The schematic illustrations of CJTDs in the first and successive layers of $KCuF_3$ are shown in Figures 4.7(e) and (f), respectively.

The tilting nature of perovskite oxides is closely associated to the stability of an oxide to form perovskite structures. This stability is represented by the tolerance factor, t:

$$t = \frac{(R_A + R_B)}{\sqrt{2}\,(R_B + R_O)} \tag{4.1}$$

where R_A, R_B and R_O are ionic radii of A-site, B-site and oxygen, respectively. Woodward and Reaney (2005) have categorized the distortion of perovskites based on the collation of extensive structural data and calculation of the tolerance factor as listed in Table 4.1.

With decreasing value of t, A-site cations become too small to occupy cuboctahedral interstices, so oxygen octahedra rotate and undergo tilting to reduce the volume of the interstice, therefore improving the structural stability of the perovskite unit cell. A further decrease of t beyond the values listed in Table 4.1 will further reduce the stability of the perovskite structure, and eventually result in the formation of a non-perovskite configuration.

The information on the ionic radii for every element of BFCO required for the determination of the tolerance factor of BFCO is listed in Table 4.2 (Shannon, 1976).

The ionic radius of Bi^{3+} (coordination number = 12) is extrapolated to be $\sim$ 1.3 Å

Table 4.1: The distortion of perovskites in terms of in-phase and anti-phase tilting categorized by the value of tolerance factor.

t	Distortion of perovskites
$0.985 < t < 1.06$	Untilted
$0.964 < t < 0.985$	Anti-phase tilting
$t < 0.964$	In-phase and anti-phase tilting

Table 4.2: The ionic radii of bismuth, chromium, iron and oxygen (Shannon, 1976)

Ion	Coordination Number	Ionic Radius (Å)
Bi^{3+}	12	1.3
Cr^{3+}	6	0.615
Fe^{3+}	6	0.645
O^{2-}	12	1.40

(Woodward et al., 2003). The tolerance factor of BFO and BCO was calculated as follows:

$$t_{BFO} = \frac{(1.3 + 1.4)}{\sqrt{2}\,(0.645 + 1.4)} = 0.933$$

$$t_{BCO} = \frac{(1.3 + 1.4)}{\sqrt{2}\,(0.615 + 1.4)} = 0.947$$

As both BFO and BCO possess $t < 0.964$, the combination of both compounds, BFCO, is extremely likely to show both in-phase and anti-phase tilting, which may be responsible for the appearance of extra reflections in the SAED pattern.

The extra reflections present in the diffraction patterns from different zone axes can be classified according to its responsible factors, i.e., anti-phase tilting (α-reflections), anti parallel shifts of the A-site cations (β-reflections) and in-phase tilting (γ-reflections), as illustrated in Figure 4.8 (Reaney et al., 1994).

By comparing the experimental CBED and the schematic patterns derived by Reaney

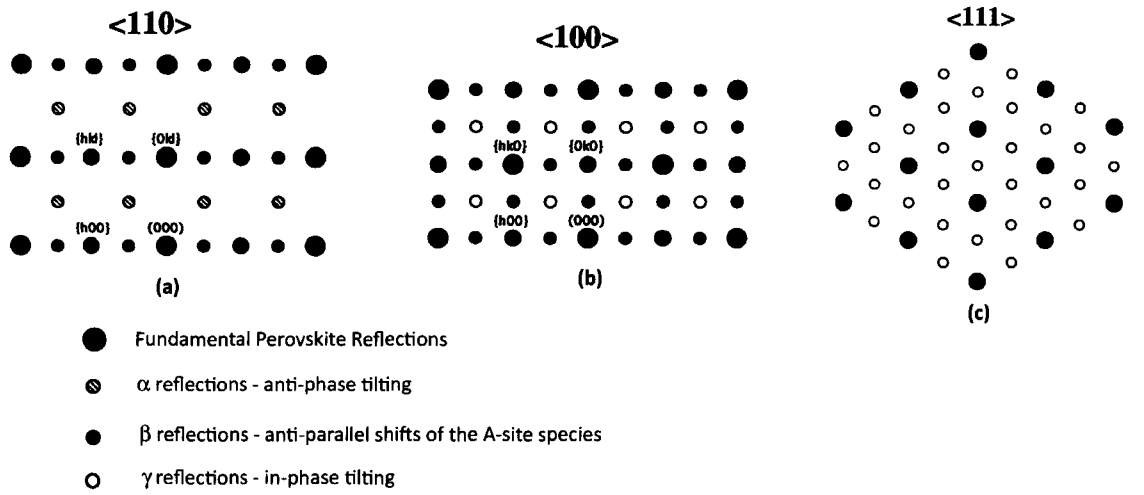

Figure 4.8: Schematics of diffracton patterns at different zone axes for pseudo-cubic settings where α, β and γ are in the $\{h+1/2,\ k+1/2,\ l+1/2\}$, and $\{h+1/2,\ k,\ l\}$, and $\{h+1/2,\ k+1/2,\ l\}$ (where $h \neq k$) positions. (from Reaney et al., 1994)

et al. (1994), it can be deduced that the extra weak reflections at ZA<110>, as indicated by the white arrows in Figure 4.9(b), correspond to anti-phase tilting and the 1:1 ordering of B-site cations along [111] direction. The weak reflections at ZA<100> as indicated by the white arrows in Figure 4.9(c), however, correspond to neither in-phase tilting nor anti-parallel shifts of A-site cations.

Further investigation by measuring the d-spacings of the extra reflections beside the major reflections in the CBED patterns at both ZA<100> and ZA<110> of BFCO 1/1 indicate that those reflections appear due to the presence of secondary phase Bi_2O_3. The experimental and the theoretical d-spacings of the extra reflections are listed in Table 4.3. The reference unit cell of Bi_2O_3 used for obtaining the theoretical d-spacing is a cubic unit cell with lattice parameters of $a=b=c=$ 0.545 nm, $\alpha = \beta = \gamma = 90^{\circ}$ and space group Pn-3m (#224) taken from Powder Diffraction by Zavylova (1972). The correction factor (CF) was obtained by taking the ratio between the theoretical and the experimental d-spacings of the STO substrate. The CF value at a camera length of 770 mm, used for acquiring all the CBED patterns, is $\sim$ 0.93.

Figure 4.10(a) points out the extra reflections pertaining to Bi_2O_3, and the corresponding reflections and indices of those reflections are schematically represented in Figure 4.10(b). The indices of the Bi_2O_3 reflections in the CBED pattern in the

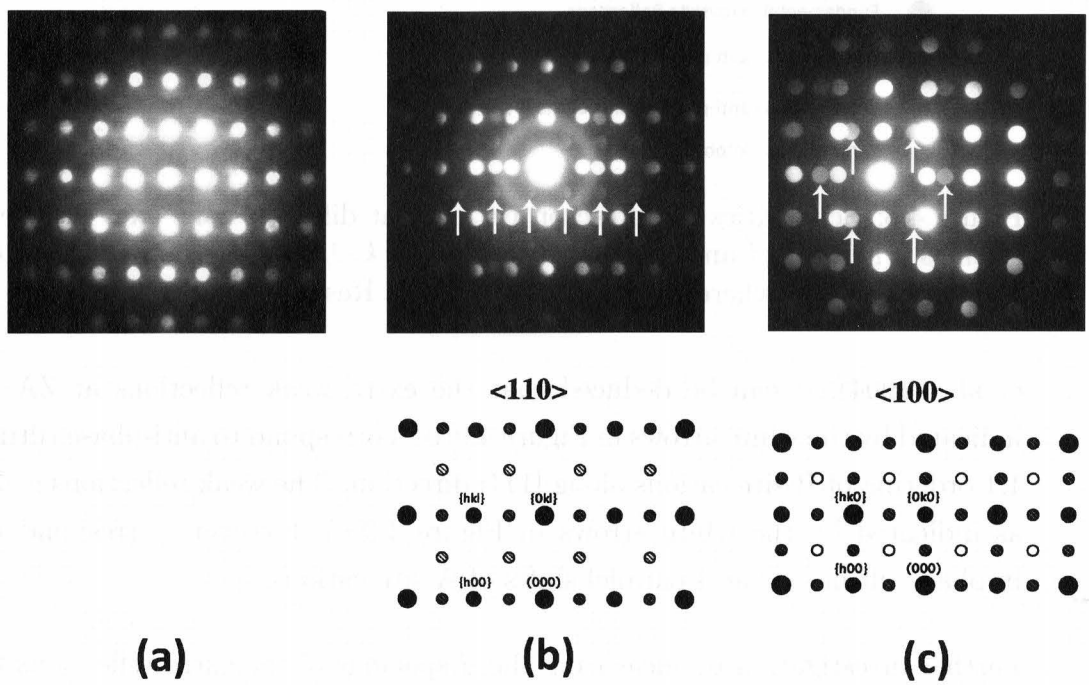

Figure 4.9: CBED patterns recorded in the direction parallel to the ZA<110>$_{STO}$ of (a) STO substrate and (b) BFCO film; CBED pattern recorded in the direction parallel to the ZA<100>$_{STO}$ of (c) BFCO film. White arrows in (b) indicate the extra reflections due to antiphase tilting of BO_6 octahedra or B-site cationic ordering along <111> direction. White arrows in (c) indicate the extra reflections along (*0kl*) directions, which correspond to neither in-phase tilting nor anti-parallel shifts of A-site cations.

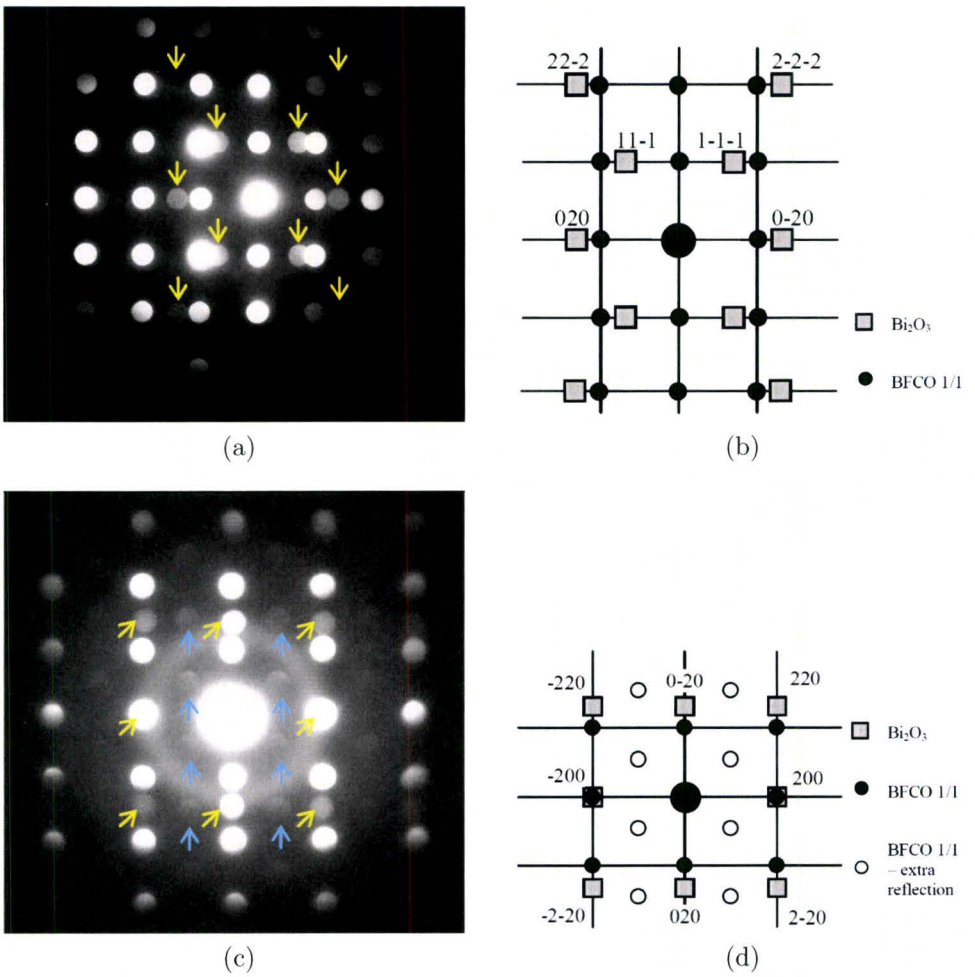

Figure 4.10: (a) The CBED pattern and (b) the schematic of the corresponding reflections and indices in the direction parallel to the ZA <100> of BFCO 1/1, where the Bi_2O_3 reflections are indicated by yellow arrows. (c) The CBED pattern and (d) the schematic of the corresponding reflections and indices in the direction parallel to the ZA <110> of BFCO 1/1, where the Bi_2O_3 reflections are indicated by yellow arrows and the extra weak reflections by blue arrows.

Table 4.3: The experimental and the theoretical d-spacings of the extra reflections, as indicated in Figure 4.10 by the yellow arrows. The 2R column corresponds to the distance between two collinear reflections. The CF value for a camera length of 770 mm is ~ 0.93.

ZA <100>BFCO 1/1					
2R (mm)	d_{expt} (nm)	d_{expt} * CF (nm)	d_{theo} Bi_2O_3 (nm)	$\Delta d_{expt\text{-}theo}/d_{theo}$ (%)	index
12.4	0.4160	0.3869	0.3853	0.42	10-1
15.4	0.3350	0.3116	0.3146	-0.97	11-1
17.8	0.2898	0.2695	0.2725	-1.09	0-20
ZA <110>BFCO 1/1					
2R (mm)	d_{expt} (nm)	d_{expt} * CF (nm)	d_{theo} Bi_2O_3 (nm)	$\Delta d_{expt\text{-}theo}/d_{theo}$ (%)	index
17.2	0.2999	0.2789	0.2725	2.37	200
18	0.2866	0.2665	0.2725	-2.18	020
24.7	0.2089	0.1942	0.1927	0.80	220

direction parallel to the ZA $<100>_{BFCO\ 1/1}$ are in accordance to the reflections in the direction parallel to the ZA <110> of Bi_2O_3. The Bi_2O_3 reflections are also observed in the CBED pattern of the sample oriented at the ZA $<110>_{BFCO\ 1/1}$ (Figure 4.10(c)), as pointed out by yellow arrows. The extra weak reflections present along ($1/2$, $1/2$, $1/2$), pointed out by blue arrows, do not correspond to the pseudo-cubic BFCO 1/1 reflections nor the Bi_2O_3 reflections, but instead they correspond to B-site cationic ordering and anti-phase tilting as previously discussed. The indices of the Bi_2O_3 reflections in the CBED pattern recorded in the direction parallel to the ZA $<110>_{BFCO\ 1/1}$ are shown in Figure 4.10(d).

The presence of Bi_2O_3 in the BFCO 1/1 film was investigated by EDX experiments. EDX maps of the elements present in the BFCO 1/1 film, shown in Figures 4.11(b)-(f), indicate that Bi signals are uniform within the entire film. However, there are some signal variations along lateral directions in the Fe and Cr maps, namely local excess and depletion of both elements at specific regions within the film. The signal variation is rather different from what was observed in Section 4.1.2, in that the modulation direction is along the lateral direction rather than along the growth direction. Moreover, the area where excess Fe is present does not necessarily show a depletion of Cr. Such compositional modulation of Fe and Cr, accompanied with a uniform

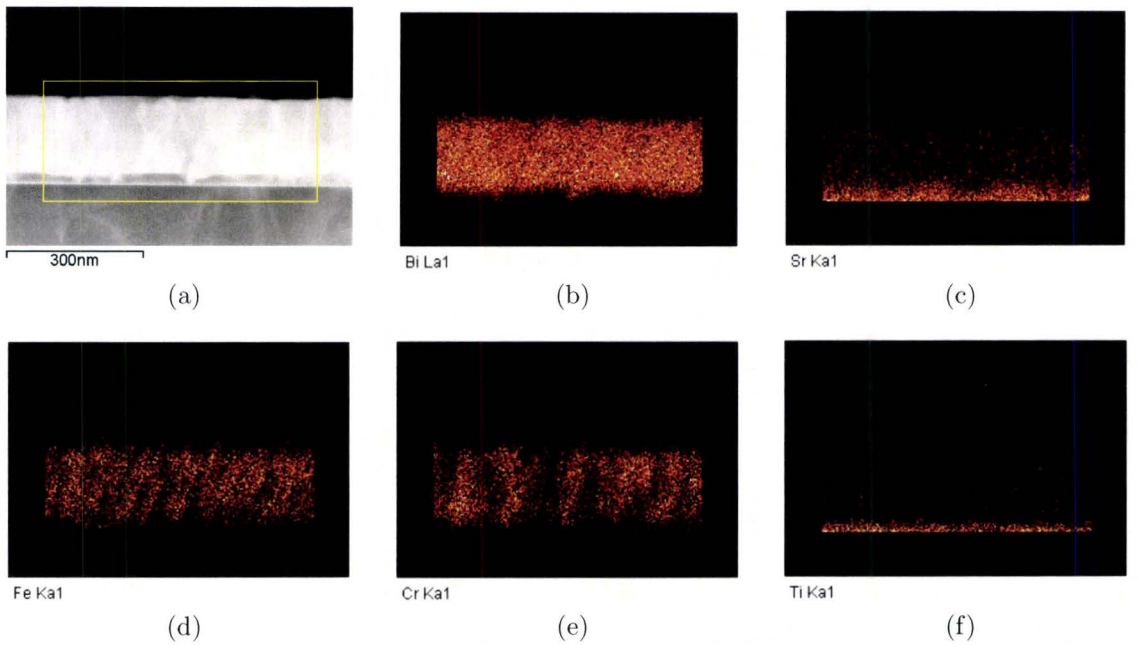

Figure 4.11: (a) The ADF image of BFCO 1/1 from which the elemental maps were acquired. (b)-(f) The elemental maps of Bi, Sr, Fe, Cr and Ti, respectively.

signal of Bi, suggests that there are Bi-rich regions associated to the formation of a secondary phase, Bi_2O_3, giving rise to extra reflections in the CBED patterns.

The formation of Bi_2O_3 during the growth of $BiFeO_3$ thin films has been investigated as a function of pressure and temperature of deposition by Bea, et al. (2005). They have reported that away from the optimum temperature of 580 °C and pressure of 10^{-2} mbar, phases other than $BiFeO_3$ are likely to form. At lower T or higher P, Bi_2O_3 can form and at lower P or higher T, Fe_2O_3 can form. Even though deposition of the BFCO 1/1 film was carried out at 700 °C and 10^{-2} mbar, deposition by PLD is considered a non-equilibrium process, and thus the film characteristics may not be consistent with what has been reported by Bea, et al. (2005). The presence of a Bi_2O_3 phase in a BFCO 1/1 film is considered detrimental, in that it creates electrical shortcuts through the films which increases the leakage current, preventing the BFCO 1/1 films to be implemented as ferroelectric elements in functional heterostructures.

Up to this point, the electron diffraction studies of BFCO 1/1 in the direction parallel to the ZA <110> highlighted the finding of extra weak reflections, which suggest

that the anti-phase tilting of corner-sharing oxygen octahedra and the Fe and Cr B-site cationic ordering are both present in the BFCO 1/1 film. Tilting of octahedra is commonly associated with phase transitions from ferroelectric to paraelectric, in perovskite compounds (Reaney, 2007). As such, the octahedral tilting will most likely influence ferroelectric polarization instead of magnetic polarization. From the physical measurement of the magnetic response by Nechache, et al. (2006), the BFCO 1/1 sample demonstrated a remarkable improvement in saturation magnetization. In this case, the extra weak reflections in CBED pattern at ZA <110> are indicated by white arrows in Figure 4.9(b) can be attributed to the presence of B-site cationic ordering along the <111> direction of perovskite BFCO 1/1, responsible for the increase in the saturation magnetization.

The weak reflections in the CBED pattern in the direction parallel to the ZA $<100>_{\text{BFCO 1/1}}$ as indicated by yellow arrrows in Figures 4.10(a) and (c) can be attributed to the presence of a secondary Bi_2O_3 phase. Further investigation was carried out in order to verify the presence of charge ordering due to charge variation of B-site cations. EELS experiments were performed to confirm the valence of both Fe and Cr cations in the BFCO 1/1 films.

4.1.4 Determination of Fe and Cr Valence by Electron Energy Loss Spectroscopy

The EELS investigation is designed for determining the valence of Fe and Cr within the BFCO film, which may shed some insight into presence of ordering other than B-site cationic ordering, such as charge ordering. Charge ordering takes place due to a variation of oxidation state or valence between elements occupying the B-site in the perovskite unit cell. Since Fe and Cr are multivalent elements, there are several possible pairs of Fe and Cr valence while maintaining charge neutrality of the sample, as listed in Table 4.4.

Since the Bi ion possesses a valence of 3+ and there are two Bi ions in BFCO 1/1, giving a total of positive charge of 6+, the first and second possibilities in Table 4.4 are reasonable to balance the total oxygen valence of -12. However, the third

Table 4.4: List of possible combination of valences of Fe and Cr in BFCO film while maintaining charge neutrality

Possibility	Fe	Cr
1	3+	3+
2	2+	4+
3	3+	2+

possibility, where Cr ions assume 2+ valence, it is not feasible for Fe ions to assume a 4+ valence. Therefore, the third possibility is viable only if significant oxygen vacancies are present in the film, or in other words, the film is oxygen deficient with a formula of Bi_2FeCrO_{6-x} with (x= 0.5).

A previous report on the synthesis of BFO films by PLD by Bea, et al. (2005) described that the optimum growth condition while avoiding parasitic phases such as Bi_2O_3 and Fe_2O_3 was achieved with an oxygen partial pressure of 10^{-5} bar and substrate temperature of 580 °C. It was also reported that an oxygen pressure of 10^{-5} bar is sufficient to prevent formation of oxygen vacancies in the BFO film. During deposition of the BFCO film, the material target used was perfectly stoichiometric and the oxygen partial pressure was maintained at 10^{-5} bar with a growth temperature of 700 °C. Based on the similarity of oxygen partial pressure used for growing BFCO 1/1 in this study with that used by Bea for deposition of BFO films, it can be stated that the probability of formation of oxygen vacancies in the sample was relatively low, and therefore the third possibility may be ruled out of consideration.

EELS spectra for Cr and Fe were acquired with the VG HB 601 STEM operated at an acceleration voltage of 100 kV and energy resolution at the Zero Loss Peak of $\sim$ 0.4 eV. The EELS spectra of the BFCO films are displayed in Figures 4.12(b) and (d) corresponding to the Cr $L_{2,3}$ and Fe $L_{2,3}$ edges, respectively. For comparison, experimental spectra of Cr $L_{2,3}$ (Cr_2O_3) and Fe $L_{2,3}$ edges (α-Fe_2O_3) obtained at a resolution of both 0.65 eV and 0.15 eV (Mitterbauer et al., 2003) are also displayed in Figures 4.12(a) and (c), respectively.

Qualitatively, the similarity between experimental and reference spectra of Cr $L_{2,3}$ and Fe $L_{2,3}$ suggests that both edges have a valency of 3+. Further, the quantitative

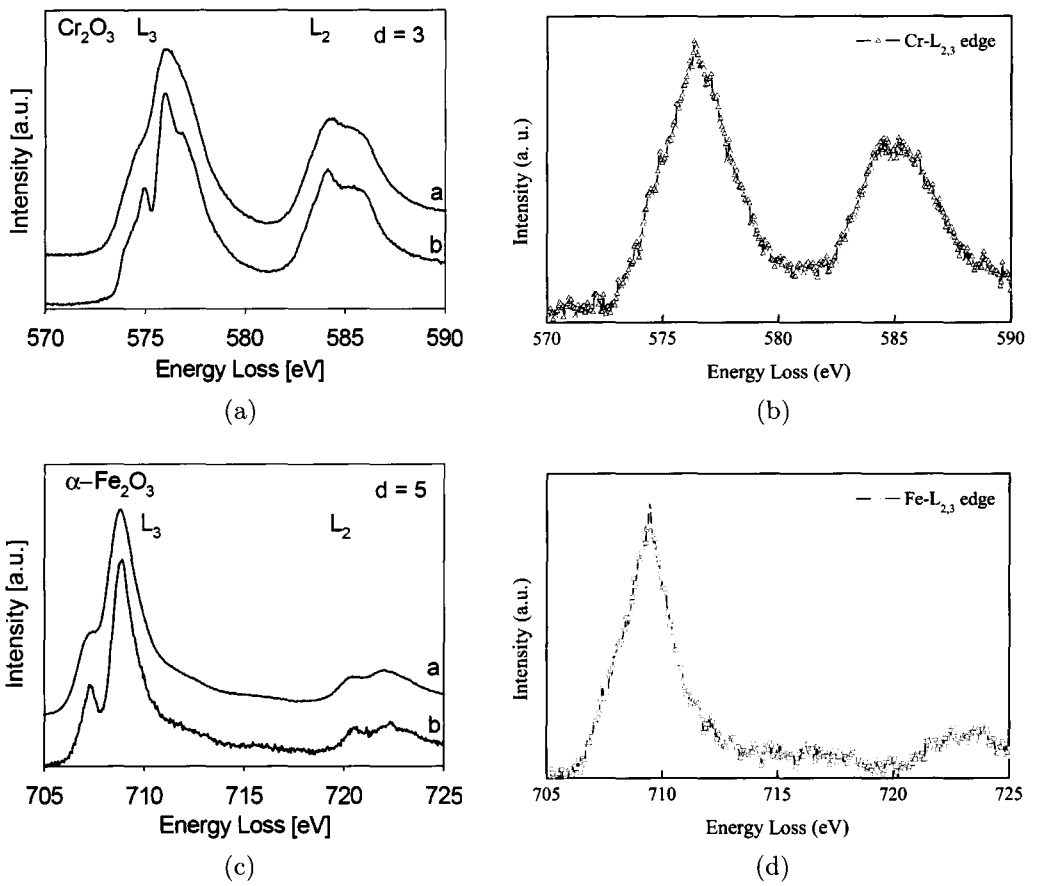

Figure 4.12: (a) and (c) Reference spectra of Cr L-edge and Fe L-edge taken by non-monochromated (top, energy resolution $\sim$ 0.65 eV) LaB_6 CM20 and monochromated (bottom, energy resolution $\sim$ 0.15 eV) Tecnai F20 microscopes. (Mitterbauer et al., 2003), (b) and (d) Experimental spectra of Cr $L_{2,3}$ edge and Fe $L_{2,3}$ edge taken by VG HB 601 STEM (100 kV, energy resolution at the Zero Loss Peak of $\sim$ 0.4 eV).

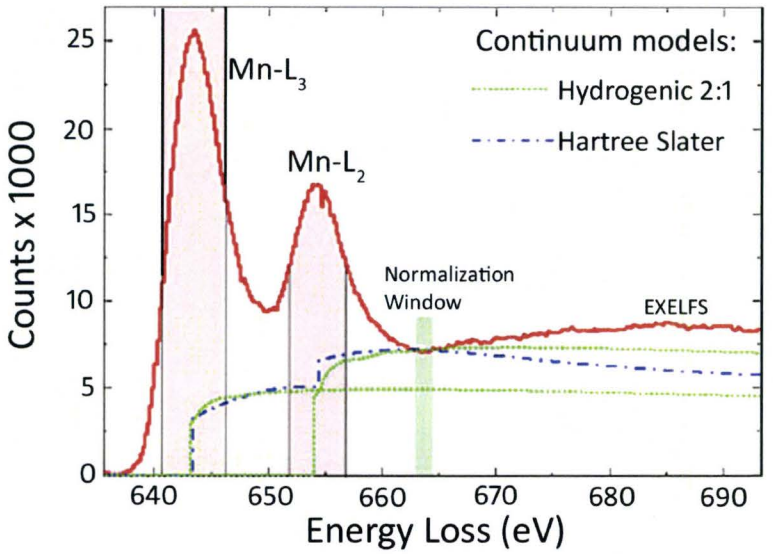

Figure 4.13: Background subtracted Mn-$L_{2,3}$ ionization edge in MnO_2. The cross section removal by Hartree–Slater and modified double-step hydrogenic continuum models are performed at peak maxima with height ratio of 2:1. The shaded regions indicates the positions of normalization and integration windows. (from Schmid and Mader, 2006)

determination of the valence of both elements was carried out by integrating the area under the L_2 and L_3 peak after background and cross-section removal. The background and cross-section removal was done following the procedure proposed by Botton, et al. (1995) and Schmid and Mader (2006) on Mn-oxides. The cross-section removal methods of the background subtracted Mn $L_{2,3}$ edge in MnO_2 are illustrated in Figure 4.13. The continuum model used for the subtraction of the atomic continuum of the EELS results here was Hartree-Slater where the widths of integration for Fe and Cr L-edges were 3 eV and 5 eV, respectively. The result of the experimental L_3/L_2 ratio of Fe and Cr from the BFCO film is presented in Table 4.5, along with some reference values of the two elements in other compounds.

The near edge structures at the oxygen K-edge can be interpreted as a combination of the two characteristics of the O K-edge in the Cr^{3+} and Fe^{3+} environments, as reported by Mitterbauer, et al. (2003). Following the argument described therein using a simple one-electron excitation scheme, the structure of O K-edge spectra can be interpreted as the transition of one electron from the 1s or 2p orbital to various partially occupied or unoccupied orbitals of metal oxides. In the perovskite structure

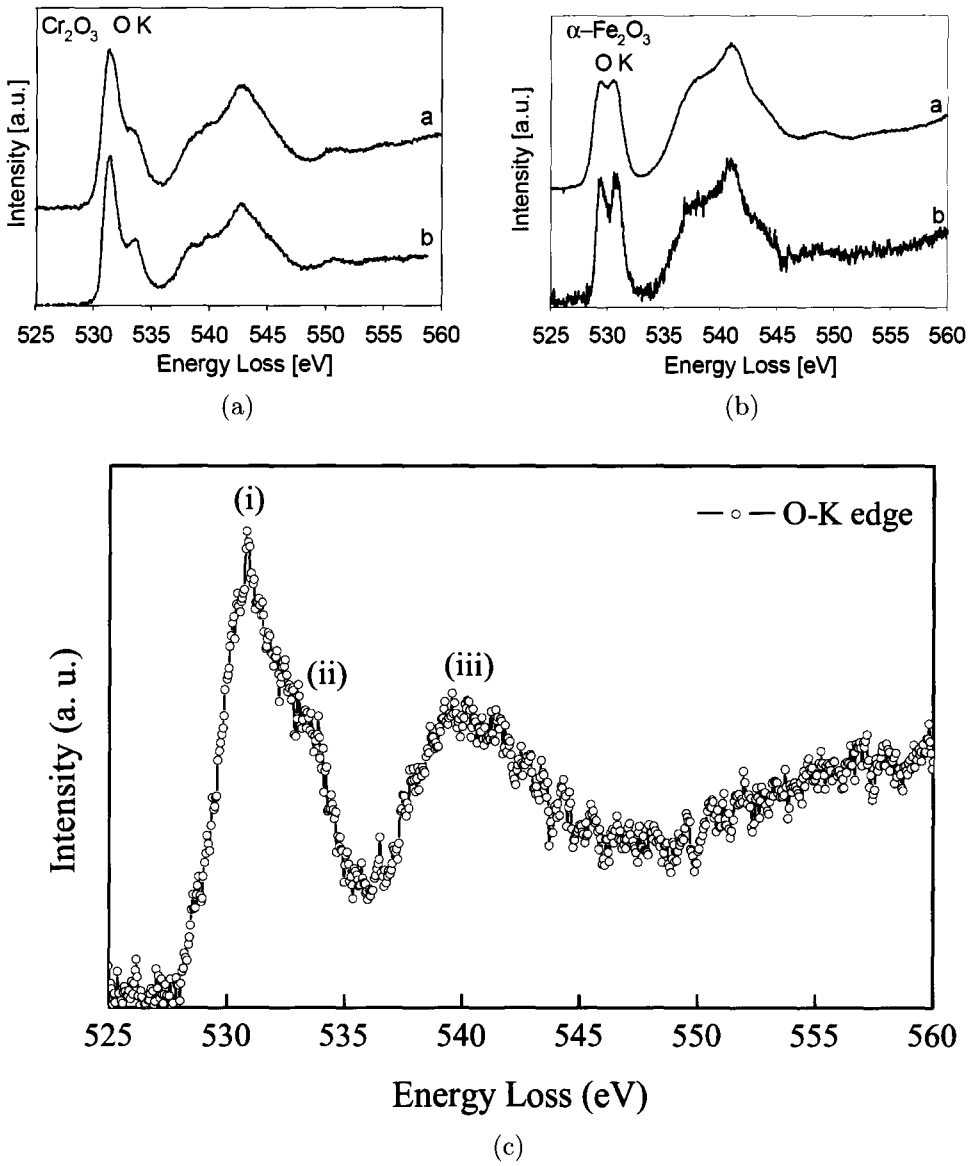

Figure 4.14: (a) and (b) Reference spectra of O K-edge from Cr_2O_3 and α-Fe_2O_3 as taken by non-monochromated (top, energy resolution $\sim$ 0.65 eV) LaB_6 CM20 and monochromated (bottom, energy resolution $\sim$ 0.15 eV) Tecnai F20 microscopes; (c) Experimental O K-edge from the BFCO film acquired with VG HB 601 STEM(100 kV, energy resolution at the Zero Loss Peak of $\sim$ 0.4 eV). (Mitterbauer et al., 2003)

Table 4.5: The L_3/L_2 ratio of experimental and reference Fe and Cr and its corresponding valence.

	Element	**Compound**	**L_3/L_2 ratio**	**Valence**
Reference				
Daulton and Little, 2006	Cr	Cr_2O_3	1.671 ± 0.012	3+
		CrO_2	1.478 ± 0.002	4+
Cave et al., 2006	Fe	$FeSiO_4$	4.22 ± 0.06	2+
		Fe_2O_3	5.64 ± 0.10	3+
Schmid and Mader, 2006	Fe	α-Fe_2O_3	5.1 ± 0.1	3+
Chen et al., 2007	Fe	γ-Fe_2O_3	5.21	3+
Our Experiments				
	Cr	BFCO 1/1	1.634 ± 0.007	3+
	Fe	BFCO 1/1	5.415 ± 0.172	3+

assuming an octahedral symmetry, the molecular orbitals available for such transitions according to dipole selection rule are: $2t_{2g}$ (M 3d-O 2pπ), $3e_g$ (M 3d-O 2pσ), $3a_{1g}$ (M 4s-O 2pσ) and $4t_{1u}$ (M 4p-O 2pπ), respectively with increasing energetic order, where M corresponds to the metal or B-site cation. In BFCO films, the availability of both molecular orbitals of t_{2g} and e_g from both Fe and Cr cations allows the electronic transition to the hybridized M 3d-O 2p orbitals, resulting in the broadening of the first two peaks of O K-edge, indicated by (i) and (ii), in comparison to O K-edge in Cr_2O_3 or Fe_2O_3 alone. Further, electronic transition to the hybridized M 4s-O 2p and M 4p-O 2p orbitals occurs at higher energy level, as indicated by peak (iii).

Overall, the structure of O-K edge, shown in Figure 4.14, offers some insights:

- peaks (i) and (ii) can be associated with the transition of O 1s electrons to O 2p states hybridized with M 3d states ($t_{2g}$and e_g) of both Fe and Cr; and
- peak (iii) can be associated with the transition of electrons to O 2p states hybridized with M 4s and M 4p states. Taking into account multiple-electron configuration interactions, such transitions may also be attributed to the intrashell multiple scattering of 1^{st} coordination O-shell due to neighbouring atoms. (Mitterbauer et al., 2003)

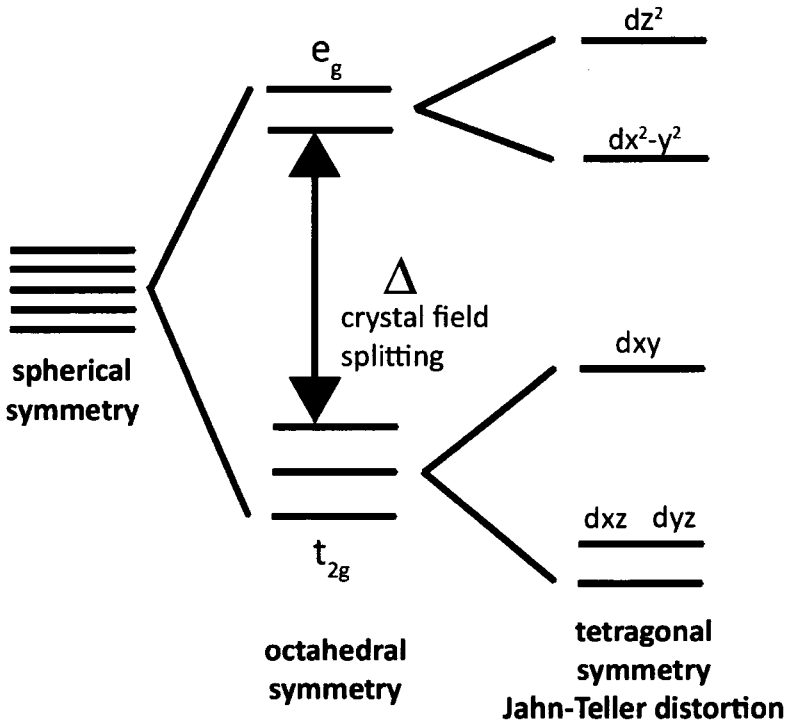

Figure 4.15: Splitting of the energy level of orbitals due to the crystal field effect (octahedral symmetry) and further due to the Jahn-Teller distortion (tetragonal symmetry).

The extra broadening of the experimental spectra was likely due to tilting or distortion of the octahedra. The distortion of octahedra, for example the Jahn-Teller distortion, may perturb some of the octahedral symmetry by a tetragonal distortion as some of the bond lengths increase and some others decrease, resulting in the further split of the t_{2g} and e_g energy levels, as illustrated in Figure 4.15. In addition to the tilting or distortion of the octahedra, the instability of the high tension of the STEM as well as the longer acquisition time in the core loss energy region also contribute to the broadening of the EELS spectra.

In summary, both qualitative and quantitative analyses of EELS results show that both Fe and Cr in the BFCO film have the same valence of 3+. Consequently, charge ordering due to variation of valence of B-site cations can be ruled out as the factor responsible for the extra weak reflections in the CBED pattern of BFCO 1/1 films at ZA <110> (Figure 4.10(c)). Therefore, the extra weak reflections in the CBED pattern at ZA <110> can be attributed to B-site cationic ordering and anti-phase

Table 4.6: The list of origins of the weak and the extra weak reflections in the CBED patterns of the BFCO 1/1 film.

Zone axis	Origins of weak reflections	Associated Properties
<110>	The anti-phase tilting of BO_6 octahedra	Ferroelectric Polarization
	The B-site cationic ordering	Magnetic Polarization
<100>	The formation of a secondary phase, Bi_2O_3	Short circuit between electrodes

tilting of oxygen sharing octahedra. The anti-phase tilting has no influence on the magnetic properties, but influences the ferroelectric properties instead. The B-site cationic ordering, i.e., Fe and Cr, along the <111> direction of the pseudo-cubic unit cell are likely to be responsible for the increase in the saturation magnetization of the BFCO 1/1 film.

The weak reflections in CBED patterns obtained at ZA <100> (Figure 4.10(a)) can be attributed to the presence of the secondary phase, Bi_2O_3. The EDX results, demonstrating the compositional modulation of Fe and Cr along the lateral direction in the BFCO 1/1 film, supported the presence of a Bi-rich phase, which is likely to be Bi_2O_3, as suggested by CBED patterns analysis.

For clarity, the possible origins of the weak reflections observed in the CBED patterns of the BFCO 1/1 film in the direction parallel to both the ZA<110> and the ZA<100> (Figure 4.9(b) and (c)) are summarized in Table 4.6.

4.2 $Bi_2(Fe_{0.5}Cr_{1.5})O_6$ (BFCO 1/3)

In the previous section, it was concluded that the high saturation magnetization in BFCO film is quite likely to be associated with Fe-Cr B-site cationic ordering, as observed in the CBED pattern of the BFCO 1/1 film at ZA <110> (Figure 4.9(b) in Section 4.1.3). Such strong magnetism has been hypothesized to be caused by the exchange interaction between Fe-Cr cations, which are ordered along the <111> pseudo-cubic direction. As the stoichiometric composition of the film is altered to BFO/BCO 1/3 (BFCO 1/3) and assuming that the exchange interaction persists, the magnetism is expected to be significantly decreased due to more dominant Cr-Cr antiferromagnetic interactions than Fe-Cr interactions. The next step in this section will be dedicated to investigating the structure of BFCO 1/3 in comparison to that of BFCO 1/1, which causes different interactions impacting its physical properties. The atomic structure was observed using both high resolution TEM and HAADF imaging.

The BFCO 1/3 films (sample ID BFC 48) were epitaxially grown on (111) oriented Nb-doped STO substrates. The thin films were deposited by using dual cross beam pulsed laser deposition. The two targets used were Bi-rich targets of $Bi_{1.1}FeO_3$ and $Bi_{1.1}CrO_3$. The fluence of two synchronized KrF excimer laser beams with 284 nm wavelength were controlled to adjust the iron and chromium content in the film. Further details of the BFCO 1/3 films growth were described by Nechache, et al. (2007).

The physical property measurements, namely piezo-response and magnetic response, of BFCO 1/3 have been reported by (Nechache et al., 2007) demonstrating some remarkable features in comparison to those of BFCO 1/1, as displayed in Figures 4.16(a) and (b) and Figure 4.17. The ferroelectric polarization in BFCO 1/3 suggests a 180° polarization switching, indicated by the relatively symmetrical sign change in both x(lateral)- and z(growth)- components, with voltage bias reversal.

Even though the magnitude of polarization in the z-direction (growth or out-of-plane direction) in both BFCO 1/3 and BFCO 1/1 was comparable, the magnitude of polarization in the x (lateral)-direction was much less in BFCO 1/1 compared to BFCO 1/3. In BFCO 1/1 the magnitude of polarization in the z-direction was seven times

stronger than in the x-direction. This indicates that the polarization vector in BFCO 1/1 was dominant along the out-of-plane direction or along <111> crystallographic direction. The strong polarization in the z-direction maybe related to anti-phase tilting previously observed in electron diffraction patterns recorded in a direction parallel to the ZA $<110>_{\text{BFCO 1/1}}$.

In contrast, the magnitude of polarization in BFCO 1/3 along the z-direction was actually three times less than that in the x-direction. This suggests that the polarization vector in BFCO 1/3 is no longer parallel to the <111> crystallographic direction, indicated by the significant presence of polarization along the x-direction. Such deviations of polarization vector in BFCO 1/3 relative to BFCO 1/1 may be related to the decrease in the anti-phase tilting along the <111> crystallographic direction.

Furthermore, the magnetization of BFCO 1/3 is far less than that of BFCO 1/1 (Figure 4.17), as previously expected because of the reduced Fe-Cr ferromagnetic interactions. The factor responsible for the decrease in saturation magnetization of BFCO 1/3 has been suggested to be due to the more dominant Cr-Cr exchange antiferromagnetic interaction instead of the Fe-Cr ferromagnetic superexchange interaction. Both intriguing responses of BFCO 1/3 in terms of piezo-response and magnetic response may be linked to the ordering of B-site cations and modification of the exchange interaction between them. (Nechache et al., 2007)

In both cases of piezoelectric and magnetic responses of BFCO 1/3, the experimental results demonstrate a significant deviation from what has been observed in BFCO 1/1. TEM investigation is employed in order to gain more insights to the atomic and electronic structure responsible for the deviation.

4.2.1 Layered patterns of BFO/BCO (1/3)

The overall morphology of thin films consisting of a combination of BFO and BCO with a 1:3 stoichiometric ratio (BFCO 1/3, sample ID BFC 48) is shown in Figure 4.18(a). The 80 nm thick film exhibited layered patterns parallel to the surface of the substrate. There was also a slight directional variation along the in-plane direction, as subtly marked by the presence of grain boundaries. The surface of the film was

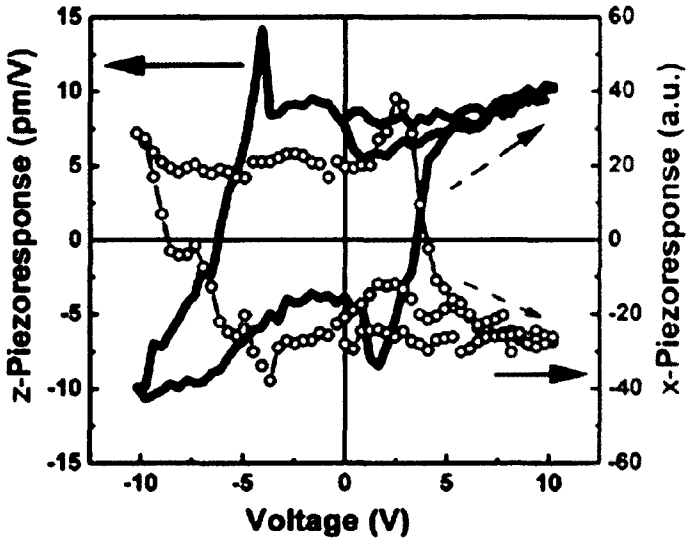

(a)

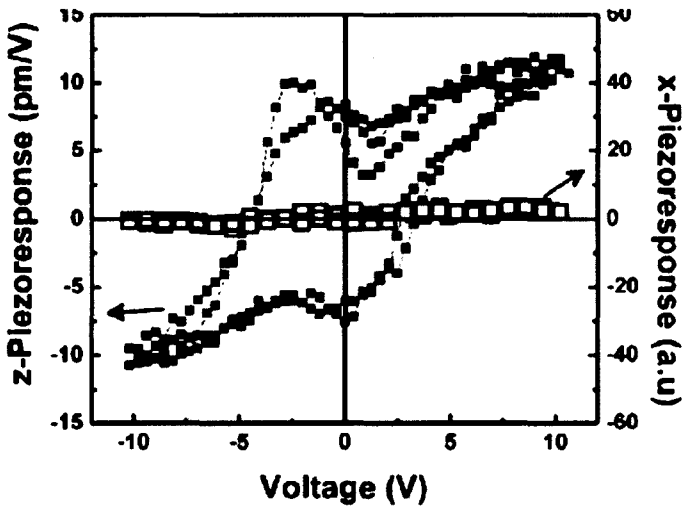

(b)

Figure 4.16: The in-field hysteresis loop of piezo force microscopy (PFM) are displayed for (a) BFCO 1/3 (111)-oriented film and (b) BFCO (BFCO 1/1) (111)-oriented film, respectively. The PFM signals were recorded in z- (growth) and x- (lateral) directions. (from Nechache et al., 2007)

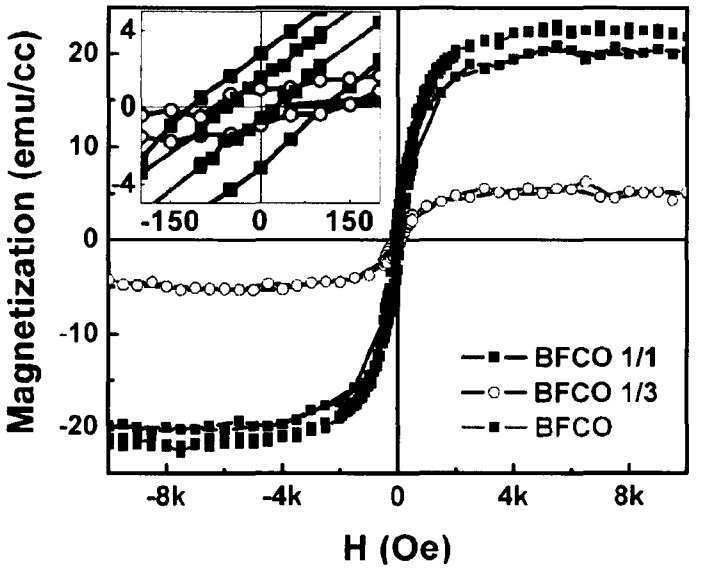

Figure 4.17: The hysteresis-magnetization (M-H) curves of BFCO 1/1 and BFCO 1/3 film grown by dual-beam PLD and BFCO 1/1 film grown by conventional PLD (legend: BFCO). All films were grown on a (111)-oriented substrate. (from Nechache et al., 2007)

extremely smooth, with only a one or two unit cell height variation, as shown in Figure 4.18(b).

Meanwhile, the interface between the BFCO 1/3 film and the substrate does not clearly show a sharp edge (Figures 4.18(c) and (d)) due to the presence of some amorphous phase. The loss of sharpness at the interface may also be caused by slight misorientation between film and substrate. The transition from double-layer into four-layer stacking was also observed at the interface in Figure 4.18(d). However, the non-sharp interface, indicating the loss of direct contact between film and substrate, does not result in the absence of an epitaxial relationship.

4.2.2 EDX Analysis of BFCO 1/3 film

The results of quantification of EDX spectra acquired from several points at two different sites of the BFCO 1/3 film shown in Figures 4.19(a) and (b) are listed in Table 4.7 (in atomic percentage). The composition was calculated using the INCA

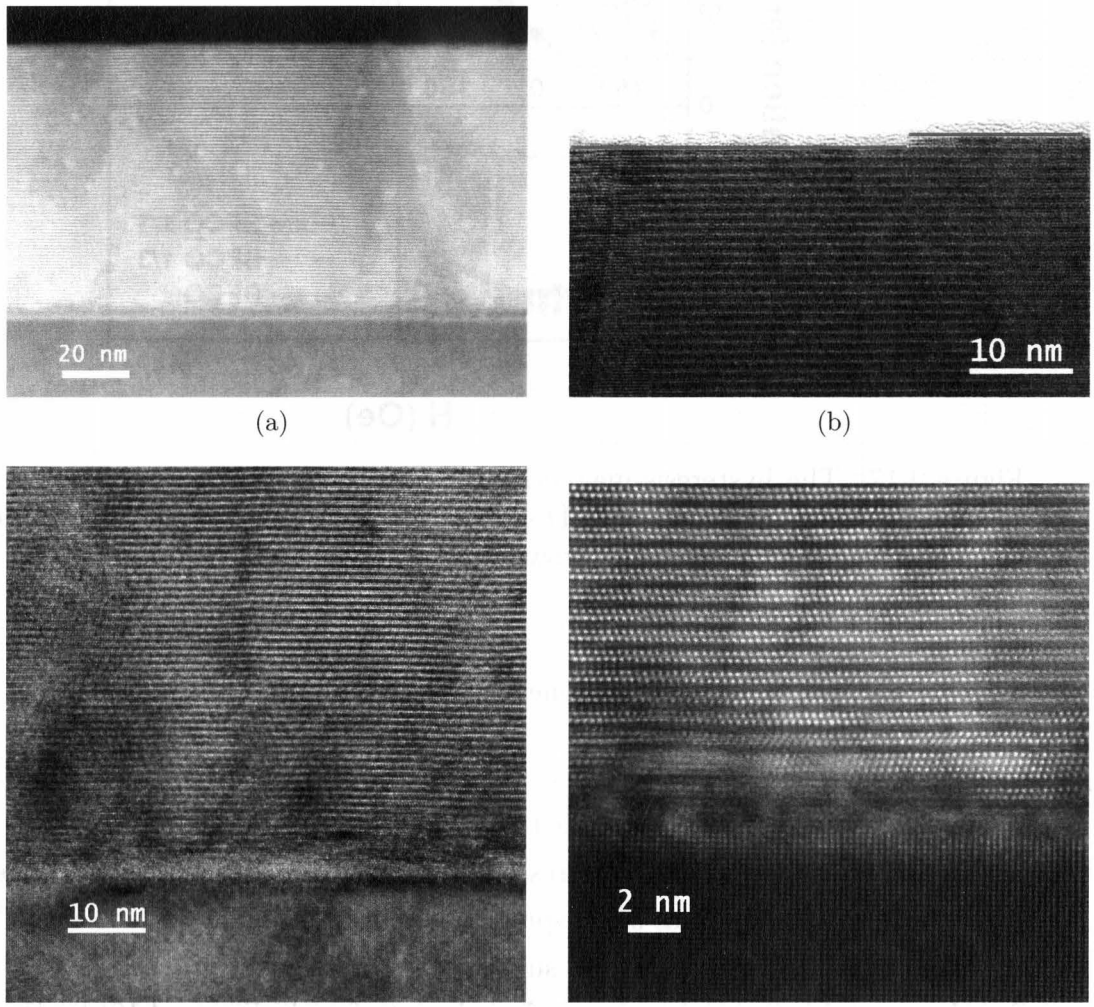

(a) (b)

(c) (d)

Figure 4.18: (a) Non C_S-corrected ADF image of BFCO 1/3 thin film recorded with the sample oriented at the ZA $<101>_{STO}$ indicates a smooth film with a slight variation of grain orientation along in-plane (horizontal) direction. C_S-corrected HRTEM (phase-contrast) images of BFCO 1/3 recorded from (b) top surface of the film and (c) interface region. (d) The probe-corrected ADF image of the film-substrate interface in the direction parallel to the ZA $<121>_{STO}$ showing clearly the presence of an amorphous phase and the transition from a double-layer configuration into a four-layer configuration.

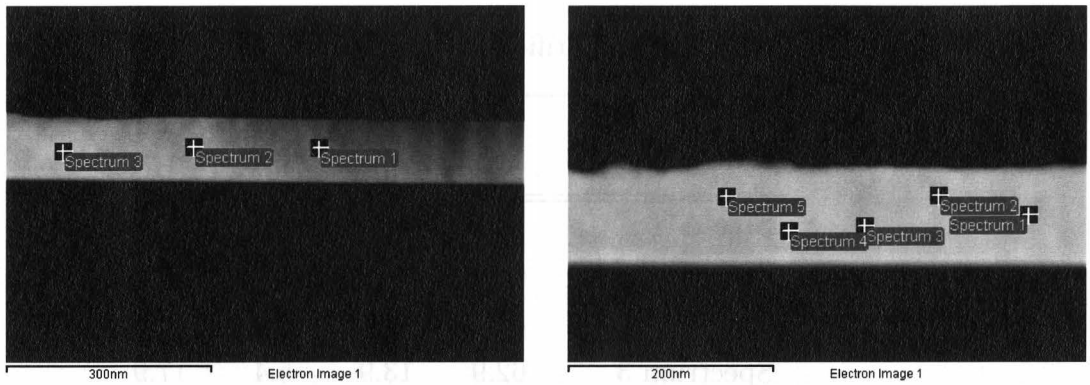

(a) (b)

Figure 4.19: The ADF images taken by the INCA software showing the location, namely (a) site A and (b) site B, from which the EDX signals were extracted.

EDX analysis software (*Oxford Inc.*) using Si Kα1 as the ratio standard element, TEM sample thickness of $\sim$ 200 nm and sample density of $\sim$ 7.9 g/cm^3. The thicker area was deliberately selected to improve counting statistics. The information in the literature to date on the experimental bulk density was available only for BFO, that is $\rho = 7.9$ g/cm^3 (Zaharescu, et al., 2005), but not for BCO. As a first approximation in the quantification iteration, it was assumed that the density of BFCO 1/3 is the same as that of BFO, regardless of the compositional differences between BFO and BCO. In addition, the calculated density of BFCO 1/3 based on the density of the individual elements is $\sim$ 7.94 g/cm^3.

When normalizing based on Bi, the elemental composition of the BFCO 1/3 film is enlisted in Table 4.8.

Taking the average of all spectra from each element, the composition of the BFCO 1/3 film is $BiFe_{0.3}Cr_{0.8}O_{3.2}$. The atomic ratio of Cr/Fe of 2.54 shows a deviation from the aimed stoichiometric value of $BiFe_{0.25}Cr_{0.75}O_3$. The deviation of the Fe/Cr ratio by varying the sample thickness for quantification from 50 nm to 200 nm was about 2 %. Despite the compositional deviation from aimed stoichiometry, the elemental distribution in this film was uniform throughout as shown in Figures 4.20(a-e).

Table 4.7: The results of quantification of EDX spectra of the BFCO 1/3 film

	Concentration (atomic %)			
	O	**Cr**	**Fe**	**Bi**
Site A				
Spectrum 1	65.8	13.1	4.9	16.2
Spectrum 2	64.2	14.6	6.2	15.0
Spectrum 3	62.9	13.9	5.4	17.9
Std. Deviation	1.4	0.7	0.7	1.4
Site B				
Spectrum 1	58.4	16.2	6.1	19.4
Spectrum 2	57.2	16.8	6.6	19.3
Spectrum 3	55.6	17.1	6.8	20.5
Spectrum 4	54.9	17.3	6.7	21.2
Spectrum 5	54.6	17.5	6.9	21.1
Std. Deviation	1.6	0.5	0.3	0.9

Table 4.8: The elemental composition of the BFCO 1/3 film

	O	**Cr**	**Fe**	**Bi**
Site A				
Spectrum 1	4.1	0.8	0.3	1.0
Spectrum 2	4.3	1.0	0.4	1.0
Spectrum 3	3.5	0.8	0.3	1.0
Site B				
Spectrum 1	3.0	0.8	0.3	1.0
Spectrum 2	3.0	0.9	0.3	1.0
Spectrum 3	2.7	0.8	0.3	1.0
Spectrum 4	2.6	0.8	0.3	1.0
Spectrum 5	2.6	0.8	0.3	1.0

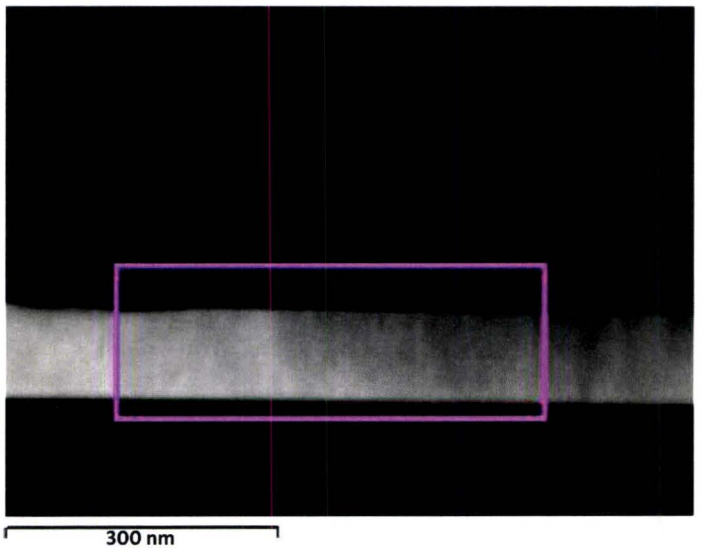

(a)

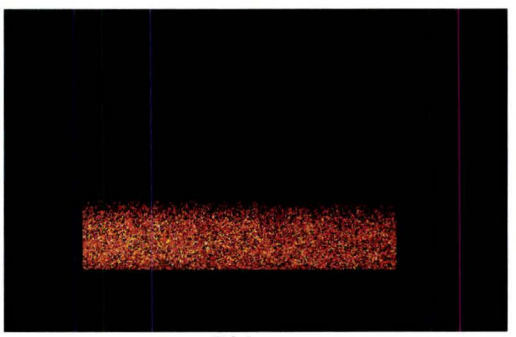

(b)

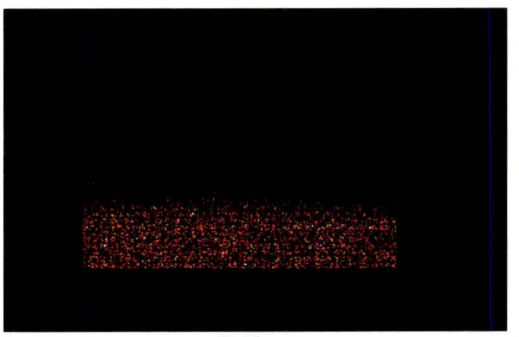

(c)

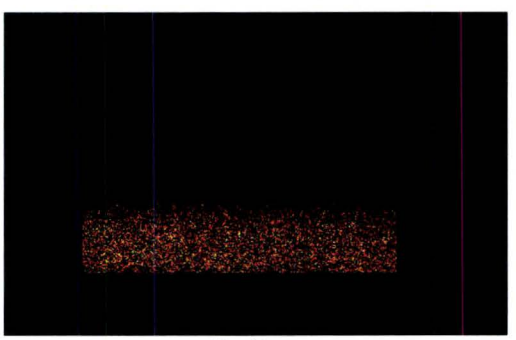

(d)

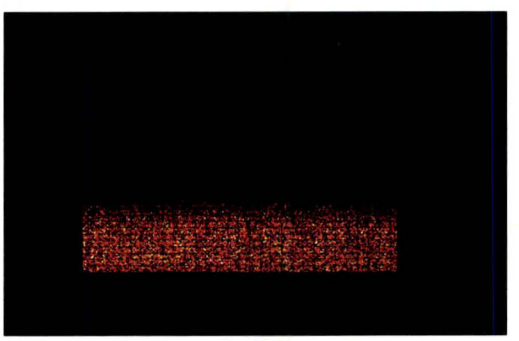

(e)

Figure 4.20: (a) The ADF image of BFCO 1/3 (sample ID BFC 48) shows the area from which the elemental maps of Bi, O, Fe and Cr (b-e), respectively, were generated.

4.2.3 Analysis of SAED Patterns and XRD2 3D Reciprocal Space

Based on the investigation of BFCO 1/1, the unit cell of BFCO 1/3 has been predicted to be a double perovskite structure with Fe^{3+} and Cr^{3+} cations ordered along the <111> direction (Nechache et al., 2007). An investigation using electron and X-ray diffraction was performed to check whether the BFCO 1/3 unit cell is in agreement with predictions.

Experimental SAED patterns of BFCO 1/3 recorded with the sample oriented at zone axis (ZA) $<101>_{STO}$ and ZA $<121>_{STO}$ are displayed in Figures 4.21(a) and (b). The closest match of these diffraction patterns in terms of reciprocal spacing only, but not in terms of the whole pattern, were reproduced using the JEMS simulated SAED patterns of a double perovskite unit cell of BFCO 1/3 in the direction parallel to the ZA $<102>_{BFCO\ 1/3}$ and the ZA $<121>_{BFCO\ 1/3}$, as displayed in Figures 4.21(c) and (d).

In addition, the atomic projections from JEMS associated to those particular zone axes of double perovskite BFCO 1/3, namely ZA $<102>_{BFCO\ 1/3}$ and ZA $<121>_{BFCO\ 1/3}$, do not agree with the atomic configuration observed in the experimental high resolution ADF images, as shown side-by-side in Figures 4.22(a) and (b). The ADF images show double layers of Bi, which were not observed in both atomic projections of the double perovskite structure. This comparison suggests that the BFCO 1/3 film possesses a different configuration of unit cell than a double perovskite unit cell previously suggested. Hence, in order to understand the lattice parameters and unit cell structure of this new material, we analyzed the FFT (the reciprocal space) of the HAADF images.

The reciprocal space maps of the corresponding ADF images in Figures 4.22(a) and (b), derived by applying the Fast Fourier Transform, are shown in Figures 4.22(c) and (d), respectively. The FFTs at both zone axes of $<101>_{STO}$ and $<121>_{STO}$ are relatively consistent in reproducing the main features present in the experimental SAED patterns. In the vertical direction, both the major reflections and weak reflections are consistently observed in the SAED patterns and FFT of the images at both ZA

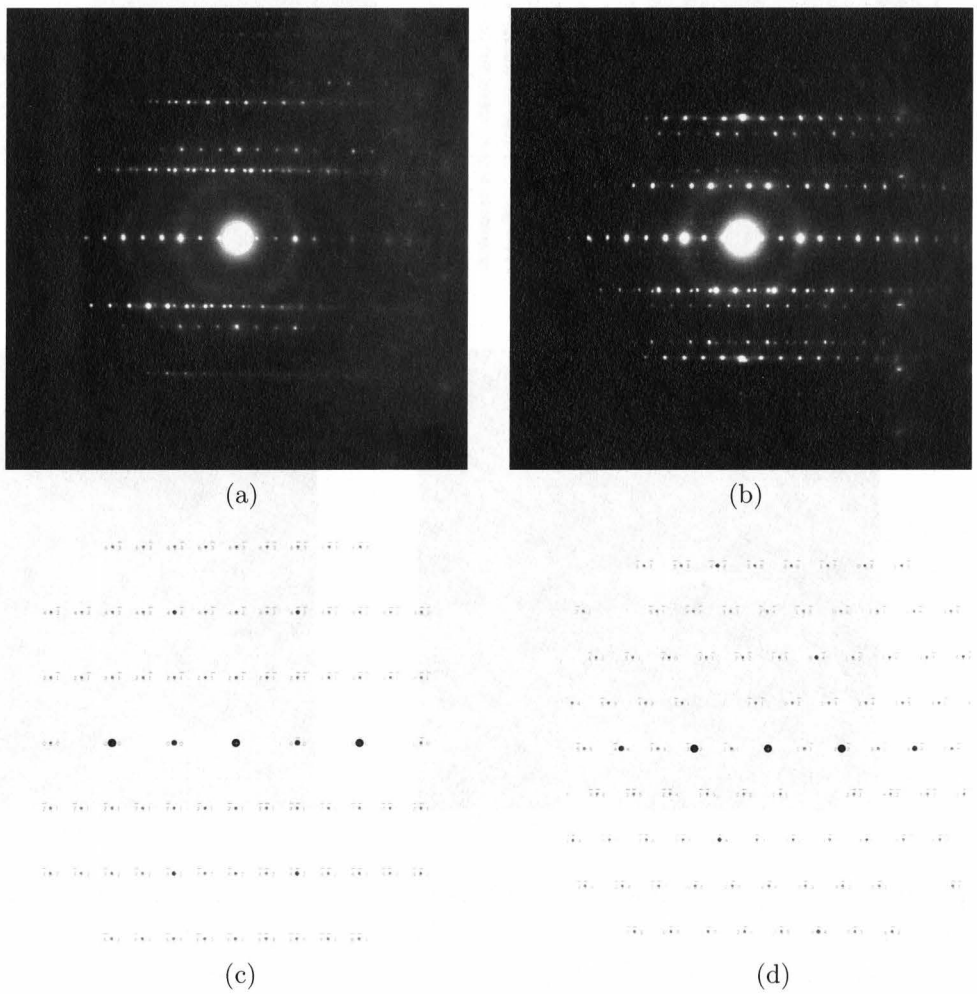

Figure 4.21: The experimental SAED patterns of BFCO 1/3 film with the sample oriented at (a) the ZA $<101>_{STO}$ and (b) the ZA $<121>_{STO}$. The JEMS simulated SAED patterns of a double perovskite BFCO 1/3 structure in the direction parallel to (c) ZA $<102>_{BFCO\ 1/3}$ and (d) ZA $<121>_{BFCO\ 1/3}$.

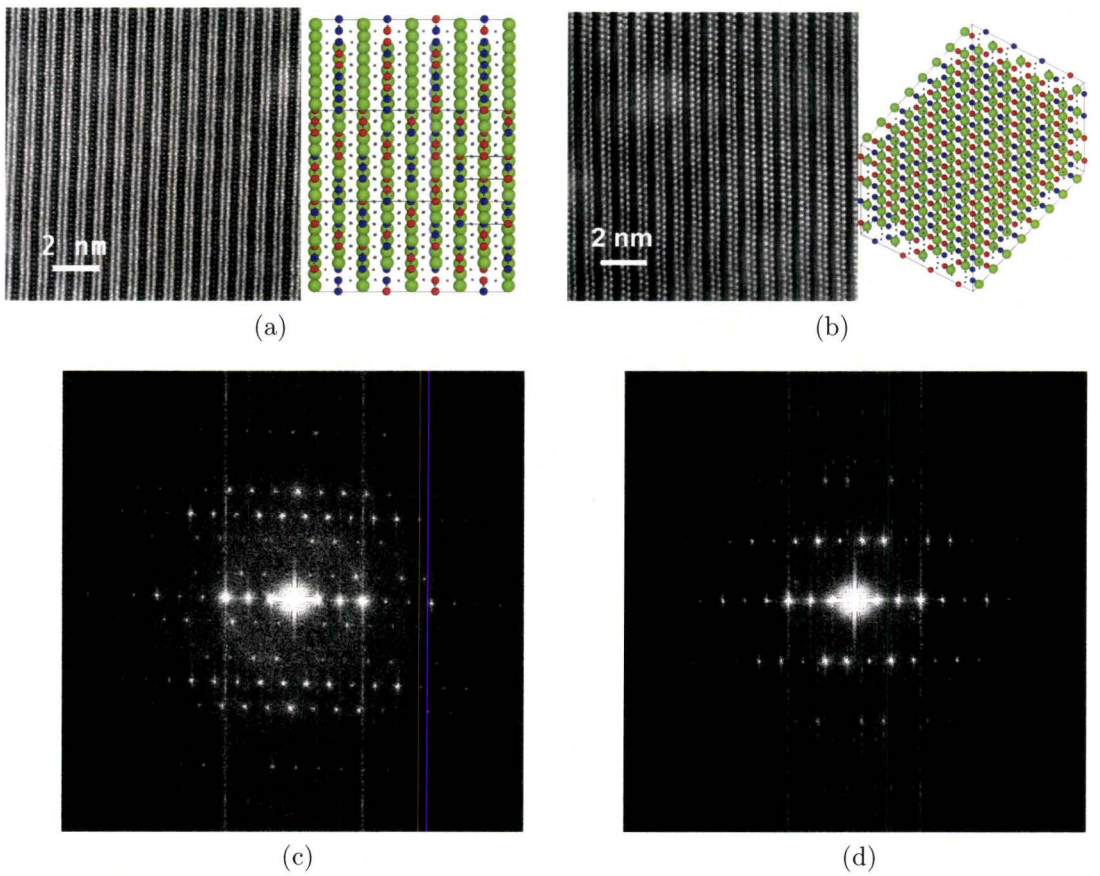

Figure 4.22: (a) C_S-corrected HAADF image of BFCO 1/3 film with the sample oriented at the ZA $<101>_{STO}$ and JEMS atomic projection of double perovskite in the direction parallel to ZA $<102>_{BFCO\ 1/3}$; (b) C_S-corrected HAADF image of BFCO 1/3 film with the sample oriented at ZA $<121>_{STO}$ and JEMS atomic projection of double perovskite in the direction parallel to ZA $<121>_{BFCO\ 1/3}$ (Bi = green, Fe = blue, Cr = red, and O = black); (c-d) The Fast Fourier Transform of HAADF images in (a) and (b) only reproduce the major reflections in the experimental SAED patterns.

$<101>_{STO}$ and ZA $<121>_{STO}$. Such consistency suggests that both the major and weak reflections are arising from the structure in the BFCO 1/3 film.

Despite the consistency between the FFTs of the HAADF images and the experimental SAED patterns along the vertical direction, the splitting of major reflections along the horizontal direction in the experimental SAED patterns was not observed in the FFTs. Such lack of agreement between the SAED patterns and the FFTs of the HAADF images can be attributed to the lack of resolution of the features in the image, even though the SAED pattern and the image were taken from the same area. Furthermore, the area from which HAADF images were acquired was much smaller in comparison to the area from which SAED patterns were recorded. The HAADF image only probes a localized area of 20 nm $\times$ 20 nm, while the SAED patterns was recorded from a much larger area defined by the size of the virtual SAED aperture, which in this case was about $\sim$ 10 microns. Both the lack of resolution of features in the HAADF image and the difference in the probed area contribute to the discrepancies of features between the SAED patterns and the FFTs of the HAADF images.

The splitting was also consistently observed in 3D reciprocal space maps acquired by XRD2 experiments (Figure 4.23(a)). The split of the horizontal major reflections in the SAED pattern can be attributed to twinning along the growth direction. The occurence of twinning is similar to that observed in BFO films as reported by Lebeugle, et al. (2008) (Figure 4.24), which resulted in physical buckling of the crystal. The twin lines may not be easily probed in ADF imaging, especially those which are parallel to the viewing direction, due to the limited depth of focus of $\sim$ 10-20 nm in probe corrected STEM. The depth of focus limitation is likely to limit the probing of the twin lines in the ADF images, resulting in the absence of splitting of the horizontal major reflections in the FFT. Nevertheless, the presence of twins along growth direction is consistent with the reciprocal space map from XRD2 experiments.

Further analysis was performed by filtering or masking the reflections in the FFTs, so that the atomic spacing pertaining to specific reflections can be identified. The mask was applied on the FFT of the ADF image taken with the sample oriented at the ZA $<101>_{STO}$ sequentially from the longest to the shortest vertical spacing in reciprocal space as shown in Figures 4.25(a) and (c) and Figures 4.26(a) and (c). Their corresponding inverse FFTs are displayed in Figures 4.25(b) and (d) and Figures

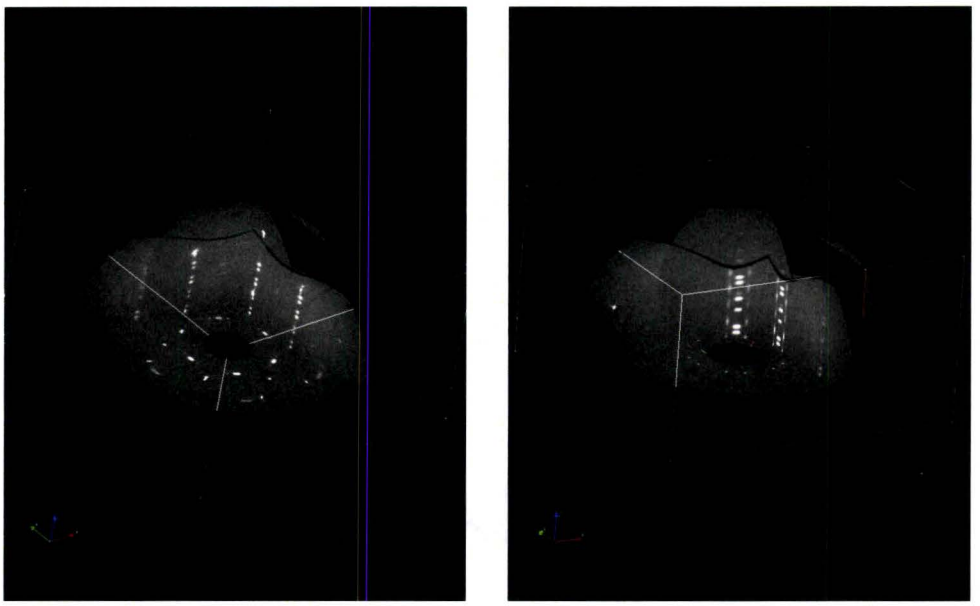

(a) (b)

Figure 4.23: Cross-sections of 3D XRD2 reciprocal space maps generated by the *Max3D* software. The cross-over between two vertical planes formed $\sim 120^{o}$ angle to each other. (a) Similar splitting of major reflections along the vertical direction was also observed in the SAED pattern as the horizontal major reflections. (b) The pair of faint reflections alongside the major reflections may contribute to the appearance of the weak reflections in SAED pattern along vertical direction due to overlapping reflections in projection.

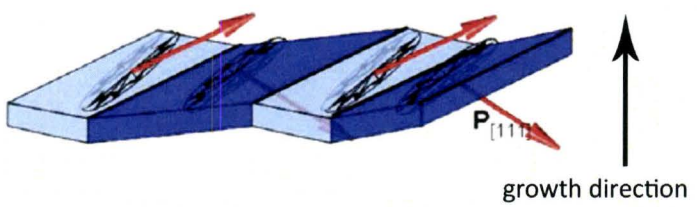

Figure 4.24: The twinning present along the growth direction of BFCO 1/3 (from Lebeugle et al., 2008)

4.26(b) and (d).

The reflections from the longest vertical distance in the FFT show more clearly the spacing between atoms within the Bi double-layer (Figure 4.25(b)). Meanwhile, the inverse FFT from the masked reflections at the second longest reciprocal spacing, as shown in Figure 4.25(c), is associated with the distance of atoms in between the Bi double-layer (Figure 4.25(d)). A slight modulation along the Bi double-layer is observed in the inverse FFT from the masked reflections at the second shortest reciprocal spacing, as shown in Figure 4.26(b). The modulation becomes more distinct in the inverse FFT from the masked reflections at the shortest reciprocal spacing, as shown in Figure 4.26(d).

The inverse FFTs indicate that both the weak and major reflections are originating from atomic configurations and structural modulations in the Bi double-layer in the unit cell of BFCO 1/3. The second shortest (Figure 4.26(a)) and the shortest (Figure 4.26(c)) reflections in the vertical direction present in both FFTs and experimental SAED patterns are incommensurate, in that its repeat unit is not an integer multiple of the unit cell. Such incommensurate reflections indicates the possibility of incommensurate ordering or a formation of a superstructure within the sample, demonstrated by the modulation in the Bi double-layer. The FFT analyses, however, were unable to define the epitaxial relationship due to the lack of information on the unit cell.

As the information from electron diffraction is generated from a specific and localized region in the sample, it may vary from one region to another. Therefore, in order to obtain more comprehensive structural information from a much larger area of the film, a texture analysis experiment using a XRD2 technique was performed on the same sample and resulted in a three-dimensional (3D) reciprocal lattice map. The instrument used was a Bruker Smart APEX2, available at the McMaster Analytical X-Ray Diffraction Facility (MAX), Department of Chemistry. An illustration on the geometry of the experiment is shown in Figure 4.27. The illuminated area on the sample was $\sim$ 0.5 mm. The experiment was performed with a detector length of 5 cm and ϕ (phi)-scan with a collection angle from 0^{o} – 360^{o} using increments of 0.5^{o}. Extra collection series were also performed for Ω (omega)-scan from 10^{o} – 60^{o} with increments of 0.5^{o}. The total number of 2D frames collected was 820.

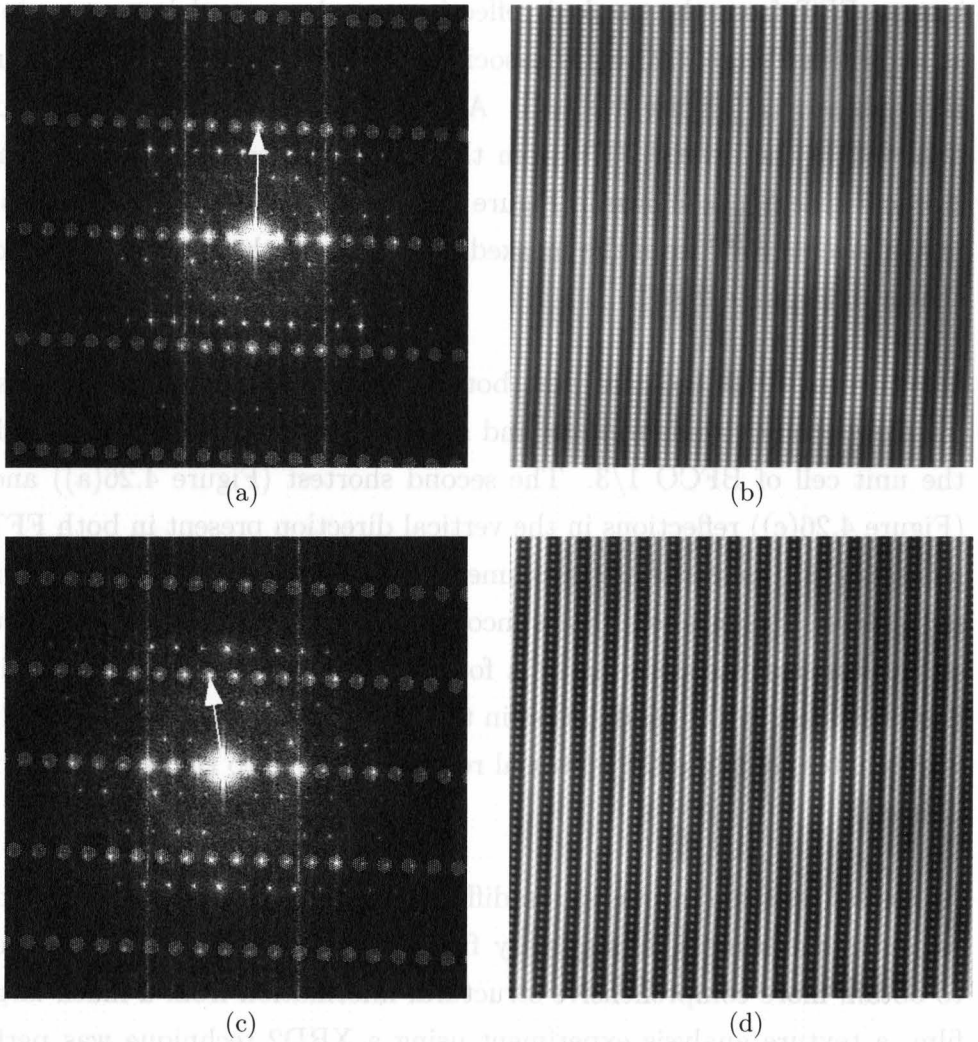

Figure 4.25: Two different masks for filtering the reflections pertaining to the film were applied on the FFT of the ADF image of BFCO 1/3 with the sample oriented at the ZA $<101>_{STO}$. The mask was applied on the longest and second longest vertical distance in reciprocal space as shown in (a) and (c) and the associated inverse FFTs are shown in (b) and (d).

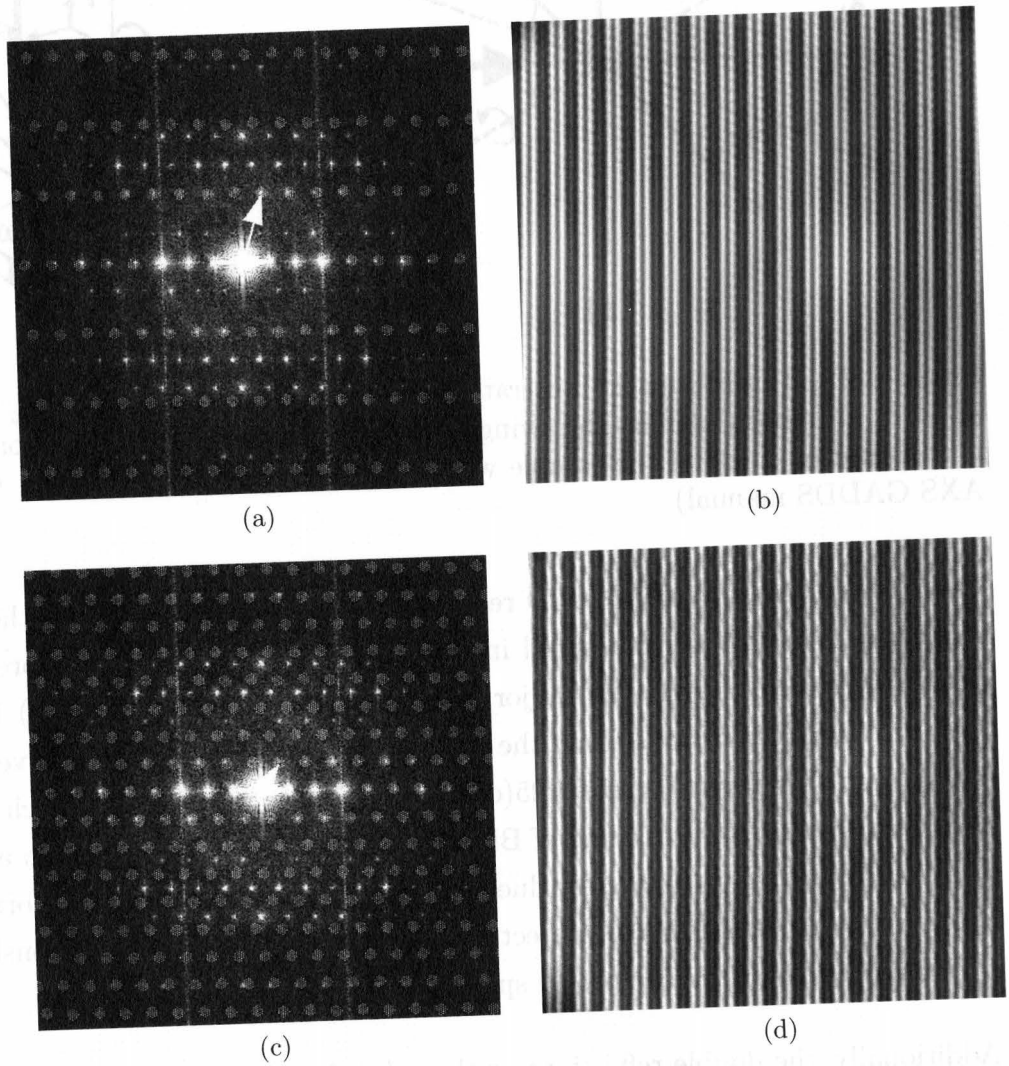

Figure 4.26: Two different masks for filtering the reflections pertaining to the film were applied on the FFT of the ADF image of BFCO 1/3 witht the sample oriented at ZA <101>$_{STO}$. The mask was applied on the second shortest and the shortest vertical distance in reciprocal space as shown in (a) and (c) and the associated inverse FFTs are shown in (b) and (d).

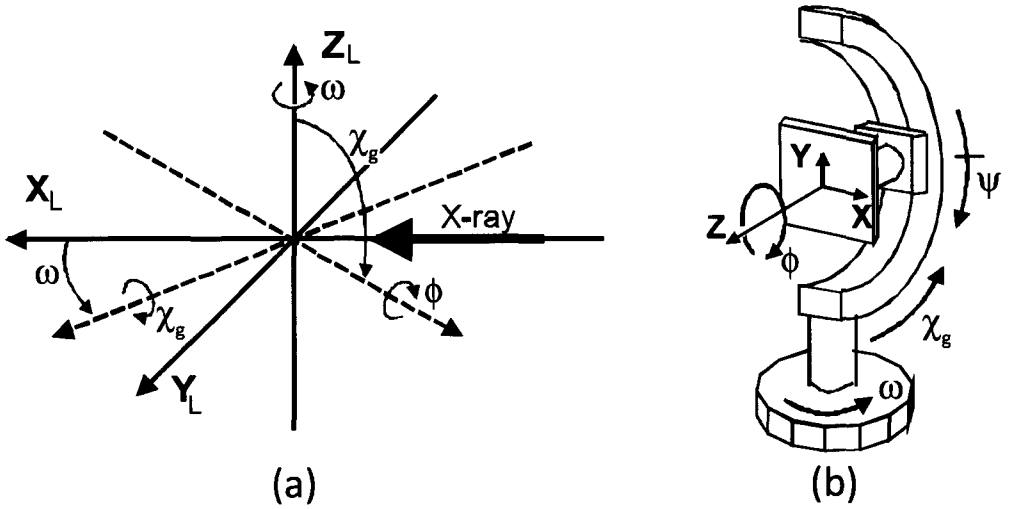

Figure 4.27: The schematic illustration of XRD2 collections, where χ_g (chi) is fixed at 54.7°, Ω (omega) defines the swing angle between sample and detector, and ϕ (phi) is the rotation angle of the sample with respect to the incident X-ray. (from Bruker AXS GADDS manual)

Two different cross sections of 3D reciprocal space map generated by the *Max3D* visualization software are presented in Figures 4.23 (a) and (b). The presence of the weaker reflections beside the major XRD reflections (Figure 4.23(b)) is consistent with the SAED reflections along the vertical direction previously observed in Figures 4.21(a) and (b). From Figures 4.25(c) and (d), it was revealed that such weak reflections correspond to the spacing of Bi atoms within the double-layer. In addition, the weak reflections may also appear due to either the variation of in-plane orientation, or the overlapping reflections in projection due to the 120° angular relationship between major reflections in the reciprocal space map.

Additionally, the double reflections or the split of major reflections along the vertical (z) direction in XRD2 pattern, consistent to the split of SAED major reflections along horizontal direction, can be attributed to the presence of twinning along growth direction. The split of the major reflections at the base (x-y plane) of the reciprocal space cross section also indicates that there is an in-plane variation of unit cell orientation in the lateral direction of the film.

Overall, the weak reflections and the split of major reflections were observed in both

SAED patterns and XRD2 3D reciprocal space maps. The vertical weak reflections in SAED patterns are generated by the structure of BFCO 1/3 and the variation of in-plane orientations. The split of major reflections along the horizontal direction are due to twinning along the growth direction, perpendicular to the film-substrate interface. The twin lines were parallel to the viewing direction in the hi-resolution ADF image, and therefore they were not observed. All reflections are characteristics of the unit cell of BFCO 1/3, not of that of the substrate. The investigations so far did not reveal the presence of ordering or formation of superstructure within the BFCO 1/3 film.

4.2.4 Lattice Parameters Determination

Even though SAED patterns and 3D reciprocal space maps of BFCO showed remarkable consistency, and all the signature of associated reflections are identified, the unit cell structure and its lattice parameters of BFCO 1/3 film on (111)-oriented substrate are still unknown. Thus, XRD2 was utilized to provide some insights into the determination of the lattice parameters.

The sequence of the XRD2 experiments are listed in Table 4.9, with the detector length fixed at 17 cm and the chi (χ_g) angle fixed at 54.74°. The parameters represent the position of the sample with respect to the X-ray source and the CCD camera detector, as schematically illustrated in Fig. 4.27(b). The frame corresponds to the 2D-data recorded in the CCD camera at every single experimental configuration described by the specific values of 2θ, omega (ω), phi (ϕ), and chi (χ_g) .

The XRD results were merged and then refined by using Total Pattern Analysis Solution software (*TOPAS*, Bruker AXS). The merged raw data (black, top curve) and the refined results (blue and red curves) after structural refinement are shown in Figure 4.28. In general, the refinement process was able to fit all the peaks present in the experimental data with a goodness of fit value of Rwp = 1.886. The difference curve, black bottom curve in Figure 4.28, also demonstrates the goodness of fit. The refinement gives a monoclinic unit cell (space group #14, P 2_1/n) with lattice parameters as follows: a = 10.9764 Å, b = 10.8479 Å, and c = 15.9073 Å, with $\alpha = \gamma = 90°$ and

Table 4.9: The experimental parameters applied during the acquisition of XRD spectra for lattice parameters determination. The axis '3' corresponds to the phi(ϕ)-axis, parallel to the normal direction of the sample. The width indicates the phi (ϕ) increment.

Frame	2θ (°)	omega ω (°)	phi ϕ (°)	chi χ_g (°)	axis	width (°)	number of frame	acquisition time (s)
001	20	10	-30	54.74	3	60	3	120
004	40	20	-30	54.74	3	60	3	120
007	60	30	-30	54.74	3	60	3	120
010	80	40	-30	54.74	3	60	3	120

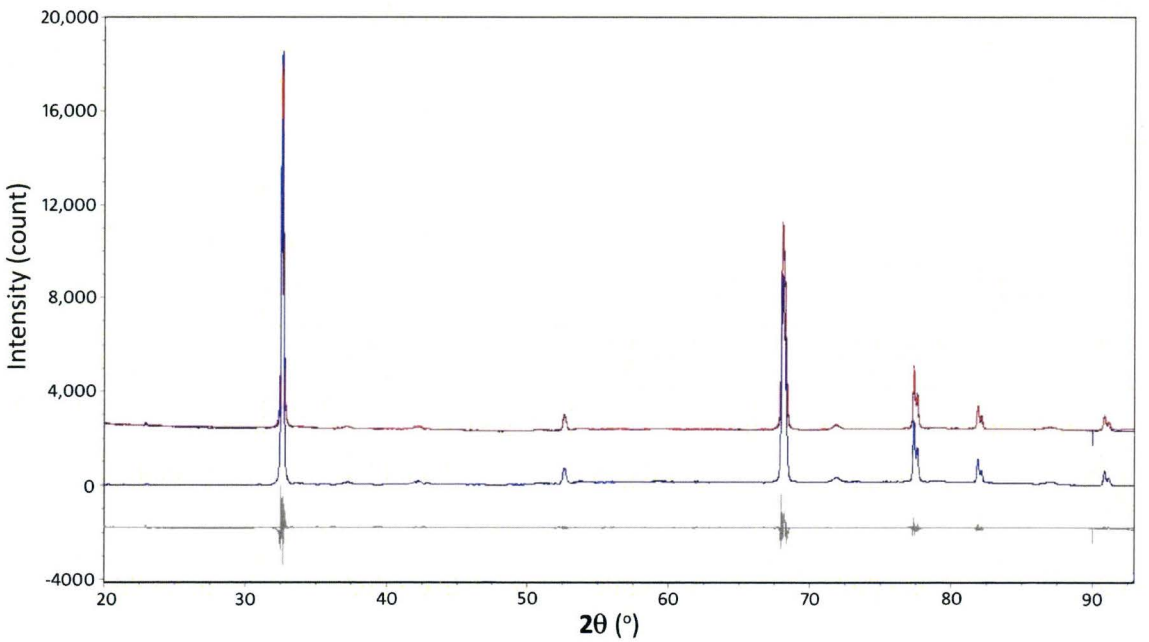

Figure 4.28: The I-2θ data of the BFCO 1/3 film on (111)-STO substrate acquired by XRD2 for lattice parameter determination. The black curve is the raw experimental data, the red and blue curves are the fits to the data, and the bottom black curve is the difference between experimental and fitted data.

$\beta = 90.3°$.

4.2.5 Simulated SAED Patterns and Atomic Projection

After obtaining the lattice parameters of BFCO 1/3 from XRD experiments by using *TOPAS* refinement, a cross-check can be performed by incorporating the refined lattice parameters into the JEMS software, to generate simulated SAED patterns that can be compared to the experimental ones. However, since information on lattice parameters alone is not sufficient to generate a simulated SAED pattern, the atomic positions within the unit cell should be estimated.

Previously in Section 4.2.3, the experimental ADF images did not show agreement with the atomic projection of the double perovskite structure. This disagreement indicates that the unit cell of BFCO 1/3 is not double perovskite as suggested earlier by Nechache, et al (2007). The next possible unit cell structure that can be used in describing the atomic configuration observed in the ADF images is the Ruddlesden-Popper (RP) unit cell, which is a layered perovskite unit cell with A_2BO_4 formula, where the adjacent perovskite is displaced by $^1/_2$ of the body diagonal along the <111> direction. Illustrations depicting the ideal perovskite structure and the RP layered perovskite structure are displayed in Figures 4.29(a) and (b), respectively.

The RP structure provides a good starting point for estimation of the atomic positions in the BFCO 1/3 unit cell. The unit cell adjustment was conducted by incorporating different occupancy for B-site cations, namely Fe and Cr, of 0.25 and 0.75, respectively. Afterwards, further addition of both Fe and Cr was incorporated into the unit cell so as to match the stoichiometry ratio between Fe/Cr and Bi. Then, the positions of Fe and Cr in the unit cell were shifted accordingly such that the atomic projection of the unit cell matched the structure observed in the experimental ADF image at both zone axes, as shown in Figures 4.30(a) and (b). Once these steps were accomplished, several SAED pattern simulations were carried out. The simulated SAED patterns that reproduce the experimental SAED patterns only in terms of the major reflections are shown in Figures 4.30(d) and (f).

Further verification was done by comparing the interplanar or d spacings from the

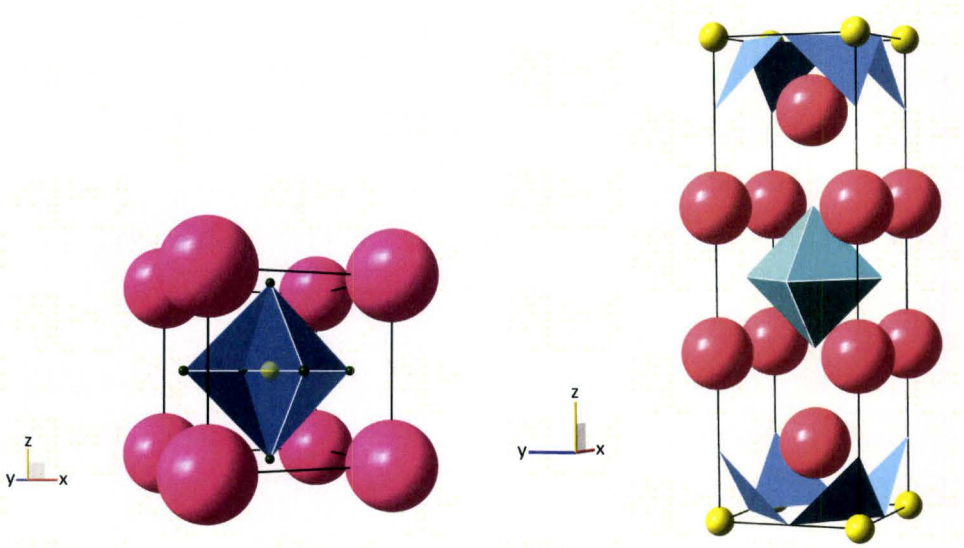

(a) (b)

Figure 4.29: Schematic illustrations of (a) the ideal perovskite and (b) the Ruddlesden-Popper layered perovskite structures.

simulated SAED patterns and those calculated from the experimental SAED patterns. As the camera length of the microscope was not accurately known, a correction factor (CF) is required to calculate the exact interplanar spacing from the experimental diffraction pattern. The CF is obtained from a calibration based on the well-known theoretical value of $SrTiO_3$ at a specific camera length. In this case, the CF for the 530 mm camera length is ~ 0.956.

The tabulated comparisons of d spacings at both ZA$<101>_{STO}$ || ZA$<122>_{BFCO\ 1/3}$ and ZA$<121>_{STO}$ || ZA$<121>_{BFCO\ 1/3}$ between experimental and simulated SAED patterns show an agreement in terms of only the major reflections, but not all reflections in the whole pattern. The lack of weak reflections in the simulated pattern was expected as the estimation of atomic position is not entirely accurate. In addition, the simulated pattern only takes into account the diffraction from the modified RP unit cell without the in-plane variation of unit cell orientations and the presence of twinnings, which are actually present in the BFCO 1/3 film. Nevertheless, the lattice parameters obtained from the XRD refinement give simulated SAED patterns, which reproduce only the major reflections in the experimental SAED patterns. Such limited agreement suggests that the lattice parameters obtained from XRD2 I-2θ ex-

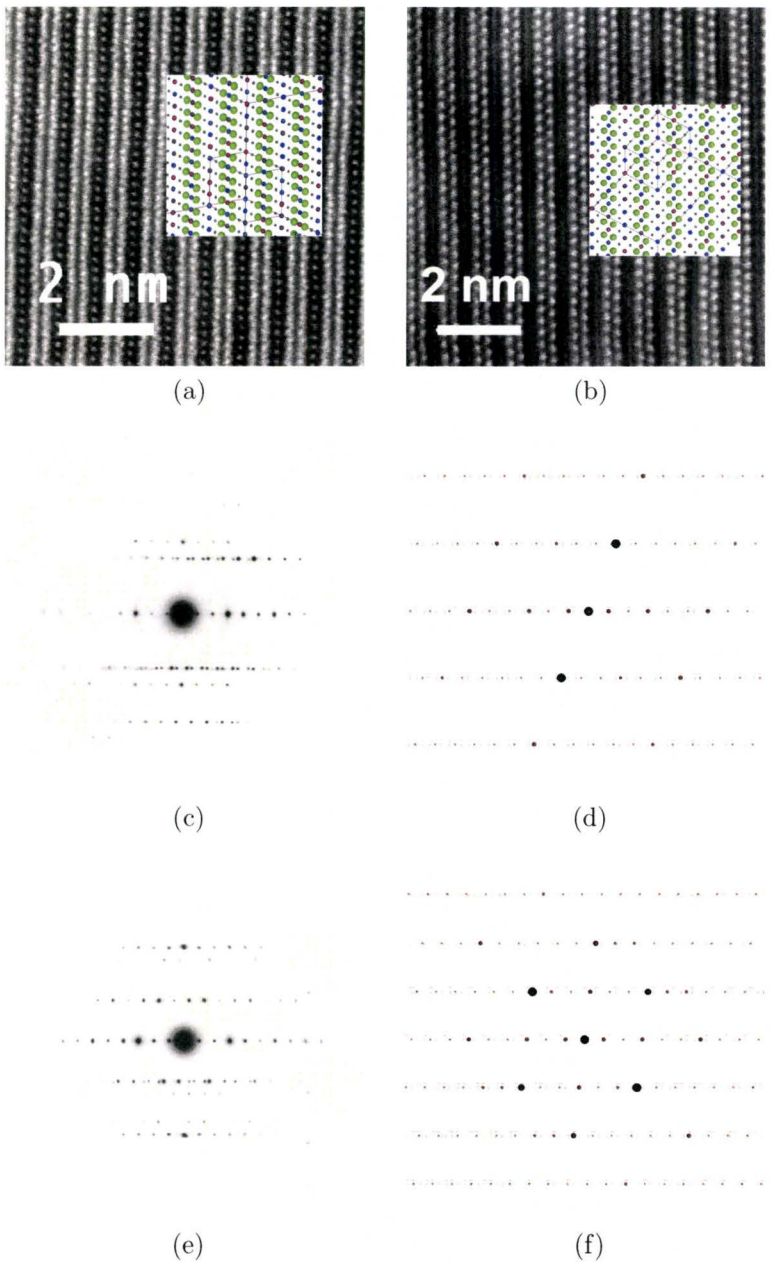

Figure 4.30: C_S-corrected HAADF images with insets of the atomic projection in the direction parallel to the ZA $<101>_{STO}$ or $<122>_{BFCO}$ and the ZA $<121>_{STO}$ or $<121>_{BFCO}$ are displayed in (a) and (b). Side-by-side comparisons between experimental and simulated SAED patterns are shown in (c-d) and (e-f) at the ZA $<101>_{STO}$ and the ZA $<121>_{STO}$, respectively. Note that the experimental and simulated SAED patterns are not at the same scale.

Table 4.10: List of reflections in the SAED pattern recorded with the sample oriented at the ZA<101>$_{STO}$ || ZA<122>$_{BFCO\ 1/3}$ monoclinic

$2R_{expt}$ (mm)	d_{expt}(nm)	d_{expt}*CF	d_{theo}(nm)	*hkl*	$\Delta d/d_{theo}$ (%)
horizontal					
3.7	0.95973	0.917502	0.90515	-101	1.36
7.3	0.486438	0.465035	0.45258	-202	2.75
11	0.322818	0.308614	0.30172	-303	2.28
vertical					
13.2	0.269015	0.257178	0.26255	4-1-1	-2.05
13.3	0.266992	0.255244	0.25973	-402	-1.73
14	0.253643	0.242482	0.24486	-420	-0.97
14.5	0.244897	0.234121	0.23816	41-3	-1.70

Table 4.11: List of reflections in the SAED pattern recorded with the sample oriented at the ZA<121>$_{STO}$ || ZA<121>$_{BFCO\ 1/3}$ monoclinic

$2R_{expt}$ (mm)	d_{expt}(nm)	d_{expt}*CF	d_{theo}(nm)	*hkl*	$\Delta d/d_{theo}$ (%)
horizontal					
3.7	0.95973	0.917502	0.90515	-101	1.36
7.3	0.486438	0.465035	0.45258	-202	2.75
11	0.322818	0.308614	0.30172	-303	2.28
vertical					
10	0.3551	0.339476	0.34672	22-2	-2.09
10.2	0.348137	0.332819	0.35806	-12-3	-7.05
11.7	0.303504	0.29015	0.29777	-32-1	-2.56
11.1	0.31991	0.305834	0.32071	02-4	-4.64

periments were in accordance to those observed from the electron diffraction, but the atomic positions based on the RP modification are not accurate. The unit cell of BFCO 1/3 can be summarized as a monoclinic unit cell (space group #14, P 2_1/n) with lattice parameters a= 10.9764 Å, b= 10.8479 Å, and c= 15.9073 Å, with $\alpha = \gamma = 90°$ and β= 90.3°.

In conclusion, even though the exact structure of BFCO 1/3 has not been determined experimentally, the atomic positions of a modified Ruddlesden-Popper layered perovskite unit cell provided a good starting point for estimating the atomic positions of BFCO 1/3. The agreement between the atomic projections of the estimated structure and the atomic structure in experimental HAADF images, at both $<121>_{\text{BFCO 1/3}}$ and $<122>_{\text{BFCO 1/3}}$ zone axes, suggests that the proposed estimated structure provides a good starting point for further determination or refinement of the atomic positions of BFCO 1/3. The estimated unit cell structure of BFCO 1/3 deviates from the double perovskite structure previously predicted but still maintains a monoclinic structure with lattice parameters twice of those of BFCO 1/1.

4.2.6 Elemental Distribution of BFCO 1/3 at Atomic Scale by EELS

In order to confirm the elements present along the dark (low intensity) band in between and inside the Bi double-layer, EELS linescans were performed perpendicular to the Bi double layer. The acquisition of EELS signal was carried out using probe corrected STEM with a 2.5 mm entrance aperture and acquisition time of 10 seconds per pixel at 300 kV. The length of the linescans was about 2 - 2.5 nm and were divided into 20 to 25 pixels. Atom-by-atom EELS acquisition was made possible due to the use of the probe corrector in our microscope, with which the angle of convergence can be widened up to 17 mrad thus allowing much higher current density and more EELS signal.

Throughout the acquisition period of the line scan, sample drift was relatively small and easily compensated by a cross-correlation algorithm that was performed every 10 spectra. The major challenge during the EELS acquisition was due to the presence of

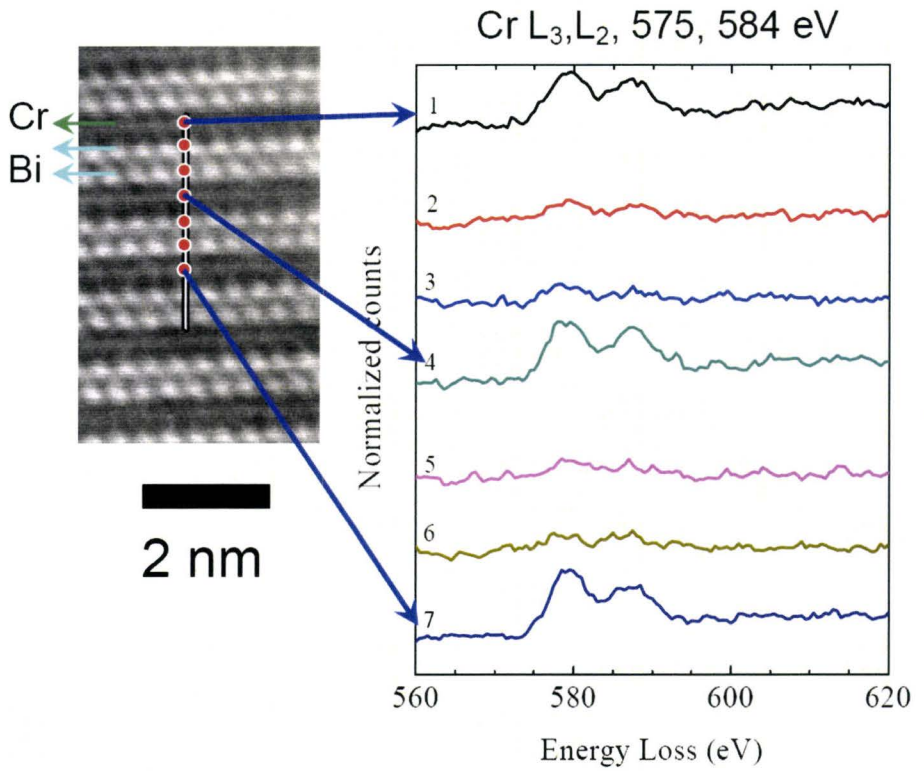

Figure 4.31: Cr L_3 and L_2 signals (575 eV, 584 eV) along EELS linescan were detected along the dark (low intensity signals) band in the ADF image, as pointed out by the arrows.

a strong variation in the background due to the Bi layers. One of the best optimized EELS linescans representing modulation of the Cr $L_{2,3}$ signals across the atomic layers is presented in Figure 4.31.

The Cr signals emerged solely from the dark band in between the bright Bi double-layers. However, there was no Cr signal detected from within a Bi-double layer. These results indicate that B-site cations are dominantly located in between the Bi-double layers, within the dark band regions.

Further, the results of EELS mapping experiments using the probe-corrected Titan are displayed in Figures 4.32(b-d), revealing the location of Fe and Cr within the sample. It is clear that the Cr signal (Figure 4.32(b)) is much stronger than the Fe signal (Figure 4.32(c)) in accordance to the 1:3 ratio of Fe:Cr in the sample. In addition, Fe and Cr signals are strongly concentrated in the dark band of the HAADF

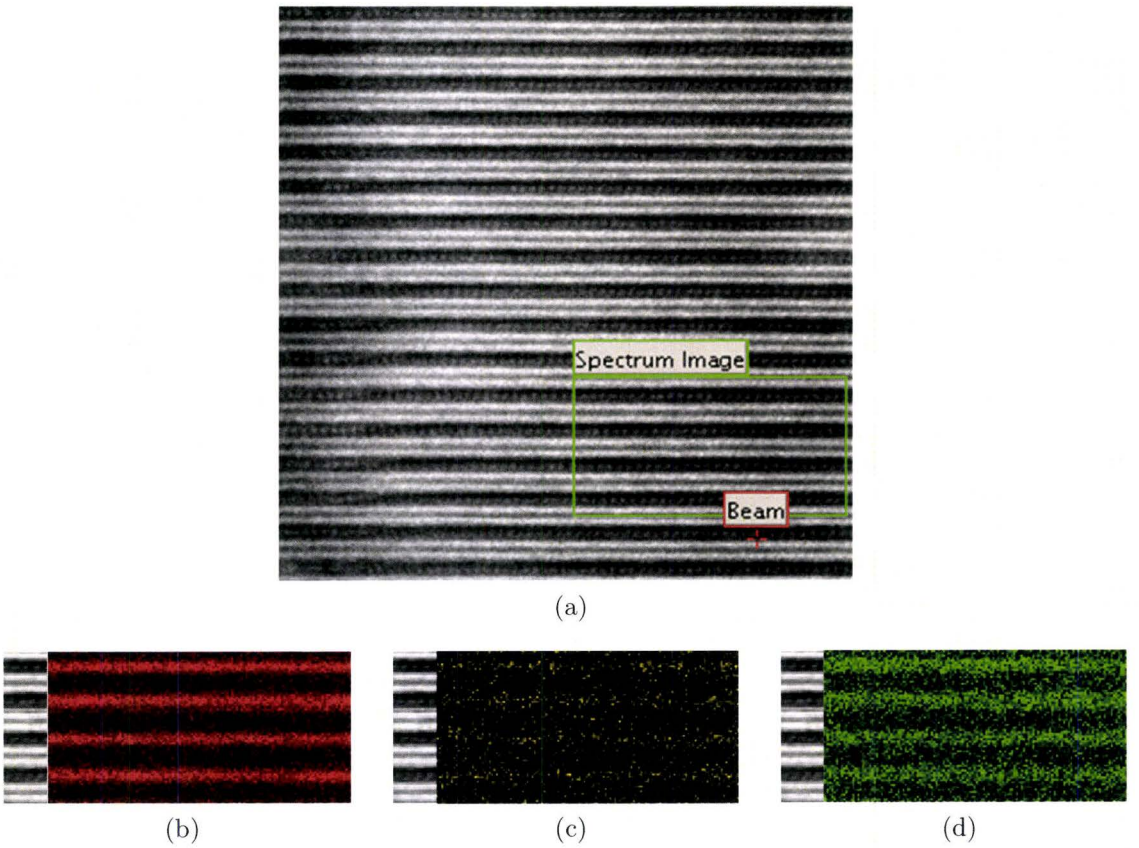

(a)

(b) (c) (d)

Figure 4.32: (a) HAADF image from which EELS spectrum image was acquired from BFC 48 sample is indicated by green rectangle. The overlap of HAADF image and extracted (b) Cr $L_{2,3}$ (575, 584 eV), (c) Fe $L_{2,3}$ (708, 721 eV) and (d) O K (532 eV) maps, respectively. The EELS spectrum image is 128 $\times$ 64 pixel with dwell time of 30 ms/pixel and frame time of $\sim$5 minutes. (*Courtesy of: Sorin Lazar, FEI Electron Optics, The Netherlands* and *McMaster University*)

image, in between the Bi double-layer. The weak Fe and Cr signals present within the Bi-double layer indicates that the Bi double-layer may also contain some amount of Fe and Cr. The increased signal of O (Figure 4.32(d)) along the dark band of the HAADF image shows that there is more oxygen in between the Bi double-layer than within the Bi double-layer itself.

Both EELS linescans and EELS maps reveal the locations of Fe and Cr atoms in the BFCO 1/3 sample. Such compositional information at atomic resolution is in agreement with the atomic projection simulated based on the modified RP model of BFCO 1/3. The atomic projections (Figures 4.30(a) and (b)) also indicate that

some Cr or Fe signals should be observed not only in between the Bi double-layer but also within the Bi-double layers. Despite the good agreement between the atomic projection and the HAADF images as well as the EELS maps, the exact atomic positions within BFCO 1/3 still need to be further refined to be able to completely simulate SAED patterns that reproduce the experimental SAED patterns.

If more samples of BFCO 1/3 with different orientations become available in the future, a more accurate determination of the atomic positions of the modified RP unit cell can be achieved by performing XRD and EELS experiments. Based on the HAADF images, another possible unit cell structure of BFCO 1/3 is the Aurivillius unit cell, $Bi_2(Fe/Cr)O_6$, which consists of alternating Bi_2O_2 and $Bi_{n-1}(Fe/Cr)_nO_{3n+1}$ layers with n=1. However, further modification of the structure will be necessary to compensate the discrepancy of stoichiometry between experimental $Bi_2(Fe_{0.5}/Cr_{1.5})O_6$ and the Aurivillius unit cell $Bi_2(Fe/Cr)O_6$.

4.3 $Bi_{4-x}La_xTi_3O_{12}$ (BLT)

After studying the possible charge and cationic ordering in BFCO 1/1 and demonstrating that combined BFO and BCO with a 1/3 ratio formed an unexpected structure in relation to their magnetic and ferroelectric properties, we focused our attention on the structural investigation in a closely related Bi-based oxide, $Bi_{4-x}La_xTi_3O_{12}$ (BLT). BLT, a Bi-based layered perovskite compound of similar interest to combined BFO/BCO, has many potential applications, but similar to the combined BFO/BCO compounds, there are several unexplained structural phenomena that are still not understood, as discussed in the literature review (Section 2.5.4). There has been a lot of debate in the literature in calculating and determining the exact location of La dopants in the parent $Bi_4Ti_3O_{12}$ (BiT) unit cell, mostly through refinement of X-ray diffraction and neutron powder diffraction data (Kim et al., 2007, 2008; Hervoches and Lightfoot, 2000; Hur et al., 2004). In addition, even though the mechanism of fatigue resistance in BLT has been associated with the location of La ions (Ding et al., 2001, 2001, b), it is still open as a subject of discussion. Both issues regarding the exact location of La ions and its effect on the fatigue resistance have not been fully understood. Thus, the objective of the structural investigations is to resolve this debate and contribute to the understanding of the mechanism of fatigue resistance. This work will require the use of aberration corrected TEMs for high-resolution imaging as well as the new capabilities of analytical TEM.

The focus of the experiments was to probe the atomic structure of BLT and provide insights on any related defects within the sample or across the film-substrate interface using HAADF imaging. Further, atom-by-atom EELS was used to probe the distribution of La ions in the BiT unit cell.

The epitaxial BLT films were grown by pulsed laser deposition in a single deposition run using a KrF excimer laser (λ = 248 nm) on (111)- and (100)-oriented $SrRuO_3$ (SRO) deposited on $SrTiO_3$ (STO) substrates (sample ID: BL 10 and BL 06, respectively) at 700 °C. Oxygen pressures were set to 300 and 100 mTorr for BLT and SRO layers, respectively. The deposition was performed by Olivier Gautreau in INRS - Énergie, Matériaux et Télécommunications, Varennes, Québec, and the details of the deposition process was reported by Gautreau et al. (2008). After deposition, the sam-

ples were cooled to 400 °C at a rate of 5 °C/ min in 1350 mTorr of oxygen, and then annealed for 1 hour at this temperature before being cooled to room temperature.

4.3.1 Compositional Analysis and Elemental Distribution by EDX

EDX compositional analysis of a BLT thin film on (111) STO was performed across the sample, as shown in Figure 4.33, with at least five different energy spectra acquired from different regions of the film. The quantitative analysis was done using Si Kα_1 as the ratio standard element with the estimated TEM sample thickness of $\sim$ 250 nm and sample density of $\sim$ 8.04 g/cm^3(Seth and Schulze, 1989). The thicker area was deliberately selected to improve the counting statistics. The unnormalized data (from spectrum 1 to spectrum 6) acquired from various locations within the BLT film, as shown in Figure 4.33, are presented in Table 4.12.

The thickness was estimated by calculating the atomic percentage of each elements in BLT from the EDX data with an increment of 50 nm, from 50 nm up to 400 nm. The TEM foil thickness, which showed the closest value to the stoichiometry, was $\sim$ 250 nm and was called the estimated thickness. In addition, spectrum 7 from the SRO buffer layer and spectrum 8 from the STO substrate were acquired to check the accuracy of the estimated thickness based on their stoichiometry and calculated separately from BLT, due to their different density. The calculated atomic percentage of STO with the thickness of $\sim$ 250 nm and density of $\sim$ 5.19 g/cm^3 demonstrated stoichiometric $SrTiO_3$. However, a similar calculation on SRO for the same thickness value showed a deviation from the stoichiometric value of $SrRuO_3$, and gave a composition of $SrTi_{0.4}Ru_{1.2}O_2$ instead. The stoichiometry deviation is due to the peak overlap between Ru Lα_1 (2.559 keV) and Bi Mα_1 (2.423 keV), that overestimates the atomic percentage of Ru. The Ti observed in the calculation was most likely contributed by the Ti from both the STO substrate and the top BLT layer.

Normalization of the spectra with respect to the Bi atomic concentration, with an assumed value of 3.25 according to the nominal stoichiometric value while excluding

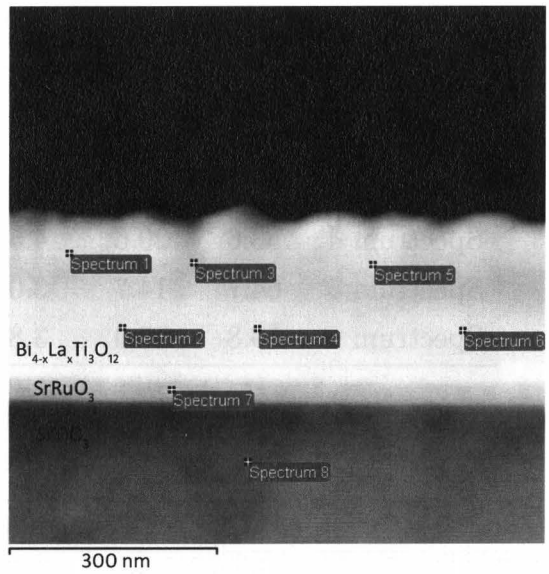

(a)

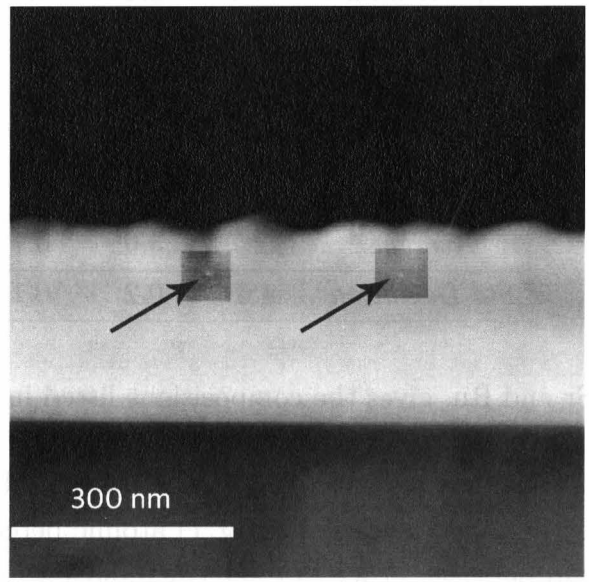

(b)

Figure 4.33: (a) The region from which EDX spectra were acquired and (b) the same region after the EDX spectra acquisition. Spectra 1-6 were taken from the BLT thin film (sample ID BL 10), spectrum 7 from the SRO buffer layer, and spectrum 8 from the STO substrate. The bright spots in the enhanced contrast area pointed out by the arrows in (b) indicate the beam damage that occurred during the acquisition.

Table 4.12: EDX data acquired from various different regions of the BLT thin film (in atomic percentage).

	O	**Ti**	**La**	**Bi**
Spectrum 1	75.4	10.6	2.6	11.4
Spectrum 2	64.5	16.2	3.8	15.5
Spectrum 3	62.4	16.3	3.1	18.2
Spectrum 4	53.6	20.6	4.5	21.3
Spectrum 5	64.7	14.7	3.0	17.6
Spectrum 6	59.8	17.3	3.8	19.1

Table 4.13: The normalized values based on the assumed stoichiometric Bi value of 3.25

	O	**Ti**	**La**	**Bi**
Spectrum 1	21.4	3.0	0.7	3.3
Spectrum 2	13.6	3.4	0.8	3.3
Spectrum 3	11.1	2.9	0.6	3.3
Spectrum 4	8.2	3.1	0.7	3.3
Spectrum 5	12.0	2.7	0.6	3.3
Spectrum 6	10.2	3.0	0.7	3.3
Average	12.7	3.0	0.7	3.3
Std Deviation	4.6	0.2	0.1	0.0

the values of Sr and Ru, gives the compositions listed in Table 4.13.

From the data presented in Table 4.12, it is clear that there is a significant standard deviation for Ti and O. The deviation of Ti atomic percentage may be attributed to the peak overlap between Ti Kα_1 (4.511 keV) and La Lα_1 (4.651 keV). The amount of La and Ti is less in spectrums 1, 3, and 5 (on the top part of the region) compared to the amount of the same elements in spectrums 2, 4, and 6 (near the film-substrate interface). Such a difference in composition is expected due to a slight thickness variation from the bottom to the top part of the film; the bottom part of the film being thicker. The thickness variation along the growth direction of the film was likely due to an artefact from ion milling during TEM sample preparation. Moreover, the

locations from which the spectra were acquired showed evidence of beam damage, as displayed in Figure 4.33(b). The beam damage may induce the loss of oxygen, which resulted in the underestimated atomic percentage of oxygen. Both the slight thickness variation and radiation beam damage contribute to the significant standard deviations in the normalized amount of the elements, especially oxygen, of the six spectra in Table 4.13.

Overall, the average composition of the BLT film, based on normalization to Bi, was $Bi_{3.3}La_{0.7}Ti_3O_{12.7}$ with an estimated sample thickness of the region of $\sim$ 250 nm and density of BLT = 8.04 g/cm^3 (Seth and Schulze, 1989). The La value was $\sim$ 0.1 less than the nominal La value of 0.75. In addition, the large standard deviation value for oxygen of $\sim$4 - 5 atomic percent, i.e., 40% of the amount of oxygen, was attributed due to beam damage and the slight thickness variation in the BLT film.

An ADF image and EDX elemental maps of the same sample but at a lower magnification are displayed in Figure 4.34. Even though there was a slight thickness variation, indicated by the ADF contrast variation from the bottom to the top of the film with a darker contrast on the top of the film, the EDX elemental maps of the BLT film demonstrated a relatively uniform elemental distribution throughout the sample. The oxygen maps shows a slightly higher concentration at the top of the film, but there is no elemental segregation observed in the other elemental maps. In brief, the average stoichiometry of cross-sectional BLT film was $Bi_{3.3}La_{0.7}Ti_3O_{12.7}$ without any evidence of localized segregation of the elements.

4.3.2 Structural Investigation in Atomic Scale

Two different BLT samples on two different substrate orientations, namely (001) and (110) STO, were investigated during the course of the study. The BLT film epitaxially grown on a SRO/(111)STO substrate by PLD showed uniform film thickness of $\sim$250 nm with columnar grains with a lateral width of 100-150 nm, as shown in Figure 4.35(a). The *a*- or *b*-axis of the BLT unit cell formed a 57° angle with the interface, indicating that the *c*-axis of BLT also formed a 57° angle to the normal direction, which is the (111) orientation of SRO and STO. This epitaxial relationship between

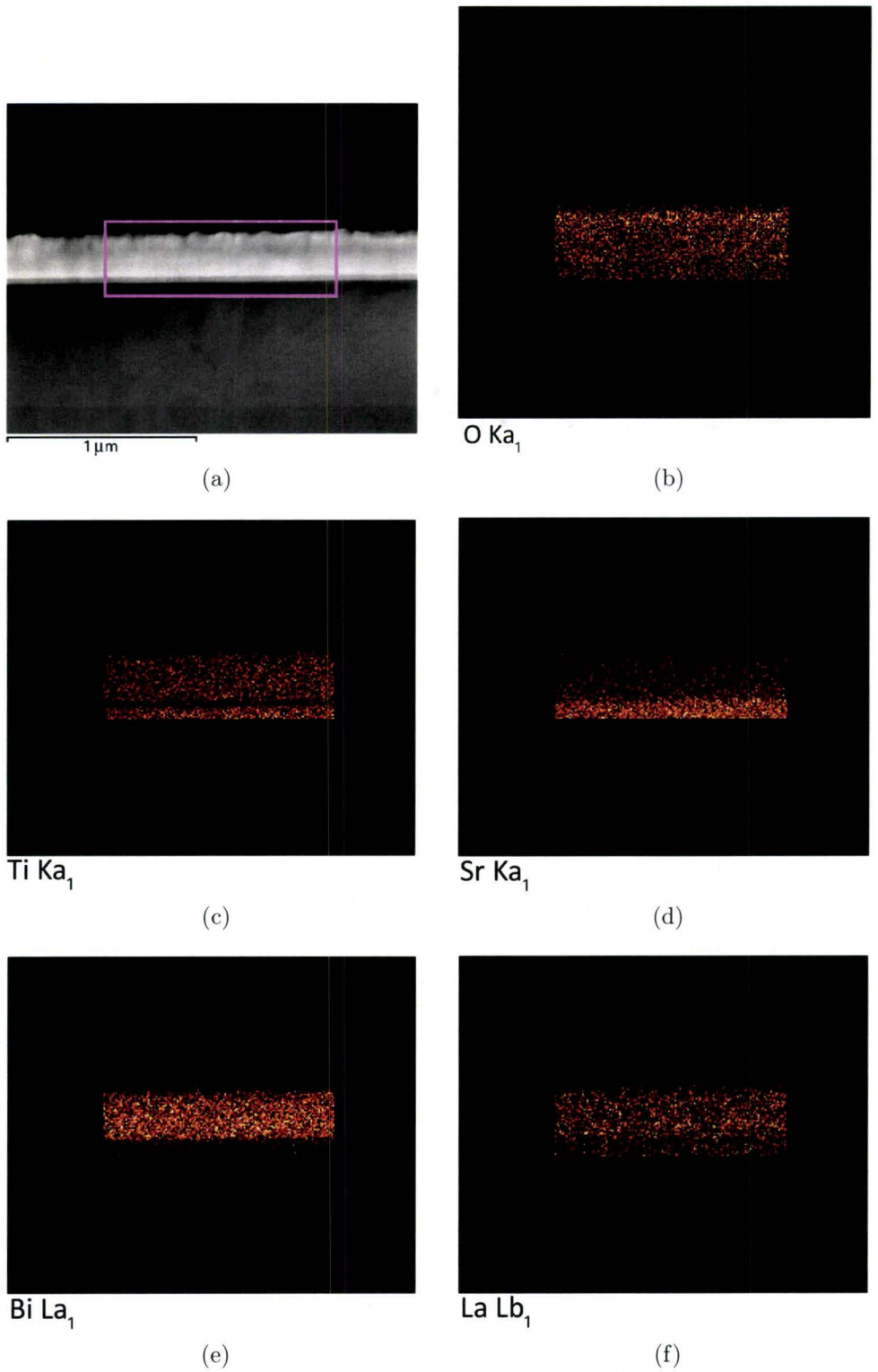

(a) (b) (c) (d) (e) (f)

Figure 4.34: (a) The ADF image of BLT (sample ID BL 10) shows the region from which EDX maps are generated. The EDX maps of O, Ti, Sr, Bi and La are shown in (b) to (f), respectively.

BLT and STO is also consistent with the overlap of the SAED patterns of the BLT film (Figure 4.36(a)) and the STO substrate (Figure 4.36(b)). Therefore it can be deduced that the epitaxial relationship is $(104)_{BLT}$ || $(111)_{SRO}$ || $(111)_{STO}$.

Meanwhile the BLT film grown on the (100) STO substrate (Figure 4.35(b)) displayed a c-axis normal to the interface and parallel to the growth direction, with a thickness of $\sim$ 250 nm. The epitaxial relationship for this film was $(001)_{BLT}$ || $(001)_{SRO}$|| $(001)_{STO}$. The top surface of the BLT film on (100) STO was relatively flat in comparison to the surface of BLT film grown on (111) STO, which shows a faceted triangular shape. In contrast, the BLT film grown on (100) STO shows no presence of a columnar structure, which was clearly formed in the BLT film on (111) STO.

The epitaxial relationships of both BLT films on STO (111) and STO (001) were also confirmed by the XRD θ-2θ scans presented in Figures 4.37(a) and (b), respectively. In Figure 4.37(a), the I-2θ spectrum shows the peaks corresponding to the STO (111) and (222) planes as well as the BLT (104) plane. In addition, the peaks marked with # and $*$ are also observed, corresponding to the STO (111) planes generated from Cu-Kβ and W-Lα. The spectrum in Figure 4.37(a) confirms that the BLT film on (111) STO substrate demonstrated the (104) preferrential orientation in the out-of-plane direction. Meanwhile, in Figure 4.37(b), the BLT film shows peaks corresponding to $(00l)$ planes (with l= 8, 10, 12, 14, ...), which indicate that the preferrential orientation of the BLT film on (001) STO substrate is along its c-axis in the out-of-plane direction.

A higher magnification HAADF image acquired with probe corrected STEM exposes a structure consisting of the $Bi_2Ti_3O_{10}$ triple perovskite-like layers alternated with a double-layer of Bi_2O_2, as indicated in the Figure 4.38. In addition, the position and configuration of Bi, Ti and O atoms in the experimental ADF image of BLT are in agreement with the theoretical model of the BLT unit cell proposed by Kim, et al. (2005). The simulated HAADF image based on the theoretical model is displayed as the inset marked with a red rectangle in Figure 4.38. The agreement between the experimental image and the simulated one is very good.

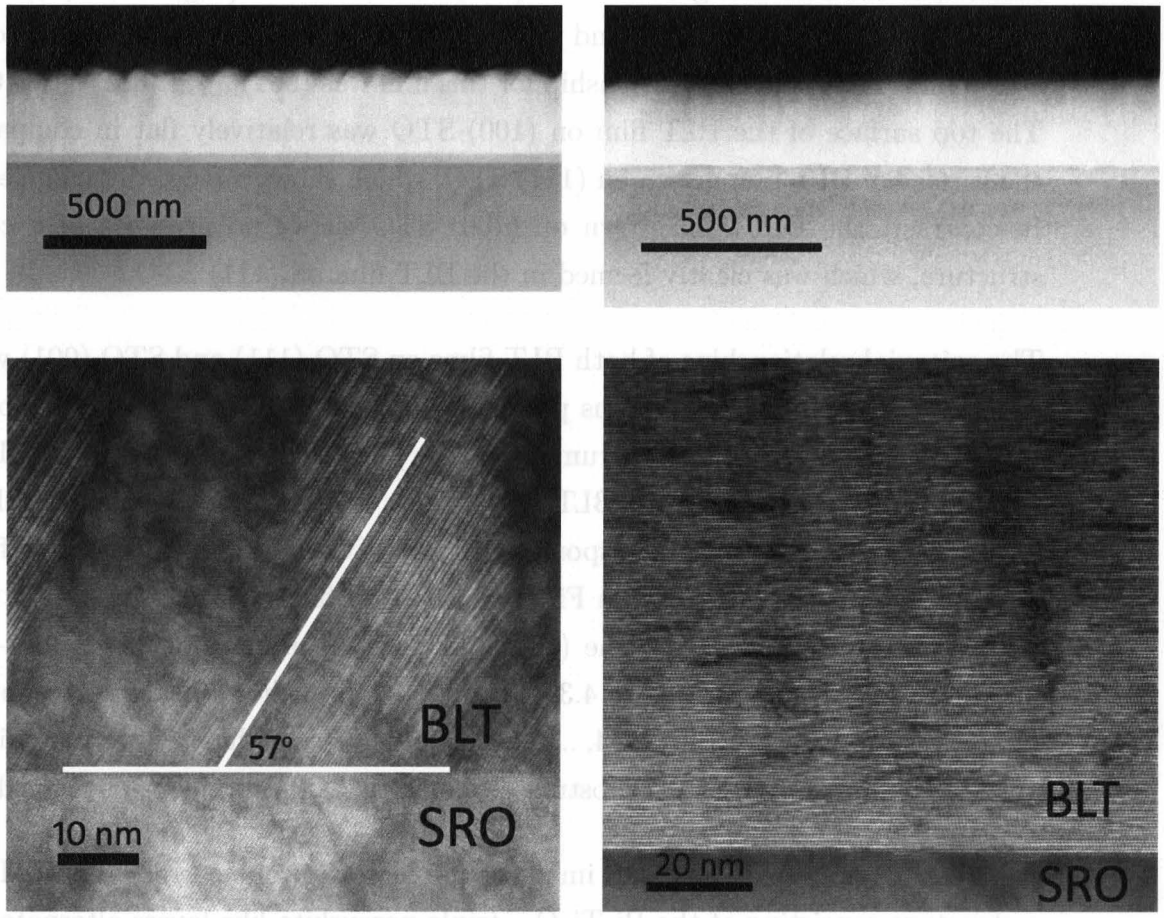

(a) (b)

Figure 4.35: Low angle ADF images (acquired without probe corrector) of ~250 nm thick BLT film epitaxially grown on (a) SRO/(111) STO in a direction parallel to the zone axis (ZA) $<110>_{STO}$ and (b) SRO/(100) STO in a direction parallel to the zone axis $<100>_{STO}$. The BLT film on (111) STO was grown with the *a*-axis forming a 57° angle to the interface, while the BLT film on (100) STO was grown with the *c*-axis normal to the interface.

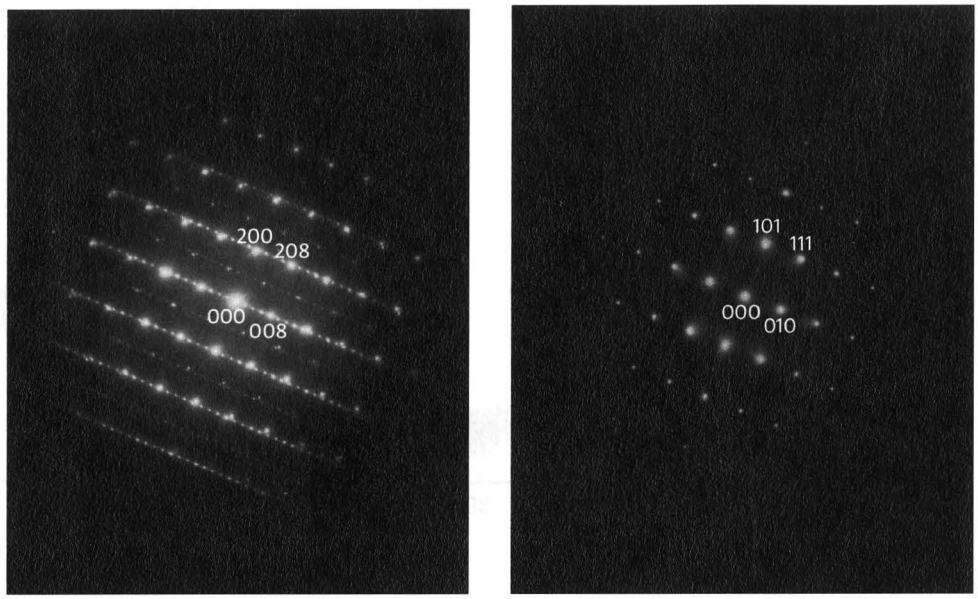

(a) (b)

Figure 4.36: SAED patterns of (a) the BLT film and (b) the STO substrate.

4.3.2.1 Presence of Out-of-Phase Boundary and Structural Modulation

Both the atomic resolution ADF images of BLT on (111)-STO shown in Figures 4.39(a) and (b) were acquired without using the probe corrector. Figure 4.39(a) reveals the presence of out-of-phase boundaries (OPB), as highlighted by the dashed red rectangle. These defects are considered to be misregistry or translational shift by a fraction of a unit cell parameter along the *c*-axis of the BLT unit cell. Previously reported by Chu, et al. (2002), the misregistry between adjacent unit cells in BLT polycrystalline powders was referred as intergrowth defects and only observed at the edge of the crystal, exhibiting a rock-salt-like structure instead of a fluorite-like structure. Chu, et al. also stated that such defects are only observed in BLT but not in BiT, which may be related to La ions substituting Bi ions in the Bi_2O_2 layer. Similar translational defects have been reported and claimed to be commonly found in epitaxial complex oxide films, such as Ruddlesden-Popper phases and Aurivillius phases (Zurbuchen et al., 2007). These defects are usually attributed to the limited structural arrangement during growth and constraints from the underlying substrate.

The presence of OPBs may have an influential impact on fatigue behaviour since

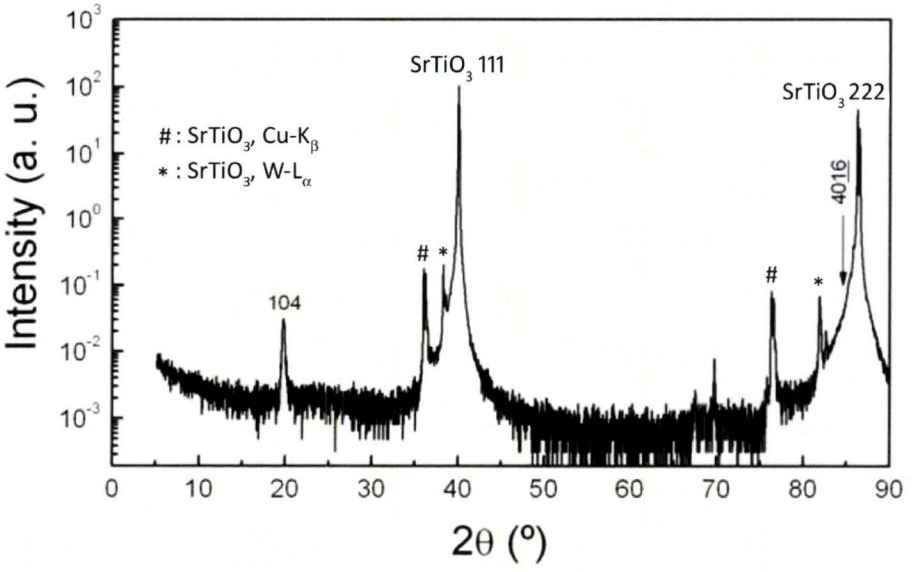

(a)

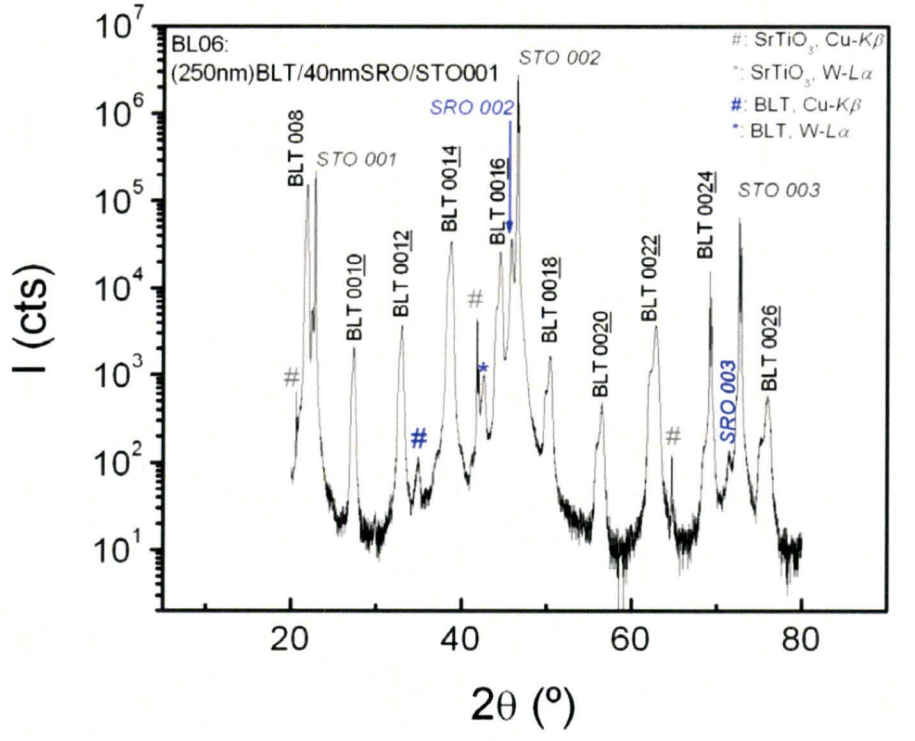

(b)

Figure 4.37: XRD θ-2θ scan of BLT films on (a) (111) $SrRuO_3/SrTiO_3$ substrate and (b) (001) $SrRuO_3/SrTiO_3$. The spectra show non-ideal peaks generated from the Cu-Kβ and W-Lα sources. (*Courtesy of: Olivier Gautreau*)

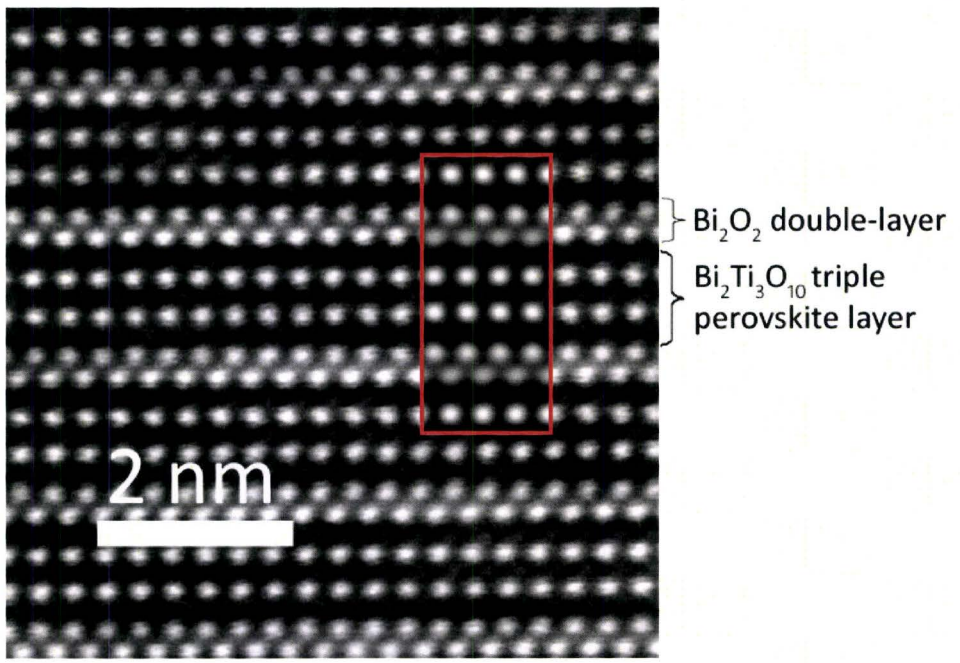

Figure 4.38: An atomic resolution HAADF image of BLT on (001)STO acquired using the probe corrector is displayed. The inset marked with a red rectangle is the simulated HAADF image of the BLT film parallel to the zone axis $<110>_{BLT}$ with the space group of *B1a1*, following the unit cell structure and atomic coordinates from the neutron diffraction refinement (Kim et al., 2005). The parameters used for the simulation were acceleration voltage of 300 kV, C_S value of 0.002 mm, condenser aperture of 5 mrad, sample thickness of 40 nm, defocus of 0 nm (at the top of the sample), and inner-outer detector angle of 45-113 mrad. (*The simulated HAADF image is courtesy of Yang Shao*)

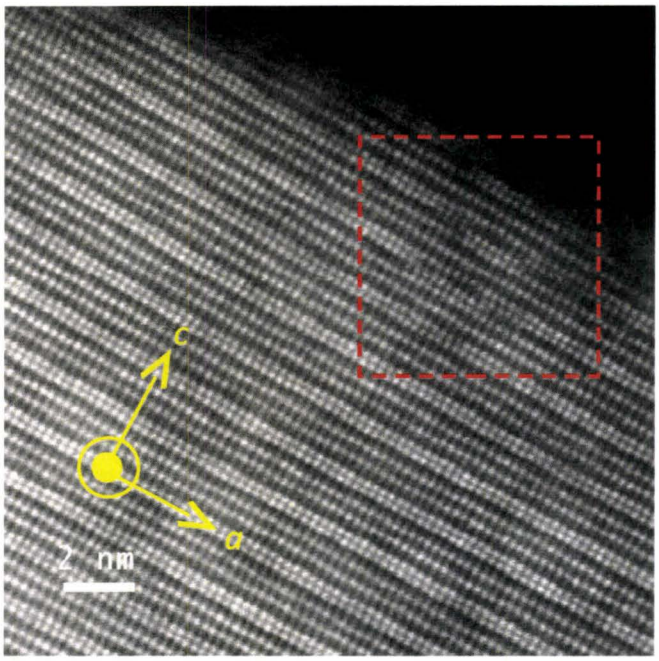

(a)

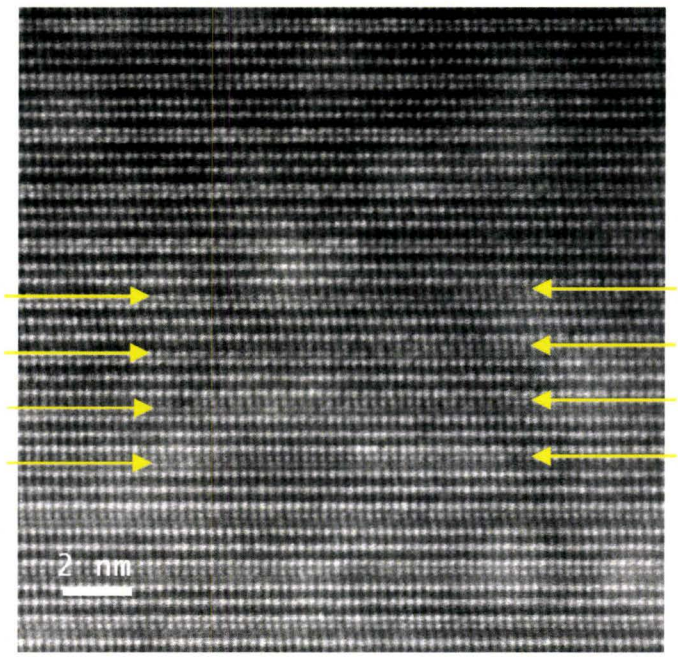

(b)

Figure 4.39: (a) A non-probe corrected atomic resolution ADF image of the BLT film, recorded with the sample oriented at the ZA $<010>_{BLT}$, shows translational defects highlighted inside the dashed red square. (b) Another type of defect, showing vanishing and appearing rows pointed out by yellow arrows, are located between the Bi_2O_2 layer and the perovskite-like layer, at the region of the film closer to the substrate.

anti-phase boundaries (APBs) have previously been associated with a new domain-switching mechanism, which resulted in the improvement of fatigue resistance of BLT in comparison to BiT. Previous studies by Ding, et al. (2001) demonstrated that APBs, which are OPBs with translational shift of one half of a unit cell, only appeared in BLT, yet not in BiT, consistent with the observation reported by Chu, et al. (2002). Such APBs have been suggested to be responsible in contributing to improved fatigue resistance of BLT by providing extra nucleation sites for ferroelectric domains during polarization reversals. Hence, the nucleation of domains can occur not only at the electrode/ferroelectric interface but also at the APBs (Ding et al., 2001). Even if nucleation at the electrode/ferroelectric interface is suppressed, the domain switching process will not be inhibited due to the presence of APBs, resulting in a negligible decrease in remanent polarization up to 10^{10} read/write cycle.

The importance of OPBs may be related to that of APBs. Ding, et al. (2001) have proposed the role of APBs, which present in SBT but not in PZT, as illustrated in Figure 4.40. The presence of APBs helps for easier nucleation of ferroelectric domains during polarization reversals. In PZT, which contains no APBs, domain nucleation during switching occurs only at the film-electrode interface (Figure 4.40(a-d)). In contrast, in SBT containing APBs, the nucleation of new domains during switching takes place both at the film-electrode interface and at the APBs (Figure 4.40(e-h)).

Fatigue in ferroelectrics is commonly associated with domain pinning due to the presence of oxygen vacancies generated because of the volatility of Bi-ions. In the case of BLT, the extent of oxygen vacancy formation due to Bi volatility is reduced by the substitution of La dopants, so that less oxygen vacancies are present in BLT in comparison to BiT. However, since La ions only partially subtitute for the Bi ions, some oxygen vacancies are still likely to form and concentrate at the electrode-film interface, inhibiting the nucleation of new opposite domains during polarization reversals. The presence of OPBs or APBs in BLT, acting as nucleation sites for new domains during polarization reversals, helps the polarization reversals to proceed despite the presence of oxygen vacancies concentrated at the electrode-film interface (Ding, et al.2001, 2001, b, Chu, et al. 2002). Therefore, even though the film-electrode interface may get saturated with oxygen vacancies preventing domain reversals, domain nucleation can still proceed at the APBs. Following this argument, the presence of

APBs, as well as OPBs, improves the fatigue resistance of BLT films.

Another type of defect present in the BLT film grown on (111)-STO is observed in the non-probe corrected ADF image recorded with the sample oriented at the ZA$<010>_{BLT}$, as shown in Figure 4.39(b). The defects are observed at the region of the film closer to the substrate and are indicated by yellow arrows. The yellow arrows on the left indicate the vanishing rows of Bi_2O_2 layer. On top of the vanishing rows, extra rows of atoms appear as highlighted by the yellow arrows on the right side. These regions, where some BLT unit cells may overlap with other unit cells experiencing a translational shift along the c-axis direction, are defined as *"defected"* regions. Such defects were also observed, even more clearly, in BLT films grown on (100)-STO, as shown in Figure 4.41(a), which was acquired with the sample oriented with the ZA $<100>_{BLT}$. The alternating defect-free and defected regions appear as a structural modulation along the lateral direction, parallel to the interface with a spatial wavelength of about 5-6 nm near the interface area and diminishes with increasing film thickness.

In order to more clearly see the modulation, a numerical Fast Fourier Transform filtering method was applied to the original ADF image. One of the major reflections in the FFT pertaining to $c/3$ was then masked so that only the periodic spacing pertaining to that specific reflection was present. Finally, the masked FFT was inverted back into an image as shown in Figure 4.41(b), which clearly displays the structural modulation.

The cause of the structural modulation in BLT is not obvious. However, the variation of contrast at the BLT/SRO interface as observed in Figure 4.41(a) suggests a correlation between the formation of a defect-free or defected region and the first atomic layer of deposited on the SRO surface. An earlier investigation on BiT thin film growth on STO by Pan, et al. (2003) revealed that the growth always starts with the central TiO_2 layer in the middle of the triple perovskite block, which is shared by both the BiT film and STO substrate. Further, they also described that an atomic step of one unit cell height on the TiO_2-terminated STO surface will induce the presence of out-of-phase boundaries, assuming that the growth sequence of BiT is the same on both sides of the step. Even though the presence of OPBs in BiT is contradictory to what has been reported by Chu, et al. (2002) and Ding, et al.

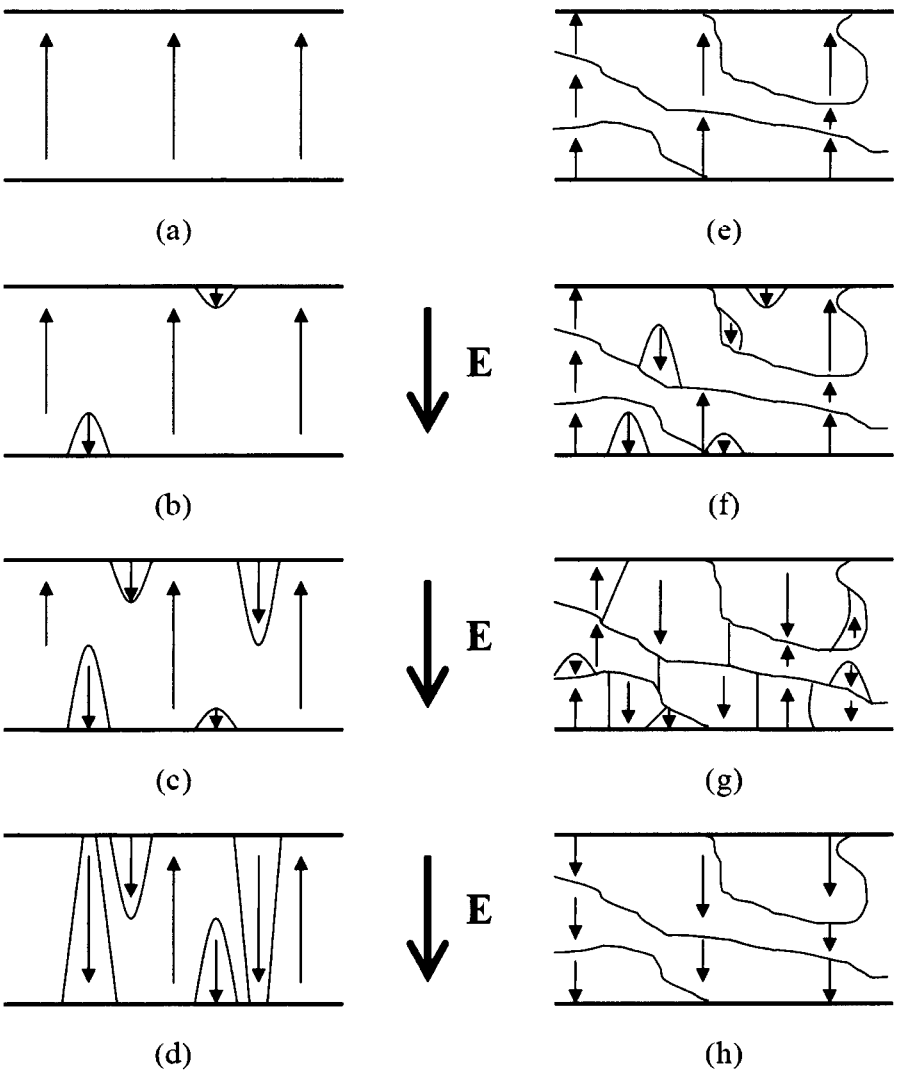

Figure 4.40: Schematic illustrations of polarization reversals (switching) in PZT (a-d) and SBT (e-h). The APBs, which only exist in SBT and are depicted as irregular curves in (e-h), help in the nucelation of new domains during switching. The arrows indicate the direction of polarization in each ferroelectric domain. The bold arrows and letter Es indicate the direction of the electric field. (adapted from Ding et al., 2001)

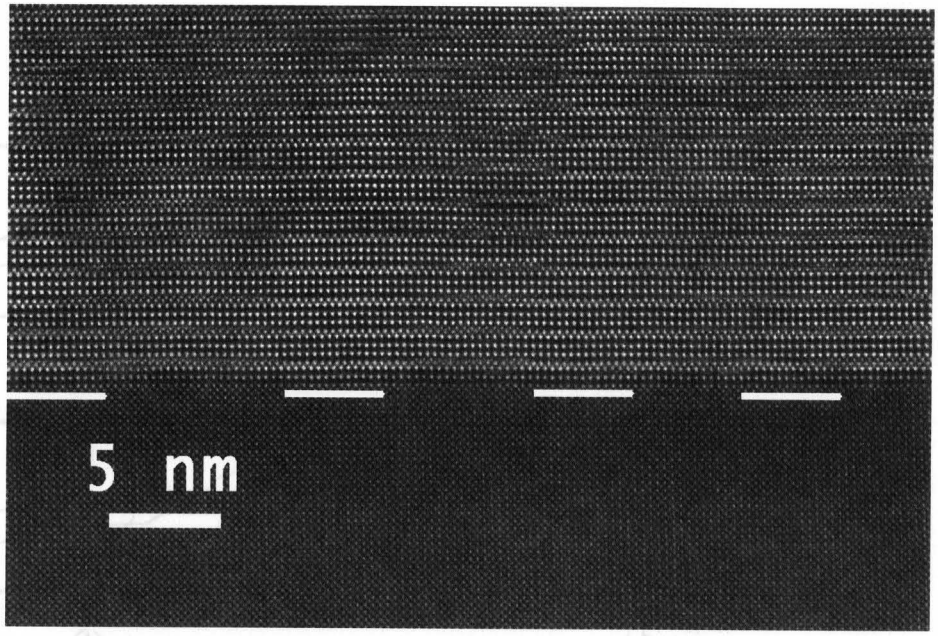

(a)

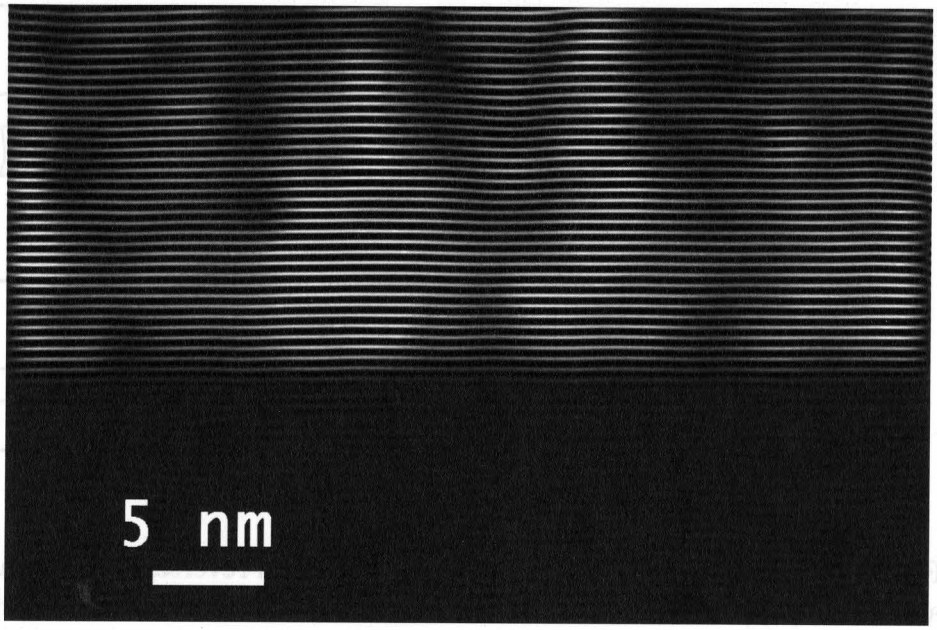

(b)

Figure 4.41: (a) A probe-corrected atomic resolution HAADF image of BLT film grown on (100)-STO substrate recorded in a direction parallel to the ZA $<110>_{BLT}$ shows a modulation of ideal and defected regions along the lateral direction. The white lines indicate the approximate width of the defect-free atomic layers located at the SRO/BLT interface. (b) A numerically filtered image of (a) enhances the specific periodicity of $c/3$ in the BLT unit cell and clearly shows the structural modulation, represented as bright and dark patches, along the lateral direction.

(2001), it is clear that the first atomic layer grown on specific surface-terminated substrates governs the stacking configuration of the thin film growth. Thus, in order to understand the formation of defect-free and defected regions in BLT, it is important to study the preferred nucleation layer or the first atomic layer of BLT deposited on the SRO buffer layer as well as the surface termination layer of SRO.

When the first layer of atoms shows bright contrast (underlined with white lines in Figure 4.41(a)), the subsequent atomic layers configure as defect-free unit cells. This observation is even more clearly demonstrated in Figure 4.42(b), where bright layers at the interface induce the formation of defect-free unit cells. In contrast, the region above the first layer with dark contrast (the non-underlined layer in Figure 4.41(a)) forms defected unit cells. The numerically filtered HAADF image (Figure 4.41 (b)) showed the alternating bright and dark patches in the BLT film, representing the alternating region of defect-free and defected unit cells, respectively.

The atomic structure of the defect-free region located at the top part of the film away from the film-substrate interface (Figure 4.42(a)) shows the presence of a herringbone pattern of intensity tails of Bi ions within the perovskite layers, which is indicated by white arrows in the shadowed region. The simulation of a BLT unit cell based on the atomic positions obtained from the refinement of neutron diffraction experiments reported by Kim, et al. (2005), as shown previously as the inset in Figure 4.38, demonstrates a very good agreement with the experimental HAADF image. It suggests that the structure of the BLT unit cell from the neutron diffraction refinement is correct. The observed intensity trails are not originated from the Bi ions, but instead they appeared due to the presence of Ti ions. The intensity tails in the experimental image due to the presence of Ti confirms the presence of TiO_6 octahedral tilting in the BLT film. The fact that the intensity tails are not faithfully pointing in the same direction in every perovskite layer confirms that the intensity tails were not artefacts generated during scanning acquisition, but really are characteristic of the sample. The evidence of octahedral tilting in BLT unit cell is in agreement with what has been previously reported and responsible for the relatively large value of remanent polarization of BLT (Park et al., 1999). Another HAADF image at the BLT-SRO interface (Figure 4.42(b)) demonstrates that the first atomic layer determines the stacking configuration along the growth direction. The boundary between

defect-free and defected regions is shown with a vertical yellow line.

Further analysis of the interface was focused at the region between defected and defect-free regions. The corresponding distribution of HAADF intensity signals of the first atomic layer at the interface, marked by a blue rectangle in Figure 4.42(a), is shown in Figure 4.42(c). The HAADF intensity signals are proportional to the scattering probabilities depending on the atomic number (Z) of element. The distribution of intensity signals indicates that the layer of atoms with lower HAADF intensity (dark contrast) is subsequently followed with the defected unit cells. In contrast, the higher HAADF intensity (bright contrast) atomic layer is followed with the defect-free unit cells. The lower HAADF intensity at the interface may be attributed to the La atoms (Z=57) substituting for Bi atoms (Z= 83) in the BLT layer or the overlapping of La on Bi along the beam direction, as illustrated in Figure 4.43. Since the difference of atomic number between Sr and Ru is relatively small (Z_{Sr}= 38; Z_{Ru}= 44), the HAADF intensity of Sr and Ru will be relatively similar, as shown in the substrate region. Therefore, it will be quite unlikely to distinguish Sr from Ru based on the observation of HAADF intensity. The significant variation of HAADF intensity at the interface (Figure 4.42(c)) is likely to be caused by the presence of either La or Bi, composing the first atomic layer grown on SRO layer, which is governed by surface-termination of SRO substrate.

The differences in the first atomic layer can arise from two different surface terminations of the SRO substrate, namely SrO-terminated or RuO_2-terminated. Since Sr occupies the A-site in the perovskite unit cell, while Ru occupies the B-site (the octahedra), the SrO-terminated surface will be subsequently followed by a B-site cation, which is Ti in TiO_2 in the next layer. However, if the substrate is RuO_2-terminated, it is likely that the next deposited atomic layer will consist of A-site cation, which is Bi or La in this case.

Based on two different surface terminations of the SRO substrate, there are two possible stacking sequences of the BLT unit cells. The first possibility is the SrO-terminated SRO surface followed by TiO_2 layer as the first deposited atomic layer. The formation of the TiO_2 layer, which lies in the middle of the triple perovskite-like block of the BiT parent unit cell, as the first deposited atomic layer is energetically favorable, as has been reported for BiT thin films grown on STO substrate by Pan, et

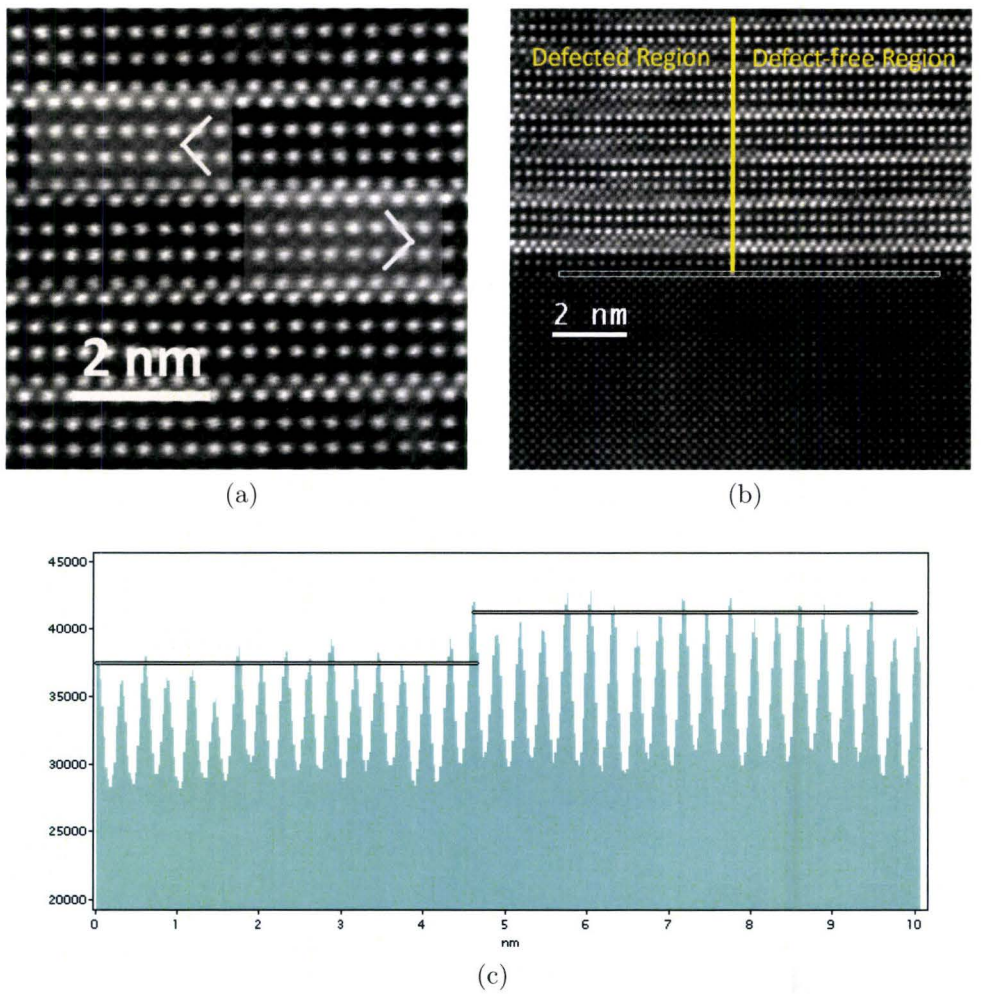

(a) (b)

(c)

Figure 4.42: A probe-corrected HAADF image of BLT on (100) SRO/STO recorded with the sample oriented at the ZA $<110>_{BLT}$ shows (a) a defect-free region at the top part of the sample and (b) alternating defect-free and defected regions along the BLT/SRO interface separated by a yellow vertical line. The shadowed areas in (a) indicate herringbone pattern intensity trails, which appear due to the position of Ti ions in the BLT unit cells. These patterns confirm the presence of octahedral tilting in the BLT unit cell. (c) The distribution of the intensity signal in the HAADF image along the first layer of atoms in the region identified by a blue rectangle in (b). Since HAADF intensity represents the contrast related to the atomic number (Z) of element, the higher signal intensity indicate the presence of higher Z elements, and vice versa.

al. (2003). Such stacking will form a defect-free region on the SrO-terminated surface. The second case is the RuO_2-terminated SRO surface, which can be followed by either a BiO or LaO layer. The variation of HAADF intensity over the interface (Figure 4.42(c)), which is likely to be originated from the difference of Z between La and Bi, indicates that the first layer with lower HAADF intensity is always followed with a defected region, and the first layer with higher HAADF intensity is followed with a defect-free region. This suggests that if the BiO layer forms after RuO_2-terminated surface, the stacking will form a defect-free region. But, if the LaO layer forms after RuO_2-terminated surface, the following stacking will form a defected region. These arguments, however, are lacking in terms of the mechanism on how La layers generate defected regions and Bi layers generate defect-free regions. So far, there has not been any report regarding the favourable energy state on the formation of either the defect-free or the defected BLT unit cells. In the future, calculations of the energy of formation of the BLT unit cell with different first atomic layer on different surface termination as mentioned above will be useful to further understand the mechanisms.

Besides the surface termination of the substrate, the formation of defect-free and defected regions in the BLT film may also be influenced by the OPBs. Both ADF images recorded with the sample oriented at the ZA$<010>_{BLT}$ (Figure 4.39(a)) and at the ZA$<110>_{BLT}$ (Figure 4.42(b)) show that the OPBs are present in both *a*- and *b*-axes direction of the BLT unit cell. Therefore, the OPBs can be regarded as two-dimensional defects in the lateral direction parallel to the film-substrate interface. The presence of two-dimensional defects in Bi-based layered perovskites have been reported on $Ba_2Bi_4Ti_5O_{18}$ in the form of the rectangular-shaped grain boundaries (Hesse et al., 2000), and on $Sr_4Bi_4Ti_7O_{24}$ in the form of spiral-shaped boundaries(Zurbuchen et al., 2007). Along the beam direction, at which the ADF images were recorded, the defect-free unit cells are not uniformly present throughout the thickness of the TEM foil. There are regions where some defect-free unit cells may overlap with other cells, which undergo a translational shift along the *c*-axis direction, and form the so-called *"defected"* region. In this case, the OPBs lie normal to the film-substrate interface but perpendicular to the beam direction, which makes the OPBs invisible along the viewing direction. Due to the two-dimensional nature of OPBs, the overlapping unit cells will not be uniformly present in the direction parallel to the film-substrate interface, but instead they will alternate with the original or non-overlapping unit cells.

These alternating regions are the reasons why extra atomic rows appear and vanish in Figure 4.39(b), and why modulation between ideal regions and defected regions appear in Figure 4.41(a).

An illustration representing a translational shift by a fraction of the c lattice parameter ($c/8$) along the beam or viewing direction is depicted in Figure 4.43. The illustration also shows an OPB perpendicular to the beam direction. In the beam direction, or the viewing direction, the overlap of the two unit cell configurations gives a similar structure to that observed in Figure 4.39(b). The translational shift between the two regions is likely to be influenced by the first atomic layer deposited during the growth process. Note that Bi ions in the BLT unit cell can be classified into two types, namely Bi_1 and Bi_2, located in the perovskite-like layer and the Bi_2O_2 layer of BLT unit cell, respectively. On one hand, if the first deposited layer consists of La ions, which readily substitute for Bi ions in the Bi_2O_2 layer (as demonstrated in the EELS mapping experiment discussed later in Subsection 4.3.2.2), the configuration of the unit cell starts with Bi_2 type followed by triple perovskite-like layers. On the other hand, if the first layer starts with Bi ions, the unit cell configuration starts with Bi_1 type followed by double perovskite-like layers.

Referring back to the RuO_2-terminated SRO surface, there are two possible layers as the first atomic layer deposited at the film-substrate interface, i.e., BiO layer or LaO layer. Taking the BiO layer as the first atomic layer, the BLT stacking will follow the configuration depicted at the right-side of Figure 4.43. The second possibility, starting with LaO as the first atomic layer, the BLT stacking will follow the left-side configuration in Figure 4.43. Considering that the surface termination is not necessarily uniform over the two dimensions of the SRO substrate, it is likely that the left-side and the right-side BLT configurations may overlap along the beam direction. The region consisting of the overlap of the two configurations appears as the defected region, whose first atomic layer showed lower HAADF intensity signals due to the presence of La substituting Bi_2 ions in the first atomic layer. Meanwhile the defect-free configuration always starts with Bi_1 ions as the first atomic layer, which show higher HAADF intensity signals compared to La ions.

Based on the explanation above, the presence of defected and defect-free regions in the BLT film is mainly influenced by (i) the surface termination of the SRO substrate,

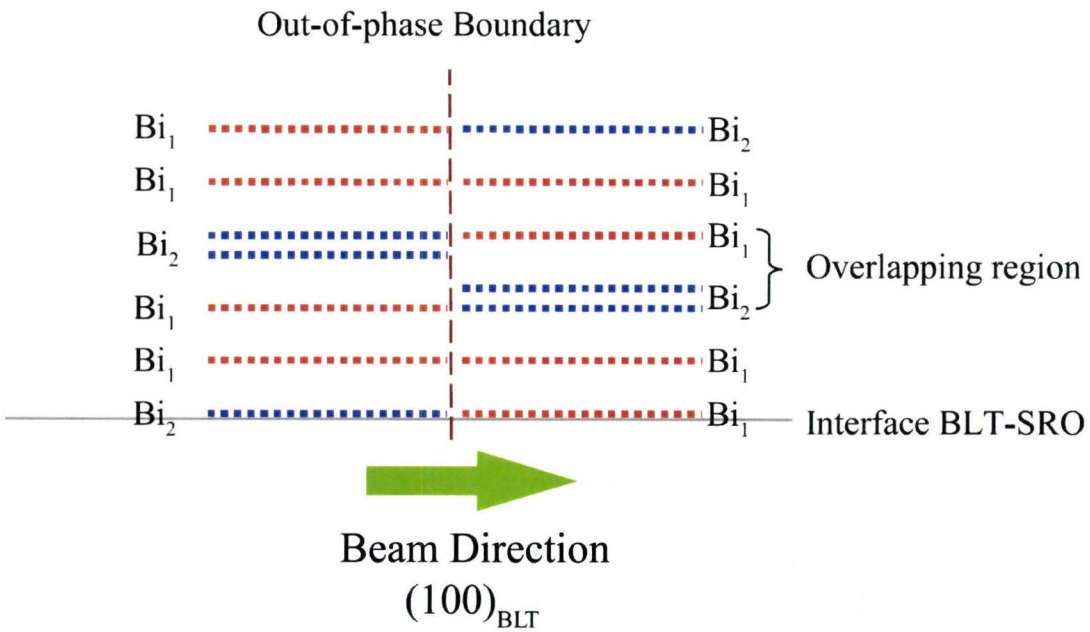

Figure 4.43: An illustration describing a misregistry of BLT unit cells along the beam direction, i.e., (100) BLT, which creates an appearance of extra rows between the Bi_2O_2 layer and the perovskite-like layer due to the overlap of the two unit cell configurations. Bi_1 corresponds to Bi ions in the perovskite-like layer, and Bi_2 to Bi ions in the Bi_2O_2 layer. EELS investigations show that La ions are more dominant in substituting Bi ions in the Bi_2O_2 layer.

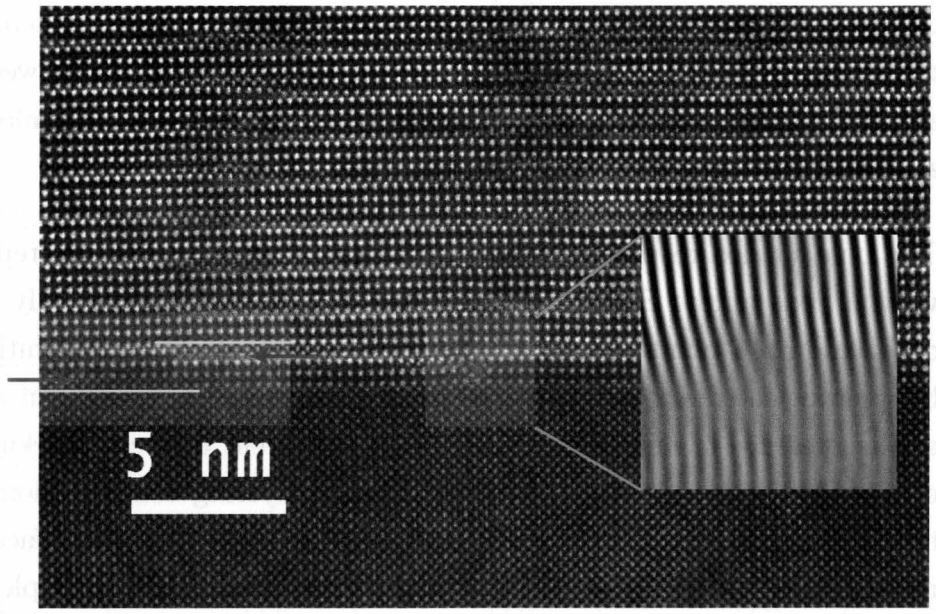

Figure 4.44: The BLT/SRO interface shows the presence of an atomic step inclined to the viewing axis (highlighted in the blue shaded rectangle) and dislocation (highlighted in the green shaded square). The border of the interface atomic step is indicated by the yellow lines, while the red arrows point out the vanishing atomic rows. The inset is a masked, numerically-filtered image corresponding to the green shaded square, which shows a dislocation at the interface.

whether it is SrO-terminated or RuO_2-terminated, (ii) the first deposited atomic layer, whether it is TiO_2, LaO or BiO layer, and (iii) the two-dimensional nature of the OPBs. The SrO-terminated surface generates the defect-free region. However, the RuO_2-terminated surface generates two different regions, i.e., the defect-free region when the next atomic layer is BiO layer, and the defected region when the next atomic layer is LaO layer. This difference in the first deposited atomic layer also governs the the translational shift on both sides of the OPBs. The first deposited atomic layer, whether it is an LaO or BiO layer, creates a variation of unit cell stacking leading to the formation of OPBs. The presence of two-dimensional OPBs, which are parallel to the film-substrate interface, creates alternating regions of overlapping unit cells with different growth order. The overlap of unit cells containing OPBs perpendicular to the beam direction generates the defected region. In contrast, the non-overlapping unit cells generates the defect-free region.

The presence of OPBs along both a- and b-axis of BLT unit cells, however, is not only

caused by the variation of the first deposited atomic layer, but also other factors pertaining to surface roughness of the substrate and lattice misfit between the substrate and the deposited film. A different region along the interface revealed this situation, as shown in Figure 4.44.

The blue shaded rectangle highlights the presence of an atomic step inclined to the viewing axis at the BLT/SRO interface, as indicated by gradually fading intensity of atomic rows pointed out by red arrows. The interface step initiates the border between defected and defect-free regions during growth, which can also be regarded as the presence of misregistry between two different unit cell stackings. Zurbuchen, et al. (2007) have stated that assuming the layering configuration of the growing film is the same, the atomic-scale topography of the substrate surface can induce the nucleation of out-of-phase domains in the growing film. For example, a translational shift introduced between the two regions separated by the interfacial step is depicted for $ABi_2B_2O_9$ on STO in Figure 4.45 (a). In our case, assuming that the stacking configuration is maintained to be the same, one unit cell height variation in the SRO layer will cause a shift of ~0.4 nm, which corresponds to about $^1/_8$ of the c-lattice parameter of the BLT layer. The translational shift between the regions adjacent to the surface step causes a misregistry of adjacent unit cells of $\sim {}^c/_8$ resulting in the formation of out-of-phase boundary (OPB).

The green shaded square in Figure 4.44 highlights the presence of a dislocation, which also introduced an out-of-phase boundary between defect-free and defected regions. Zurbuchen, et al. (2007) have explained that dislocations may perturb the structural correlation along the lateral direction and cause a different layering configuration between regions bordered by the dislocation, as illustrated in Figure 4.45(b) for $A_3B_2O_7$. The lattice misfit between the film and the substrate induces distortions which lead to instability of a BO_6 octahedra. Therefore, at the core of the dislocation, the larger AO with 6-fold coordination has a greater tendency to replace the BO_6 octahedra. This interruption in the first atomic layer causes the split of two separate nuclei alongside the dislocation, which then grow with different stacking configuration. However, the region between the two out-of-phase nuclei is left empty in the schematic illustration shown in Figure 4.45(b) for $A_3B_2O_7$ indicating the arrangement is rather hypothetical since the nucleation mechanism has not been observed experimentally in a layered

oxide (Zurbuchen et al., 2007). In the Figure 4.44, the region above the dislocation shows an extra row of atoms forming a defected region.

In brief, the surface termination of the substrate and the first atomic layer of the film govern the formation of ideal and defected regions in BLT thin films. Different surface terminations also lead to different stacking configurations, which results in the formation of OPBs between adjacent unit cells. Other factors contributing to the formation of OPBs are surface roughness of the substrate and misfit dislocations along the interface. The non-uniformity of the substrate surface or surface steps may induce translational shifts by a fraction of lattice parameters on either side of the steps, while maintaining the same stacking configuration of the film. Meanwhile, misfit dislocations give rise to different stacking configurations of the film on either sides of the dislocations.

4.3.2.2 La Location in BLT

Aberration correction of the probe-forming lens leads to beams with much higher current than the uncorrected beam. These aberration-corrected beams enable EELS experiments to be performed at the atomic level. In this case, EELS linescans were utilized in order to investigate the location of La ions in BLT unit cells, in the Bi_2O_2 layer, in the perovskite-like layer, or in both layers with different levels of occupancy. The results of EELS linescans obtained with the sample oriented with the beam parallel to the ZA $<110>_{BLT}$, showing the $M_{4,5}$ edge of La at 832 eV and 849 eV, are presented in Figures 4.46 (a) and (b) in the Bi_2O_2 layer and the perovskite-like layer, respectively.

The distribution of the La signal along the linescan after background subtraction shows that La ions are present in both the Bi_2O_2 layer and the perovskite-like layer. Nevertheless, the La occupancy in the perovskite-like layer is much less in comparison to that in the Bi_2O_2 layer, as indicated by a factor of three times more counts in Figure 4.46(a) than in Figure 4.46(b). This evidence differs from the previous reports and observations with neutron (Kim et al., 2005) and X-ray diffraction(Kim et al., 2007).

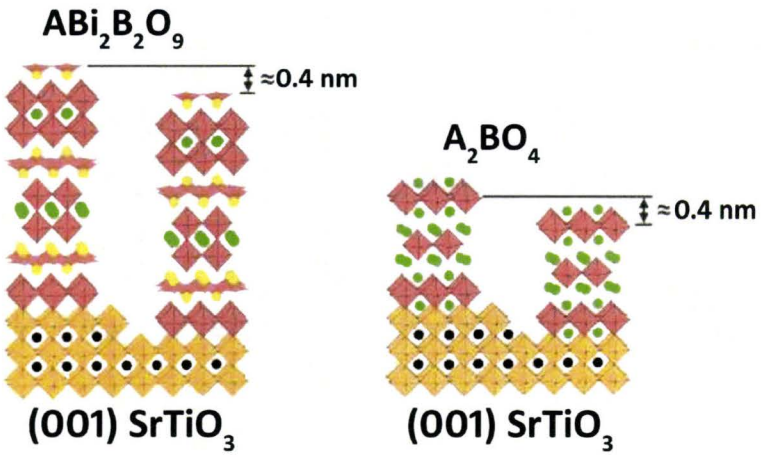

(a)

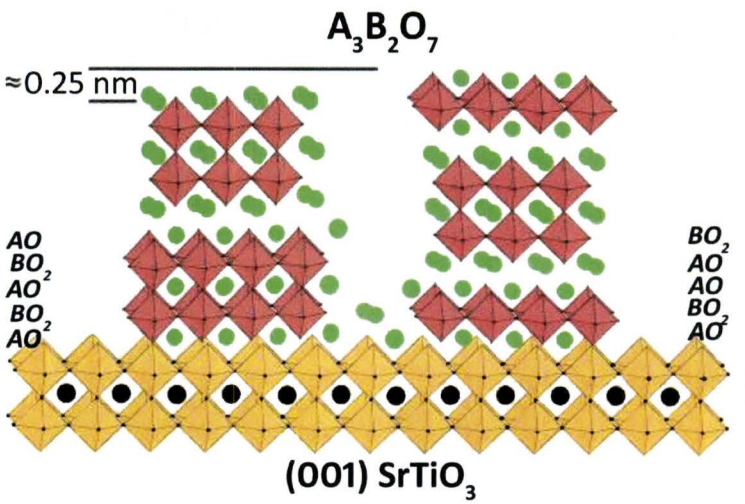

(b)

Figure 4.45: Nucleation mechanisms of layered perovskite on $SrTiO_3$ may be induced by (a) steric nucleation, in which the same layering unit cells nucleate at an interface step and form out-of-phase boundary, and (b) at a misfit dislocation which perturbs the structural correlation of the nucleating layers, causing two regions beside the dislocation to grow with different stacking configurations. (from Zurbuchen et al., 2007)

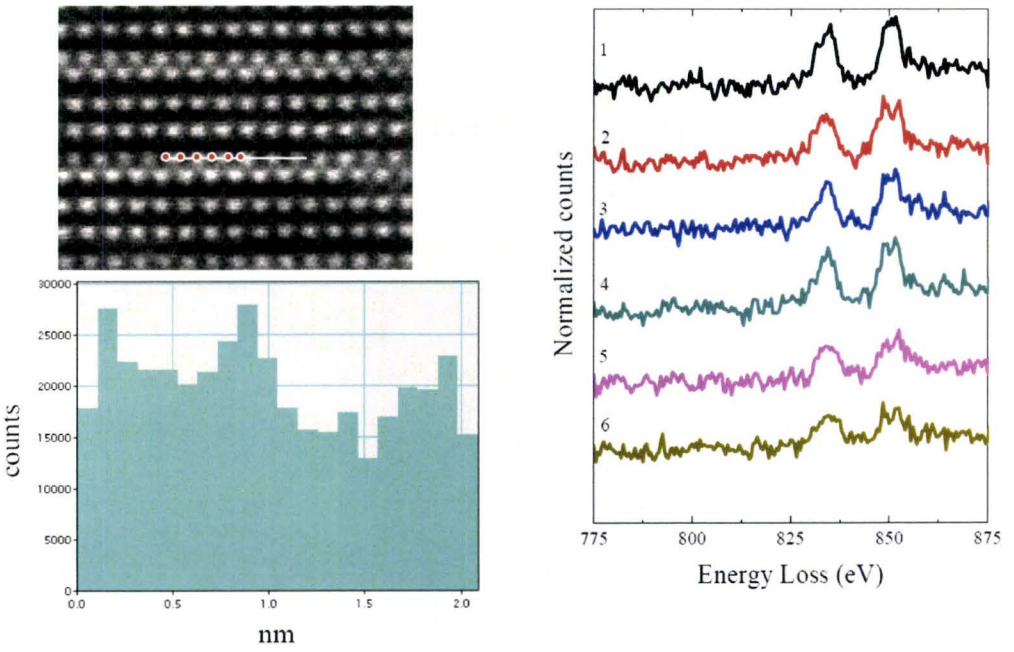

(a)

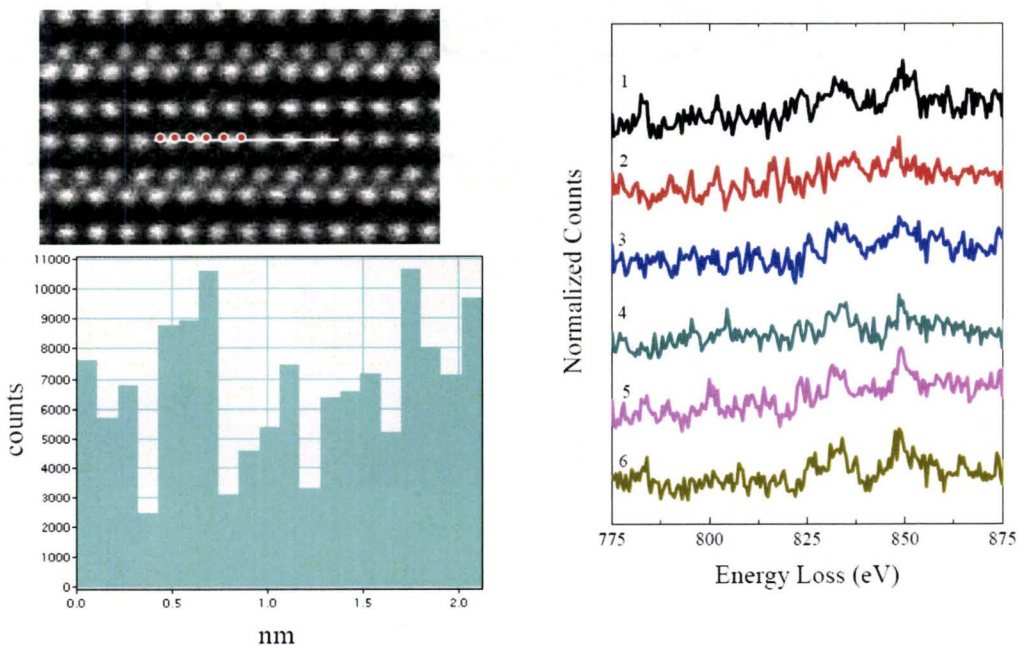

(b)

Figure 4.46: Background subtracted EELS linescans in the BLT unit cell viewed along ZA<110>$_{BLT}$were performed along (a) the Bi_2O_2 layer and (b) the perovskite-like layer. The location where the EELS linescan was performed in the BLT unit cell is indicated by the white line. The red dots along the white line (from left to right) are associated with the numbered EELS spectra.

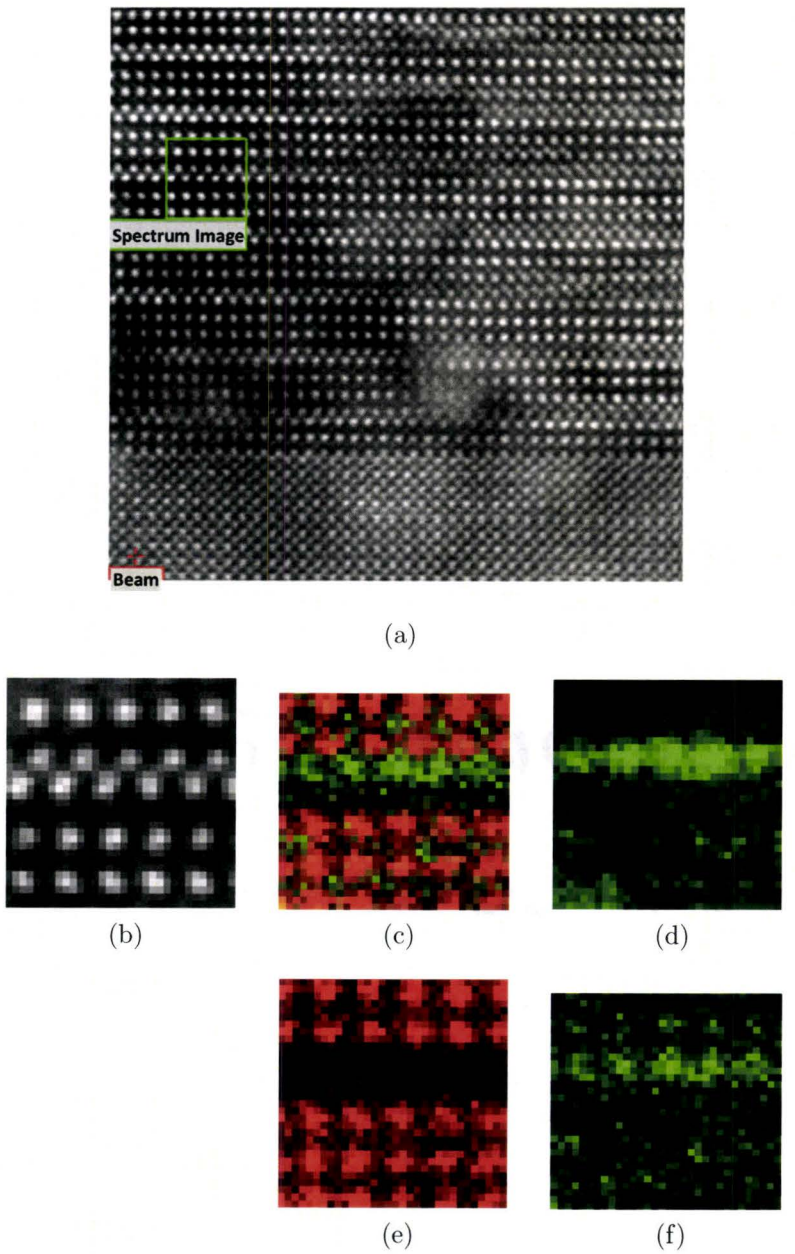

Figure 4.47: (a) HAADF image indicating the location of the ideal region in BL 06 sample, highlighted by a green rectangle, used for EELS mapping; (b) HAADF intensity recorded simultaneously while the EELS spectra in the region of interest (the green rectangle in (a)) were acquired; (c) the EELS composite Ti (red) and La (green) map, (d) La N edge (99 eV) signal, (e) Ti L edge (456 eV) signal, and (f) La M edge (832 eV) signal. The EELS sprectrum image is 32 $\times$ 32 pixel with dwell time of 30 ms/pixel. (*Courtesy of: Sorin Lazar, FEI Electron Optics, The Netherlands* and *McMaster University*)

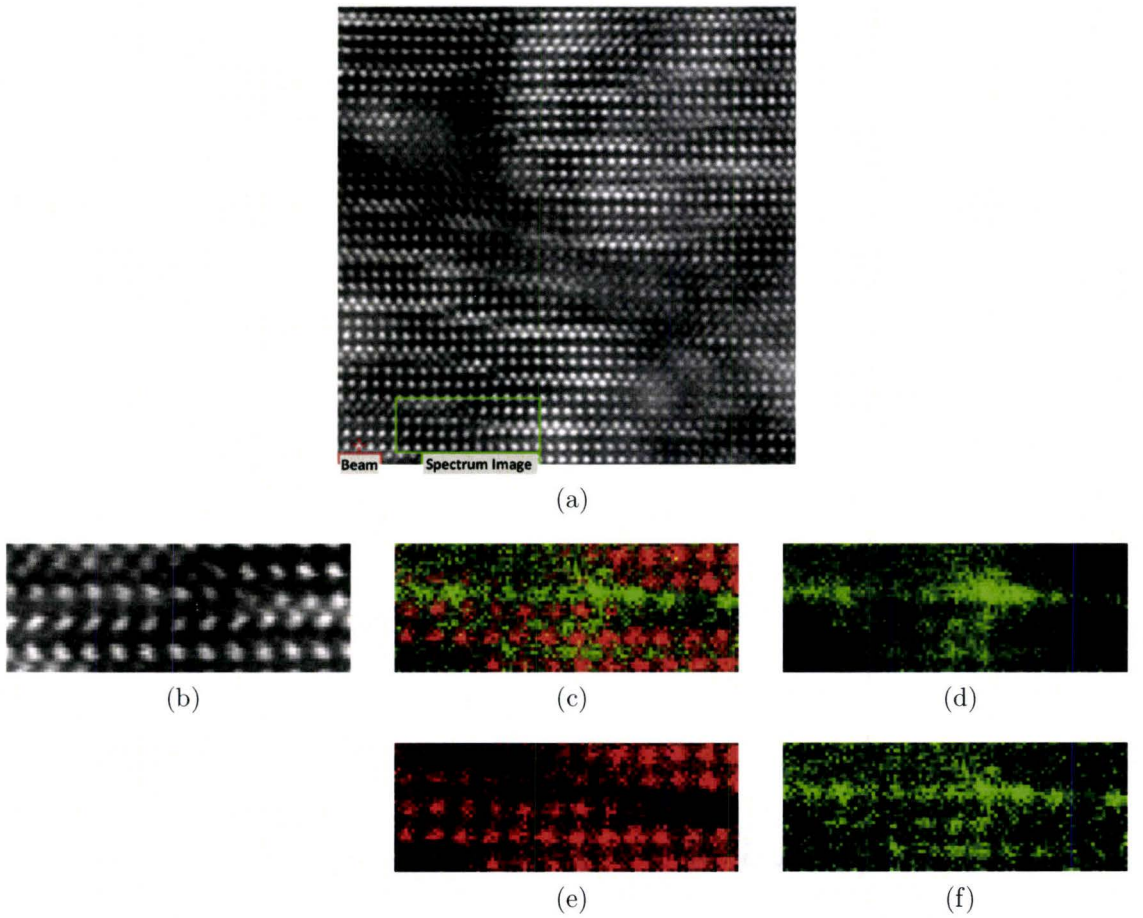

Figure 4.48: (a) HAADF image indicating the location of the defected region in BL 06 sample, highlighted by a green rectangle, used for EELS mapping; (b) HAADF intensity recorded simultaneously while the EELS spectra in the region of interest (the green rectangle in (a)) were acquired; (c) the EELS composite Ti (red) and La (green) map, (d) La N edge (99 eV) signal, (e) Ti L edge (456 eV) signal, and (f) La M edge (832 eV) signal. The EELS spectrum image is 96 $\times$ 36 pixel with dwell time of 40 ms/pixel and frame time of 4 minutes. (*Courtesy of: Sorin Lazar, FEI Electron Optics, The Netherlands* and *McMaster University*)

In addition, results from EELS mapping experiments from defect-free and defected regions in the BL 06 sample are presented in Figures 4.47 and 4.48, respectively. Interestingly, the La N and La M maps (Figures 4.47(d) and (f)) show that La ions are predominantly present in the Bi_2O_2 layer. Furthermore, the maps also show that the La ions specifically occupy the top plane of the Bi_2O_2 layer. This evidence is in contrast to the assumption that La ions are more likely to substitute for Bi in the perovskite-like blocks.

Since the ionic radii of Bi^{3+} (1.17 Å) and La^{3+} (1.16 Å) are very similar, it is interesting to find out the cause of the preferential location of La. The tendency of La to substitute for Bi in Bi_2O_2 layer may be driven by stress relaxation of the strained layer. Strain build-up in the Bi_2O_2 layer has been predicted due to the tolerance factor, i.e., the size matching of the fluorite- and perovskite-like blocks. The mismatch between the a-parameter of the Bi_2O_2 layer of 3.80 Å and that of the perovskite-like blocks of $BiLaTi_3O_{12}$ of 3.89 Å causes strain in the smaller fluorite blocks (Hervoches and Lightfoot, 2000). Taking into consideration that stress relief in the layered perovskites can be achieved in different ways, i.e., by octahedral tilting and lowering of the overall symmetry or by cation diorder, it is more likely for La in $Bi_{3.25}La_{0.75}Ti_3O_{12}$ to relieve the strain build up via partial disorder, and occupy the Bi_2O_2 layers instead of perovskite-like blocks. Based on the argument of Hervoches and Lightfoot, La ions prefer to adopt a more symmetrical environment than Bi in the Bi_2O_2 layers, which may be accomodated by their displacement along the c-axis. Evidence of displacement along the c-axis in order to achieve a more symmetrical environment has been reported for Sr^{2+} in $Bi_{1.8}Sr_{2.2}Ti_{0.8}Nb_{2.2}O_{12}$(Hervoches and Lightfoot, 2000). The Sr^{2+} ions shift upwards in the Bi_2O_2 layer to achieve approximately equal bond lengths (Figure 4.49(b)). This displacement along the c-axis in order to gain a more symmetrical enviroment in the Bi_2O_2 layer may explain the tendency of La occupying the top plane of the Bi_2O_2 layer.

In the defected region, it is also clear that La ions are concentrated in areas where the translational shift between unit cells occurs. The additional tendency of La ions to occupy the OPBs may be related to the high fatigue resistance of BLT, as previously explained in Subsection 4.3.2.1. The occurence of OPBs in BLT but not in BiT might be the reason for its high fatigue resistance. The OPBs can supply additional nucle-

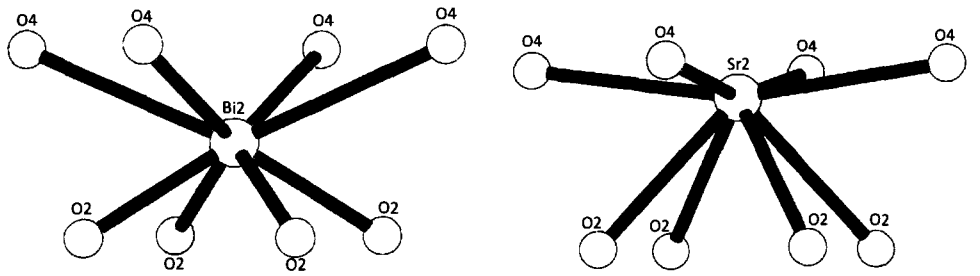

Figure 4.49: (a) The "off-center" coordination environment of Bi ion in the Bi_2O_2 layer and (b) the more symmetrical local environment of Sr ion in the Bi_2O_2 layer. The Sr2 ion is offset of $\sim$ 0.8 Å from the Bi2 ion along the c-axis in order to achieve more regular local geometry with eight approximately equal bond lengths (Hervoches and Lightfoot, 2000).

ation sites of ferroelectric domains during polarization switching making nucleation of those domains not solely dependent on the film-electrode interface (Ding et al., 2001).

Furthermore, the fact that more La ions substitute for Bi ions in the Bi_2O_2 layer actually helps maintain the assymetrical environment of Bi in the perovskite-like blocks, represented by octahedral tilting in Figure 4.42(a) in Section 4.3.2.1. Previously, it has been hypothesized that the extent of octahedral tilting will diminish due to La substitution of Bi in the perovskite-like layer (Hur et al., 2004). However, since most La occupies Bi sites in the Bi_2O_2 layer, the extent of octahedral tilting within the perovskite-like layer is maintained in similar way as that in the BiT parent unit cell. The argument is supported by experimental measurement of remanent polarization. The relatively large value of remanent polarization in BLT is due to octahedral tilting as Bi ions are shifted from their equilibrium position along the a- or b-axis, as observed in Figure 4.42(a).

The preferential substitution of La in the Bi_2O_2 layer is also consistent with previous observations of defected regions induced by surface termination of the substrate and the first atomic layer grown at the film-substrate interface. The first atomic layer governs the stacking sequence during epitaxial growth of the BLT film. When the substrate is SrO-terminated, a TiO_2 layer is formed as the first atomic layer and the BLT unit cell follows a defect free configuration. In the RuO_2-terminated surface,

the first atomic layer may be composed of a BiO or LaO layer. In the case of BiO as the first atomic layer, the rest of the stacking will follow the defect-free unit cell configuration. However, if a LaO layer forms as the first atomic layer, the following unit cell configuration will actually form a defected unit cell with extra atomic rows between the Bi_2O_2 layer and the perovskite blocks. As the variation of surface termination is present in two-dimensions, the defect-free and defected regions appear in alternating periodicity along the lateral direction, especially at the region close to the film-substrate interface.

The presence of out-of-phase boundaries (OPBs), translational defects due to misregistry of the unit cell by a fraction of the unit cell parameter have been clearly observed in the HAADF images of the BLT films. The OPBs have been explained to be influenced by different unit cell configurations depending on the surface roughness or the surface termination of the substrate, the first atomic layer deposited as well as the defects at the interface, such as dislocations. The impact of the presence of OPBs in BLT in terms of its fatigue resistance has not been determined yet. According to literature (Ding et al., 2001, 2001, b), the OPBs observed in BLT but not in BiT may be responsible for the high-fatigue resistance of BLT. The OPBs can act as nucleation sites for ferroelectric domains during polarization switching so that the sole dependency of nucleation on the film-electrode interface is reduced.

The EELS investigation and the atomic resolution HAADF images revealed results that are different from literature in terms of the location of La ions. The literature (Kim et al., 2007, 2008; Park et al., 1999; Hur et al., 2004) reported the tendency of La ions to substitute for Bi ions in the perovskite-like layer. In this study, the La ions have been observed to mostly occupy the top plane of the Bi_2O_2 layer and only a small fraction of the La ions substitutes for the Bi ions in the perovskite-like layer. The preferential location of La is explained as a means of stress relief from the lattice mismatch between perovskite-like and Bi_2O_2 layers. Following the observation of a Sr^{2+} shift in $Bi_{1.8}Sr_{2.2}Ti_{0.8}Nb_{2.2}O_{12}$ as reported by Hervoches and Lightfoot (2000), the preference of the La ions to occupy the top layer of Bi_2O_2 layer may be explained, in that La ions undergo a vertical shift along the c-axis direction of the BLT unit cell to occupy a more symmetrical environment.

Chapter 5

Summary and Future Work

In this study, the benefits of the new generation of aberration-corrected TEMs in improving spatial resolution has been demonstrated by investigations related to the structure-property relationships of several ferroelectric and multiferroic Bi-based perovskite oxides, which were grown by PLD. The more direct interpretation and the suppressed delocalization in HRTEM images, as well as the achievement of atomic resolution in HAADF images, demonstrated in the observation across interfaces and thin films in this study the capability and stability of the FEI-Titan TEM. The information limit of this new generation of TEM was $\sim$ 0.65 Å.

Investigations using both selected area diffraction and convergent beam diffraction of a BFCO 1/1 thin film on a SRO /(111)STO substrate with the sample oriented at the ZA$<110>_{STO}$ showed extra reflections along the $<111>$ direction which correspond to either anti-phase tilting of BO_6 octahedra or ordering of B-site cations. The relatively large saturation magnetization, one order of magnitude higher in BFCO 1/1 relative to that of BFO alone, strongly indicates that B-site cationic ordering is likely to be present in the film. In addition, when the sample is oriented along the ZA $<100>_{STO}$ the CBEDP of BFCO 1/1 also showed non-periodic extra reflections which have been attributed to presence of the secondary phase, Bi_2O_3.

Using the quantitative L_3/L_2 ratio of EELS experiments performed on BFCO 1/1 confirmed the valence of Fe and Cr to be 3+, and therefore no charge ordering is

present in BFCO 1/1. The O K-near edge structure of BFCO revealed transitions to the unoccupied $2p$ levels hybridized with the $3d$-t_{2g} and e_g of both Fe and Cr. Such transitions result in broadening of the O-K edge structure of BFCO 1/1, which consists of the superimposed structures of O K-edges in the Fe^{3+} and the Cr^{3+} environments. In addition, longer acquisition time and instability of the high tension of STEM may also contribute to the broadening of the O-K edge structure.

Further investigations on samples where the ratio of BFO and BCO deposition is 1 to 3, i.e., BFCO 1/3 on (111)SRO/STO substrates, revealed the presence of a layered structure with Bi double-layers that was not observed in the BFCO 1/1 phase. The fact that the piezoelectric response of the BFCO 1/3 sample on (111)SRO/STO deviated significantly from the <111> direction and the magnetization of BFCO 1/3 was much lower than that of BFCO 1/1 strongly suggests that B-site cationic ordering is no longer present in BFCO 1/3. The appearance of Bi-double layers in the HAADF image strongly indicates that the unit cell structure of the BFCO 1/3 sample was different from the double perovskite structure of BFCO 1/1.

The structure refinement from the θ-2θ XRD experiments of BFCO 1/3 gave a monoclinic unit cell with space group #14 (P 2_1/n) and lattice parameters of: $a = 10.9764$ Å, $b = 10.8479$ Å, and $c = 15.9073$ Å, with $\alpha = \beta = 90°$ and $\gamma = 90.3°$. The atomic resolution ADF images revealed a unit cell configuration that resembles a Ruddlesden-Popper structure. Therefore, the RP structure served as the starting point for estimation of atomic positions in the unit cell of BFCO 1/3. The modification and refinement of atomic position was iterated based on the agreement of d-spacings with those calculated from the experimental SAEDPs. Despite the agreement in d-spacings of simulated SAEDPs of BFCO 1/3, the exact pattern of experimental SAEDP of BFCO 1/3 was not reproduced, due to the lack of precise information regarding the atomic positions in the unit cell. Further complication in interpreting the SAEDPs comes from the presence of variations of the in-plane unit cell orientations and of twinning along the growth direction, as revealed by 3D X-ray Diffraction reciprocal space maps.

The EELS linescan and mapping of BFCO 1/3 revealed that the B-site cations, i.e., Fe and Cr, are present predominantly in the dark band between Bi-double layers. Only a small amount of Fe and Cr is present within the Bi-double layer. This compositional distribution is in agreement with the simulated atomic projection using a modified

RP model.

Despite the agreement between the HAADF images and EELS maps with the simulated atomic projection, the simulated SAEDPs were not fully in agreement with the experimental ones. In order to refine the unit cell as well as atomic position of BFCO 1/3, further investigation requires samples at different orientations, which were not available during the study period. Pending the availability of samples in the future, the determination of atomic position in the BFCO 1/3 unit cell is definitely crucial for better fundamental understanding of BFCO 1/3. Another unit cell model that may be used as a starting point for determination of the BFCO 1/3 unit cell is the Aurivillius type with alternating Bi_2O_2 fluorite-like layer and $Bi_{n-1}(Fe/Cr)_nO_{3n+1}$ perovskite-like layer with n=1.

The investigation of the BLT samples aimed to pinpoint the exact location of La dopant atoms in the BiT unit cell in order to contribute to the understanding of the mechanism of good fatigue resistance of BLT thin films in comparison to BiT. The EELS experiments revealed the exact position of La ions in the BiT parent unit cell that is pre-dominantly in the top part of the Bi_2O_2 layer, instead of in the perovskite-like layers as has been reported in the literature. The dominant La substitution in the Bi_2O_2 layer indicates that the anisotropic bonding of Bi-O in the perovskite layers is maintained and therefore similar to that in BiT. The preservation of the degree of octahedral tilt in BLT as that in BiT is responsible for its relatively large remanent polarization. The evidence of octahedral tilt in BLT was visually captured in probe-corrected HAADF images. In addition, La ions also concentrated at the defected area where a translational shift between adjacent unit cells occurs. This indicates that there seems to be a significant relationship between the presence of La ions and the formation of the translational defects, especially since such defects are only observed in BLT but not in BiT.

The HAADF images showed the presence of out-of-phase boundaries (OPBs) in BLT, which could be responsible for the fatigue-free behaviour during polarization reversals of up to 10^{10} cycles. According to the argument proposed by Ding et al. (2001) on the anti-phase boundaries (APBs), which is basically OPBs with a translational shift of $1/2$ the unit cell parameter, the impact of OPBs on the fatigue resistance of BLT can be explained. The OPBs provide extra nucleation sites for ferroelectric domains, so

that during polarization reversals, ferroelectric domain nucleation can occur not only at the film-electrode interface, but also at the OPBs. Even though the accumulation of oxygen vacancies occurs at the film-electrode interface, domain reversals can still proceed at the OPBs, and therefore gives a fatigue-free characteristic of the BLT compared to BiT.

The HAADF images acquired at the interface of BLT and SRO revealed that the generation of OPBs is mainly influenced by (i) the surface roughness and the surface termination of the substrate, (ii) the first atomic layer deposited on the substrate, and (iii) the dislocations due to lattice misfit between the film and the substrate. When the SRO buffer layer is SrO-terminated, the successive layer is likely to be TiO_2 and followed by a defect-free unit cell configuration. However, for RuO_2-terminated substrate, both the BiO layer and the LaO layer are likely to be the successive layer. The following configuration of unit cells after the BiO layer will be defect-free, yet those after the LaO layer will be defected. However, the mechanism on how the defect-free and the defected regions are formed based on the first deposited atomic layer is still an open question. In the future, elemental EELS mapping across the BLT/SRO interface will be able to determine the exact surface termination, and therefore explain the exact mechanism of the formation of the defect-free and defected regions in BLT films. The dislocations present at the interface due to lattice misfit also perturb the coherent configuration, resulting in different unit cell configurations between the adjacent regions.

Some future works regarding this study are as follows:

1. Investigating the plan view TEM sample of BFCO 1/3 films on (111)-oriented substrate to confirm variation of unit cell directions in the in-plane direction and to identify the type of twinning present in the films. In addition, the plan view TEM sample helps to provide more information about the atomic positions of the BFCO 1/3 unit cells.

2. Determination of the atomic positions of the modified RP unit cell by perfoming XRD and EELS experiments, provided that more samples of BFCO 1/3 films with different orientations are available. As an alternative to the modified RP unit cell, the Aurivillius unit cell $Bi_{n-1}(Fe/Cr)_nO_{3n+1}$ with n=1 may be a possible

unit cell structure of BFCO 1/3.

3. Determination of the first atomic layer of BLT films deposited on SRO substrate by performing EELS experiments at the film-substrate interface. This information will give insights on the mechanism of formation of both defected and defect-free regions in the BLT films and confirm the hypothesis on the effect of substrate terminations on structural growth of the BLT films.

The advances in TEM field by integration of aberration correctors and monochromators have made the simultaneous acquisition of high spatial resolution imaging and spectroscopy possible. The high spatial resolution in both HRTEM and HAADF imaging provides information at the atomic level, which contributes further towards better understanding of the chemistry at interfaces, the formation of defects, the growth mechanisms and properties of a wide-range of materials, especially in complex structures. The capability of atomic resolution EELS mapping is advantageous in the field of materials research in understanding the local composition and bonding environments of specific elements in various compounds. In addition, the simultaneous collection of high-angle scattering signals with an HAADF detector and the EELS signal provides a direct correlation between the spectrocopic information and the specific location in the sample.

Appendix A

Titan Ray Diagrams in TEM/STEM Modes

TEM and STEM operating modes have similarities in terms of the ray diagrams through the reciprocity principle (Zeitler and Thomson, 1970). The ray diagrams pertaining to TEM and STEM operations in Titan 80-300 are displayed in Figure A.1(a) and (b), respectively. The interchange between these two modes can be performed in simple and easy way, provided that the correct alignment files are available. A major difference between the two modes lies in the strength of the C3 condenser lens and the mini condenser lens. In TEM mode, usually the mini condenser lens is ON, and the microscope operates in microprobe mode. In contrast, in STEM mode, the mini condenser lens is OFF; the microscope operates in the nanoprobe mode. After loading the right alignment file, only a little fine tuning of the pivot points and rotation center is needed to achieve near optimal alignment for atomic resolution imaging.

The major difference in terms of optics between a Titan 80-300 and conventional TEM lies in the condenser system, namely the presence of the C3 condenser lens. The C3 condenser lens enables the C2-C3 zoom capability of illuminated area (or beam diameter) while maintaining parallel illumination in TEM mode and of beam convergence in STEM mode. The zoom system is represented in Figure A.2, where an image in between the two lenses can be moved up and down without changing the

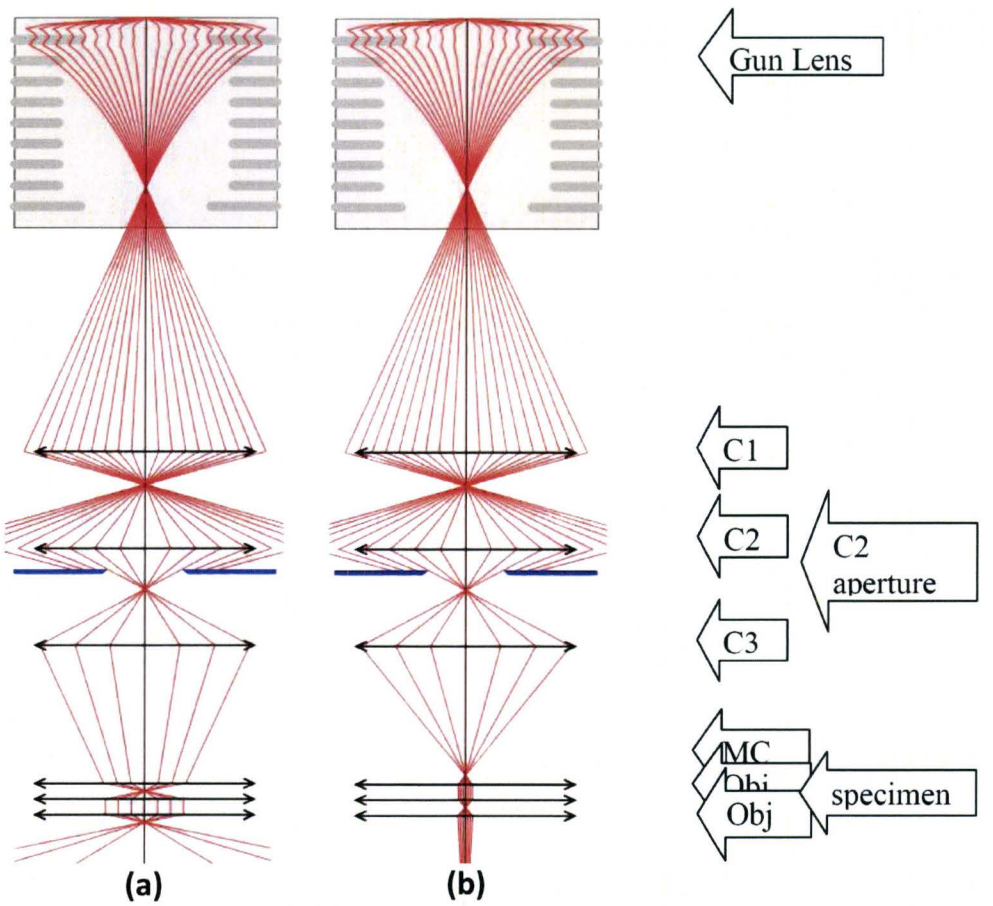

Figure A.1: The two basic settings of (a) TEM (parallel illumination) and (b) STEM (probe illumination). The locations of lenses, aperture and specimen are indicated by the arrows on the side, where C1, C2, C3 and MC are first condenser, second condenser, third condenser and mini condenser lens, respectively. (from FEI-Titan manual)

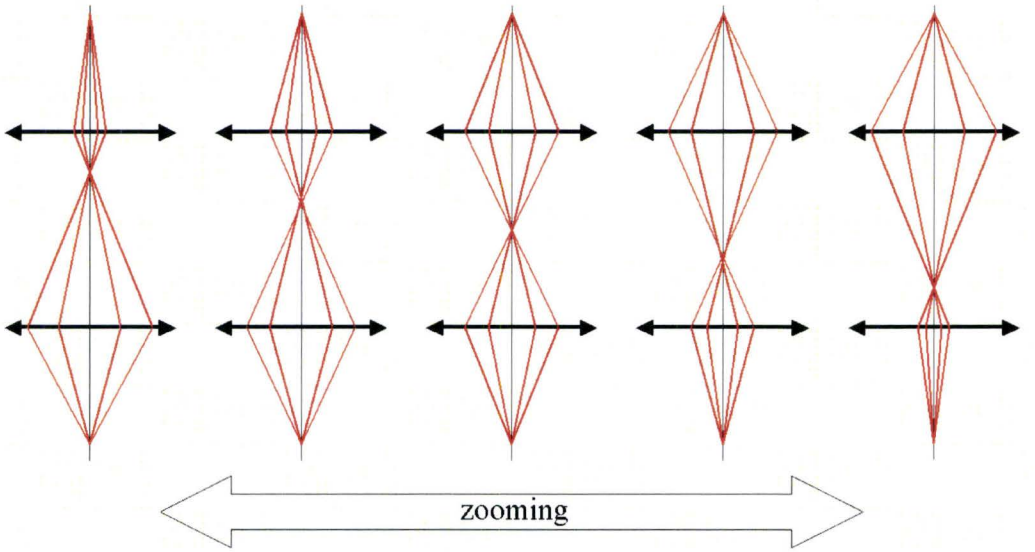

Figure A.2: The C2-C3 system zooming system in a Titan 30-800 TEM (from FEI-Titan manual).

position of the image in front of the first lens or that of the image after the second lens. Such features were not available in any conventional TEM.

In TEM mode, however, the C3 lens can be easily switched off when the C2-C3 zoom system is misaligned. Figures A.3 (a) to (c) display the ray diagrams where C3-lens was off, similar to the conventional TEM system, showing the beam changes from converging to parallel and finally to diverging, as the strength of the C2 lens is decreased. Despite the unused C3 condenser lens in TEM mode, the image resolution achieved was still much better than that achieved by conventional TEM due to the presence of an image corrector that compensates for the spherical aberration coefficient of objective lens.

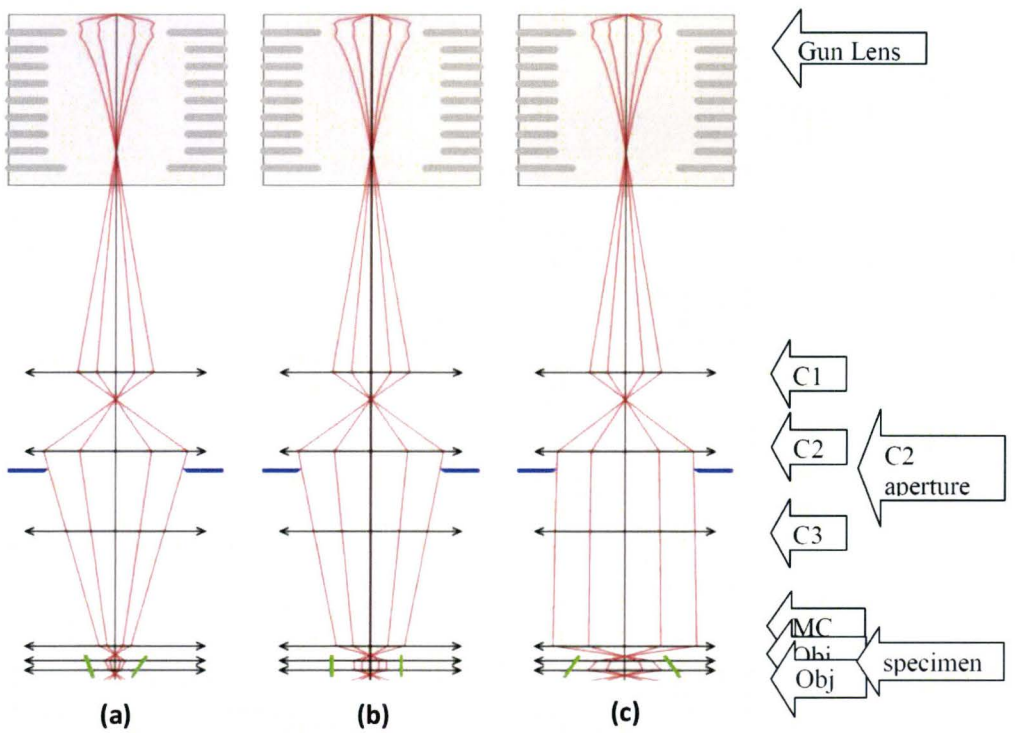

Figure A.3: Ray diagrams of Titan operation in TEM mode with the C3 lens 'OFF', where the electron beam changes from converging (a) to parallel (b) and to diverging (c) with increasing area of illumination. The locations of lenses, aperture and specimen are indicated by the arrows on the side. (from FEI-Titan manual)

Appendix B

List of Software

- GATAN Digital Micrograph^{TM} v. 1.6.0 for acquiring and processing of TEM images and spectra.
- JEMS (Java Electron Microscopy Software) v. 2.0819w2005 by P. Stadelmann for calculating Contrast Transfer Function, simulating Selected Area Diffraction Pattern (SADP), Convergent Beam Electron Diffraction Pattern (CBEDP), and phase contrast/ high resolution TEM (HRTEM) images.
- CrystalKitX v. 1.9.3 for constructing unit cell structures and interfaces.
- MacTempasX v. 2.2.6 for HRTEM and ADF STEM image simulation.
- Michael Robertson's Multislice code based on Kirkland's code (Kirkland, 1998) for HRTEM and ADF image simulation with flexibility to vary the angular detector range and to perform faster calculations with multiple CPUs. The sequence for running the simulation is schematically displayed in Figure B.1. (Email contact: michael.robertson@acadiau.ca)

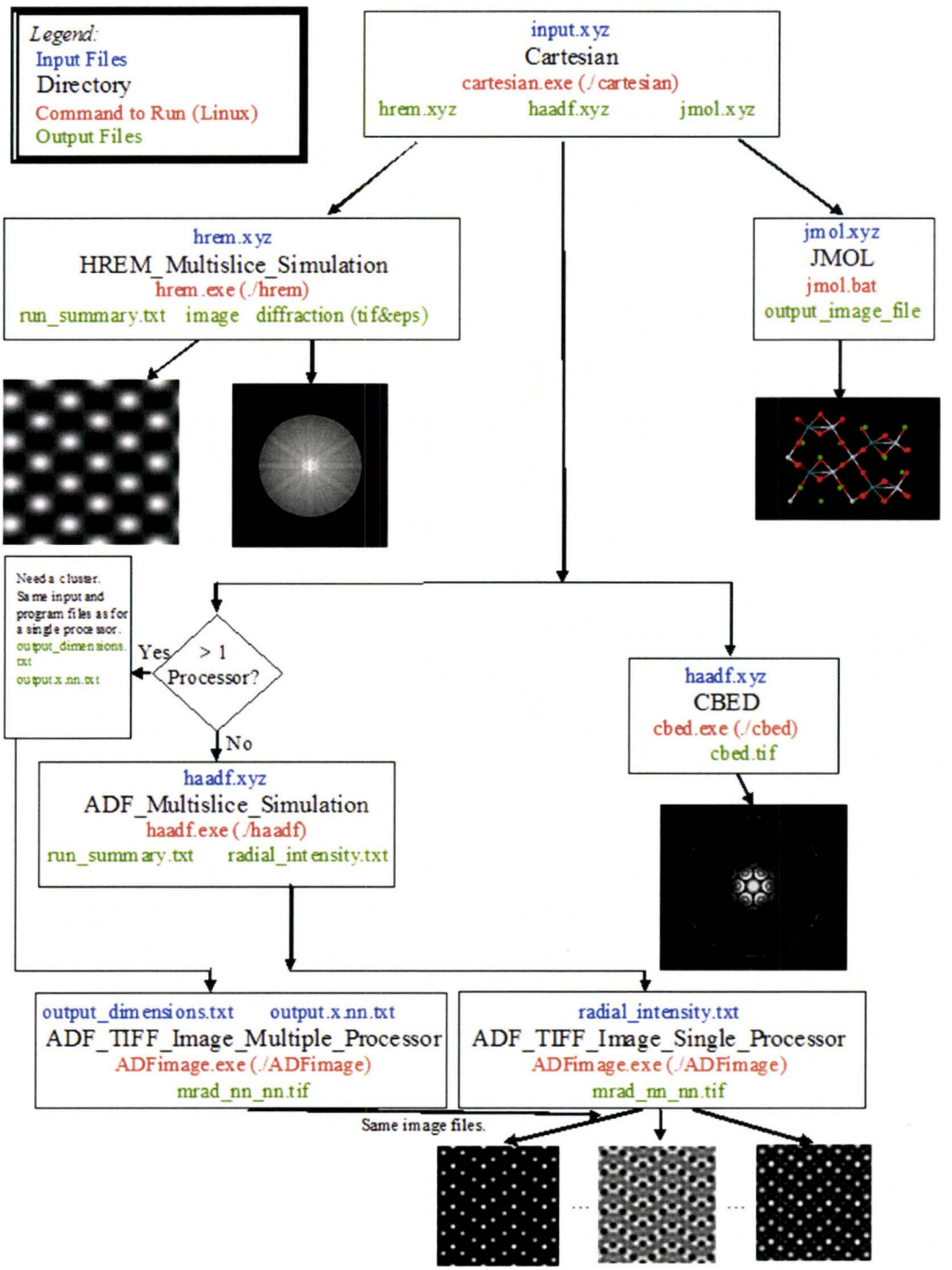

Figure B.1: The step-by-step schematic for running Michael Robertson's codes (from: CCEM Summer School 2008).

Bibliography

Allied 2008, December. http://www.alliedhightech.com.

Bae, J. C., Kim, S. S., Choi, E. K., Song, T. K., Kim, W.-J., & Lee, Y.-I. 2005, Thin Solid Films *472*(1-2), 90–95.

Baettig, P., Ederer, C., & Spaldin, N. A. 2005, Physical Review B *72*(21), 214105.

Bai, F. M., Wang, J. L., Wuttig, M., Li, J. F., Wang, N. G., P., P. A., Zvezdin, A. K., Cross, L. E., & Viehland, D. 2005, Applied Physics Letters *86*(3), 032511.

Bea, H., Bibes, M., Barthelemy, A., Bouzehouane, K., Jacquet, E., Khodan, A., Contour, J.-P., Fusil, S., Wyczisk, F., Forget, A., Lebeugle, D., Colson, D., & Viret, M. 2005, Applied Physics Letters *87*(7), 072508.

Bea, H., Bibes, M., Fusil, S., Bouzehouane, K., Jacquet, E., Rode, K., Bencok, P., & Barthelemy, A. 2006, Physical Review B *74*(2), 020101(R).

Bea, H., Bibes, M., Ott, F., Dupe, B., Zhu, X. H., Petit, S., Fusil, S., Deranlot, C., Bouzehouane, K., & Barthelemy, A. 2008, Physical Review Letters *100*(1), 017204.

Bleloch, A. & Lupini, A. 2004, Materials Today *7*(12), 42–48.

Botton, G. A., Appel, C. C., Horsewell, A., & Stobbs, W. M. 1995, Journal of Microscopy *180*(3), 211–216.

Buseck, P., Cowley, J., & Eyring, L. (Eds.) 1989. *High-Resolution Transmission Electron Microscopy - and Associated Techniques.* Oxford University Press.

Cave, L., Al, T., Loomer, D., Cogswell, S., & Weaver, L. 2006, Micron *37*(4), 301–309.

Chen, K. F., Lo, S. C., Chang, L., Egerton, R., Kai, J. J., Lin, J. J., & Chen, F. R. 2007, Micron *38*(4), 354–361.

Chon, U., Shim, J. S., & Jang, H. M. 2003, Materials Science Forum, 439, 1–6.

Chu, M.-W., Ganne, M., Caldes, M. T., & Brohan, L. 2002, Journal of Applied Physics *91*(5), 3178–3187.

Daulton, T. L. & Little, B. J. 2006, Ultramicroscopy *106*(7), 561–573.

Davies, P. K., Wu, H., Borisevich, A. Y., Molodetsky, I. E., & Farber, L. 2008, Annual Review of Materials Research, 38, 369–401.

de Araujo, C. A.-P., Cuchiaro, J. D., McMillan, L. D., Scott, M. C., & Scott, J. F. 1995, Nature *374*(6523), 627–629.

Ding, Y., Liu, J. S., Maclaren, I., Wang, Y. N., & Kuo, K. H. 2001, Ferroelectrics *262*(1), 37–46.

Ding, Y., Liu, J. S., Qin, H. X., Zhu, J. S., & Wang, Y. N. 2001, Applied Physics Letters *78*(26), 4175–4177.

Ederer, C. & Spaldin, N. A. 2005, Physical Review B *71*(6), 060401(R).

Egerton, R. F. 1996. *Electron Energy-Loss Spectroscopy in the Electron Microscope* (2nd ed.). New York: Plenum Press, USA.

Egerton, R. F. 2007, Ultramicroscopy *107*(8), 575–586.

Falke, M., Falke, U., Bleloch, A., Teichert, S., Beddies, G., & Hinneberg, H. J. 2005, Applied Physics Letters *86*(20), 203103.

Falke, U., Bleloch, A., Falke, M., & Teichert, S. 2004, Physical Review Letters *92*(11), 116101.

Gajek, M., Bibes, M., Fusil, S., Bouzehouane, K., Fontcuberta, J., Barthelemy, A. E., & Fert, A. 2007, Nature Materials *6*(4), 296–302.

Gautreau, O., Harnagea, C., Gunawan, L., Botton, G. A., Normandin, F., Veres, T., Pintilie, L., Alexe, M., & Pignolet, A. 2008, Journal of Physics D: Applied Physics *41*(11), 112002.

Haertling, G. H. 1999, Journal of the American Ceramic Society *82*(4), 797–818.

Haider, M., Rose, H., Uhlemann, S., Kabius, B., & Urban, K. 1998, Journal of Electron Microscopy *47*(5), 395–405.

Haider, M., Rose, H., Uhlemann, S., Schwan, E., Kabius, B., & Urban, K. 1998, Ultramicroscopy *75*(1), 53–60.

Hervoches, C. H. & Lightfoot, P. 2000, Journal of Solid State Chemistry *153*(1), 66–73.

Hesse, D., Zakharov, N. D., Pignolet, A., James, A. R., & S, S. 2000, Cryst. Res. Technol., 35, 641–651.

Hetherington, C. J. D. 2004. Strategies for one angstrom resolution. In *Electron Microscopy and Analysis 2003*, Institute of Physics Conference Series, pp. 219–224. 179.

Hill, N. A. 2000, Journal of Physical Chemistry B *104*(29), 6694–6709.

Hill, N. A., Baettig, P., & Daul, C. 2002, The Journal of Physical Chemistry B *106*(13), 3383–3388.

Hill, N. A. & Rabe, K. M. 1999, Physical Review B *59*(13), 8759–8769.

Hur, S. G., Park, D. H., Kim, T. W., & Hwang, S.-J. 2004, Applied Physics Letters *85*(18), 4130–4132.

Hwang, H. Y. 2006, Science *313*(5795), 1895–1896.

Ishiwara, H., Okuyama, M., & Arimoto, Y. (Eds.) 2004. *Ferroelectric Random Access Memories: Fundamentals and Applications.* Springer Verlag, New York.

Jia, C. L., Contreras, J. R., Schubert, J., & Lentzen, M. 2003, Journal of Crystal Growth *247*(3-4), 381–386.

Jia, C. L., Lentzen, M., & Urban, K. 2004, Microscopy and Microanalysis *10*(2), 174–184.

Jia, C. L., Lentzen, M., & Urban, K. 2005, Microscopy and Microanalysis *11*(2), 113–115.

Jia, C. L., Schubert, J., Heeg, T., Mi, S. B., Chen, H. Y., Joschko, B., Burianek, M., Muhlberg, M., & Urban, K. 2006, Acta Materialia *54*(9), 2383–2391.

Joshi, P. C. & Krupanidhi, S. B. 1993, Applied Physics Letters *62*(16), 1928–1930.

Kanzig, W. 1987, Ferroelectrics *74*(1), 285–291.

Kijima, T., Kimura, S., Kawahara, Y., Ohe, K., Yada, M., & Machida, M. 1999, Journal of Solid State Chemistry *146*(1), 60–64.

Kim, D. H., Christen, H. M., Varela, M., Lee, H. N., & Lowndes, D. H. 2006, Applied Physics Letters *88*(20), 202503.

Kim, S. J., Moriyoshi, C., Kimura, S., Kuroiwa, Y., Kato, K., Takata, M., Noguchi, Y., & Miyayama, M. 2007, Applied Physics Letters *91*(6), 062913.

Kim, T. W., Hur, S. G., Han, A. R., Hwang, S. J., & Choy, J. H. 2008, Journal of Physical Chemistry C *112*(9), 3434–3438.

Kim, Y. I., Nahm, S. H., Yoon, D. J., & Gregory, D. H. 2005, Journal of Electroceramics *14*(3), 265–271.

Kirkland, E. J. 1998. *Advanced Computing in Electron Microscopy*, Volume 250. New York: Plenum Press., USA.

Knapp, M. C. 2006. *Investigation into the structure and properties of ordered perovskites, layered perovskites, and defect pyrochlores.* Ph. D. thesis, The Ohio State University.

Krivanek, O. L., Dellby, N., & Lupini, A. R. 1999, Ultramicroscopy *78*(1-4), 1–11.

Krivanek, O. L., Dellby, N., Spence, A. J., Camps, R. A., & Brown, L. M. 1997. Aberration correction in the stem. In *Electron Microscopy and Analysis 1997*, Institute of Physics Conference Series, pp. 35–40. 153.

Krivanek, O. L., Nellist, P. D., Dellby, N., Murfitt, M. F., & Szilagyi, Z. 2003, Ultramicroscopy *96*(3-4), 229–237.

Krumeich, F. 2007, August 29. Eth zurich - electron microscopy. http://www.microscopy.ethz.ch.

Lebeugle, D., Colson, D., Forget, A., Viret, M., Bataille, A. M., & Gukasov, A. 2008, Physical Review Letters *100*(22), 227602.

Lowndes, D., Geohegan, D. B., Puretzky, H. H., Norton, D. P., & Rouleau, C. M. 1996, Science *273*(5277), 898–903.

Lufaso, M. W. & Woodward, P. M. 2004, Acta Crystallographica B *60*(1), 10–20.

Lupini, A. R., Varela, M., Borisevich, A. Y., Travaglini, S. M., & Pennycook, S. J. 2004. Advances in aberration corrected stem at ornl. In *Electron Microscopy and Analysis 2003*, Institute of Physics Conference Series, pp. 211–214. 179.

Maurice, J. L., Imhoff, D., Contoury, J. P., & Colliex, C. 2006, Philosophical Magazine *86*(15), 2127–2146.

Mitterbauer, C., Kothleitner, G., Grogger, W., Zandbergen, H., Freitag, B., Tiemeijer, P., & Hofer, F. 2003, Ultramicroscopy *96*(3-4), 469–480.

Murakami, M., Fujino, S., Lim, S. H., Long, C. J., Salamanca-Riba, L. G., Wuttig, M., Takeuchi, I., Nagarajan, V., & Varatharajan, A. 2006, Applied Physics Letters *88*(15), 152902.

Nave, R. 2006, June 20. Hyper physics - light and vision. http://hyperphysics.phy-astr.gsu.edu/Hbase/phyopt/Raylei.html.

Nechache, R., Harnagea, C., Gunawan, L., Carignan, L. P., Maunders, C., Menard, D., Botton, G. A., & Pignolet, A. 2007, IEEE Transactions on Ultrasonics Ferroelectrics and Frequency Control *54*(12), 2645–2652.

Nechache, R., Harnagea, C., Pignolet, A., Normandin, F., Veres, T., Carignan, L. P., & Menard, D. 2006, Applied Physics Letters *89*(10), 102902.

Niitaka, S., Azuma, M., Takano, M., Nishibori, E., Takata, M., & Sakata, M. 2004, Solid State Ionics *171*(1-4), 557–559.

Ohring, M. 2002. *Materials Science of Thin Films: Deposition and Structure.* Academic Press.

Pan, X. Q., Jiang, J. C., Theis, C. D., & Schlom, D. G. 2003, Applied Physics Letters *83*(12), 2315–2317.

Park, B. H., Hyun, S. J., Bu, S. D., Noh, T. W., Lee, J., Kim, H. D., Kim, T. H., & Jo, W. 1999, Applied Physics Letters *74*(13), 1907–1909.

Park, B. H., Kang, B. S., Bu, S. D., Noh, T. W., Lee, J., & Jo, W. 1999, Nature *401*(6754), 682–684.

Pennycook, S. J., Varela, M., Hetherington, C. J. D., & Kirkland, A. I. 2006, MRS Bulletin *31*(1), 36–43.

Ramesh, R. & Spaldin, N. A. 2007, Nature Materials *6*(1), 21–29.

Reaney, I. M. 2007, Journal of Electroceramics *19*(1), 1–8.

Reaney, I. M., Colla, E. L., & N., S. 1994, Japanese Journal of Applied Physics *33*(7A), 3984–3990.

Robertson, M., Burns, M., & Morisson, T. 2006, Microscopical Society of Canada Bulletin *33*(1), 19–28.

Rose, H. 1990, Optik *85*(1), 19–24.

Rose, H. H. 2009, J Electron Microsc (Tokyo) *58*(3), 77–85.

Sande, J. B. V. & Hall, E. L. 1979, Journal of The American Ceramic Society *62*(5), 246–254.

Sawada, H., Tomita, T., Naruse, M., Honda, T., Hambridge, P., Hartel, P., Haider, M., Hetherington, C., Doole, R., Kirkland, A., Hutchison, J., Titchmarsh, J., & Cockayne, D. 2005, Journal of Electron Microscopy *54*(2), 119–121.

Scherzer, O. 1947, Optik, 2, 114–132.

Scherzer, O. 1949, Journal of Applied Physics *20*(1), 20–29.

Schmid, H. K. & Mader, W. 2006, Micron *37*(5), 426–432.

Scott, J. F. 2007, Nature Materials *6*(4), 256–257.

Seth, V. K. & Schulze, W. A. 1989, January, IEEE Transactions on Ultrasonics, Ferroelectrics, and Frequency Control *36*(1), 41–49.

Shannon, R. D. 1976, Acta Crystallographica A *32*(5), 751–767.

Spence, J. C. H. 2003. *High-Resolution Electron Microscopy (Monographs on the Physics and Chemistry of Materials) 3rd edition.* Oxford University Press.

Sugawara, F., Iiida, S., Syono, Y., & Akimoto, S.-i. 1968, J. Phys. Soc. Jpn. *25*(6), 1553–1558.

Uhlemann, S. & Haider, M. 1998, Ultramicroscopy *72*(3-4), 109–119.

Valasek, J. 1921, Physical Review *17*(4), 475–481.

Williams, D. B. & Carter, C. B. 1996. *Transmission Electron Microscopy: A Textbook for Materials Science* (2nd ed.). New York: Plenum Press, USA.

Woodward, D. I. & Reaney, I. M. 2005, Acta Crystallographica Section B-Structural Science, 61, 387–399.

Woodward, D. I., Reaney, I. M., Eitel, R. E., & Randall, C. A. 2003, Journal of Applied Physics *94*(5), 3313–3318.

Zach, J. & Haider, M. 1995, Optik *98*(3), 112–118.

Zaharescu, M., Fruth, V., Berger, D., Lanculescu, A., Tenea, E., & Groza, J. R. 2005. Preparation and characterization of bifeo3. Poster.

Zeitler, E. & Thomson, M. 1970, Optik, 31, 258–280, 359–366.

Zemlin, F., Weiss, K., Schiske, P., Kunath, W., & Herrmann, K. H. 1978, Ultramicroscopy *3*(1), 49–60.

Zurbuchen, M. A., Tian, W., Pan, X. Q., Fong, D., Streiffer, S. K., Hawley, M. E., Lettieri, J., Jia, Y., Asayama, G., Fulk, S. J., Comstock, D. J., Knapp, S., Carim, A. H., & Schlom, D. G. 2007, Journal of Materials Research *22*(6), 1439–1471.